FACULDADE DE ENGENHARIA DA UNIVERSIDADE DO PORTO

Optimization of Gyroid-shaped Structures Manufactured by Fused Filament Fabrication in Polylactic Acid

Ana Isabel Lopes Pais

DISSERTAÇÃO DE MESTRADO



Mestrado Integrado em Engenharia Mecânica

Supervisor: Professor Doutor Fernando Jorge Lino Alves

Co-Supervisor: Professor Doutor Jorge Américo Oliveira Pinto Belinha

July, 2020

Optimization of Gyroid-shaped Structures Manufactured by Fused Filament Fabrication in Polylactic Acid

Ana Isabel Lopes Pais

Mestrado Integrado em Engenharia Mecânica

July, 2020

Abstract

Weight reduction is one of the main concerns when designing any component as it reduces material cost and green house gas emissions, among other aspects. Several numerical approaches exist in the literature with the objective of making any component with known mechanical solicitations optimized in terms of mass minimization and stiffness maximization.

Thus, the objective of this work is the development of optimized structures with geometry retention taking advantage of cellular materials, namely the gyroid infill, and generating functionally graded cellular structures with higher stiffness-to-weight ratio.

The BESO (Bi-evolutionary structural optimization) approach as well as remodelling algorithms based on biological phenomena, namely bone remodelling, were employed for obtaining the density map which the functional gradient is based on. Smoothing functions were tested as a possibility of enhancing stiffness as abrupt density changes are avoided. This density map was materialized into a stereolitographic file (*.stl*).

The gyroid infill was characterized in order to create a remodelling law inspired on bone material laws. The gyroid law was implemented in the analysis software FEMAS which presented the density map as an output.

Each gradient was made by assembling solids corresponding to density levels based on the density maps, and then, adding an infill at the corresponding density.

Two numerical methods were tested, the Finite Element Method and the Natural Neighbout Radial Point Interpolation Method which is a meshless method. Simulations consisted on three distinct and benchmark flexural load cases and specimens were printed using FFF technology in PLA (E = 3145 MPa, ν = 0.3). Then, each specimen was tested experimentally according to the appropriate load case. Numerical results correlated to the experimental results.

Finally, a practical application in bone tissue scaffold was suggested since, in the literature, surface shapes where the gyroid is included (TPMS - Triply Periodic Minimal Surfaces) are proposed as a base of fabricating bone scaffold both with uniform and variable density. This practical application was also tested experimentally and correlated to numerical results.

Keywords: Additive Manufacturing, Structural Optimization, Bone Remodelling, Gyroid Infill

Resumo

A redução de peso é uma das maiores procupações durante o projecto de um componente ao reduzir o custo do material, emissões de gases responsáveis pelo efeito de estufa, entre outros aspetos. Existe na literatura diversas abordagens numéricas com o objetivo de tornar otimizado em termos de redução de massa e maximização de rigidez, qualquer componente de que se conheça a solicitação mecânica a que está sujeito.

Deste modo, o objetivo deste trabalho é o desenvolvimento de estruturas otimizadas com manutenção de geometria tirando partido dos materiais celulares, nomeadamente o preenchimento de giroide e gerar estruturas celulares com gradiente funcional com elevada rigidez específica.

A abordagem BESO (Otimização estrutural bi-evolucionária), assim como algoritmos de remodelação baseados em fenómenos biológicos, nomeadamente a remodelação óssea, foram utilizados para obtenção do mapa de densidades no qual o gradiente funcional é baseado. Testaram-se funções de suavização com o objetivo de aumentar a rigidez ao evitar mudanças abruptas de densidade. O mapa de densidades foi então materializado num ficheiro *.stl*.

O preenchimento em giróide foi caracterizado de modo a gerar a lei de remodelação inspirada em leis de remodelação de tecido ósseo. A lei de remodelação de giróide foi implementada no software de análise FEMAS que apresenta o mapa de densidades como output do programa.

Cada gradiente foi concretizado através da concatenação de sólidos correspondentes a cada nível de densidade baseado nos mapas de densidade e, posteriormente, preenchidos à densidade respetiva.

Testaram-se dois métodos numéricos, o Método dos Elementos Finitos e um método sem malha (NNRPIM). As simulações consistiram em três casos de carga à flexão distintos e conhecidos, e os provetes foram impressos usando FFF (impressão 3D por extrusão de filamento) em PLA (E = 3145 MPa, ν = 0.3). Seguidamente, cada provete foi ensaiado experimentalmente de acordo com o caso de carga apropriado. Os resultados numéricos correlacionaram com os resultados experimentais.

Finalmente, sugeriu-se uma aplicação prática de replicação de tecido ósseo pois, na literatura, as TPMS (Superfícies Mínimas Triplas Periódicas) nas quais se inclui o giróide são propostas como base para o fabrico de tecido ósseo quer com densidade uniforme ou variável. Esta aplicação prática foi também testada experimentalmente e correlacionada com resultados numéricos.

Keywords: Fabrico Aditivo, Otimização Estrutural, Remodelação Óssea, Preenchimento em Giróide

Acknowledgements

Sure enough that it is not possible to identify here every person or entity without whom this work would not be completed, I would like to express my deepest and truest gratitude to the following persons:

My supervisor, Professor Jorge Lino for the opportunity I have been given and for the exceptional availability shown throughout the course of this thesis, and to my co-supervisor, Professor Jorge Belinha for all the valuable suggestions and clarifications which were vital.

FEUP and the Department of Mechanical Engineering for providing me with the necessary tools as well as providing me with their facilities.

All technicians in the workshop of the Mechanical Engineering department for the collaboration in machining of tools used for the experimental part of this thesis.

The colleagues and friends I found in LDPS, always available and happy to help. I owe so much of my 3D printing knowledge to their *know-how* and experience.

The friends I made throughout these 5 years. The friendship and knowledge we have shared were truly crucial to get to this point. I wish you all the best of luck and success for your future lives.

My cousin, Manuel Salvador who has kindly lend me his tools and workshop to work during quarantine when I was not able to leave the city where I reside.

My Family! My brother Jorge and sisters Margarida and Catarina who make me work to be the best I can. My grandmother Adelaide who I deeply respect and admire, a true role model. My uncle and aunt, Pedro and Cristiana who have always been my friends as long as I can remember and little Benedita as well.

My parents, Fátima and Jorge. I cannot possibly imagine all the work that has been and continues to be placed in the education which I was given as well as that of my brothers. They are my true friends and role models. Thank you for always helping me more than humanly possible. May I make you proud!

Ana

Institutional Acknowledgements

The author truly acknowledges the work conditions provided by the Applied Mechanics Division (SMAp) of the department of mechanical engineering (DEMec) of Faculty of Engineering of the University of Porto (FEUP), and by the MIT-Portugal project "MIT-EXPL/ISF/0084/2017", funded by Massachusetts Institute of Technology (USA) and "Ministério da Ciência, Tecnologia e Ensino Superior - Fundação para a Ciência e a Tecnologia" (Portugal).

Additionally, the authors gratefully acknowledge the funding of Project NORTE-01-0145-FEDER-000022 - SciTech - Science and Technology for Competitive and Sustainable Industries, cofinanced by Programa Operacional Regional do Norte (NORTE2020), through Fundo Europeu de Desenvolvimento Regional (FEDER).

Finally, the author acknowledges the synergetic collaboration with the collaborators of "Computational Mechanics Research Laboratory CMech-Lab" (ISEP/FEUP/INEGI), and its director, Prof.Dr. Jorge Belinha, and its senior advisors, Prof.Dr. Renato Natal Jorge and Prof.Dr. Lúcia Dinis.

Contents

1 Introduction **1**
- 1.1 Framework . . . 1
- 1.2 Objectives . . . 2
- 1.3 Structure of the report . . . 4

2 Contextualization **5**
- 2.1 Functionally graded cellular structures and infill optimization for AM . . . 5
  - 2.1.1 Functionally graded cellular structures obtained with topology optimization algorithms . . . 9
  - 2.1.2 Density variable gyroid infill obtained by cross sectional stress analysis . 12
  - 2.1.3 Triply periodic minimal surfaces applied to tissue engineering . . . 14
- 2.2 Gyroid structure . . . 16
- 2.3 Additive manufacturing . . . 17
  - 2.3.1 Fused filament fabrication . . . 19
  - 2.3.2 Materials . . . 20
  - 2.3.3 Equipment . . . 22
  - 2.3.4 Economic aspects . . . 23

3 Numerical Methods **25**
- 3.1 Finite element method . . . 25
- 3.2 NNRPIM: Natural Neighbour Radial Point Interpolation Method . . . 27
  - 3.2.1 Meshless methods . . . 27
  - 3.2.2 Natural Neighbour Radial Point Interpolation Method . . . 30

4 Bone Remodelling and Structural Optimization **37**
- 4.1 Bone remodelling . . . 38
  - 4.1.1 Material laws . . . 38
  - 4.1.2 Bone remodelling algorithms . . . 38
- 4.2 Structural optimization . . . 44
  - 4.2.1 SIMP . . . 44
  - 4.2.2 ESO . . . 46
  - 4.2.3 BESO . . . 47

5 Methodology **51**
- 5.1 Overview . . . 51
- 5.2 Materials and methods . . . 52
- 5.3 Creation of the *g-code* file . . . 53
  - 5.3.1 Matlab code . . . 53

5.3.2 Smoothing parameters . . . 55
5.3.3 Slicing software . . . 57
5.4 Printing parameters . . . 58
5.5 Calibration of infill densities . . . 59
5.6 Gyroid law . . . 60
5.7 Stiffness evaluation . . . 64

6 Numerical Simulation Results **67**
6.1 Load cases . . . 68
6.2 Discretization . . . 68
6.2.1 FEM . . . 69
6.2.2 NNRPIM . . . 70
6.3 Structural optimization - Parabolic law . . . 70
6.3.1 Load case 1 . . . 71
6.3.2 Load case 2 . . . 73
6.3.3 Load case 3 . . . 75
6.4 Structural optimization - Linear law . . . 77
6.4.1 Load case 1 . . . 78
6.4.2 Load case 2 . . . 81
6.4.3 Load case 3 . . . 84
6.5 Gyroid remodelling - Law case 1 . . . 89
6.5.1 Load case 1 . . . 90
6.5.2 Load case 2 . . . 94
6.5.3 Load case 3 . . . 97
6.6 Gyroid remodelling - Law case 2 . . . 100
6.6.1 Load case 1 . . . 100
6.6.2 Load case 2 . . . 103
6.6.3 Load case 3 . . . 105
6.7 Bone remodelling . . . 106
6.8 Computational effort . . . 109
6.9 Result discussion . . . 109

7 Experimental Study **111**
7.1 Printed specimens . . . 111
7.2 Common issues . . . 115
7.3 Necessary accessories for testing . . . 116
7.4 Flexural testing . . . 117
7.4.1 Structural optimization - Parabolic law . . . 118
7.4.2 Structural optimization - Linear law . . . 125
7.4.3 Gyroid remodelling law 1 . . . 132
7.4.4 Gyroid remodelling law 2 . . . 141
7.5 Influence of printing direction . . . 146
7.6 Comparison with numerical simulations . . . 147
7.6.1 Summary . . . 148
7.7 Result discussion . . . 150

8 Femur Scaffold Analysis: a preliminary study **153**
8.1 Model and boundary conditions . . . 153
8.2 Analysis . . . 155
8.2.1 Linear elasto-static analysis . . . 155
8.2.2 Remodelling analysis . . . 157
8.3 Printing of the prototypes . . . 165
8.4 Experimental testing . . . 166
8.5 Result discussion and conclusions . . . 168

9 Conclusions **171**
9.1 General conclusions . . . 171
9.2 Future work . . . 172

Bibliography **175**

A Matlab script **189**
A.1 Inputs . . . 189
A.2 FEM_STL.m . . . 190
A.3 Meshless_stl.m . . . 191
A.4 Common script . . . 192
A.4.1 mesh.m . . . 194
A.4.2 smoothing.m . . . 195
A.4.3 groups.m . . . 196
A.4.4 createSolids . . . 198
A.4.5 triangulateSolids.m . . . 198

B Technical Drawings **203**
B.1 Tool for 4 point flexural testing . . . 203
B.2 Support for the specimens while testing . . . 204
B.3 Positioning tool . . . 204
B.4 Support tool for testing of the femur scaffold specimens . . . 205

C Printed and Tested Specimens **207**
C.1 Structural optimization - Parabolic Law . . . 207
C.2 Structural optimization - Linear law . . . 214
C.3 Gyroid remodelling law 1 . . . 217
C.4 Gyroid remodelling law 2 . . . 223
C.5 Femur scaffold prototypes . . . 226

List of Figures

Figure 1.1 Cellular solids based on the gyroid shape. Adapted from (Abueidda et al., 2019) . . . 1
Figure 1.2 Overview of the methodology which is being proposed in this thesis . . . 3

Figure 2.1 Skinframe lightweight structure as proposed by Wang et al. (2013) 6
Figure 2.2 Interior honeycomb-like structures as proposed by Lu et al. (2014) 6
Figure 2.3 Library of unit truss cells. Adapted from (Nguyen and Vignat, 2016) . . . 7
Figure 2.4 Optimized engine braket based on the BESO algorithm. Adapted from (Tang et al., 2015) . . . 8
Figure 2.5 Lattice structure design based on the geometric mesh. Adapted from (Chen, 2006) . . . 8
Figure 2.6 Example of the mapping process for mechanical properties (a) material properties diagram; (b) 3D mapping result. Adapted from (Li et al., 2018b). . . . 9
Figure 2.7 Optimization strategies for ann MBB beam (a) load and boundary conditions; (b) uniform gyroid structure; (c) standard TO approach; (d) shape retaining optimization; (d) direction constrained optimization. Adapted from (Li et al., 2018b) 10
Figure 2.8 Methodology used by Li and Yao (2019) for obtaining FGS based on a density map. Adapted from (Li and Yao, 2019). . . . 10
Figure 2.9 Three-dimensional structural unit. Adapted from (Li and Yao, 2019) . . . 11
Figure 2.10 Results of the infill optimization of shell parts.vf is the volume fraction of the part and c is the compliance value Adapted from (Wu, 2018). . . . 12
Figure 2.11 Methodology proposed where (a) is the original object; (b) is the local density distribution after stress analysis and (c) is the final object with the gradual infill. Adapted from (Li et al., 2016). . . . 13
Figure 2.12 Detailed explanation of the methodology proposed. Adapted from (Li et al., 2016). . . . 13
Figure 2.13 Schematic representation of the influence of parameter t on the relative density of gyroid structures: (a) Gyroid structure with gradual infill from t = 0 to t = 1.413 and (b) percentage of the sectional area as a function of parameter t. Adapted from (Li et al., 2016). . . . 13
Figure 2.14 Design method proposed by Feng et al. (2018b) for the creation of density graded structures . . . 14
Figure 2.15 Bone tissue scaffold examples composed of TPMS structures. Adapted from (Yoo, 2011a) . . . 15
Figure 2.16 Common triply periodic minimal surfaces. Adapted from (Feng et al., 2018b) 16
Figure 2.17 Schematics of gyroid surface, gyroid cellular and gyroid foam. Adapted from (Yang et al., 2019). . . . 18

Figure 2.18 Gyroid compressive behaviour at several density values where a) is tested horizontally to the printed layers and b) is tested vertically to the printed layers. Adapted from (Abueidda et al., 2019) 18
Figure 2.19 Schematic representation of the FDM/FFF process. Adapted from (Silva, 2019; Wohlers et al., 2018) 19
Figure 2.20 Additive Manufacturing workflow. Adapted from (Vitale et al., 2016) . . . 20
Figure 2.21 Stress-strain results of tensile specimens printed in three different desktop printers. U stands for Ultimaker, M stands for MakerBot and Z stands for Zortrax. Adapted from (Braconnier et al., 2020) 23
Figure 2.22 Sales evolution and areas of application for industrial equipment according to the Wohlers report of 2019 (Wohlers, 2019) 24
Figure 2.23 Sales evolution and areas of application for desktop equipment according to the Wohlers report of 2019 (Wohlers, 2019) 24

Figure 3.1 Representation of a domain Ω in triangles and quadrilaterals. Adapted from (Reddy, 2005). 26
Figure 3.2 Path from a real structure to a computational model. Adapted from (Onate, 2013). 27
Figure 3.3 Influence domains adapted from (Belinha, 2014) 29
Figure 3.4 Node dependent numerical discretization. Adapted from (Belinha, 2014) . 31
Figure 3.5 Obtaining the Voronoi diagram of a discrete nodal distribution through the concept of natural neighbours. a) to d) demonstrate how a single cell is obtained, e) represents the Voronoi cell for node n_0 and f) represents the Voronoi diagram. Adapted from (Belinha, 2014). 32
Figure 3.6 a) "First-degree" influence cell and b) "Second-degree" influence cell. Adapted from (Belinha, 2014) 33
Figure 3.7 Gaussian quadrature procedure. Adapted from (Belinha, 2014) 33
Figure 3.8 Obtaining the subcells from a Voronoi cell. Adapted from (Belinha, 2014) 34
Figure 3.9 Division of a regular cell into triangular subcells. Adapted from (Belinha, 2014) 34

Figure 4.1 Elasticity modulus in the axial direction. Adapted from Belinha (2014) . . 39
Figure 4.2 Elasticity modulus in the transverse direction. Adapted from Belinha (2014) 39
Figure 4.3 Bone remodelling algorithm. Adapted from (Belinha, 2014) 43
Figure 4.4 Flowchart of the BESO method. Adapted from (Huang and Xie, 2010) . . 50

Figure 5.1 Procedural steps taken in the course of this work 52
Figure 5.2 Ender 3 printer from Creality 3D (Creality, 2018) 53
Figure 5.3 Input windows in the Matlab script 54
Figure 5.4 Smoothing function type 1 56
Figure 5.5 Smoothing function type 2 56
Figure 5.6 Smoothing function type 3 57
Figure 5.7 Slicing software 58
Figure 5.9 Tensile specimen 61
Figure 5.8 Tensile test results 61
Figure 5.10 Compression test results for the gyroid infill at 20% and 50% nominal infill density. Adapted from (Silva, 2019) 62
Figure 5.11 Gyroid remodelling law results 63
Figure 5.12 Compression stress approximation for both cases 64

Figure 6.1 Schematic diagram of the numerical study present in this work 68
Figure 6.2 Load cases at study 69
Figure 6.3 Convergence study results 69
Figure 6.4 Element type used in the FEM analysis 70
Figure 6.5 Full integration scheme 70
Figure 6.6 Remodelling laws in structural optimization 71
Figure 6.7 Schematic representation of the truss structure obtained with the structural optimization remodelling with a parabolic material law 71
Figure 6.8 Density distribution obtained with the structural optimization with a parabolic law using the FEM and the NNRPIM for the load case of Figure 6.2b 72
Figure 6.9 Stiffness evaluation for load case 1 using a structural optimization analysis with a parabolic law using the the FEM and the NNRPIM 73
Figure 6.10 Structure into which the structural optimization for load case 2 evolves . . 73
Figure 6.11 Density distribution obtained with the structural optimization with a parabolic law using the FEM and the NNRPIM for the load case of Figure 6.2c 74
Figure 6.12 Stiffness evaluation for load case 2 using a structural optimization analysis with a parabolic law using the FEM and the NNRPIM 75
Figure 6.13 Density distribution obtained with the structural optimization using a parabolic law using the FEM and the NNRPIM for the load case of Figure 6.2d 76
Figure 6.14 Stiffness evaluation for load case 3 using a structural optimization analysis with a parabolic law using the FEM and the NNRPIM 77
Figure 6.15 Density distribution obtained with the structural optimization with a linear material law using the FEM and NNRPIM for the load case of Figure 6.2b 78
Figure 6.16 Comparison of the behaviour of different sets of remodelling parameters for the structural optimization analysis with a linear law using the FEM and the NNRPIM in load case 1 79
Figure 6.17 Stiffness evaluation for load case 1 using a structural optimization analysis with a linear law (IR = 0.00 and RR = 0.10) using the FEM and the NNRPIM . . 80
Figure 6.18 Stiffness evaluation for load case 1 using a structural optimization analysis with a linear law (IR = 0.00 and RR = 0.05) using the FEM and the NNRPIM . . 81
Figure 6.19 Density distribution obtained with the structural optimization with a linear material law using the FEM and NNRPIM for the load case of Figure 6.2c 82
Figure 6.20 Comparison of the behaviour of different sets of remodelling parameters for the structural optimization analysis with a linear law using the FEM and NNRPIM in load case 2 83
Figure 6.21 Stiffness evaluation for load case 2 using a structural optimization analysis with a linear law (IR = 0.00 and RR = 0.10) using the FEM and the NNRPIM . . 84
Figure 6.22 Stiffness evaluation for load case 2 using a structural optimization analysis with a linear law (IR = 0.00 and RR = 0.05) using the FEM and the NNRPIM . . 85
Figure 6.23 Density distribution obtained with the structural optimization with a linear material law using the FEM and NNRPIM for the load case of Figure 6.2d 86
Figure 6.24 Comparison of the behaviour of different sets of remodelling parameters for the structural optimization analysis with a linear law using the FEM and NNRPIM in load case 3 87
Figure 6.25 Stiffness evaluation for load case 3 using a structural optimization analysis with a linear law (IR = 0.00 and RR = 0.10) using the FEM and the NNRPIM . . 88
Figure 6.26 Stiffness evaluation for load case 3 using a structural optimization analysis with a linear law (IR = 0.00 and RR = 0.05) using the FEM and the NNRPIM . . 89

Figure 6.27 Schematic representation of a truss structure obtained with optimization techniques seen in the literature for load case 1 90
Figure 6.28 Density distribution obtained with the remodelling with gyroid remodelling law 1 using the FEM and the NNRPIM for the load case of Figure 6.2b 91
Figure 6.29 Stiffness evaluation for load case 1 with a gyroid remodelling analysis (law 1) using the FEM and the NNRPIM 92
Figure 6.30 Density distribution obtained with gyroid remodelling law 1 using the FEM and the NNRPIM for the load case of Figure 6.2b with α = 0.00, β=0.05 and a maximum number of times that a point can remodel of 2 93
Figure 6.31 Comparison of the behaviour of different sets of remodelling parameters using the FEM and NNRPIM in load case 1 with gyroid remodelling law 1 94
Figure 6.32 Density distribution obtained with gyroid remodelling law 1 using the FEM and the NNRPIM for the load case of Figure 6.2c 95
Figure 6.33 Density distribution obtained with gyroid remodelling law 1 using the NNRPIM for the load case of Figure 6.2c with α = 0.00, β = 0.05 and a maximum number of times that a point can remodel of 2 96
Figure 6.34 Comparison of both sets of remodelling parameters for the gyroid remodelling analysis with gyroid remodelling law 1 96
Figure 6.35 Stiffness evaluation for load case 2 with a gyroid remodelling analysis (law 1) using the FEM and the NNRPIM 97
Figure 6.36 Density distribution obtained with gyroid remodelling law 1 using the FEM and the NNRPIM for the load case of Figure 6.2d 98
Figure 6.37 Stiffness evaluation for load case 3 with a gyroid remodelling analysis (law 1) using the FEM and the NNRPIM 99
Figure 6.38 Density distribution obtained with gyroid remodelling law 1 using the FEM and the NNRPIM for the load case of Figure 6.2d with α = 0.05, β = 0.05 and a maximum number of times that a point can remodel of 2 100
Figure 6.39 Density distribution obtained with gyroid remodelling law 2 using the FEM and the NNRPIM for the load case of Figure 6.2b 101
Figure 6.40 Stiffness evaluation for load case 1 obtained with a gyroid remodelling analysis (law 2) using the FEM and the NNRPIM 102
Figure 6.41 Density distribution obtained with gyroid remodelling law 2 for FEM and NNRPIM for the load case of Figure 6.2c 103
Figure 6.42 Stiffness evaluation for load case 2 obtained with a gyroid remodelling analysis (law 2) using the FEM and the NNRPIM 104
Figure 6.43 Density distribution obtained with gyroid remodelling law 2 for FEM and NNRPIM for the load case of Figure 6.2d 105
Figure 6.44 Stiffness evaluation for load case 3 obtained with a gyroid remodelling analysis (law 2) using the FEM and the NNRPIM 106
Figure 6.45 Density distribution obtained with the bone remodelling analysis using the FEM and NNRPIM for the load case of Figure 6.2b with α = 0.00, β=0.10 and a maximum number of times that a point can remodel of 2 107
Figure 6.46 Density distribution obtained with the bone remodelling analysis using the FEM and NNRPIM for the load case of Figure 6.2c with α = 0.00, β=0.10 and a maximum number of times that a point can remodel of 2 108
Figure 6.47 Density distribution obtained with the bone remodelling analysis using the FEM and NNRPIM for the load case of Figure 6.2d with α = 0.00, β=0.10 and a maximum number of times that a point can remodel of 2 109

Figure 7.1 Schematic representation of printing direction and respective placement of parts on the printing bed 114
Figure 7.2 Printed specimens example - Load case 1 114
Figure 7.3 Printed specimens example - Load case 2 115
Figure 7.4 Printed specimens example - Load case 3 115
Figure 7.5 Common defects in printed parts due to bad adhesion of the first layer to the building surface 116
Figure 7.6 Four point bending tool - technical drawing in Annex B 117
Figure 7.7 Support to prevent the specimens from falling during testing - technical drawing in Annex B 117
Figure 7.8 Positioning tool - technical drawing in Annex B 117
Figure 7.9 Structural optimization specimens which did not undergo any smoothing . 118
Figure 7.10 Experimental results for the structural optimization (parabolic law) specimens subject to load case 1 119
Figure 7.11 Comparison of horizontally and vertically printed specimens for load case 1, smoothing type 1 with a maximum distance ratio of 0.1, both for FEM and NNRPIM 120
Figure 7.12 Experimental results for the structural optimization (parabolic law) specimens subject to load case 2 121
Figure 7.13 Comparison of horizontally and vertical printed specimens for load case 2, smoothing type 1 with a maximum distance ratio of 0.1, both for FEM and NNRPIM 121
Figure 7.14 Experimental results for the structural optimization (parabolic law) specimens subject to load case 3 122
Figure 7.15 Comparison of horizontally and vertical printed specimens for load case 3, smoothing type 1 with a maximum distance ratio of 0.1, both for FEM and NNRPIM 123
Figure 7.16 Stiffness comparison between methods (FEM and NNRPIM) for all load cases using structural optimization with a parabolic law 124
Figure 7.17 Stiffness-to-weight ratio comparison between methods (FEM and NNRPIM) for all load cases using structural optimization with a parabolic law 125
Figure 7.18 Truss-like specimens based on structural optimization simulations with a linear material law for load case 1 126
Figure 7.19 Comparisson of experimental results for the structural optimization specimens with linear and parabolic material law subject to load case 1 126
Figure 7.20 Comparison between an original and reinforced structure in order to show that the inclusion of the areas at a transition density may bring benefit to the structure despite the increase in mass 127
Figure 7.21 Reinforced truss-like structures for based on FEM and NNRPIM structural optimization simulations with a linear material law for load case 2 128
Figure 7.22 Comparisson of experimental results for the structural optimization specimens with linear and parabolic material law subject to load case 2 128
Figure 7.23 Truss-like structures for based on FEM and NNRPIM structural optimization simulations with a linear material law for load case 3 129
Figure 7.24 Comparisson of experimental results for the structural optimization specimens with linear and parabolic material law subject to load case 3 130
Figure 7.25 Stiffness comparison between methods (FEM and NNRPIM) for all load cases using structural optimization with a linear law 131
Figure 7.26 Stiffness-to-weight ratio comparison between methods (FEM and NNRPIM) for all load cases using structural optimization with a linear law 132

Figure 7.27 Experimental results for the gyroid remodelling law 1 specimens subject to load case 1 . . . 133
Figure 7.28 Comparison of horizontally and vertical printed specimens for load case 1, smoothing type 1 with a maximum distance ratio of 0.1 using the gyroid remodelling law 1 . . . 134
Figure 7.29 Influence of parameter β in the performance of structures obtained with gyroid remodelling law 1, for load case 1 . . . 135
Figure 7.30 Experimental results for the gyroid remodelling law 1 specimens subject to load case 2 . . . 136
Figure 7.31 Comparison of horizontally and vertical printed specimens for load case 2, smoothing type 1 with a maximum distance ratio of 0.1 using the gyroid remodelling law 1 . . . 137
Figure 7.32 Experimental results for the gyroid remodelling law 1 specimens subject to load case 3 . . . 138
Figure 7.33 Comparison of horizontally and vertical printed specimens for load case 3, smoothing type 1 with a maximum distance ratio of 0.1 using the gyroid remodelling law 1 . . . 139
Figure 7.34 Stiffness comparison between methods (FEM and NNRPIM) for all load cases using gyroid remodelling law 1 . . . 140
Figure 7.35 Stiffness-to-weight ratio comparison between methods (FEM and NNRPIM) for all load cases using gyroid remodelling law 1 . . . 141
Figure 7.36 Comparison of specimens without any smoothing function applied and smoothing function type 1 for the gyroid remodelling law 1 and gyroid remodelling law 2 for load case 1 . . . 142
Figure 7.37 Comparison of specimens without any smoothing function applied and smoothing function type 1 for the gyroid remodelling law 1 and gyroid remodelling law 2 for load case 2 . . . 143
Figure 7.38 Comparison of specimens without any smoothing function applied and smoothing function type 1 for the gyroid remodelling law 1 and gyroid remodelling law 2 for load case 3 . . . 144
Figure 7.39 Stiffness comparison between methods (FEM and NNRPIM) for all load cases using gyroid remodelling law 2 . . . 145
Figure 7.40 Stiffness-to-weight ratio comparison between methods (FEM and NNRPIM) for all load cases using gyroid remodelling law 2 . . . 146
Figure 7.41 Comparison between layer position of horizontally and vertically printed specimens . . . 147

Figure 8.1 Two-dimensional approximation of the boundary conditions used for the simulations . . . 154
Figure 8.2 Femur 3D model An (2013) . . . 154
Figure 8.3 Voxelization and meshing of the part . . . 155
Figure 8.4 Voxelixed 3D model with boundary conditions . . . 155
Figure 8.5 Stress distribution for the femoral bone with similar loading to that of 8.1. Adapted from Belinha (2014) . . . 156
Figure 8.6 Equivalent Von-Mises Stress distribution for the elasto-static analysis . . . 156
Figure 8.7 Femur remodelling with the gyroid remodelling law 1 using the FEM . . . 158
Figure 8.8 Femur remodelling with the gyroid remodelling law 1 using the NNRPIM 159
Figure 8.9 Femur remodelling with the gyroid remodelling law 2 using the FEM . . . 160
Figure 8.10 Femur remodelling with the gyroid remodelling law 2 using the NNRPIM 161

Figure 8.11 Femur remodelling with a bone remodelling law using the FEM 162
Figure 8.12 Femur remodelling with a bone remodelling law using the NNRPIM . . . 163
Figure 8.13 Bone remodelling displaying the trabecular structure of the femoral bone through 2D analyses using the two numerical methods employed in these thesis. Adapted from (Peyroteo et al., 2018). 164
Figure 8.14 High density structures from the femur prototypes 164
Figure 8.15 Stiffness evolution with density for the gyroid remodelling analysis applied to the femur scaffold 165
Figure 8.16 Example of a femur prototype based on the FEM simulation with the gyroid remodelling law 1 for an apparent density of 0.6 g/cm^3, which is equivalent to 50% volume fraction 166
Figure 8.17 Sectional cut of two prototypes at the two tested volume fractions 166
Figure 8.18 Fixation tool and femur scaffold prototype during testing 167

Figure A.1 Correct solid vs inaccurate convex hull 199

Figure B.1 Four point flexural testing tool. This part was manufactured via CNC milling in steel. 203
Figure B.2 Support for the specimens while testing to avoid tumbling. This part fits inside the slot on the tool already available in the testing machine and was printed via FFF in PLA. 204
Figure B.3 Positioning tool. This part was printed via FFF in PLA. 204
Figure B.4 Fixation tool for testing of the femur-shaped prototypes. This assembly was built in aluminium and is designed in order to fit into the already existing slot in the testing machine. 205

Figure C.1 Load case 1 - FEM 208
Figure C.2 Load case 1 - NNRPIM 209
Figure C.3 Load case 2 - FEM 210
Figure C.4 Load case 2 - NNRPIM 211
Figure C.5 Load case 3 - FEM 212
Figure C.6 Load case 3 - NNRPIM 213
Figure C.7 Load case 1 - FEM 214
Figure C.8 Load case 1 - NNRPIM 214
Figure C.9 Load case 2 - FEM 215
Figure C.10 Load case 2 - NNRPIM 215
Figure C.11 Load case 3 - FEM 216
Figure C.12 Load case 3 - NNRPIM 216
Figure C.13 Load case 1 - FEM 217
Figure C.14 Load case 1 - NNRPIM 218
Figure C.15 Load case 2 - FEM 219
Figure C.16 Load case 2 - NNRPIM 220
Figure C.17 Load case 3 - FEM 221
Figure C.18 Load case 3 - NNRPIM 222
Figure C.19 Load case 1 - FEM 223
Figure C.20 Load case 1 - NNRPIM 223
Figure C.21 Load case 2 - FEM 224
Figure C.22 Load case 2 - NNRPIM 224
Figure C.23 Load case 3 - FEM 225

Figure C.24 Load case 3 - NNRPIM 225
Figure C.25 Femur scaffold prototypes 226

List of Tables

Table 2.1 Mechanical and physical properties of the most commonly used thermoplastics. The information displayed in this table was gathered from several online sources and compiled by the author of this thesis. 21
Table 2.2 FFF processing properties of the most commonly used thermoplastics. The information displayed in this Table was gathered from several online sources and compiled by the author of this thesis. 21

Table 5.1 Mechanical and printing properties of FormFutura's Premium PLA (FormFutura, 2020) 53
Table 5.2 Results of the measurements for the infill density calibration 59
Table 5.3 Interpolation table from the infill density calibration procedure 60
Table 5.4 Tensile test results for the specimens with 20% nominal infill 61
Table 5.5 Tensile test results for the specimens with 50% nominal infill 62
Table 5.6 Tensile test results for the specimens with 80% nominal infill 62

Table 7.1 Printed specimens for the Structural Optimization analysis with a parabolic material law 112
Table 7.2 Printed specimens for the analysis of structural optimization with a linear material law 112
Table 7.3 Printed specimens for the Gyroid Remodelling analysis with law 1 113
Table 7.4 Printed specimens for the Gyroid Remodelling analysis with law 2 114
Table 7.5 Summary of results for the structural optimization specimens (parabolic law) subject to load case 1 created with FEM and NNRPIM 119
Table 7.6 Summary results of the comparative analysis of horizontally and vertical printed specimens for load case 1, smoothing type 1 with a maximum distance ratio of 0.1, both for FEM and NNRPIM 120
Table 7.7 Summary of results for the structural optimization specimens subject to load case 2 created with FEM and NNRPIM 121
Table 7.8 Summary results of the comparative analysis of horizontally and vertical printed specimens for load case 2, smoothing type 1 with a maximum distance ratio of 0.1, both for FEM and NNRPIM 122
Table 7.9 Summary of results for the structural optimization (parabolic law) specimens subject to load case 3 created with FEM and NNRPIM 123
Table 7.10 Summary results of the comparative analysis of horizontally and vertical printed specimens for load case 3, smoothing type 1 with a maximum distance ratio of 0.1, both for FEM and NNRPIM 123
Table 7.11 Summary of results for the structural optimization specimens subject to load case 1 created with FEM and NNRPIM 127

Table 7.12 Comparison between an original and reinforced structure for the specimens based on NNRPIM structural optimization simulations using a linear material law 127
Table 7.13 Summary of results for the structural optimization specimens subject to load case 2 created with FEM and NNRPIM 129
Table 7.14 Summary of results for the structural optimization specimens subject to load case 3 created with FEM and NNRPIM 130
Table 7.15 Summary of results for the gyroid remodelling law 1 subject to load case 1 created with FEM and NNRPIM 133
Table 7.16 Summary results of the comparative analysis of horizontally and vertical printed specimens for load case 1, smoothing type 1 with a maximum distance ratio of 0.1, both for FEM and NNRPIM using the gyroid remodelling law 1 . . . 134
Table 7.17 Influence of parameter β in the performance of structures obtained with gyroid remodelling law 1, for load case 1 135
Table 7.18 Summary of results for the gyroid remodelling law 1 subject to load case 2 created with FEM and NNRPIM 136
Table 7.19 Summary results of the comparative analysis of horizontally and vertical printed specimens for load case 2, smoothing type 1 with a maximum distance ratio of 0.1, both for FEM and NNRPIM using the gyroid remodelling law 1 . . . 137
Table 7.20 Summary of results for the gyroid remodelling law 1 subject to load case 3 created with FEM and NNRPIM 138
Table 7.21 Summary results of the comparative analysis of horizontally and vertical printed specimens for load case 3, smoothing type 1 with a maximum distance ratio of 0.1, both for FEM and NNRPIM using the gyroid remodelling law 1 . . . 139
Table 7.22 Summary results of the comparative analysis of printed specimens based on the simulations using the gyroid remodelling law 1 and gyroid remodelling law 2 for for load case 1 142
Table 7.23 Summary results of the comparative analysis of printed specimens based on the simulations using the gyroid remodelling law 1 and gyroid remodelling law 2 for for load case 2 143
Table 7.24 Summary results of the comparative analysis of printed specimens based on the simulations using the gyroid remodelling law 2 and gyroid remodelling law 2 for for load case 3 144
Table 7.25 Predicted stiffness for a 5mm plate at a density level of 0.6 g/cm^3 - Structural optimization analysis 148
Table 7.26 Predicted stiffness for a 5mm plate at a density level of 0.6 g/cm^3 - Gyroid remodelling analysis 148
Table 7.27 Predicted stiffness for a 5mm plate at a density level of 0.6 g/cm^3 - Gyroid remodelling analysis with law 1 ($\beta = 0.05$) 148
Table 7.28 Proportion of stiffness for each set of specimens compared to the original simulation for the specimens based on structural optimization simulations with a parabolic law 149
Table 7.29 Proportion of stiffness for each set of specimens compared to the original simulation for the specimens based on structural optimization simulations with a linear law 149
Table 7.30 Proportion of stiffness for each set of specimens compared to the original simulation for the specimens based on gyroid remodelling simulations with law 1 149

Table 7.31 Proportion of stiffness for each set of specimens compared to the original simulation for the specimens based on gyroid remodelling simulations with law 1 and a β value of 0.05 150
Table 7.32 Proportion of stiffness for each set of specimens compared to the original simulation for the specimens based on gyroid remodelling simulations with law 2 150

Table 8.1 Experimental test results for the femur scaffold specimens 167
Table 8.2 Predicted stiffness results at the tested density levels 168

Table B.1 Part list 205

Acronyms and Symbols

ABS	Acrylonitrile butodiene styrene
AM	Additive Manufacturing
ASA	Acrylonitrie styrene acrylate
BESO	Bi-evolutionary Structural Optimization
CAD	Computer-Aided Design
CH	Convex Hull
DT	Delaunay Triangulation
ESO	Evolutionary Structural Optimization
FDM/FFF	Fused Deposition Modelling/ Fused Filament Fabrication
FE	Finite Element
FEM	Finite Element Method
IR	Inclusion Ratio
LDPS	Laboratorio de Desenvolvimento de Produtos e Serviços
MDR	Maximum distance ratio
NNRPIM	Natural Neighbour Radial Interpolation Method
PA	Polyamide
PC	Polycarbonate
PEI	Polyeteremide
PETG	Polyetilene Teraphtalate Glicol
PLA	Polylactic Acid
PP	Polypropilene
PTFE	Polytetrafluoroethylene
PVA	Polyvinyl alcohol
RPIM	Radial Point Interpolation Method
RR	Rejection Ratio
SIMP	Solid Isotropic Material with Penalization
SO	Structural Optimization
STW	Stiffness-to-weight
TO	Topology Optimization
TPMS	Triply Periodic Minimal Surface

σ	Stress
ε	Strain
E	Elasticity modulus
ν	Poisson coefficient
α	Growth rate
β	Decay rate
ρ	(Apparent) Density
V	Volume
U	Strain energy density
K	Stiffness
ξ	Interest variable
Ω	Domain

Chapter 1

Introduction

1.1 Framework

This present work is based on the gyroid shape (Figure 1.1), first discovered in 1970 by Schoen (1970), which belongs to the Triply Periodic Minimal Surfaces group. Its complex shape becomes easy to manufacture and study through the use of Additive Manufacturing (AM) technologies (Abueidda et al., 2019). This shape is present as an infill shape in some slicing software such as Cura (Ultimaker, 2019) and Prusa Slicer (Prusa, 2020).

Architected materials as is the case of functionally graded cellular structures have numerous times been materialized through additive manufacturing techniques (Schaedler and Carter, 2016). There are many examples of applications in areas such as energy absorption, metamaterials, thermal performance, and bioscaffold.

Even though there is no specified application, the use of triply periodic minimal surfaces is seen as a potential process of manufacturing bone tissue scaffold. The intricate shape is indicated as it promotes tissue adhesion and the implicit function of the surface allows to reduce the elastic modulus to match that of trabecular bone and therefore to avoid stress shielding (Ma et al., 2019; Wolff, 2012; Yoo, 2011a).

Weight reduction of any components through the use of cellular gradients could also represent a potential application. The use of PLA allows for inexpensive prototyping of components to then be produced in more demanding materials and manufacturing processes since thermoplastics and

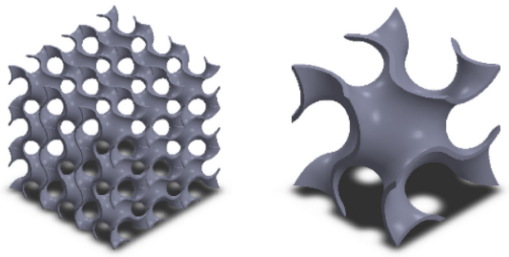


Figure 1.1: Cellular solids based on the gyroid shape. Adapted from (Abueidda et al., 2019)

ductile metals present similar behaviours in the linear-elastic domain.

The work proposed in this thesis would not be possible to experimentally test if not through Additive Manufacturing (AM) technologies. Equipment ranges in cost from some hundreds of euros to hundreds of thousands and the affordability of some equipment has paved the way for a number of individuals to endeavour into the world of design and manufacturing - The Maker Movement (Anderson, 2012). Additive manufacturing has even been deemed the next industrial revolution (Berman, 2012) and challenges companies to rethink their business and value chains (Bogers et al., 2016). Nonetheless, the possibilities regarding the complexity of shapes that in no other way could be obtained make this a very interesting area for many researchers with a large number of publications available in the literature. In addition to this, there is constant monitoring through several reports and roadmaps tracking the business and industry possibilities and interest in AM such as the Wohlers report (Wohlers, 2019) often referred to as the "*bible of 3D printing*", as Gao et al. (2015) pointed out as well as some challenges and potentialities of AM technologies for the near future. Despite all that was achieved with AM technology, there are still many critical barriers. Taking Fused Filament Fabrication (FFF) for example, numerous publications have classified it as the best technology suiting the maximum applications but still recognizing the existence of room for improvement through new methodologies or applications (Singh et al., 2020).

This work takes a simpler approach into cellular gradients and architected materials. Instead of creating a gradient based on a space function of the parameter which defines the apparent density of the gyroid surface, or adjusting each individual unit cell to the desired density, the gradient is created as a concatenation of several solids at different density levels which correspond to density intervals. Smoothing techniques are employed to avoid abrupt changes in density. Figure 1.2 shows a flowchart-like diagram of the methodology which is being proposed.

1.2 Objectives

Should this work prove successful, it would have accomplished the following points:

- Development of an adaptive gyroid remodelling law, based on bone tissue descriptive laws, which accurately represents the behaviour of gyroid infill structures manufactured in Polylactic Acid (PLA) using AM, namely FFF technology;
- Development of a script capable of transforming the output matrices from a numerical simulation educational software (FEMAS), directly into an *.stl* file with minimal user interaction;
- Concluding about which approach (structural optimization or gyroid remodelling) presents the best results structurally, through experimental testing of the specimens constructed based on the simulation results;
- Development of a smoothing function capable of avoiding abrupt density changes and enhancing stiffness of the specimen;
- Application of the previous points into a practical application, namely, bone scaffold.

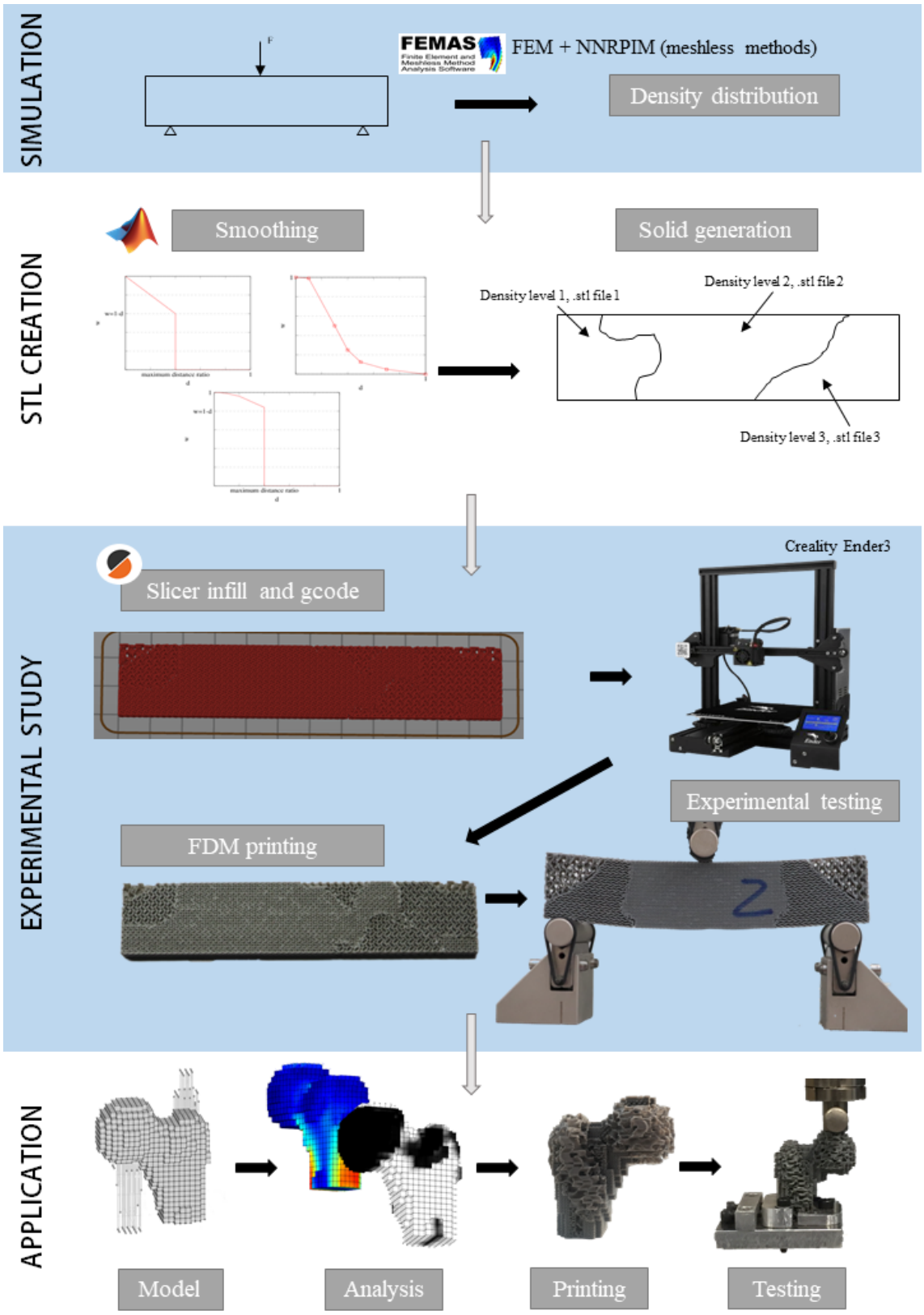


Figure 1.2: Overview of the methodology which is being proposed in this thesis

1.3 Structure of the report

This report is composed of nine chapters listed as following:

- **Chapter 1** is this introduction being made and aims at showing the reader a brief description of the methodology being proposed;
- **Chapter 2** presents a state-of-the-art review of other methodologies of optimization with cellular or lattice structures. The gyroid surface and other TPMS surfaces are introduced as a review of the motives for the choice of this infill. Lastly, additive manufacturing, with a focus on FFF is briefly introduced;
- **Chapter 3** reviews and introduces the numerical methods employed in the simulation software being used;
- **Chapter 4** reviews and introduces remodelling algorithms for optimization;
- **Chapter 5** dwells further into the methodology in itself, specifying experimental tests, additive manufacturing considerations and aspects related to the Matlab script constructed to create the *.stl* files;
- **Chapter 6** presents the results from all numerical simulations;
- **Chapter 7** presents the results from the experimental tests which were conducted;
- **Chapter 8** does a preliminary study on a practical application for the remodelling analysis done on prismatic specimens. This practical application is an example of bone tissue scaffold;
- **Chapter 9** presents conclusion, future works and final remarks.

Chapter 2

Contextualization

Additive Manufacturing allows for some shapes to be obtained that cannot be obtained by conventional manufacturing processes such as surfaces with intricate holes and complex shapes (Gibson and Ashby, 1999), which can be used as lightweight infill (Feng et al., 2018a). The review done by Feng et al. (2018a) explores some different approaches to complex topology structures.

Some properties such as energy absorption, acoustic insulation, heat conduction and buoyancy (Li et al., 2018a) can be enhanced by taking use of structural optimization and cellular materials. Some interior porous designs are inspired by naturally occurring shapes in nature as reviewed by du Plessis et al. (2019) who enumerate bio-mimetic inspiration in design for additive manufacturing. These inspirations include organic rounded shapes, and structural hierarchy. Du et al. (2020) studied a lattice structure inspired from the beetle's front wing fabricated by Selective Laser Melting in AlSi10Mg alloy which displayed enhanced energy absorption capability. The variety of shapes that can be attained with AM processes make it possible to replicate naturally occurring shapes.

2.1 Functionally graded cellular structures and infill optimization for AM

Infill optimization aims at not only minimizing the overall weight of the 3D printed object with shapes unattainable by any other fabrication process, as well as maximizing stiffness for that reduced mass. Functionally Graded Cellular Structures (FGCS) (Suresh and Mortensen, 1998) are focused on the density variable lattice or porous structure. These two concepts walk hand-in-hand as infill optimization more often than not, uses the same tools as FGCS.

Brackett et al. (2014) developed an error diffusion method to produce functionally graded cellular structures, tackling the problem of obtaining a cellular structure with variable cell size, converting a continuous image into a binary image. Wang et al. (2013) developed a methodology for obtaining skin frame structures for 3D printed objects. The lightweight structure is composed of a truss-inspired infill and a shell structure. The results obtained by this method are shown in



Figure 2.1: Skinframe lightweight structure as proposed by Wang et al. (2013)

Figure 2.1. The design problem is tackled considering the mechanical properties, balance of the model and ability to be printed.

Lu et al. (2014) took a *lightweighting* approach where the authors would reduce the amount of material through carving of the interior of the object thus obtaining an interior porous structure similar to an interior honeycomb (Figure 2.2). The Voronoi diagram was used to compute the irregular honeycomb tessellations. The problem was formulated as a "strength-to-weight" optimization finding both the ideal tessellation as well as the maximum possible hollowing. According to Feng et al. (2018a), one of the limitations of this approach is the inability to fabricate parts by powder sintering technologies as the pores are unconnected. According to Li et al. (2018b), this limitation is overcome with the methodology proposed by Wang et al. (2018) of Support-Free Hollowing.

In addition to this, Wu et al. (2016) developed a rhombic self supporting infill for AM with the intent of overcoming the difficulty of removing supports from the inside of 3D printed parts. Their approach consisted on an adaptive rhombic grid obtained with numerical optimization techniques.

Regarding foams, Martínez et al. (2016) developed a method of creating Voronoi (Voronoi, 1908) foams thus generating microstructures with controlled isotropic behaviour. One of the limitations of this methodology is the fact that the foams only exhibit their target properties in large scale objects and increasing localized stresses. The main advantage is the implicit formulation of stochastic microstructures which allows savings regarding the computation cost by avoiding representations such as mesh or voxelization. Martínez et al. (2017) developed an orthotropic k-nearest foam in order to enhance the properties of the structure depending on the load direction. Kumar

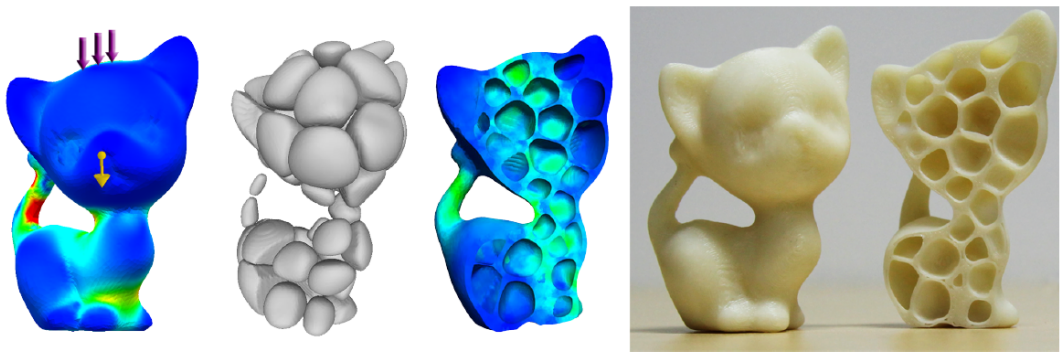


Figure 2.2: Interior honeycomb-like structures as proposed by Lu et al. (2014)

et al. (2020) developed supportless closed cell foam structures which show strong load bearing capacity compared to open cell structures and can be encapsulated with some fluid to provide strength and prevent damping.

Many works have been conducted regarding the optimization of the infill by a truss structure, or lattice structure infill. Medeiros e Sá et al. (2015) have developed a methodology for the creation of primal and dual adaptive cellular structures. Zhao et al. (2017) developed an algorithm to map a truss infill inside a polygonal model by two processes, model hollowing and truss generation. Nguyen and Vignat (2016) developed a method to create lattice structures for 3D printing by summarizing the most common unit cells (Figure 2.3) and applying or combining them in order to fulfill with the mechanical and physical requirements. Tang et al. (2015) applied a BESO algorithm in order to optimize the thickness of struts in the lattice structure instead of adding or removing struts (Figure 2.4). Chen (2006) presented a method to obtain lattice structures based on the mesh model of the object (Figure 2.5).

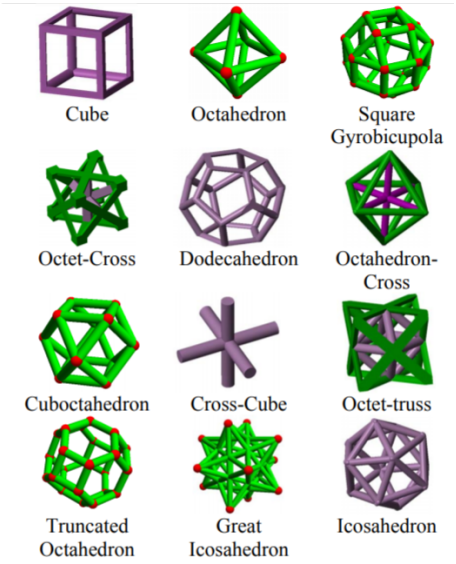


Figure 2.3: Library of unit truss cells. Adapted from (Nguyen and Vignat, 2016)

Gorguluarslan et al. (2017) presented an optimization approach with superior results than conventional optimization which takes into consideration the constraints imposed by the manufacturing process. The methodology consists on a first optimization run based on conventional methods (Bendsoe and Sigmund, 2004) and then, a second run of optimization defining as a minimum diameter the one of the fabrication process. Dong et al. (2020) proposed hybrid optimized structures combining solid structures with an optimized truss infill. Goel and Anand (2019) used topology optimization to obtain a density map for the unit cell structures. The smooth connectivity of the truss was achieved with B-splines.

In scaffold production, there is also applicability for lattice design as tissues are inherently hetereogeneous and studies are focused on replicating these scaffolds with easier and periodic structures (Giannitelli et al., 2014). For example, Cheah et al. (2003a,b) have compiled a series of

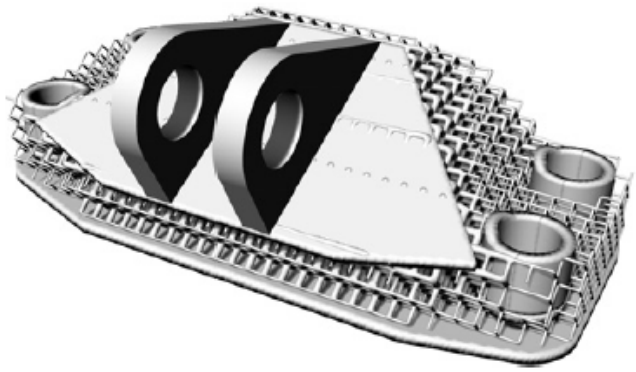


Figure 2.4: Optimized engine braket based on the BESO algorithm. Adapted from (Tang et al., 2015)

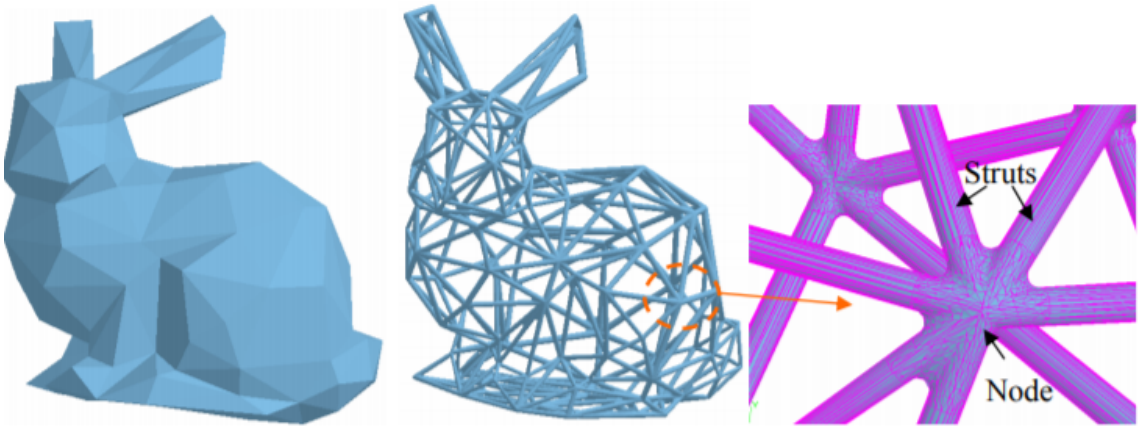


Figure 2.5: Lattice structure design based on the geometric mesh. Adapted from (Chen, 2006)

parametric structures as well as an algorithm for integration in anatomical shapes.

It should be noted that the range of known and studied of truss cell units is still somewhat small and quite simple compared to what is seen in nature. Moreover, this simplicity is often not enough to meet with current demands (Feng et al., 2018a).

2.1.1 Functionally graded cellular structures obtained with topology optimization algorithms

The work conducted by Li et al. (2018b) presents a methodology with the objective of constructing functionally graded structures based on the gyroid cell. The work initiates with the development of an implicit function to characterize the geometry of the gyroid as a function of the density parameter t. Figure 2.6 represents the graphical representation of the implicit function used to map the density spacial distribution. Then, a constitutive law is determined to obtain the elastic constants as a function of relative density.

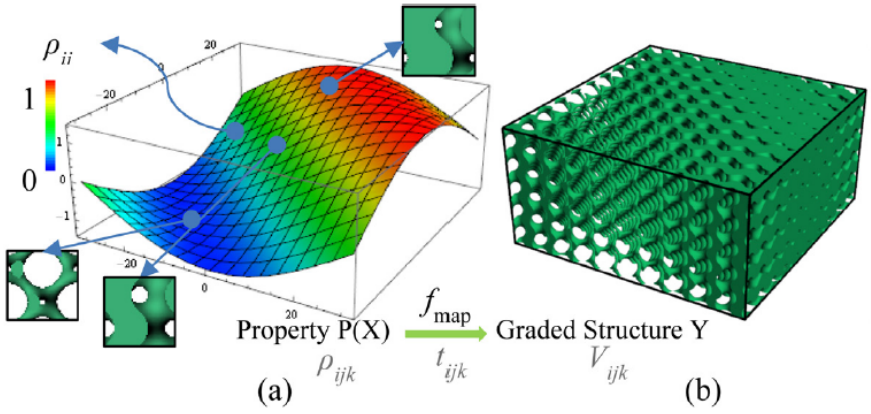


Figure 2.6: Example of the mapping process for mechanical properties (a) material properties diagram; (b) 3D mapping result. Adapted from (Li et al., 2018b).

The topology optimization process using the information obtained previously resulted in the shape-retaining and 3D-printing constrained optimized results for an MBB beam as can be seen in Figure 2.7 where it is visible that the traditional optimization method requires much more supporting structures.

The authors further analyse the stress and displacement behaviour of the different Topology Optimization (TO) methods. It was concluded that the optimization strategies obtain structures with higher stiffness than the uniform gyroid structure having the direction constrained method approximated the most of the traditional TO method.

The work conducted by Li and Yao (2019) entitled "Manufacturable Gradient-Variable Cellular Structures Design" is also based on Topology Optimization. Their methodology is shown in Figure 2.8 and it consists on obtaining a density map by topology optimization methodology, assembling the unit cell in accordance to the referred density map and printing the final cellular structure.

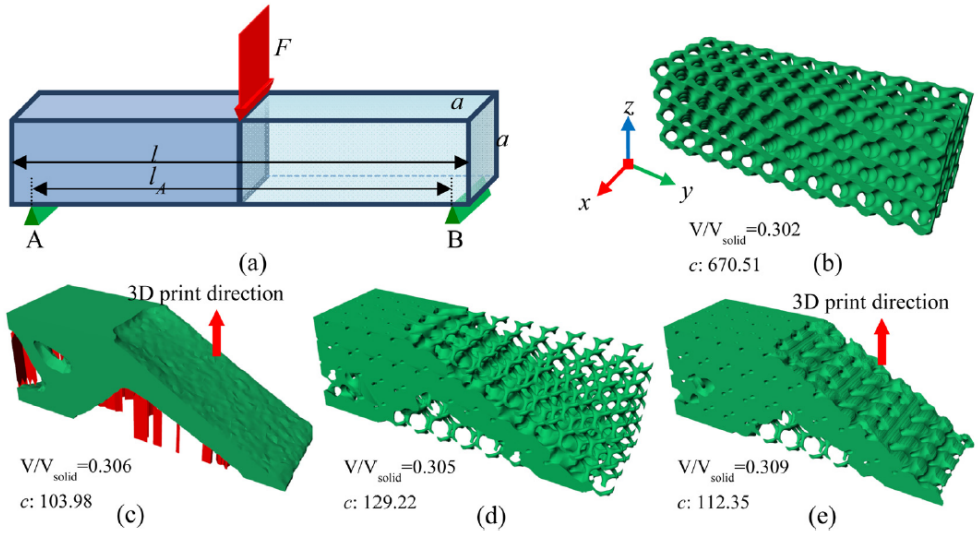


Figure 2.7: Optimization strategies for ann MBB beam (a) load and boundary conditions; (b) uniform gyroid structure; (c) standard TO approach; (d) shape retaining optimization; (d) direction constrained optimization. Adapted from (Li et al., 2018b)

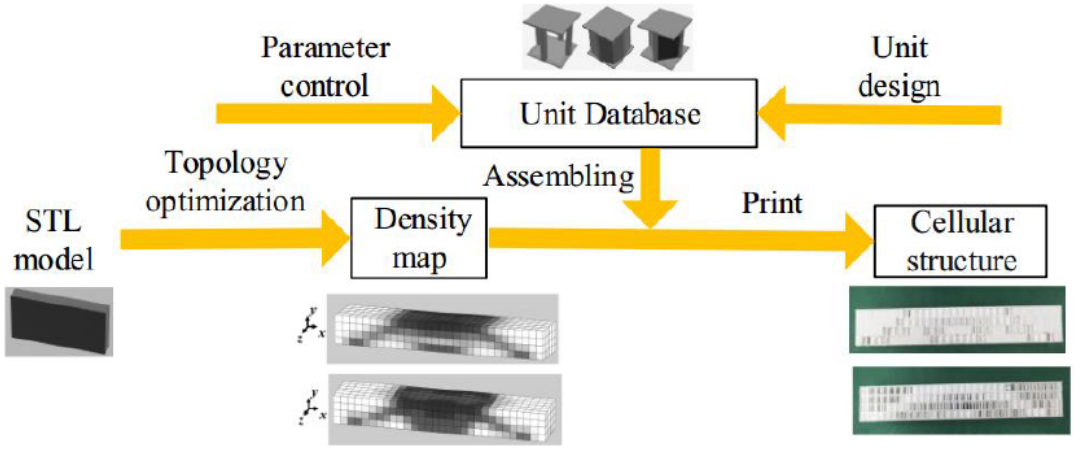


Figure 2.8: Methodology used by Li and Yao (2019) for obtaining FGS based on a density map. Adapted from (Li and Yao, 2019).

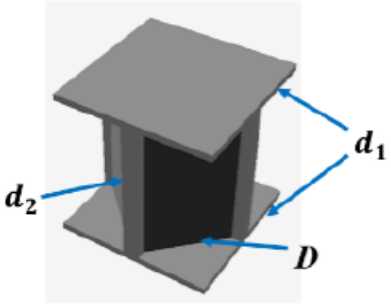


Figure 2.9: Three-dimensional structural unit. Adapted from (Li and Yao, 2019)

The authors use the Solid Isotropic Material with Penalization (SIMP) algorithm to conduct structural optimization. Then, each element of the map is replaced with a unit structure with the necessary density. This work is focused on the determination of the unit structures. These unit structures must meet with the following requirements:

1. Effectiveness of the structure
2. Stability of the structure
3. Manufacturability of the structure
4. Smooth connectivity

The density range of each structure would be between a minimum density to ensure minimum strength and possibility of manufacturing, and 1. The obtained unit was a hexahedral voxel unit with two plates (top and bottom), a central cross plate structure and an inner hexahedral prism structure as it can be seen in Figure 2.9. Relative density is a function of parameter D, which is the size of the side of the plate, while fixing d_1 and d_2 at 0.2 and 0.5mm, respectively.

Five beams were obtained which correspond to five different types to obtain the infill of the beam which go as following:

1. Designed by SIMP with the support structure generated by a commercially available slicing software;
2. Designed by Li and Yao (2019) with a penalty value of 1 in SIMP and with density values less than X_{min} mapped to empty material. The same slicing software as in *1.* generated the model;
3. Similar process to the previous specimen but having the minimum density mapped to X_{min};
4. Fabricated model with a shell structure which can be seen as a three-dimensional infill pattern with optimized material distribution;
5. Shell structure which uses a grid support structure generated by the above-mentioned slicing software with the same density distribution as beam *4*.

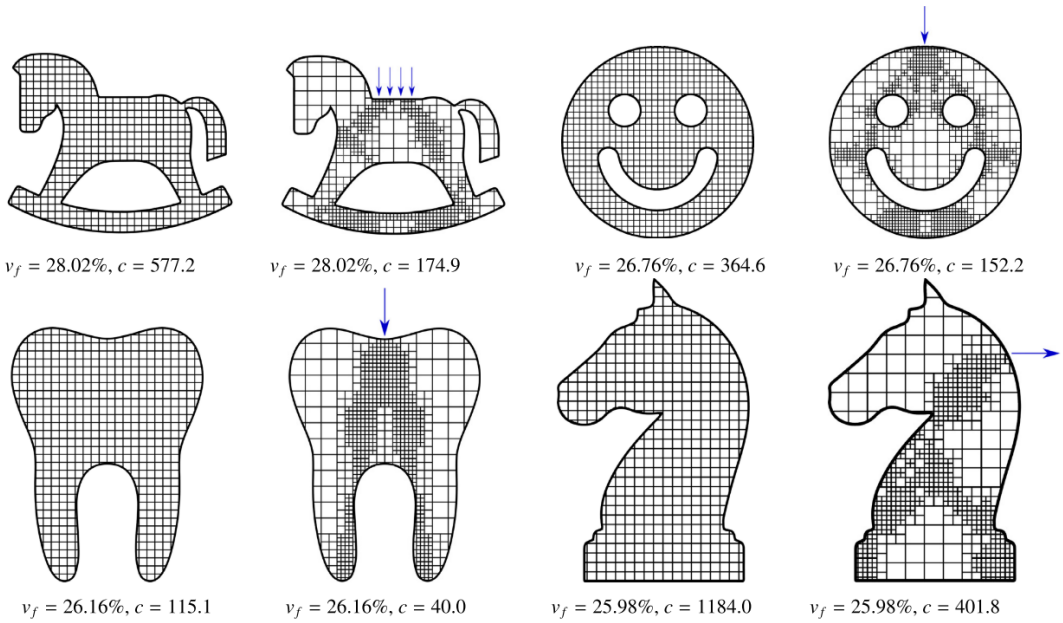


Figure 2.10: Results of the infill optimization of shell parts.*vf* is the volume fraction of the part and *c* is the compliance value Adapted from (Wu, 2018).

All beams possessed the same volume fraction. Beam 1 obtained by SIMP presented the best results. The method developed by Li and Yao (2019) presents similar stiffness to the SIMP method.

The work developed by Wu (2018) (Figure 2.10) consisted on the optimization of shell structures infilled in an optimal way using a novel algorithm which consists on a continuous optimization methods to the discrete problem of quadtree optimization which present enhanced stiffness comparing to uniform lattice structures and parts optimized through heuristical methods.

All the presented works show how a density distribution can be obtained through continuous infill change or discrete substitution of unitary element cells.

2.1.2 Density variable gyroid infill obtained by cross sectional stress analysis

It is important to distinguish common stress analyses, such as the FEM, from other methodologies. The work conducted by Li et al. (2016) consisted on obtaining a density-variable shape method to achieve the required strength of 3D objects. First, a cross-sectional analysis (Umetani and Schmidt, 2013) is done to determine areas prone to fracture. The methodology is expressed in Figure 2.11 and it is described with more detail in Figure 2.12.

The infill pattern is the gyroid structure which density can be varied as a function of parameter *t* (Figure 2.13). The proposed methodology will obtain results with areas presenting uniform infill and areas presenting gradational infill depending on the stress analysis for that section.

This methodology has proven to be successful in avoiding fracture. Maximum stress of the density variable stress areas is higher than with 100% infill but still below the maximum allowable

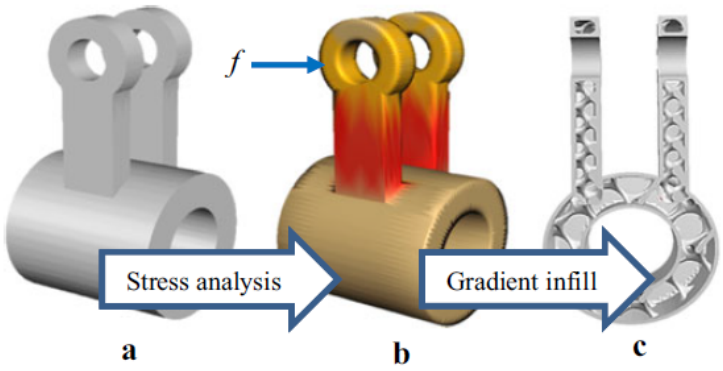


Figure 2.11: Methodology proposed where (a) is the original object; (b) is the local density distribution after stress analysis and (c) is the final object with the gradual infill. Adapted from (Li et al., 2016).

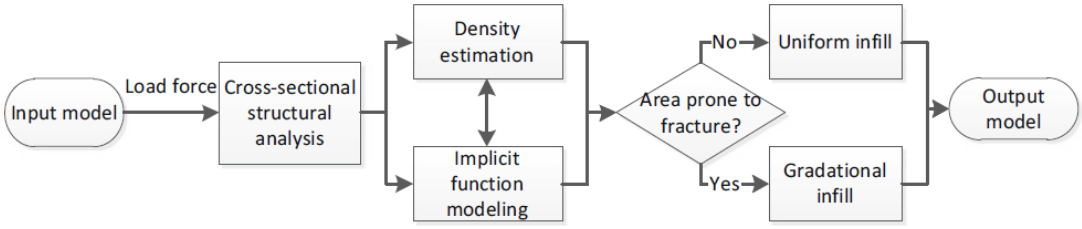


Figure 2.12: Detailed explanation of the methodology proposed. Adapted from (Li et al., 2016).

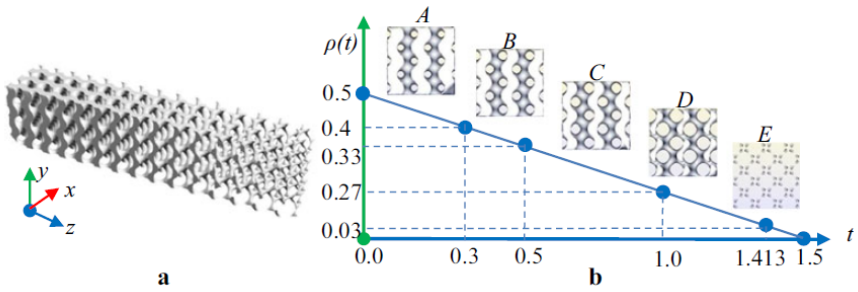


Figure 2.13: Schematic representation of the influence of parameter t on the relative density of gyroid structures: (a) Gyroid structure with gradual infill from t = 0 to t = 1.413 and (b) percentage of the sectional area as a function of parameter t. Adapted from (Li et al., 2016).

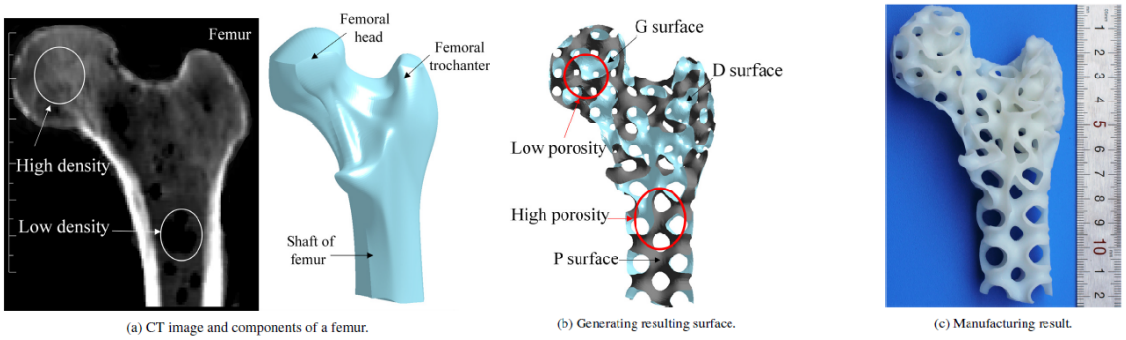


Figure 2.14: Design method proposed by Feng et al. (2018b) for the creation of density graded structures

stress of the material which means that this methodology allows for significant weight reduction.

2.1.3 Triply periodic minimal surfaces applied to tissue engineering

A Triply periodic minimal surface is an implicit surface, periodic in its three principal directions and there are several methods for its generation (Melchels et al., 2010; Rajagopalan and Robb, 2006; Yoo, 2011a,b). The porosity of the surface can be defined as a function of a parameter. Despite being periodic, anisotropy can still be present (Lu et al., 2019). Many times, TPMS have been used in tissue engineering for the design of scaffolds for prosthetics or other parts (Du et al., 2020; Yu et al., 2019; Zhang et al., 2020).

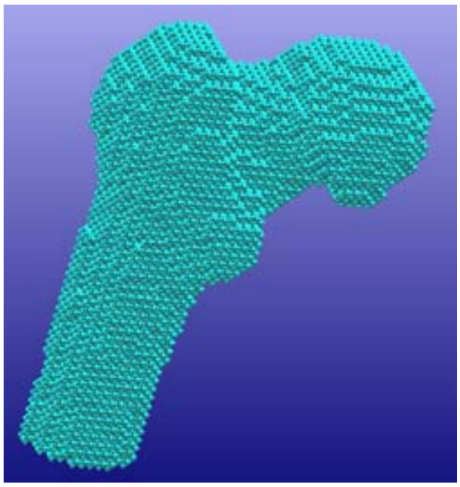
Feng et al. (2018b) developed a methodology which uses the porosity in these structures to replicate density variable structures. Medical imaging techniques are used to determine density variations in bone tissue. The method to obtain these surfaces is based on solid T-splines and thus making boolean operations unnecessary.

Figure 2.14 shows a combination of several surface types in order to obtain a density gradient from CT scans.

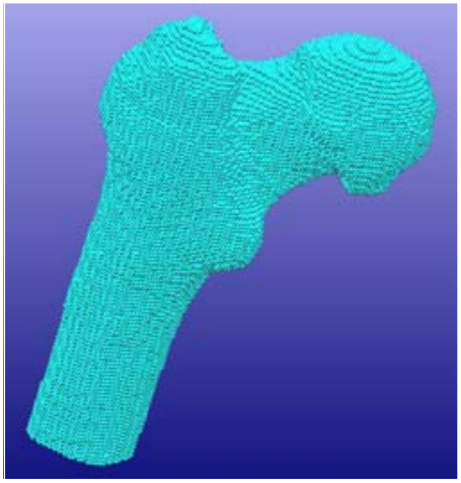
On the other hand, the work conducted by Yoo (2011a) uses voxelized solids in order to apply porosity. The structures were divided into hexahedral elements which generated the pore-making element using a mapping function consisting on interpolation of the coordinates of a brick element through shape functions, meaning that any TPM surface can be interpolated into a brick element. Thus, pore distribution is controlled by mesh size. Figure 2.15 shows several bone structures composed of different triply minimal periodic structures.

Ma et al. (2019) concluded that 316L steel gyroid structures are suitable to be applied as bone scaffolds in terms of mechanical and mass-transport properties. The porosity in the structure reduces the modulus to match that of trabecular bone. A high difference between the scaffold and bone elastic modulus can lead to stress shielding.

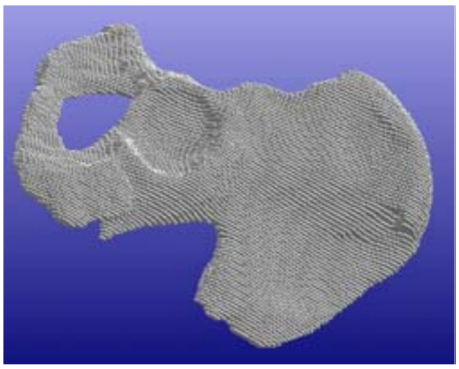
In summation, the continuous change of density and voxelization and mapping of unit cells are employed. Depending on the type of surface chosen, one alternative or the other might be easier to employ.



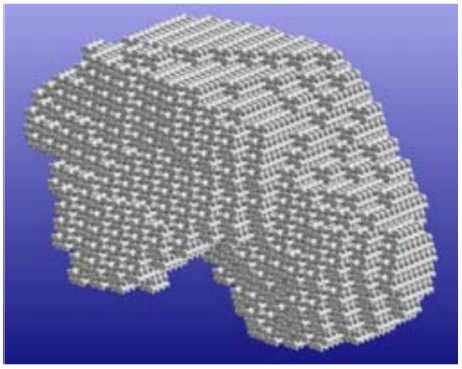
(a) Femur scaffold - IWP-surface



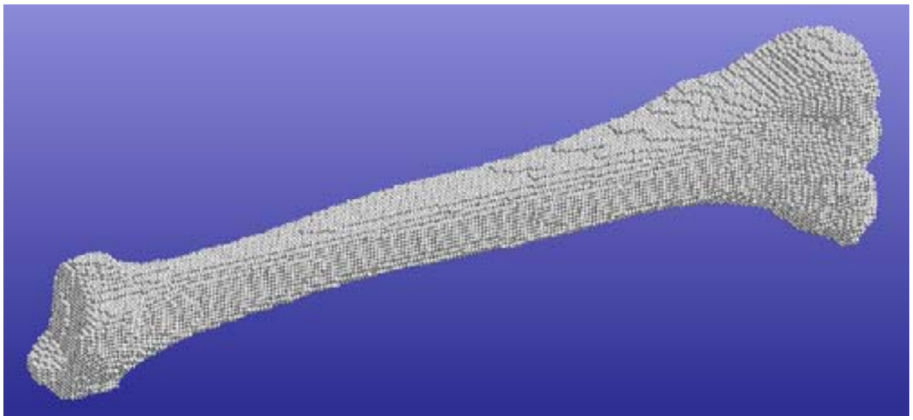
(b) Femur scaffold - P-surface



(c) Iliac scaffold - P-surface



(d) Talus scaffold - IWP-surface



(e) Tibia scaffold - P-surface

Figure 2.15: Bone tissue scaffold examples composed of TPMS structures. Adapted from (Yoo, 2011a)

2.2 Gyroid structure

The gyroid surface, discovered by Schoen (1970), belongs to the class of triply periodic minimal surfaces or TPMS which are surfaces with zero mean curvature. Some common triply periodic minimal surfaces are depicted in Figure 2.16. One of the advantages of using TPMS is obtaining a higher surface-to-volume ratio than strut-based cellular structures (Yoo, 2014). Some examples of TPMS include the Schwarz crossed layers of parallels (Schwarz, 1871), Diamond, Neovius (Neovius, 1883), Schoen's IWP, Schwarz Primitive, Fischer-Koch S and Schoen Gyroid (Schoen, 1970). The literature presents plenty of examples of experimental and testing of each of these surfaces. It should be noted however that there is a difference between solid networks or sheet-like structures when determining the properties of TPMS. It was verified by Kapfer et al. (2011) that sheet-like structures show higher moduli than solid networks

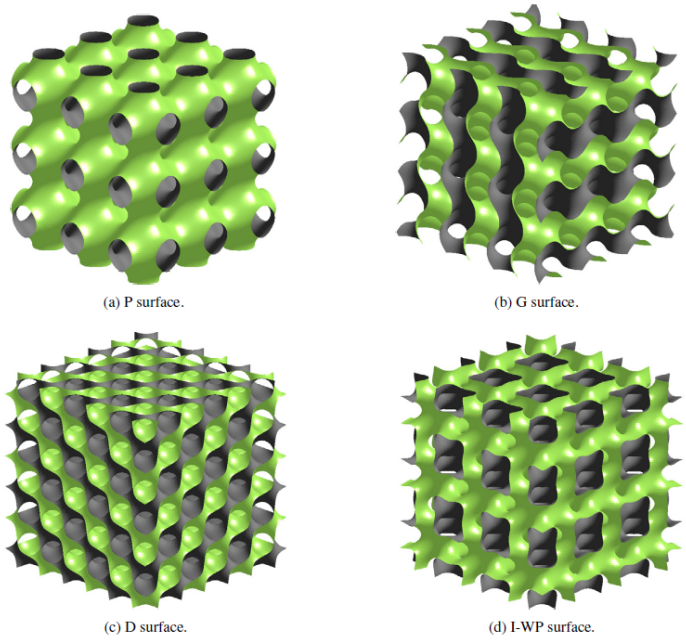


Figure 2.16: Common triply periodic minimal surfaces. Adapted from (Feng et al., 2018b)

Comparing to other cellular structures, the gyroid presents some promising mechanical properties. Abueidda et al. (2019) studied the mechanical properties of the gyroid structure correlating those results to those of FE simulations in compression tests. It was concluded that the Gyroid structures at different relative densities deform uniformly in the elastic region. For high relative densities, the gyroid deforms more uniformly beyond the elastic domain than the structures with low density. This phenomenon had already been observed in a previous study by Abueidda et al. (2017). In addition, it was shown that the compressive properties of the gyroid situate between the Neovius and IWP structures and regarding energy absorption, the gyroid behaves worse than these two but better than primitive structures.

In the work of Maskery et al. (2018), the gyroid structure as well as other two TPMS were studied which were the primitive and the diamond where it was found that the primitive has a

higher elastic modulus and is more appropriate for high stiffness applications. Yang et al. (2019) tested gyroid structures obtained through Selective Laser Melting. The effect of variable density as well as printing direction was tested. It was concluded that having the gradient in the same direction as the printing direction presents better energy absorption as well as large strain protection against densification. Maskery et al. (2017) studied the compressive behaviour of gyroid lattice structures manufactured through Selective Laser Melting in AlSi10Mg alloy. Several failure modes were detected such as the successive collapse of cells perpendicular to the loading and manufacturing direction for smaller cell sizes, crack propagation where the main direction of crack propagation happens parallel to the applied load for larger cell sizes, and diagonal shear for the smallest lattices. The gyroid implicit function is given by expression 2.1 where t is a parameter which determines the volume fraction and L is the unit cubic cell edge. Parameter t can effectively control the cross section area of the structure (Li et al., 2016).

$$\sin\frac{2\pi x}{L}\cos\frac{2\pi y}{L}+\sin\frac{2\pi y}{L}\cos\frac{2\pi z}{L}+\sin\frac{2\pi x}{L}\cos\frac{2\pi z}{L}=t \tag{2.1}$$

Giannitelli et al. (2014) distinguishes three different gyroid surface implicit functions, namely, the gyroid, the high porosity gyroid and the gyroid with gradient architecture. These implicit functions are as following:

Gyroid. $G:\cos x\sin y+\cos y\sin z+\cos z\sin x=0;$
Gyroid, high porosity. $G_{HP}:\cos x\sin y+\cos y\sin z+\cos z\sin x-k=0;$
Gyroid, gradient architecture. $G_{GA}:\cos x\sin y+\cos y\sin z+\cos z\sin x-k'z-k''=0.$

A gyroid surface, defined by implicit functions, segments the space into the gyroid cellular space and the gyroid foam (Yang et al., 2019). The gyroid foam is often called the double gyroid as both sides of the wall are composed of gyroid surfaces. The cellular space is also called the network and the foam the matrix phase (Maskery et al., 2017). This is further illustrated in Figure 2.17.

Figure 2.18 shows how the compressive behaviour of the gyroid printed in PA 200 through Selective Laser Sintering (SLS), improves with a relative density increase on different solicitation directions relatively to the printing direction. Regarding mechanical properties SLS can obtain parts with excellent properties. It is visible that there are no major differences between the behaviour on both directions.

In addition, the typical behaviour of cellular materials when compressed (Gibson and Ashby, 1999) is visible in Figure 2.18.

2.3 Additive manufacturing

Additive manufacturing processes are divided into the following categories according to the ISO / ASTM 52900 (ISO, 2015) classification:

- **Material Extrusion**: Material is selectively extruded through a nozzle or orifice. FDM belongs to this class.

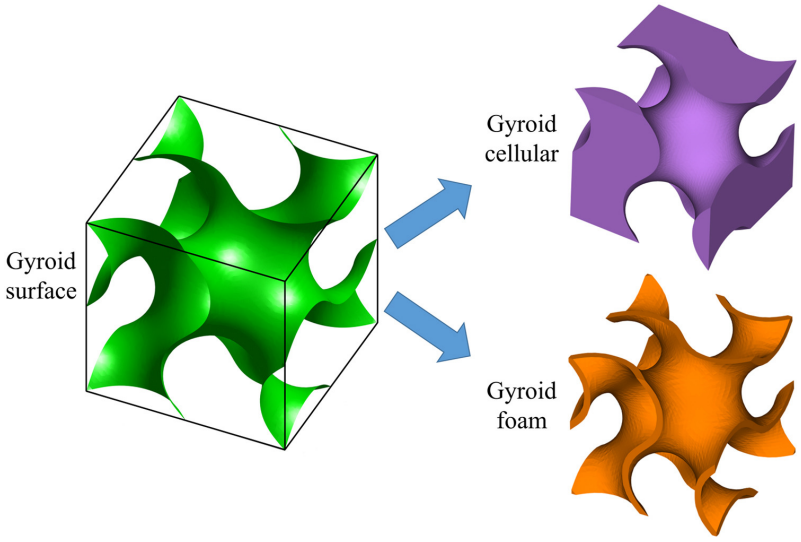


Figure 2.17: Schematics of gyroid surface, gyroid cellular and gyroid foam. Adapted from (Yang et al., 2019).

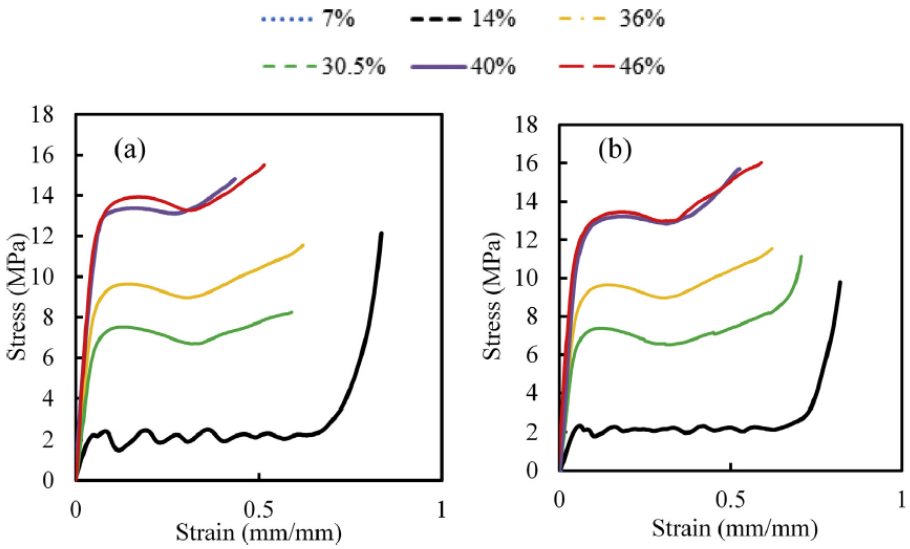


Figure 2.18: Gyroid compressive behaviour at several density values where a) is tested horizontally to the printed layers and b) is tested vertically to the printed layers. Adapted from (Abueidda et al., 2019)

- **Material Jetting**: Droplets of build material are selectively deposited. Processes belonging to this class are often compared to inkjet printing. It uses photopolymer resin which is then cured with UV light. *PolyJet* is included is this class of processes (Gregurić, 2019).
- **Binder Jetting**: A bonding liquid agent is selectively deposited to join powder materials.
- **Sheet Lamination**: Sheets of material are bonded.
- **VAT Photopolimerization**: Liquid photopolymer in a VAT is selectively cured by light-activated photopolymer.
- **Powder Bed Fusion**: Thermic energy selectively fuses regions of a powder bed.
- **Directed Energy Deposition**: Focused thermal energy is used to fuse materials by melting as they are being deposited.

2.3.1 Fused filament fabrication

Fused filament fabrication or fused deposition modelling, which is the nomenclature of the process from Stratasys, patented in 1989 (Crump, 1991), are two names for the same process of extruding material and depositing it over the previous layer. Building material in the form of a filament spool, is heated to a viscous state and deposited according to the trajectory defined by the user where the *feed rate* of the printing head is also programmed to initiate or stop extrusion according to the trajectory of the x and y axis.

The used material is not limited to thermoplastic in a melted of viscous state. Other types of particles such as composite, metal or ceramic particles, can be suspended in some form of hydrogel and be used as build material. Figure 2.19 shows a schematic representation of the FFF process.

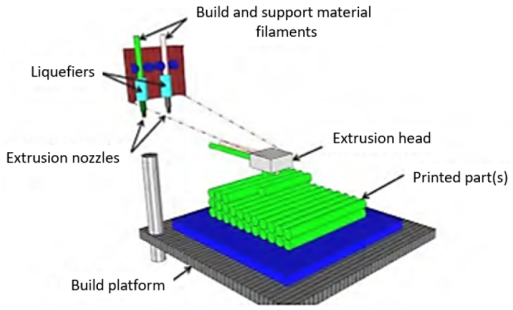


Figure 2.19: Schematic representation of the FDM/FFF process. Adapted from (Silva, 2019; Wohlers et al., 2018)

Compared to other AM processes, FFF is usually less expensive and easier to handle with the disadvantage of being slower than other processes such as binder jetting which is the fastest.

The 3D printing process using FFF starts with the creation of the CAD file which can be done by the user or with image gathering technology such as structured light projection or laser. The file must be a closed and trimmed surface which usually, when using indirect methods, requires some

post-processing. Then, the outside surface is triangulated which creates the *.stl* file. Often times, the *.stl* file can be read directly by the equipment which does the slicing. If not, or if some aspects need to be changed, there are several open-source and commercial slicing softwares which slice the file and create the g-code file read by the equipment. This workflow is schematically described in Figure 2.20.

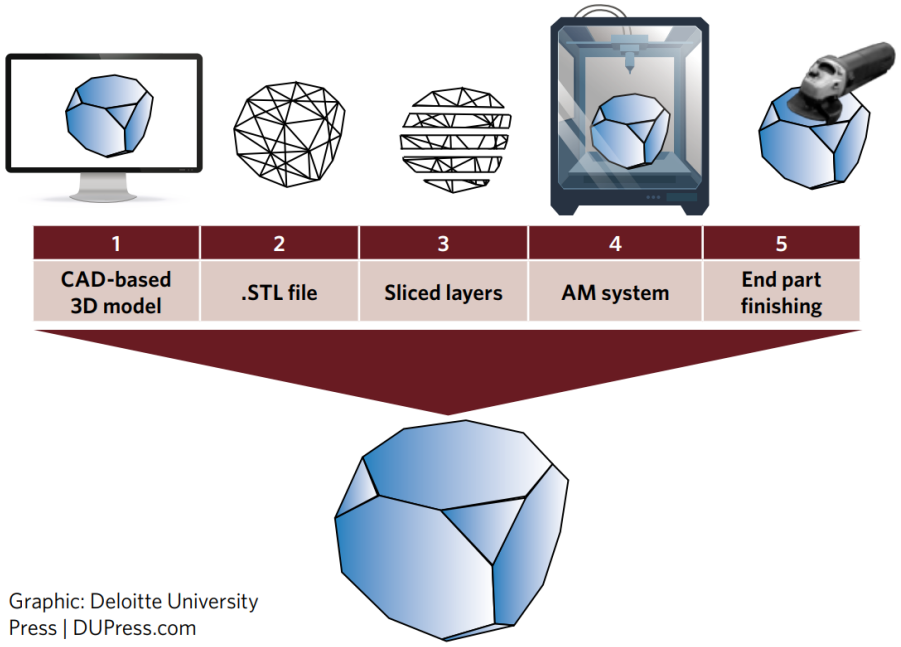


Figure 2.20: Additive Manufacturing workflow. Adapted from (Vitale et al., 2016)

2.3.2 Materials

The most commonly used materials in FDM are thermoplastics, being that the most commonly used ones are PLA (Polylactic Acid), ABS (Acrylonitrile-butene-styrene), PETG (Polyetilene Teraphtalate Glicol), ASA (Acrylonitrile-styrene-acylate), Nylon (PA - polyamide), PP (Polypropilene), PC (Polycarbonate), PVA (Polyvinyl alcohol) and PEI or Ultem (polyetheremide). The filament diameter is usually 1.75mm for smaller equipment and 2.85mm for larger equipment. Moreover, some soft and flexible polymers are being used such as TPU (thermoplastic polyurethane) and TPE (thermoplastic elastomer).

In addition, recently, thermoplastics such as PEEK(Poly-ether-ether-Ketone) which has a higher melting point than other thermoplastics has been used as material for desktop 3D printing (Upputuri, 2017). Moreover, other non-polymeric materials have been explored in the literature such as ceramic materials, bioglass, carbon nanotubes, carbon fibers, agricultural waste, among others (Singh et al., 2020).

Table 2.1 gathers some relevant mechanical and physical properties of the most commonly used materials in FDM which were mentioned previously. Processing properties relative to FFF are displayed in Table 2.2.

These materials, which much be available in the form of a filament must be fabricated with high quality because the mechanical stress (tension and compression) and melting which the filament is subject to, require elevated mechanical and thermal stability (Dizon et al., 2018). The fabrication of in-house feedstock is also possible and not a tedious-task being, however, necessary to guarantee that melting temperature is under 300°C when deciding the base for the polymer (Singh et al., 2020).

Table 2.1: Mechanical and physical properties of the most commonly used thermoplastics. The information displayed in this table was gathered from several online sources and compiled by the author of this thesis.

	E [MPa]	Density [g/cm3]	Tg [°C]
Rigid thermoplastics			
ABS	1190-2900	1.04	80-125
ASA	2200	1.07	100
Nylon (PA)	1800	1.06-1.14	50
PC	13500-21400	1.2	150
PETG	1100-20300	1.23	79-80
PLA	2960-3600	1.25	57
PP	1500-2000	0.9	-20 - (-10)
PVA	1000-5000	1.23	70
Ultem (PEI)	2900-3000	1.27	217
Soft thermoplastics			
TPE	3.6-120	0.9-1.2	-90 - (-40)
TPU	483-5500	1.28-1.66	-27

Table 2.2: FFF processing properties of the most commonly used thermoplastics. The information displayed in this Table was gathered from several online sources and compiled by the author of this thesis.

	Bed temperature [°C]	Extruder temperature [°C]	Building surface
Rigid thermoplastics			
ABS	95-110	220-250	Kapton tape, ABS slurry
ASA	90-110	235-255	Glue stick, PEI
Nylon (PA)	70-90	220-270	50
PC	80-120	260-310	Glue stick, PEI, Commercial adhesive
PETG	75-90	230-250	Glue stick
PLA	45-60	190-220	Glue stick, glass, PEI
PP	85-110	220-250	Packing tape, PP sheet
PVA	45-60	185-200	PEI, Painter's tape
Ultem (PEI)	120-150	350-380	Perf board, Kapton tape, Lightly sanded FR4
Soft thermoplastics			
TPE	70	190-250	Painter's tape, glue stick
TPU	45-60	225-245	PEI, Painter's tape

2.3.3 Equipment

Equipments for FDM/FFF can be divided into two categories, industrial equipment which usually has an outside structure and are much larger in size as well as possessing close-source software, and low cost equipment much smaller in size, usually mounted/built by the user and using open-source software (Gomez Gonzalez, 2016).

According to their movement, printers can be classified as being Cartesian, Delta, Polar or Robotic Arm. Cartesian printers are based on the cartesian coordinate system and use the three axes X, Y and Z to determine the correct positions and direction of the print head. Delta printers operate with cartesian coordinates as well combining a round printing plate with an extruder which is fixed at three triangular points which move up and down to define the position. Polar printers use the polar coordinate system and therefore have the coordinates defined by an angle and a length which means that the plate rotates and moves at the same time with the extruder moving up and down. Finally, there have been some developments incorporating robotic arms into equipments, for example employed in civil construction.

Moreover, extrusion can occur by two distinct methods, direct extrusion where the filament is pushed directly into the nozzle and Bowden extrusion where the filament is pushed and pulled through a PTFE bowden tube. Direct extrusion presents better extrusion, faster retraction which is the backwards movement of the filament to avoid stringing between movements, requires a motor with less power and allows for a wider range of materials to be used. The main disadvantage of using direct extrusion is the fact that the movements are burdened due to extra weight in the printer head. Bowden extrusion allows for cleaner movements, a larger build volume and the equipment is more compact. However, using Bowden requires a more powerful motor, the response time is slower and less materials can be used due to the maximum temperature allowed by the PTFE (Hullette, 2020).

2.3.3.1 Industrial 3D printers

Industrial grade printers are sold for an amount of more than 5000 USD and usually include an exterior cover. Accuracy is improved and larger parts can be manufactured as well as being possible to use engineering plastics with improved properties such as PC and Ultem. Overall, FDM cadence is quite reduced however, industrial equipments can produce at a larger rate than desktop low-cost equipments (Varotsis, 2020). Rize3D and Stratasys are two manufacturers who sell industrial grade equipment (Wohlers, 2019).

2.3.3.2 Low-cost/desktop 3D printers

A printer is considered to be low-cost when sold for under 5000 USD. These are much smaller in size and less accurate than industrial printers in addition to being more limited in the size of the manufactured parts. However, these are much more customizable due to the open-source philosophy and simplicity of the machine. Usually, less demanding and inexpensive materials are

prefered such as PLA and PETG. Creality3D, Prusa, Ultimaker are some manufacturers which produce low-cost equipment (Varotsis, 2020; Wohlers, 2019).

Braconnier et al. (2020) studied the influence of printing parameters of ABS is several desktop printers, namely, Ultimaker, MakerBot and Zortrax having obtained results that show how the mechanical properties of printed parts can vary from equipment to equipment (Figure 2.21).

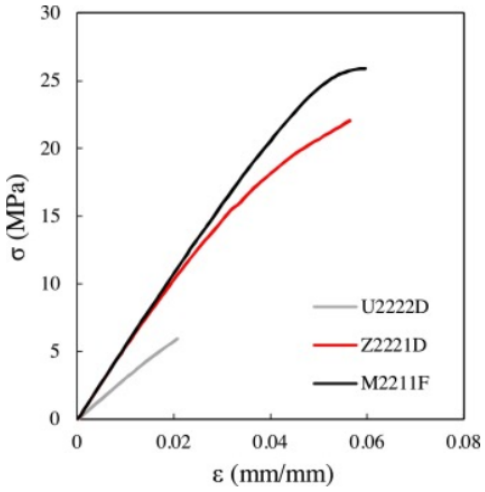
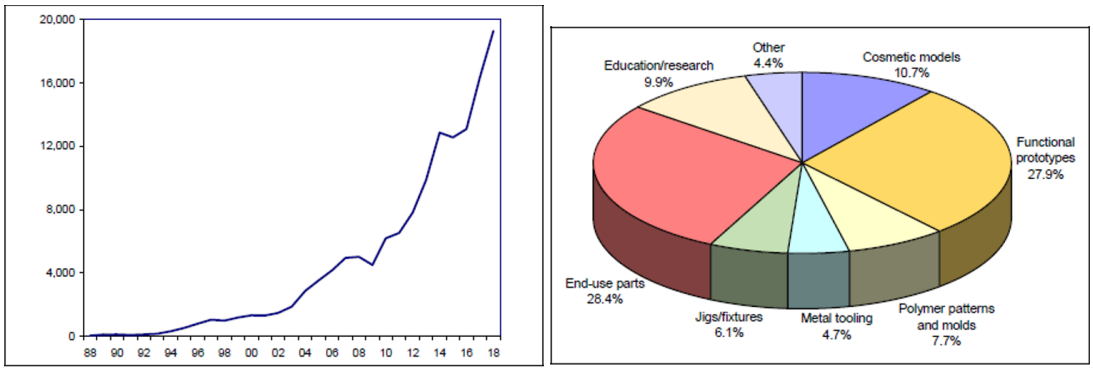


Figure 2.21: Stress-strain results of tensile specimens printed in three different desktop printers. U stands for Ultimaker, M stands for MakerBot and Z stands for Zortrax. Adapted from (Braconnier et al., 2020)

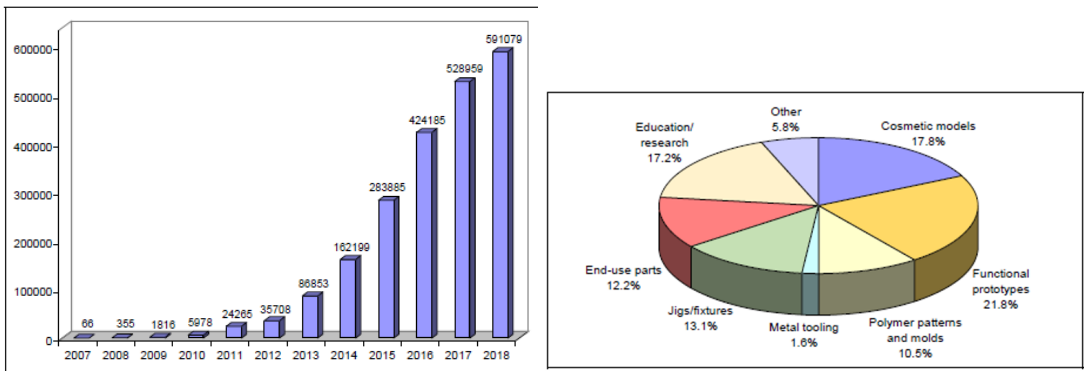
2.3.4 Economic aspects

According to the data from the Wohlers report (Wohlers, 2019), the industry has been on a constant upwards route in terms of sales with more and more equipment being sold every year. Figure 2.22 shows the increase in sales of industrial equipment and the main areas of application. Figure 2.23 shows the same information with regard to desktop and low-cost equipment. Functional prototyping is a main driver of application for both equipment types. However, end-use parts are the main application of parts produced by industrial equipment, highlighting the great quality of parts produced by these sophisticated technologies.



(a) Sales evolution (b) Areas of application

Figure 2.22: Sales evolution and areas of application for industrial equipment according to the Wohlers report of 2019 (Wohlers, 2019)



(a) Sales evolution (b) Areas of application

Figure 2.23: Sales evolution and areas of application for desktop equipment according to the Wohlers report of 2019 (Wohlers, 2019)

There are possible applications in many sectors such as biomedical, aerospace, automobile, pharmaceutical, construction, electrical, food, textile, jewellery, toys, sports, energy, among others (Singh et al., 2020), proving the applicability and versatility of AM, especially, fused filament fabrication (FFF).

Chapter 3

Numerical Methods

This chapter has the objective of briefly introducing the numerical methods which are the base of the simulations conducted for this work. Since two distinct methods are used, both are introduced in this section.

A brief introduction on the Finite Element Method (FEM) is done. However the main focus is on the meshless methods, more specifically the NNRPIM - Natural Neighbor Radial Point Interpolation Method.

3.1 Finite element method

The Finite Element Method is a very useful tool in an engineer's arsenal with a vast literature explaining and exploring that topic (Bathe, 1996; Onate, 2013; Reddy, 2005; Zienkiewicz and Taylor, 2005).

The derivation of governing equations for the majority of problems usually does not consist in that impossible of a task. However, obtaining solutions through exact methods can become an impossible task due to geometry or material complexities. To overcome this, numerical methods, such as the Finite Element Method provides solutions by transforming the differential equations of a continuum into computable algebraic equations of a discrete model of a continuum which depend on a finite set of parameters. The model for real-life problem more often than not involves thousands or even millions of equations which can only be solved with computers.

In the Finite Element Method, a given domain is approached as a collection of sub domains which cannot overlap each other, and over each of those sub domains in the governing equations is approximated by any of the traditional variational methods. This is done because it is easier to represent a complicated function as various simple polynomial equations.

The first step is to divide the domain Ω into a collection of simple sub domains called Finite Elements, Ω_e which are interpreted as independent domains by themselves.

Then, over each finite element, algebraic equations among the quantities of interest are developed using the governing equations of the problem. After that, the relationships from all elements

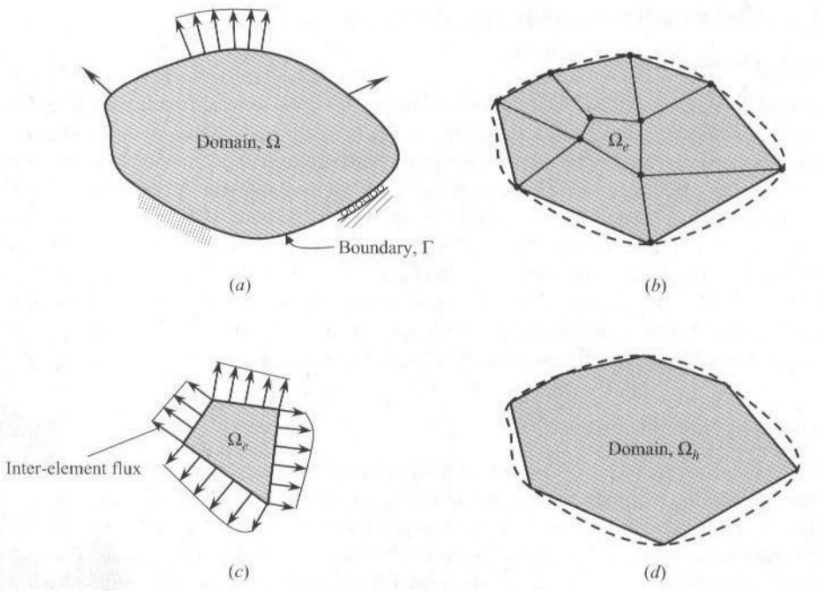


Figure 3.1: Representation of a domain Ω in triangles and quadrilaterals. Adapted from (Reddy, 2005).

are assembled using inter-element relationships. Figure 3.1, adapted from (Reddy, 2005), explicits how the domain Ω is divided into finite elements.

A structural model must include three fundamental aspects according to Onate (2013):

1. Geometrical description of the structure by means of its geometrical components such as points, lines, surfaces and volumes;

2. The mathematical expression of the basic physical laws governing the behaviour of the structure such as force-equilibrium equations and boundary conditions, and usually written in terms of differential or integral equations;

3. Specification of the physical properties of the materials and of the loads acting on the structure.

The following step in structural analysis is the implementation of the numerical method in computer code. The output of this process is the computational model. Figure 3.2, which was adapted from Onate (2013) shows how a computational model is obtained in the form of a flowchart. For the FEM, an approximation in the form of Equation 3.1 is seeked (Reddy, 2005), where u_j are the values of u_h at the element nodes, and ϕ_j are the associated approximation functions. Direct substitution of the approximations into the differential equations does not always result in a necessary and sufficient number of equations for the undetermined coefficients u_j and c_j. A procedure to overcome this problem is for example the weighted-integral form of differential equation.

$$u \approx u_h = \sum_{j=1}^{n} u_j \psi_j + \sum_{j=1}^{m} c_j \phi_j \tag{3.1}$$

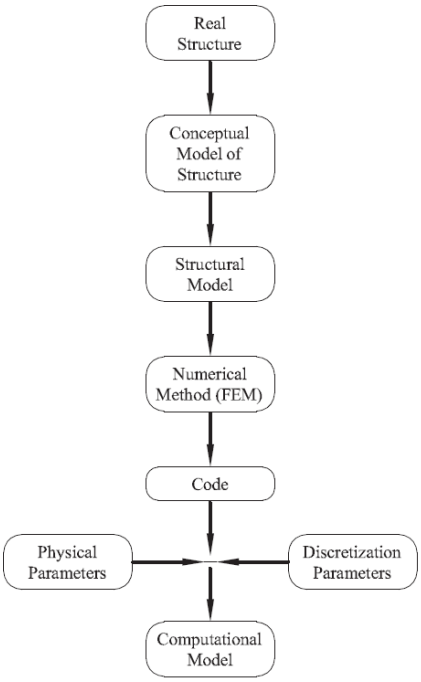


Figure 3.2: Path from a real structure to a computational model. Adapted from (Onate, 2013).

There can be more than one finite element model of the same model (governing equations). The type of model depends on the differential equations used to derive the algebraic equations for the undetermined coefficients over an element, and nature of the approximation functions used.

In summation, the FEM possess two major advantages according to Reddy (2005):

1. Accurate representation of complex geometry and inclusion of different material properties;
2. Easy representation of the total solution by functions defined within each element that capture local effects.

3.2 NNRPIM: Natural Neighbour Radial Point Interpolation Method

The NNRPIM belongs to the meshless methods. These methods have recently began to show a focus on interest by several authors (Belinha, 2014; Belytschko et al., 1996; Gu, 2005; Nguyen et al., 2008).

3.2.1 Meshless methods

In meshless methods, the nodes can be arbitrarily distributed since the field functions are approximated within an influence domain rather than an element. Contrary to the FEM, where the elements cannot overlap each other, in meshless methods the influence domains must overlap. The three fundamental parts of meshless methods are, according to Belinha (2014):

1. **Field approximation or interpolation function**. The most important are the Taylor approximation, the moving-least-square approximation, the reproducing kernel approximation, the parametric interpolation, the hp-cloud approximation function and the Sibson interpolation. Each of these require a domain of applicability where outside of the domain the function assumes the value of zero;

2. **Formulation**. Here the meshless methods can be divided in two categories, one that pursues the strong form solution through direct use of the partial differential equations, and another that seeks the week form solution which uses a variational principle to minimize the residual weight of the differential equations. These last are important as some solutions to differential problems do not achieve smooth solutions;

3. **Integration**. An integration scheme is necessary to obtain the integral of the residual weight of the differential equations, which can be done with a background mesh composed of integration points.

The only information about the nodal distribution which is needed in order to build the interpolation functions, is the spacial location of each node because it is not necessary to establish relations between the nodes, as a truly meshless method. This means that the node distribution doesn't form a mesh.

The method performance is dependent on the nodal density of the discretization, similarly to mesh dependent methods where a denser mesh provides more accurate results, a denser node distribution provides more accurate results. If the distribution is not correctly balanced that is, if areas that require higher node density than others such as boundaries, crack tips and edges and stress concentration areas, this can also decrease the accuracy of the method (Belinha, 2014; Liu, 2002, 2003).

The background mesh, which can be larger than the problem domain, is then constructed in order to integrate the weak form of the governing equations (Belinha, 2014; Belytschko et al., 1994). FEM usually uses Gaussian integration meshes which can be fitted to the problem domain or not. However, in meshless methods it is more appropriate to use the Voronoi (Voronoi, 1908) diagram. Nodal integration, which can serve also as the integration mesh, can lead to a decrease in accuracy, thus being necessary a stabilization method which increases the computational cost (Belinha, 2014; Chen et al., 2002; Elmer et al., 2012; Sze et al., 2004).

Nodal connectivity in the FEM is imposed by the elements. In meshless methods however, this is done by determining the influence domains. Therefore, for each point of interest $x_{\mathbf{I}}$, the problem domains, areas or volumes are determined and the points inside those areas constitute the influence domain relative to node $x_{\mathbf{i}}$. Usually, the points of interest correspond to the integration points of the background mesh. In some meshless methods, the collocation point methodology is used where the points of interest correspond to the nodes of the problem. The influence domains should have the same number of nodes and these can present different shapes and sizes. Figure 3.3 presents two examples of influence domains, a) where the visible shapes and sizes of the influence

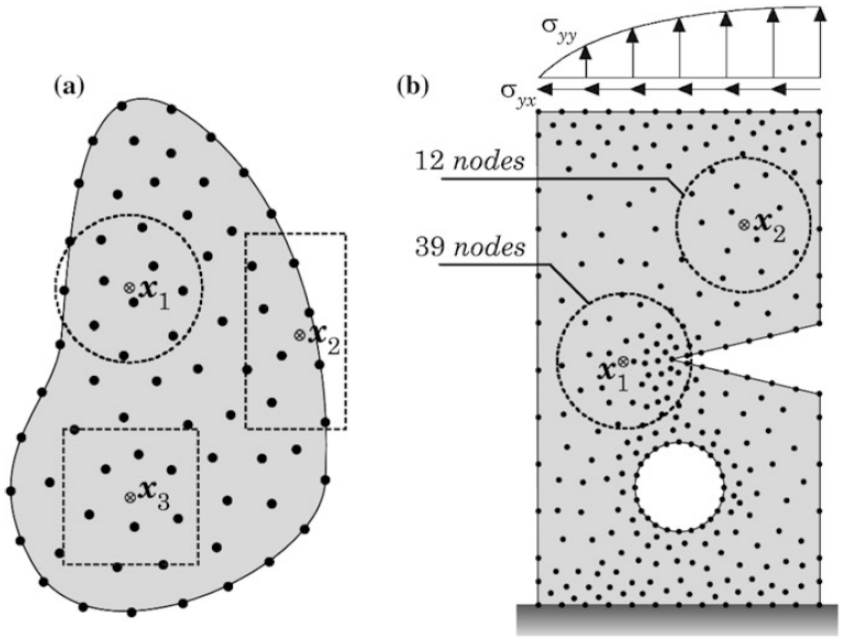


Figure 3.3: Influence domains adapted from (Belinha, 2014)

domains are visible and b) where an incorrect approach is visible since both domains present a different number of nodes (Belinha, 2014).

Having obtained the influence domains, the field variables can be obtained with the approximation interpolation function φ_i for the ith node of a point of interest. For a displacement field for example, Equation 3.2 is used to calculate the field variables where $u(x_\mathbf{I})$ is the displacement vector at the point of interest and $u(x_i)$ are the displacement components of each node x_i for the n number of nodes inside the influence domain at that point of interest.

$$\mathbf{u(x_I)} = \sum_{i=1}^{n} \varphi_i(x_I)\mathbf{u(x_i)} \tag{3.2}$$

The next step is the establishment of the equation system, whose can be formulated using approximation or interpolation functions applied to the strong or weak formulation. In meshless methods using the weak form of Galerkin, the discrete equations can be obtained by applying the weighted residual method of Galerkin to the governing differential equations (Belinha, 2014).

The appropriate solver for the system must also be chosen carefully. In static problems where a system of algebraic equations is obtained, Gauss elimination for small systems or LU decomposition for larger systems can be used. For other different types of analysis where the system is a system of eigenvalue equations, an appropriate solver such as the Jacobi method should be used (Belinha, 2014).

3.2.1.1 Other meshless methods

Some other meshless methods besides the NNRPIM which is going to be the main focus of this introduction include the Diffuse Element Method using the Moving Least Square approximations (Lancaster and Salkauskas, 1981; Nayroles et al., 1992), the Element-Free Galerkin Method (Belytschko et al., 1994), the Smooth Particle Hydrodynamics Method (Gingold and Monaghan, 1977) which originated the Reproducing Kernel Particle Method (Liu et al., 1995), the Meshless Local Petrov-Galerkin (Atluri and Zhu, 1998) method which evolved into the Method of the Finite Spheres (De and Bathe, 2000), the Finite-Point Method (Onate et al., 1996a,b, 2001), the Radial Basis Function Method (Kansa, 1990a,b).

These methods present several problems, being the lack of the Kronecker delta property on the approximation functions the most important unsolved issue (Belinha, 2014). Other methods have been more recently developed in order to overcome this obstacle such as: the Point Interpolation Method (Liu, 2001), the Point Assembly Method (Liu, 2002), the Radial Point Interpolation Method (Wang and Liu, 2002a,b), the Meshless Finite Element Method (Idelsohn et al., 2003), the Natural Neighbour Finite Element Method (Sukumar et al., 2000; Traversoni, 1994) and the Natural Element Method (Braun and Sambridge, 1995; Cueto et al., 2000; Sukumar et al., 1998). All of these use the Sibson interpolation functions.

The Natural Neighbour Radial Point Interpolation Method (Dinis et al., 2007) is a combination of the Natural Element Method and the Radial Point Interpolation Method.

More recently the Natural Radial Element (Belinha et al., 2013a,b,c) was developed.

3.2.2 Natural Neighbour Radial Point Interpolation Method

As it was previously mentioned in 3.2.1, the NNRPIM is a combination of the Natural Element Method and the Radial Point Interpolation Method, that is, it combines the Radial Point Interpolators with the Natural Neighbours geometric concept (Belinha, 2014).

3.2.2.1 Radial point interpolation method

The Radial Point Interpolation Method (RPIM) was first presented by Wang and Liu (2002a,b). The Radial Point Interpolators began with the Point Interpolation Method (Liu, 2001) which consisted in constructing polynomial interpolants based on only on a group of arbitrarily distributed points. These polynomial interpolants possess the Kronecker delta property. The Point Interpolation Method has a problem which is that, in the case that the nodes are perfectly aligned, the construction of the interpolation function will obtain a singular solution (Belinha, 2014).

Therefore, it evolved into the RPIM and to stabilize the procedure, the Radial Basis Function was added. Firstly the added function was the Gaussian function and the multiquadric radial basis function. Then, with the work developed by Kansa (1990a,b), the radial basis functions were used to solve partial differential equations.

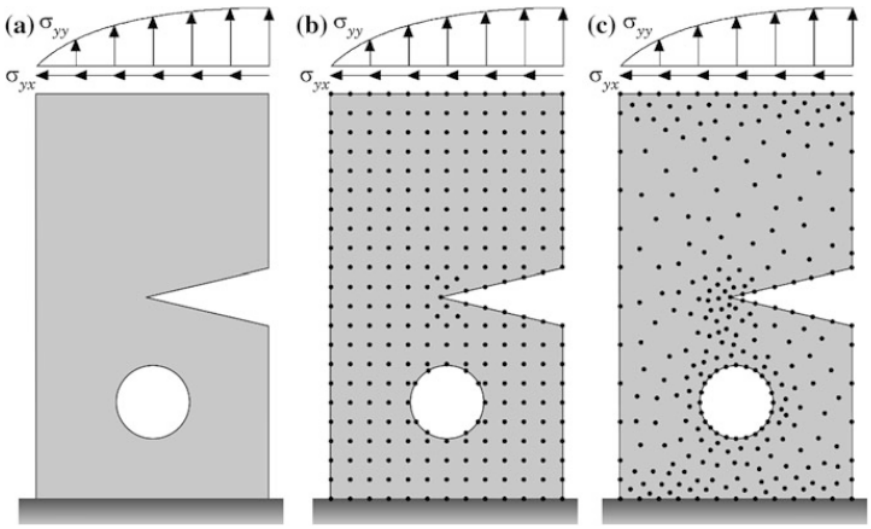


Figure 3.4: Node dependent numerical discretization. Adapted from (Belinha, 2014)

The RPIM uses the concept of "influence-domain" which generates sparse and banded stiffned matrices which is more adequate in complex geometry problems, and the work by Kansa (1990a,b) uses the concept of "global-domain" (Belinha, 2014).

3.2.2.2 Natural neighbour radial point interpolation method

The NNRPIM comes as an evolution to this process by imposing the nodal connectivity through replacement of the "influence-domain" with the "influence-cell" concept. This is achieved with the help of concepts such as the Voronoi diagram (Voronoi, 1908) which creates the "influence-cells" and the Delaunay tesselation (Delaunay, 1934), the dual of the Voronoi cells, creates the node-depending background mesh used in the integration of the NNRPIM interpolation functions. Since the background mesh is totally dependent of the nodal distribution, this can be considered a truly meshless method. In addition to this, the nodes can be arbitrarily distributed since, unlike the FEM, there are no geometric impositions in order to guarantee convergence of the method. The interpolation functions, used in the Galerkin weak form, are constructed similarly to the Radial Point Interpolation Method.

The utilization of this method follows the basic steps as any other nodal dependent discretization numerical method which can be seen in Figure 3.4 adapted from (Belinha, 2014):

- Study of the geometry and definition of the solid domain and contour;
- Definition of the boundary conditions, natural and essential;
- Discretization of the problem domain and boundary following a nodal distribution which can be regular or irregularly distributed.

Since with meshless methods nodal connectivity can't be assured by a predefined mesh as in the FEM, this connectivity must be defined following the nodal distribution. The NNRPIM

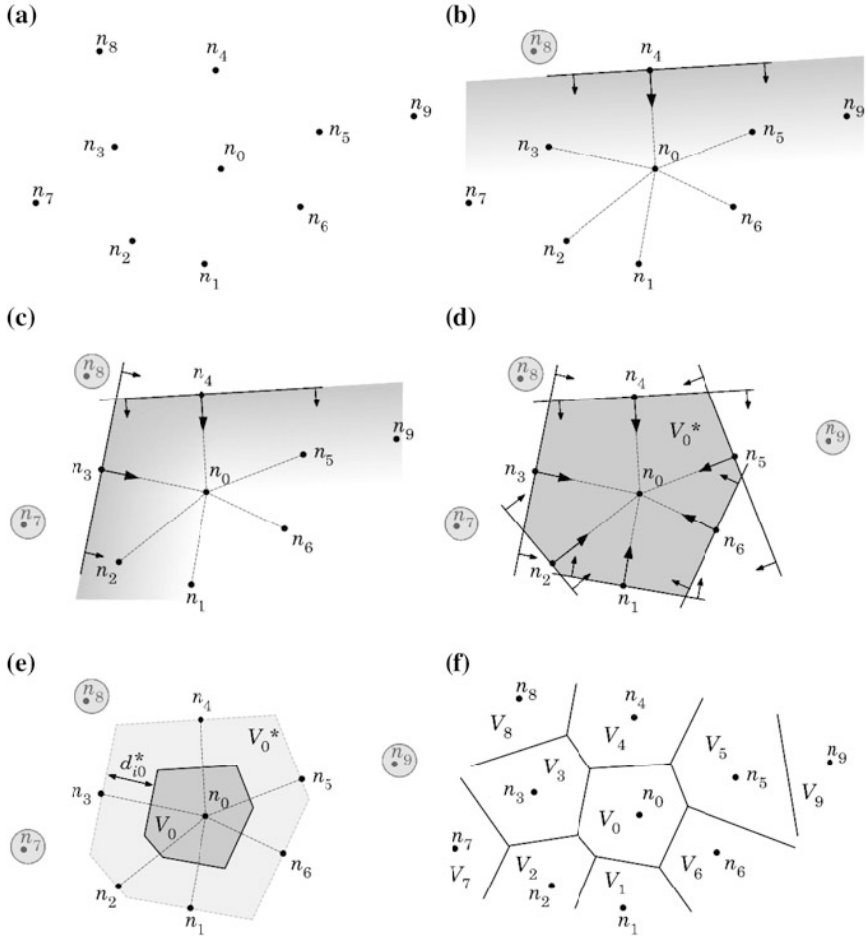


Figure 3.5: Obtaining the Voronoi diagram of a discrete nodal distribution through the concept of natural neighbours. a) to d) demonstrate how a single cell is obtained, e) represents the Voronoi cell for node n_0 and f) represents the Voronoi diagram. Adapted from (Belinha, 2014).

uses the concept of influence-cells (Dinis et al., 2007) to obtain the influence-domains previously mentioned in 3.2.1. The influence domains are determined based on the geometric and spacial relations between the Voronoi cells obtained from the Voronoi diagram of the nodal distribution and hence called influence-cells.

This Voronoi diagram uses the concept of natural neighbors (Sibson, 1981). Figure 3.5 explains how the Voronoi diagram is obtained following the natural neighbour concept. The software which is used in this work allows for the influence cell to be a "first degree" influence cell or a "second degree" influence cell. The difference between these is that a "first degree" influence cell used the natural neighbours of a said point of interest $\mathbf{x_I}$, and a "second degree" influence cell uses also the natural neighbours of the natural neighbours of that same point of interest $\mathbf{x_I}$. These last one usually presents better accuracy in results (Belinha, 2014). Figure 3.6 shows examples of these two types of influence cells.

One of the main drivers in increasing the computation cost of the method is the definition of the system of equations which describes the ruling physical phenomenon being studied. As it

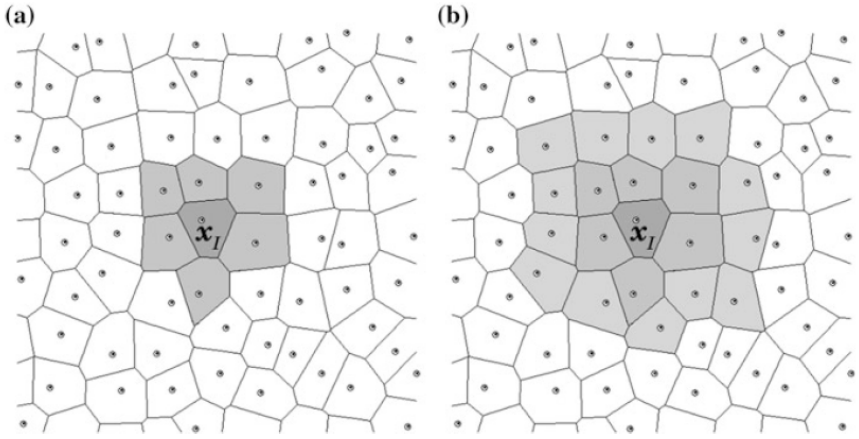


Figure 3.6: a) "First-degree" influence cell and b) "Second-degree" influence cell. Adapted from (Belinha, 2014)

was mentioned before, this system can be obtained using variational methods such as the weak form of the Galerkin. Contrary to the FEM, where the integration mesh is coincident with the element mesh, in meshless methods the degree of the shape function is generally unknown and therefore the background integration mesh cannot be established *a priori*. It is very important to define, for each meshless approach, the optimal relationship between the node field density and the background integration mesh density, which must be studied every time the shape function construction procedure is modified or the influence domains are changed.

Two integration schemes are now presented, the Gaussian Quadrature Integration (Bathe, 1996; Wang and Liu, 2002a,b; Zienkiewicz and Taylor, 2005) and the Nodal Integration Scheme. In the Gauss-Legendre integration the solid domain is divided into a regular grid and then filled with integration points according to the Gauss-Legendre quadrature rule. This is illustrated with a simple example in Figure 3.7. The initial quadrilateral is transformed in an isoparametric square and then quadrature points are applied inside the ispoarametric quadrature square using a 2x2 quadrature. Using isoparametric interpolation functions, the coordinates of the quadrature points are obtained. The integration weight of the quadrature point is obtained with the inverse of the Jacobian matrix determinant of the respective grid cell. If the grid fits the solid domain then no post-processing is necessary. Otherwise, all the integration points outside the solid domain are

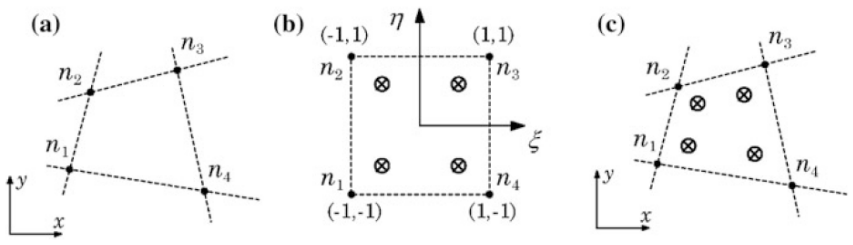


Figure 3.7: Gaussian quadrature procedure. Adapted from (Belinha, 2014)

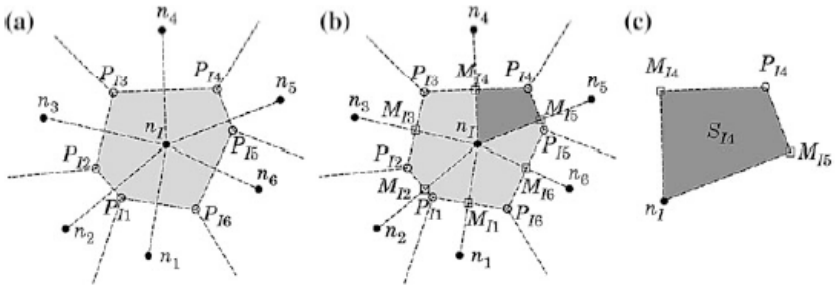


Figure 3.8: Obtaining the subcells from a Voronoi cell. Adapted from (Belinha, 2014)

removed. Regular quadrature integration meshes are most commonly used because these are simpler to apply even though fitted integration meshes present more accurate results. The numerical integration is done according to Equation 3.3 where $\widehat{w}_{\mathrm{i}}$ is the weight of the integration point and function F is defined in the solid domain Ω (Belinha, 2014).

$$\int_{\Omega} \mathbf{F}(x) d\Omega = \sum_{i=1}^{n_{\mathrm{g}}} \widehat{w}_{\mathrm{i}} \mathbf{F}(x_{\mathrm{i}})) \tag{3.3}$$

The nodal based integration consists on numerically integrating the integro-differential equations ruling the studied physical phenomenon which can be used either in one, two or three dimensional domains (Belinha et al., 2012; Dinis et al., 2007, 2008). Using this method, only the spacial information regarding the nodal distribution is necessary to build the background integration mesh which makes this a truly meshless method.

After the domain is discretized, either with a regular or with and irregular nodal distribution, the Voronoi cells for each node are determined and divided into smaller areas according to the process described in Figure 3.8. If the nodal distribution is regular, the Voronoi cells are divided in triangular subcells instead of quadrilateral subcells as it can be seen in Figure 3.9. The size $A_{\mathrm{V_I}}$ of the Voronoi cell V_{I} can be obtained through the sum of the size $A_{\mathrm{S_{Ii}}}$ of the subcells S_{Ii}. For the one dimensional domain, A represents lengths and for the two dimensional domain A represents areas and for the three dimensional domain, A represents a volume.

The simplest integration scheme that can be established using the subcells triangular and quadrilateral shapes is obtained inserting a single integration point in the barycenter of the sub-

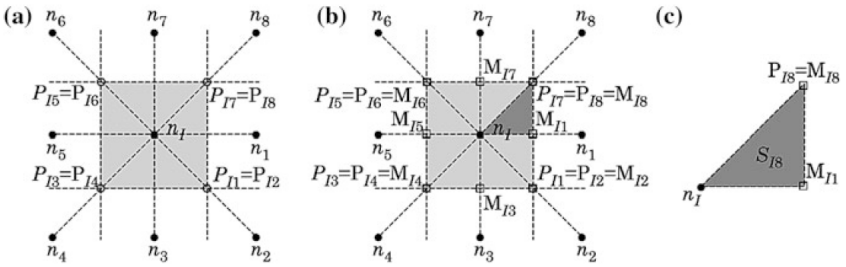


Figure 3.9: Division of a regular cell into triangular subcells. Adapted from (Belinha, 2014)

cells. The spacial location of each integration point is determined on each subcell and the weight of each integration point is the area of the respective subcell.

From this simpler method, a more general formulation can be obtained by dividing in this case the quadrilateral subcells. First, the barycenter x_c is discovered and then, the middle points of the quadrilateral edges are determined $x_{ij} = (x_i + x_j)/2$ and with this, new subcells are defined. The Gauss Legendre quadrature can be used to obtain the integration points in these quadrilaterals (Bathe, 1996; Zienkiewicz and Taylor, 2005). The integration weight of each integration point $\mathbf{x_I}$ is given by expression 3.4 where w_η and w_ξ are the Gauss Legendre quadrature weights for an isoparametric quadrilateral cell (Belinha, 2014).

$$\widehat{w_I} = w_\eta w_\xi \left(\frac{A^\square}{4} \right) \tag{3.4}$$

On the other hand, the nodal integration scheme is obtained by considering the integration point $\mathbf{x_I}$ to be coincident with the barycenter of the Voronoi cell $\mathbf{V_I}$. The weight $\widehat{w_I}$ of each integration point will then be the sum of each of the areas of the respective subcells. The spacial location of each integration point is given by Equation 3.5 where $\mathbf{x}_{S_i}$ is the barycenter of each subcell S_{Ii} and $A_{S_{Ii}}$.

$$\mathbf{x_I} = \frac{\sum_{i=1}^{n} \mathbf{x}_{S_i} A_{S_{Ii}}}{\sum_{i=1}^{n} A_{S_{Ii}}} \tag{3.5}$$

Since the nodal integration is not sufficient to accurately integrate the meshless shape functions, stabilization techniques must be employed.

For the three dimensional case, if nodal discretization is irregular the Voronoi cells are divided into hexahedron. Otherwise, it will be divided into tetrahedral subcells.

First, the three-dimensional Voronoi cells are obtained for each node in the problem domain. The Voronoi cell is partitioned into subcells and then each partition is isoparameterized and the Gauss-Legendre quadrature scheme is applied. Finally, the obtained spacial location of the integration points and respective integration weights are transformed again to the Cartesian coordinate system (Belinha, 2014).

Chapter 4

Bone Remodelling and Structural Optimization

This chapter consists on a theoretical and state-of-the-art review of the optimization methodologies employed in the practical section of this work. The aim is to use the density distributions and truss-like structures to obtain functional gradients capable of enhancing the stiffness-to-weight ratio of the tested parts.

There are several studies (Carter and Hayes, 1977; Carter and Spengler, 1978; Gibson, 1985; Goldstein, 1987; Martin, 1991; Rice et al., 1988) studies confirming the dependence of bone mechanical properties on its apparent density. Bone apparent density is given by Equation 4.1 where w_{sample} and V_{sample} are the wet mineralised mass of the sample and the volume of that same sample respectively (Belinha, 2014).

$$\rho_{app} = \frac{w_{sample}}{V_{sample}} \tag{4.1}$$

Considering that p is the porosity of the sample given by the ratio between the number of holes and the volume of the sample, apparent density can also be expressed as Equation 4.2 where ρ_0 is the maximum density.

$$\rho_{app} = \rho_0(1-p) \tag{4.2}$$

For this present work, where these laws are applied to the gyroid structure in PLA, the aim is to develop a similar expression regarding the influence of density on the mechanical properties of the gyroid infill in itself (Silva, 2019). Apparent density is calculated in an equivalent way to Equation 4.2.

Structural optimization can be divided into three categories, sizing optimization of a truss structure, shape optimization and topology optimization (Bendsoe and Sigmund, 2004; Huang and Xie, 2010).

4.1 Bone remodelling

Bone tissue can be divided in two different materials, cortical bone with a higher density and trabecular bone much less dense. For that reason, bone tissue is often described differently for cortical and trabecular bone. Correlation curves for the elasticity modulus and ultimate compression stress have been obtained by several authors (Currey, 1969, 1988; Keller, 1994; Keyak et al., 1994; Schaffler and Burr, 1988).

4.1.1 Material laws

Lotz material law (Lotz et al., 1991) takes into consideration the bone ortothropic behaviour both for cortical and trabecular bone caractherizing the elastic modulus and ultimate compression stress through mathematical Equations 4.3 and 4.4 respectively. The coefficients in question, a_1 to a_4 vary depending on the direction (axial or transverse) (Belinha, 2014).

$$E_i = a_1(\rho_{app})^{a_2} \tag{4.3}$$

$$\sigma_i^c = a_3(\rho_{app})^{a_4} \tag{4.4}$$

Belinha material law (Belinha et al., 2013d, 2012) was proposed following the conclusions in the work by Zioupos et al. (2008) which has distinguished a maximum and minimum apparent density values for bone separating the behaviour of cortical and trabecular bone 2.1g/cm^3 and 0.1g/cm^3 respectively and a transition value of 1.3g/cm^3. The proposed law consists on a mathematical law correlating the mechanical properties with the bone tissue apparent density. Figures 4.1 and 4.2 show the variation of elasticity modulus in axial and transverse directions respectively according to both laws. For the proposed law, both the elasticity modulus and the ultimate stress are third-degree polynomial functions of the apparent density (Belinha, 2014).

4.1.2 Bone remodelling algorithms

In the bone remodelling process, there is strong evidence of the correlation between the loads (stress or strain) that the area is subject to, and the shape that the bone takes. This has caused for some semi-empirical laws to come up in order to model how the bone will functionally adapt to the load case it is subject to. These laws are the basis for computational tools which aim at predicting bone adaptation under stress or strain states or changes in stiffness (Belinha, 2014).

4.1.2.1 Pauwels's model

Some of these models include the Pauwels' Model (Pauwels, 2013) which suggested a mathematical formulation of the Wolff's Law (Wolff, 2012) for the first time and consists on bone atropy in case of stress bellow the optimal axial stress and bone hypertrophy in case of values above the optimal axial stress. The Pauwels's Model was summarized by Kummer (1972) - Equation 4.5

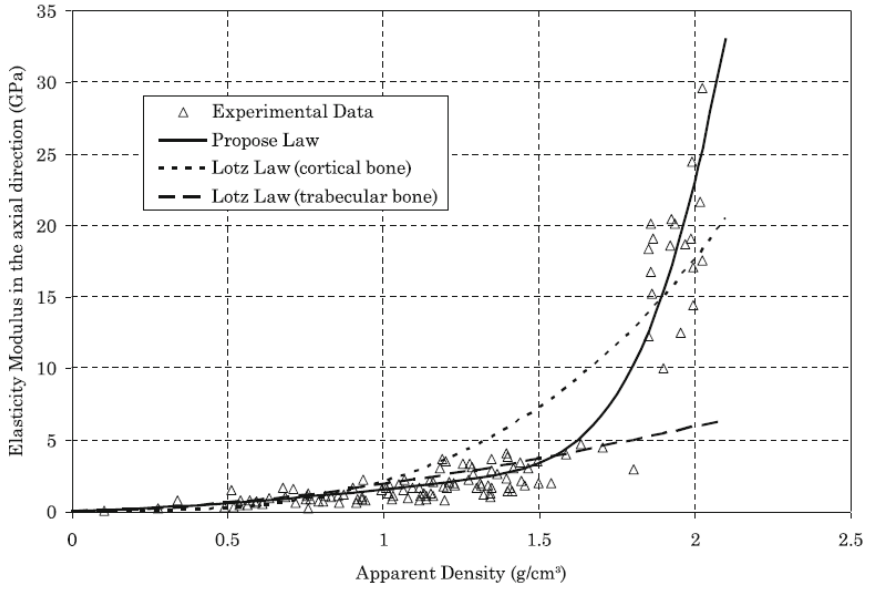


Figure 4.1: Elasticity modulus in the axial direction. Adapted from Belinha (2014)

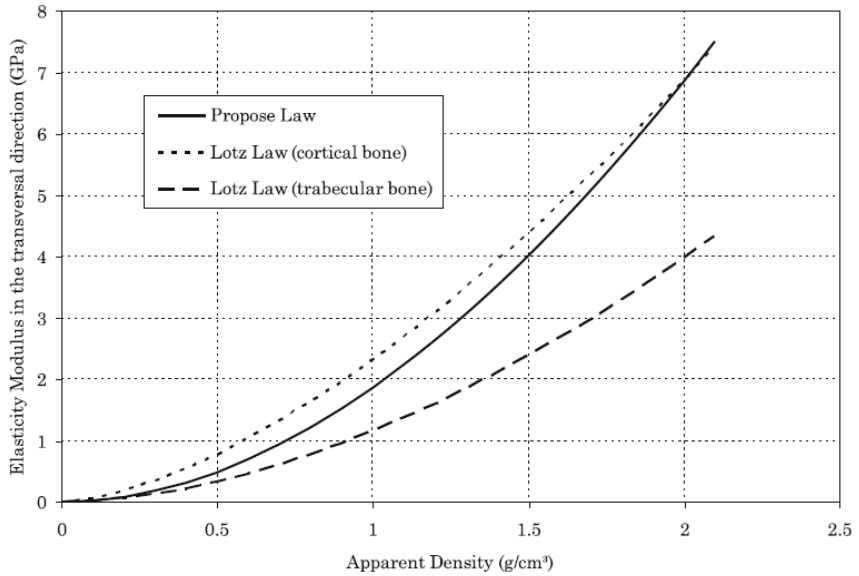


Figure 4.2: Elasticity modulus in the transverse direction. Adapted from Belinha (2014)

where β is a parameter and $\frac{\partial m}{\partial t}$ is the variation of bone mass through time.

$$\frac{\partial m}{\partial t} = \beta(\sigma - \sigma_{min})(\sigma - \sigma_n)(\sigma - \sigma_{max}) \tag{4.5}$$

4.1.2.2 Corwin's model

The Cowin's Model (Cowin and Hegedus, 1976; Cowin et al., 1992) accounts for the reorientation and changes in the anisotropic material behavior, uses the fabric tensor to develop an anisotropic model which describes the behaviour of trabecular bone. The fabric tensor is a second-order symmetric tensor, directly related to the material elasticity tensor (Cowin, 1985; Turner et al., 1990). The remodelling assumes that in equilibrium the stress and strain principal directions are coincident with the fabric tensor principal axes. It is however necessary to define a large number of parameters to conduct the remodelling analysis (Belinha, 2014).

4.1.2.3 Carter's model

The Carter's model (Carter et al., 1987, 1989; Whalen et al., 1988) similarly to the Pauwells' model, also needs a mechanical stimulus S_n (Equation 4.6) in order to maintain quasi-static remodelling and that it should be constant for the entire bone and proportional to the effective stress. Here, l is the number of load cases and m_i is the corresponding number of load cycles. The influence of the magnitude of the stress state is given by the exponent κ. The effective stress depends on the local stress state and apparent density (Belinha, 2014).

$$S_n \propto \sum_{l}^{i=1} m_i \overline{\sigma}_i^{\kappa} \tag{4.6}$$

This model, whichever material law is used, considers that the induced stress acts as a optimization tool, maximizing structural integrity while minimizing mass, which is equivalent to considering that the induced stress works as an optimization tool where an objective function is being minimized. A strain energy criteria may also be used. It differs from a stress criteria as the use of strain energy is related to the idea of stiffness maximization, whereas with stress criteria the aim is material strength optimization (Belinha, 2014; Fyhrie and Carter, 1986). When using a strain energy density criteria, a correlation between apparent density ρ_{app} and local strain energy U is obtained (Equation 4.7) which allows to estimate the apparent density as a function of the strain energy density in an equilibrium state of the remodelling process. It can also be used as an optimization criteria in an iterative optimization process.

$$\rho_{app} \propto \left(\sum_{i=1}^{l} m_i U_i^{\kappa} \right) \tag{4.7}$$

In this model it is assumed that trabeculae are oriented in the same direction as the principal stresses which results in an optimal configuration with regards to stiffness maximization. When multiple load cases are considered, a weighted combination of load cases results on a normal

vector **n** so as to obtain trabecular orientation. In this case, global normal stress is calculated as in Equation 4.8.

$$\bar{\sigma}_n(\mathbf{n}) = \left(\sum_{i=1}^{l} \frac{m_i}{\sum_{j=1}^{l} m_j} \bar{\sigma}_{n_i}^{\kappa}(\mathbf{n}) \right)^{\frac{1}{\kappa}} \tag{4.8}$$

4.1.2.4 Rodrigues' model

The Rodrigues' model (Rodrigues et al., 1999) consists on a hierarchical approach where a global model supplies strain and density information to a series of local models which describe the trabecular microstructure at each global model location. Bone adaptation is described in two levels of the bone structure, the macroscopic level defining the bone apparent density and the microscopic level which defines the trabecular structure (Belinha, 2014).

4.1.2.5 Adaptation of the Carter's model

For the work conducted in this thesis, the FEMAS software was used where this adaptation for meshless methods (Belinha et al., 2013d, 2012) of the Carter's model is implemented.

The bone remodelling nonlinear equation is presented as a differential equation (Equation 4.9) in which a temporal-spatial based functional $\rho_{app}(\mathbf{x},t)$ is minimized with respect to time and where $\rho_{app}(\mathbf{x},t) : R^{d+1} \mapsto R$ is defined for the temporal one-dimension and the spacial d-dimensions.

$$\frac{\partial \rho_{app}(\mathbf{x},t)}{\partial t} \cong \frac{\Delta \rho_{app}(\mathbf{x},t)}{\Delta t} = (\rho_{app}^{model})_{t_j} - (\rho_{app}^{model})_{t_{j+1}} = 0 \tag{4.9}$$

It is assumed that the d-dimensional domain is discretized in N nodes where $X = \{x_1, x_2, ...x_N\} \in \Omega$ leading to Q interest points where $Q = \{x_1, x_2, ...x_Q\} \in \Omega$ being that $x_i \in R^d$. The temporal domain is discretized as iterative fictitious time steps $t_j \in R$ where $j \in N$. The medium apparent density for the complete model domain is defined as $(\rho_{app}^{model})_{t_j}$ for a fictitious time t_j. Within the same iterative step, medium apparent density is given by Equation 4.10 where $(\rho_{app})_I$ is the infinitesimal apparent density on interest point x_I defined by $\rho_I = g(\sigma_I)$.

$$\rho_{app}^{model} = Q^{-1} \sum_{i=1}^{Q} (\rho_{app})_i \tag{4.10}$$

Then, $g(\sigma_I) : R^3 \mapsto R$ is defined as in Equation 4.11.

$$g(\sigma_I) = \max(\{\sigma_1^{-1}(\rho_I), \sigma_2^{-1}(\rho_I), \sigma_3^{-1}(\rho_I)\}) \tag{4.11}$$

Here, σ_j are the principal stresses obtained for the interest point x_I and are the inverse functions of $\sigma_j^{-1}(\rho_I)$ defined in the material law. Therefore, an Equation 4.12 of the principal stress σ_1 can

be obtained.

$$\sigma_1^{-1}(\rho_I) = \sigma_{axial}^{-1}(\rho_I) = \rho_{axial} = 8.14 \times 10^{-4} f_1(\sigma_1) + \frac{235.3}{f_1(\sigma_1)} - 0.439 \tag{4.12}$$

The remaining principal stresses for j = 2 and 3 can be obtained with Equation 4.13.

$$\sigma_j^{-1}(\rho_I) = \sigma_{trans}^{-1}(\rho_I) = \rho_{trans} = 1.34 \times 10^{-3} f_2(\sigma_j) + \frac{3.34 \times 10^4}{f_2(\sigma_j)} - 0.669 \tag{4.13}$$

The functions $f_1(\sigma_1) : C \mapsto R$ and $f_2(\sigma_j) : C \mapsto R$ are defined as Equations 4.14 and 4.15.

$$f_1(\sigma_1) = Re\left(-1.54 \times 10^8 + 4.47 \times 10^7 \sigma_1 + 2.44 \times 10^3 \sqrt{-2.31 \times 10^9 \sigma_1 + 3.35 \times 10^9 \sigma_1^2}\right) \tag{4.14}$$

$$f_2(\sigma_j) = Re\left(-1.25 \times 10^{11} + 1.68 \times 10^8 \sigma_j + 1.49 \times 10^4 \sqrt{-1.88 \times 10^{11} \sigma_j + 1.26 \times 10^8 \sigma_j^2}\right) \tag{4.15}$$

Equation 4.12 and 4.13 are then applied to the interest points with strain energy density values inside the following interval, where $U_m = \min(\mathbf{U})$ and $U_M = \max(\mathbf{U})$

$$U(x_I) \in [U_m, U_m + \alpha \cdot \Delta U [\cup] U_M - \beta \cdot \Delta U, U_M], \forall U(x_I) \in R \tag{4.16}$$

The strain energy density field is defined by $\mathbf{U} = U(x_1)U(x_2)...U(x_Q)$. The α and β parameters define the growth rate and the decay rate of the apparent density. The remodelling equilibrium is achieved when Equation 4.17 is verified, where α, β and $\rho_{app}^{control}$ depend on the analysed problem.

$$\frac{\Delta\rho}{\Delta t} = 0 \vee (\rho_{app}^{model})_{t_j} = \rho_{app}^{control} \tag{4.17}$$

The iterative process calculating of bone density distribution works as a cycle which runs while the medium apparent density ρ_{app}^{med} is less than the control apparent density $\rho_{app}^{control}$ or while there is medium apparent density variation between two consecutive iterations, that it, the stop criteria is if $\frac{\Delta\rho}{\Delta t} = 0$ is true.

For each load case i the stiffness matrix $\mathbf{K}^i$, displacement field $\mathbf{u}^i$, strain field ε^i, principal directions and principal stresses, strain energy density U^i and stress field σ^i are calculated. The weighted field variable is then calculated by an appropriate superposition of all load cases according to Equation 4.18, where l is the number of relevant discrete load cases and m is the corresponding number of load cycles.

$$\xi_i = \sum_{j=1}^{l} \frac{m^{(j)} \xi_i^j}{\sum_{k=1}^{l} m^{(k)}} \tag{4.18}$$

Then, the points which belong to the interval in Equation 4.16 are subjected to the remodelling process. The integration points with lower strain energy density values are calculated using the

bone material law $\sigma(n) = f(n, \rho_{app})$. The points which do not belong to the interval will remain at the same density. Once the density values are recalculated, the field variables are actualized and medium bone apparent density is calculated as in Equation 4.19.

$$\rho_{app}^{med} = \frac{1}{n} \sum_{j=1}^{n} \rho_{app}^{j} \tag{4.19}$$

This algorithm works as a topology optimization algorithm. At each step, only the points with higher or lower strain energy density values optimize the density in response to a mechanical stimulus.

For the NNRPIM, the trabecular arrangement is obtained by attributing to each Voronoi cell, the apparent density value of the integration point which represents the Voronoi cell.

Figure 4.3 represents a summary of the algorithm which was explained.

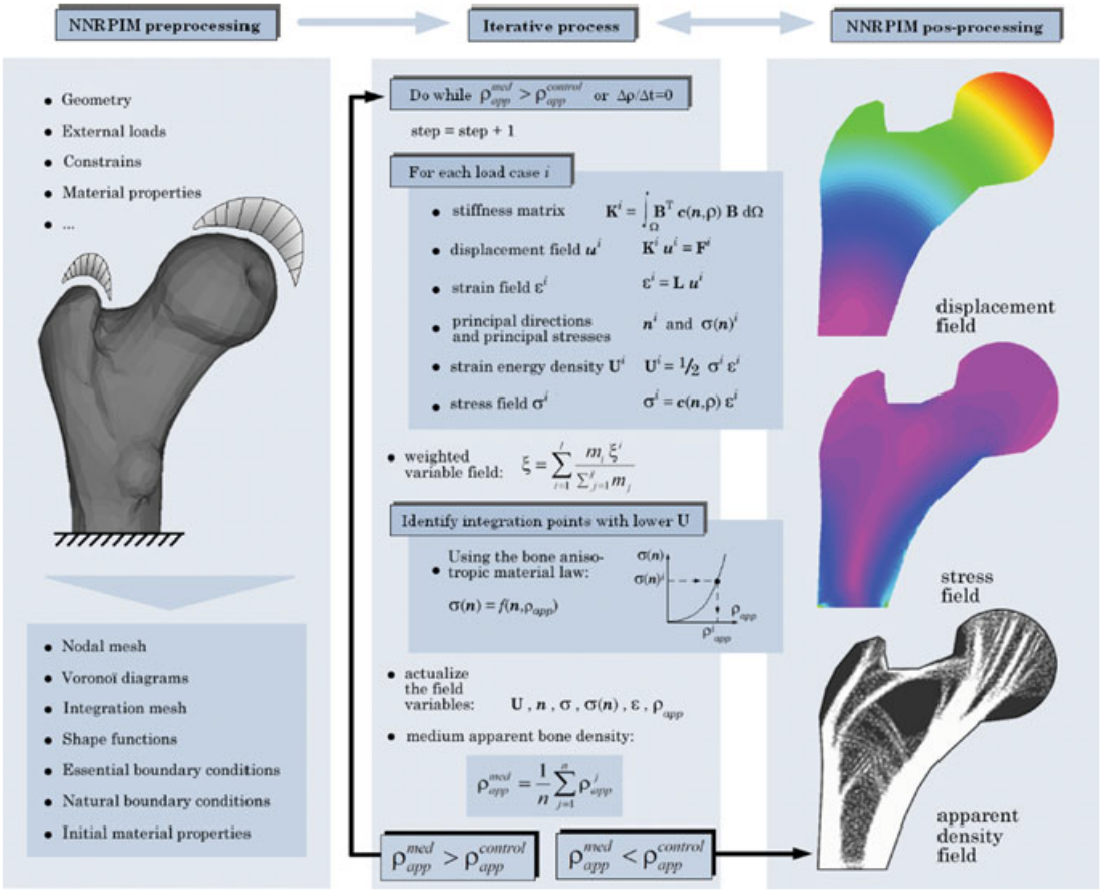


Figure 4.3: Bone remodelling algorithm. Adapted from (Belinha, 2014)

4.2 Structural optimization

The objective of structural optimization is to achieve the best possible performance in a structure for a minimum amount of material. The easiest approach to structural optimization is through size optimization, that is, changing variables such as cross-section area or thickness of the structure being optimized. Shape optimization modifies the boundaries in order to achieve an optimal design. Topology optimization can be applied to discrete or continuous structures. In discrete structures, the spacial location of bars and trusses are optimized. In continuous structures, topology optimization determines the best locations and geometries for cavities (Bendsoe and Sigmund, 2004; Huang and Xie, 2010). At this last level, it is common to see these structures replicated in constructions such as bridges or buildings.

SIMP, ESO and BESO methods are briefly explained in this section. Whereas SIMP presents an optimal solution, that is, it finds a maximum stiffness, ESO and BESO and based on intuitive, heuristic concepts which may present solutions similar to those which are known to be optimal.

4.2.1 SIMP

A body occupying a domain Ω^{mat} belonging to a larger reference domain Ω is considered. The reference domain is chosen so as to allow to define the boundary conditions. The optimization problem in question is to obtain the optimum stiffness tensor $E_{ijkl}(x)$. The energy bilinear form is given by Equation 4.20 with linearized strains (Equation 4.21) and the load linear form is given by Equation 4.22.

$$a(u,v) = \int_{\Omega} E_{ijkl}(x)\varepsilon_{ij}(u)\varepsilon_{kl}(v)d\Omega \tag{4.20}$$

$$\varepsilon_{ij}(u) = \frac{1}{2}\left(\frac{\partial u_i}{\partial x_j} + \frac{\partial u_i}{\partial x_i}\right) \tag{4.21}$$

$$l(u) = \int_{\Omega} fud\Omega + \int_{\Gamma_t} tuds \tag{4.22}$$

The minimum compliance problem, which is equivalent to maximizing stiffness is given by Equation 4.23 written in its weak variational form. U denotes the space of the kinematically admissible displacement fields, f denotes the body forces and t the boundary tractions on the traction part $\Gamma_T \subset \Gamma \equiv \partial\Omega$ of the boundary. E_{ad} represents the set of admissible stiffness tensors for the problem.

$$\begin{aligned} &\min_{u\in U,E} l(u) \\ &\text{s.t.} \\ &a_E(u,v) = l(v), \text{for all} v \in U \\ &E \in E_{ad} \end{aligned} \tag{4.23}$$

On its discretized form, the problem in Equation 4.23 becomes the form presented in Equation 4.24 where **u** and **f** are the displacement and load vectors respectively and **K** is a matrix dependent on stiffness E_e which is the stiffness for an element e.**K** can be written as Equation 4.25.

The aim of the optimization is to determine the subset Ω^{mat} in Ω. Thinking in the discrete form, this means, the objective is to come up with a "black-and-white" representation made of pixels and/or voxels which come from the finite element discretization. The set of admissible stiffness tensors consists on the tensors for which Equation 4.26 is true where E^0_{ijkl} is the stiffness tensor for the given isotropic material. To indicate the relevant function space for the problem it is written that $E_{ijkl} \in L^\infty(\Omega)$. According to Equation 4.26 the problem is formulated as a 0-1 problem, which is a discrete problem.

$$\begin{aligned} &\min_{\mathbf{u},E_e} \mathbf{f}^T\mathbf{u} \\ &\text{s.t.} \\ &\mathbf{K}(E_e)\mathbf{u} = \mathbf{f} \\ &E_e \in E_{ad} \end{aligned} \tag{4.24}$$

$$\mathbf{K} = \sum_{e=1}^{N} \mathbf{K}_e(E_e) \tag{4.25}$$

$$\begin{aligned} &E_{ijkl} = 1_{\Omega^{mat}} E^0_{ijkl} \\ &1_{\Omega^{mat}} = \begin{cases} 1 \mathbf{if} x \in \Omega^{mat} \\ 0 \mathbf{if} x \in \Omega \setminus \Omega^{mat} \end{cases} \\ &\int_\Omega 1_{\Omega^{mat}} d\Omega = \mathbf{Vol}(\Omega^{mat}) \leq V \end{aligned} \tag{4.26}$$

Usually, the integer variables are transformed into continuous variables with a penalty function being introduced which will make the solution approximate more the 0-1 discrete solution. The fixed domain problem is re-formulated as a sizing problem by modifying the stiffness matrix to depend on the density of the material.

The SIMP model in Equation 4.27 stands for Solid Isotropic Material with Penalization and has proven to be extremely efficient. The density function $\rho(x)$ is the design function which interpolates the material properties between 0 and E^0_{ijkl}, that is, if $\rho = 0$ then $E_{ijkl} = 0$ and if $\rho = 1$ then $E_{ijkl} = E^0_{ijkl}$.

$$\begin{aligned} &E_{ijkl}(x) = \rho(x)^p E^0_{ijkl}, p > 1 \\ &\int_\Omega \rho(x) d\Omega \leq V; 0 \leq \rho(x) \leq 1, x \in \Omega \end{aligned} \tag{4.27}$$

4.2.2 ESO

This methodology was proposed by Xie and Steven (1993) which at first seemed trivial (Tanskanen, 2002) but proved to have results similar to those found in well-known and validated mathematical or analytical solutions. This methodology has been further developed and solved a wide number of topology optimization problems (Xie and Steven, 1997). Nonetheless, using ESO it cannot be theoretically guaranteed that the solution which is found is optimal (Huang and Xie, 2010).

Regarding stress level optimization, the procedure is based on the fact that when the stress levels in some parts of the structure, usually indicated inefficient usage of material as the stress level should be close to the same level, at a safe value. A rejection criteria therefore is created where the structure parts at a lower stress level are considered to be under-utilized and are removed. In FEM, this translates to removal of the elements where the structure is under-utilized (Huang and Xie, 2010).

The stress level is calculated comparing the equivalent Von-Mises stress of the element with the maximum stress of the whole structure. This ratio translates to the current rejection ratio RR_i (Equation 4.28).

$$\frac{\sigma_{element}^{Von-Mises}}{\sigma_{max}^{Von-Mises}} = RR_i \tag{4.28}$$

This cycle is repeated using the same rejection ratio value until a steady state is achieved. This means that there are no more elements to remove at that rejection ratio. An evolutionary rate ER is then added to the rejection ratio (Equation 4.29).

$$RR_{i+1} = RRi + ER \tag{4.29}$$

It may be preferable to conduct the algorithm aiming at stiffness or displacement optimization. Here, the mean compliance C, which is the inverse of the stiffness, is considered. Mean compliance can be defined as in Equation 4.30 where $\mathbf{f}$ is the force vector and $\mathbf{u}$ is the displacement vector.

$$C = \frac{1}{2}\mathbf{f}^{\mathbf{T}}\mathbf{u} \tag{4.30}$$

The static equilibrium of a structure in FE analysis is given by Equation 4.31 where $\mathbf{K}$ is the global stiffness matrix

$$\mathbf{Ku} = \mathbf{f} \tag{4.31}$$

When an element i is removed, the stiffness matrix changes as in Equation 4.32 where $\mathbf{K}^*$ is the resultant stiffness matrix of the structure when element i is removed and $\mathbf{K}_i$ is the stiffness matrix of element i. This assumes that removal of element i does not have any effect in vector $\mathbf{f}$.

$$\Delta\mathbf{K} = \mathbf{K}^* - \mathbf{K} = -\mathbf{K}_i \tag{4.32}$$

Varying both terms of Equation 4.31 and ignoring a higher order term, the change in the displacement vector is given by Equation 4.33.

$$\Delta \mathbf{u} = -\mathbf{K}^{-1}\Delta \mathbf{K}\mathbf{u} \tag{4.33}$$

Combining Equation 4.30 and 4.33, Equation 4.34 is obtained where $\mathbf{u}_i$ is the displacement vector of element i.

$$\Delta C = \frac{1}{2}\mathbf{f}^{\mathbf{T}}\Delta \mathbf{u} = -\frac{1}{2}\mathbf{f}^{\mathbf{T}}\mathbf{K}^{-1}\Delta \mathbf{K}\mathbf{u} = \frac{1}{2}\mathbf{u}_i^T\mathbf{K}_i\mathbf{u}_i \tag{4.34}$$

The sensitivity number for mean compliance is given by Equation 4.35. This translates into an increment in strain energy after removal of element i in the amount of the strain energy of that element i. Using strain energy as a remodelling criterion means that compliance is being minimized and therefore stiffness is being maximized (Fyhrie and Carter, 1986).

$$\alpha_i^e = \frac{1}{2}\mathbf{u}_i^T\mathbf{K}_i\mathbf{u}_i \tag{4.35}$$

Minimizing mean compliance through the removal of elements in the most efficient way means removing those elements with lower values of α_i so that the increase in C is minimal (Huang and Xie, 2010).

The Element Removal Ratio ERR determines the number of elements to be removed at each iteration. ERR is given by the number of elements removed at each iteration over the total number of elements in the initial or current FEA model.

When optimizing for stiffness, unlike optimization for stress, there is no steady state. If a steady state is not required then computational efficiency can be improved with far less iterations. This might however cause an unstable structure during the iterations (Huang and Xie, 2010).

ESO has the advantage of easy implementation without the need of having access to any FEA source code. Also, it provides a clear structure, that is, without any grey area and can be equally applied to 2D or 3D problems. It is not necessary to create new meshes during the iterative process even if the structure is very different from the initial design. Elimination of the elements can be done assigning the material property in those elements to zero and ignoring those elements in the stiffness matrix. In addition to this, as more and more elements are removed, less equations must be solved which reduces computational time.

On the other hand, as ESO removes material from the structure when it is under-stressed, those elements may be further necessary to achieve an optimal design and it is not possible to recover them. This makes optimization on an initial design guess a much improved solution.

4.2.3 BESO

Unlike ESO, where material cannot be added to the structure, in the bi-evolutionary structural optimization method, material can be added or removed simultaneously. Where in ESO there is a Rejection Ratio RR, BESO includes a Inclusion Ratio IR which defines the number of elements being added in each iteration.

Yang et al. (1999) first conducted research on BESO for stiffness optimization where the sensitivity numbers of the void elements are estimated through linear extrapolation of the displacement field (Huang and Xie, 2010). In ESO only solid elements with the lowest sensitivity numbers are removed from the structure. In BESO, void elements having the highest sensitivity numbers are added to the structure and become solid elements.

Stress optimization can also be achieved with the BESO algorithm (Querin et al., 2000) where elements with the lowest Von-Mises stress are removed and void elements are turned into solid elements as stand near regions with high Von-Mises stress. Removed and added elements are treated separately with *RR* and *IR* respectively.

Early versions of BESO present low computational efficiency, and a large number of iterations are usually required and the final solution needs to be selected from a large number of possible results and the convergence tends to be chaotic (Huang and Xie, 2010). Another aspect that should be pointed out is that the 0/1 optimization often cannot find solutions in a continuous setting. That occurs because using different mesh sizes, the introduction of more holes without changing the structural volume will increase the efficiency of a given design which is regarded as a numerical instability. This occurrence is termed as mesh-dependency.

The method begins with domain discretization and attribution of initial properties. FEM analysis is conducted and then elemental sensitivity is calculated through Equation 4.36. This equation comes from the filter scheme for the BESO method. Before applying the filter scheme, nodal sensitivity does not carry any physical significance. These values are then averaged through a filter with a length of r_{min}. Each averaged sensitivity number is calculated through Equation 4.37. The weight ω is given by Equation 4.38 where M is the number of elements and r_{ij} is the distance between nodes i and j. $\omega(r_{ij})$ is given by $r_{min} - rij$.

$$\alpha_i = \frac{\sum_{j=1}^{K} \omega(r_{ij})\alpha_j^n}{\sum_{j=1}^{K} \omega(r_{ij})} \tag{4.36}$$

$$\alpha_j^n = \sum_{i=1}^{M} \omega_i \alpha_i^e \tag{4.37}$$

$$\omega_i = \frac{1}{M-1}\left(1 - \frac{r_{ij}}{\sum_{i=1}^{M} r_{ij}}\right) \tag{4.38}$$

The next step is averaging the sensitivity number with its history information using using Equation 4.39. This increases stability of the method (Huang and Xie, 2010, 2007). The new averaged sensitivity is saved for the next iteration.

$$\alpha_i = \frac{\alpha_i^k - \alpha_i^{k-1}}{2} \tag{4.39}$$

The target volume for the following iteration is calculated through Equation 4.40, where *ER* is the evolutionary volume ratio. Since the volume constraint V^* can be greater or smaller than the initial design volume, the target volume may increase or decrease on each iteration, hence the $\pm$

sign.

$$V_{k+1} = V_k(1 \pm ER) \tag{4.40}$$

Elements can now be added or removed. First they are sorted according to their sensitivity numbers from highest to lowest. A solid element (1) is removed if $\alpha_i \leq \alpha_{del}^{th}$ and void elements (0) are switched to 1 $\alpha_i > \alpha_{add}^{th}$. α_{del}^{th} and α_{add}^{th} are the threshold sensitivity numbers for removing or adding elements respectively. The way that these threshold levels are calculated is the following:

- Let $\alpha_{del}^{th} = \alpha_{add}^{th} = \alpha_{th}$ so that α_{th} can be determined by V_{k+1}. If there are 1000 elements in the design domain and V_{k+1} is equivalent to that of 725 elements, and $\alpha_1 < \alpha_2 < ... < \alpha_{1000}$ then α_{th} is the same as α_{725};

- Then, calculate the addition ratio AR which is given by the number of added elements divided by the total number of elements. If AR is higher than AR_{max} then α_{del}^{th} and α_{add}^{th} must be recalculated;

- α_{add}^{th} is recalculated by sorting the sensitivity numbers of void elements. The number of elements being switched into solid elements is obtained by multiplying AR_{max} by the total number of elements. α_{add}^{th} is the sensitivity number of the element ranked just bellow the last added element. α_{del}^{th} is calculated so that the removed volume is the same as $V_k - V_{k+1} -$ volume of the added elements.

While the objective volume V^* is not achieved and the convergence criterion (Equation 4.41) is not fulfilled, the cycle of FE analysis and adding/removal of elements is repeated.

$$error = \frac{\left|\sum_{i=1}^{N} C_{k-i+1} - \sum_{i=1}^{N} C_{k-N-i+1}\right|}{\sum_{i=1}^{N} C_{k-i+1}} \leq \tau \tag{4.41}$$

A flowchart of the BESO process is shown in Figure 4.4.

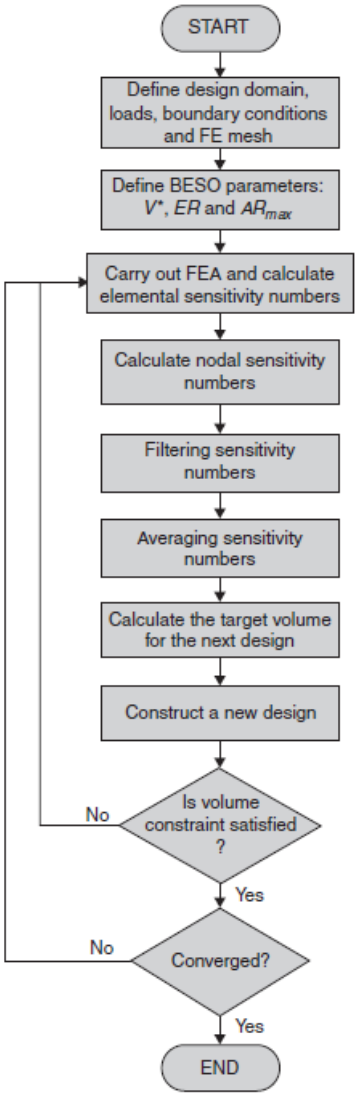


Figure 4.4: Flowchart of the BESO method. Adapted from (Huang and Xie, 2010)

Chapter 5

Methodology

5.1 Overview

The objective of this work is to develop a methodology based on smoothing techniques for the printing of functionally graded gyroid infill structures taking into account the results of optimization simulations, which is undertaken by the following stages:

- Preparation of the work through building of a Matlab script cable of generating the files for the slicing software and characterization of the gyroid material;
- Development of the gyroid law;
- Numerical simulations;
- FFF printing;
- Experimental testing;
- Practical application on a femur scaffold.

These stages were carried out by conducting the following procedures:

1. Development of a Matlab script for creating of the *.stl* file;
2. Density calibration of gyroid infilled cubic specimens;
3. Tensile testing of gyroid infilled specimens;
4. Creation of a gyroid remodelling law based on the results of the tensile tests as well as literature;
5. Law implementation on FEMAS;
6. Conduction of structural optimization and remodelling numerical simulations on prismatic specimens subject to three benchmark load cases using finite element and meshless methods;
7. Creating the g-code files taking into consideration the density differences:
8. Printing of the specimens in PLA with an FFF equipment;
9. Testing and analysis of the prismatic specimens according to the appropriate load case;
10. Voxelization and meshing of a femur solid part;
11. Application of the gyroid remodelling law to a voxelized femur model subject to load cases found in the literature;
12. Design of a test apparatus for testing of the femur scaffold specimens;

13. Testing and analysis of the femur scaffold specimens according to the appropriate load cases.

Figure 5.1 presents, in the form of a flowchart, how this work was organized in time, placing each procedure into the appropriate stage in the development of this work.

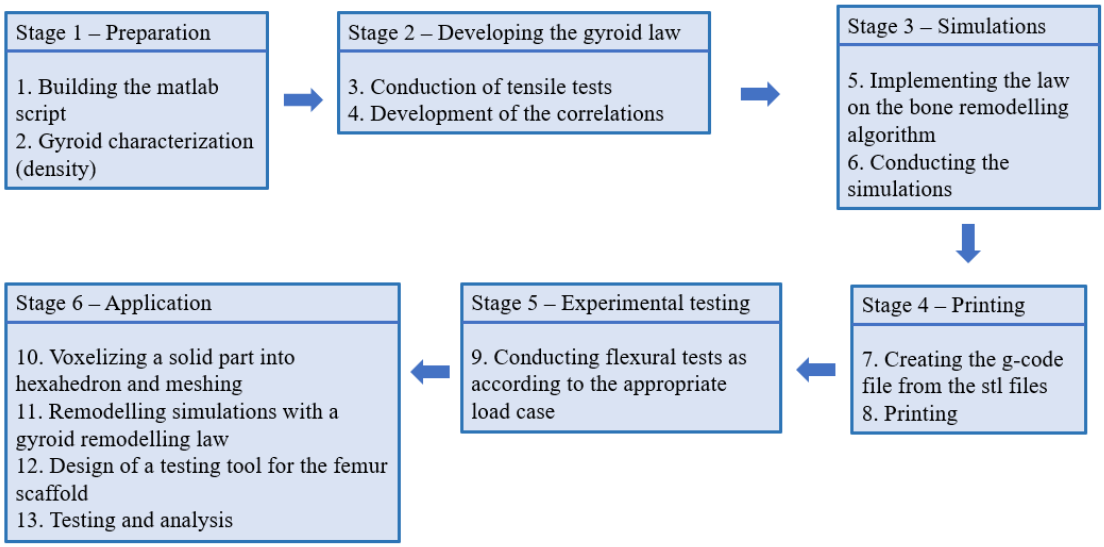


Figure 5.1: Procedural steps taken in the course of this work

This chapter presents a thorough description of every step necessary to obtain the final specimens which are then tested and compared to the initial numerical simulations. This includes the creation of the *.stl* file which is read by the slicer to write the gcode file, the printing of the specimens and the mechanical testing as well as the density calibration curve and the development of the gyroid remodelling law.

5.2 Materials and methods

The material which was employed in printing of the specimens was Premium PLA filament from FormFutura (FormFutura, 2020) in Robotic Grey. The Premium PLA designation refers to a harder, more pure PLA with improved thermal stability and slightly faster crystallization, making it more appropriate for large scale prototypes. The properties of the material can be consulted in Table 5.1. Some of the properties of the filament, according to the supplier include:

- Dimensional and shape stability after cooling;
- First layer adhesion to multiple unheated surfaces;
- Improved flow and inter-layer adhesion.

Other properties include the fact that the filament is biodegradable and odorless in processing.

The specimens were all printed using an Ender 3 FDM printer (Figure 5.2) by Creality (Creality, 2018) on a glass bed. Using a glass bed promotes a smooth finish in the first layer and has the

Table 5.1: Mechanical and printing properties of FormFutura's Premium PLA (FormFutura, 2020)

Property	Value	Test Standard
Density	1.25 g/cm^3	ASTM D1505
Melt flow rate	6g/10min	-
Impact Strength	3.4 kJ/m^2	ISO 179
Tensile Strength	105 MPa	ASTM D882
Tensile Modulus	3145 MPa	ASTM D882
Elongation at break	175%	ASTM D882
Flexural Strength	$\pm$ 54.4 MPa	-
Printing temperature	$\pm$ 190-225^{o}C	-
Melting temperature	$\pm$ 210 $\pm$ 10^{o}C	-
Viscosity at softening temperature	$\pm$62^{o}C	ISO 306

advantage of not warping over time. Due to its low thermal conductivity compared to other bed finishes, it takes a longer time to heat up. However, heat is more evenly distributed along the bed. In order to help with adhesion, some sort of glue may be employed by deposition of a thin layer in the glass bed (Grames, 2019). In addition to this, 0.4mm nozzle was used.

5.3 Creation of the *g-code* file

This section describes the steps taken in order to achieve the *g-code* file which is read by the printer, and corresponds to procedural step 1 of Stage 1 - Preparation. This involved the development of a *Matlab* script which creates the *.stl* file and the *slicing* software (or *slicer*). Therefore, the aim of this task is to have all the necessary tools to conduct procedural step 7.

5.3.1 Matlab code

The *Matlab* script defines a smaller solid containing all the elements which belong to each density level. This solid is then to be infilled at the correct density defined by the numerical simulation. In order to achieve a fair approximation of the density gradient, N levels of different densities are defined.

The script presents the following functions:



Figure 5.2: Ender 3 printer from Creality 3D (Creality, 2018)

1. Assigning to each element a density level which could have been previously smoothed, that is, the density level is assigned after the smoothing functions are applied;

2. For each density level, separating into solids defined by contact of the faces of each element, that is, create continuous solids;

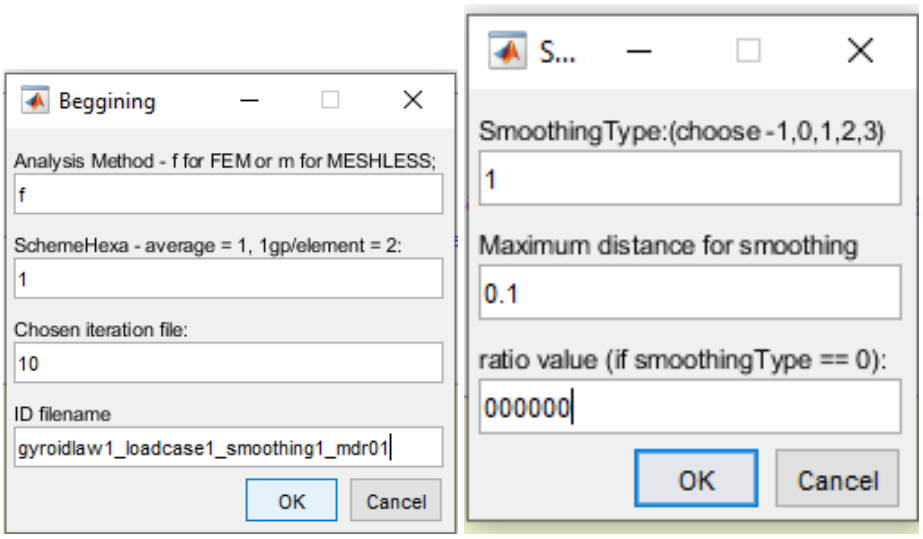
3. Triangulating those solids;

4. Writing an *.stl* file from that triangulation;

5. Concatenating the *.stl* files with all the solids of each density level and renaming it to include the infill density to be applied in the slicing software.

The aim of this script is to be as automatic as possible, taking the information that comes from the FEMAS software and creating a file that could be automatically read by the *slicer*. The user inputs the iteration file, the number of density levels, N, and all the smoothing parameters. The code is available with notes in Annex A. In order to allow for a maximum, transition and minimum density, N was defined as 3.

When running this script, the following window shown in Figure 5.3a appears which defines the type of analysis the file has origin in (FEM or NNRPIM), the iteration file which is being chosen and the code name of the file. The smoothing parameters are defined in Figure 5.3b where each smoothing type is represented by a number (-1 for no smoothing and integer numbers for the order of the polynomial function) and the maximum distance ratio is also defined. The ratio value box was not used as it corresponds to the constant of a constant function which was not used.



(a) General window (b) Smoothing window

Figure 5.3: Input windows in the Matlab script

5.3.2 Smoothing parameters

In order to avoid abrupt density gradients that is, having two very distinct density levels in contact, the specimen may be smoothed. Very abrupt gradients can occur since both cortical and trabecular bone are modelled in the gyroid material laws. This is calculated through weighted averages. This weight is calculated differently depending on the type of smoothing which is done - variable *"SmoothingType"*. The new density level is calculated by Equation 5.1. In this equation, ρ_i^* is the smoothed apparent density of element i and w_{ij} is the weighted ratio, function of the distance between the centroids of elements i and j and calculated through the smoothing function. It should be noted that even if the element has already been smoothed, the density value though which Equation 5.1 is applied is the true apparent density value ρ_{app}^i obtained from the algorithm.

$$\rho_i^* = \frac{\sum_{i=j}^{N_{elem}} w_{ij}\rho_j}{\sum_{i=j}^{N_{elem}} w_{ij}} \tag{5.1}$$

An analogy can be done between this smoothing process and that which is conducted in BESO in order to smooth the sensitivity numbers (Huang and Xie, 2010) to perform the removal/adding of elements. In this case what is being smoothed is the apparent density.

Three smoothing types were first described however only two were implemented, namely Smoothing Type 1 and Smoothing Type 2. This is further explored in Section 7.

Smoothing type 1

This is based on the first-degree polynomial function $w = 1 - d$ (Figure 5.4) where w is the weight of that element and d is the distance between the centroids of elements i and j divided by the maximum distance observed in the plate. However, in order to avoid extreme smoothing, a *maximum distance ratio* (variable: max_dist_ratio) is introduced as a parameter. If a maximum distance ratio of 0.1 is chosen, this means that only the elements at 10% of the maximum distance measured in the whole plate will be considered for the calculation of the average.

Smoothing type 2

This is based on the second-degree polynomial function $w = 1 - d^2$. This is also affected by the *maximum distance ratio* parameter. Figure 5.5 shows the referred function.

Smoothing type 3

This is based on a third-degree polynomial function. Since $w = 1 - d^3$ would present similar values to smoothing type 1 in the [0,1] interval, some points were defined (Figure 5.6) and then approximated by the least squares method which created the following function $w = 2.5959d^3 - 2.4469d^2 - 1.2034d + 1.0797$. Any values above 1 were computed to be 1 and any values below 0 were programmed to be zero.

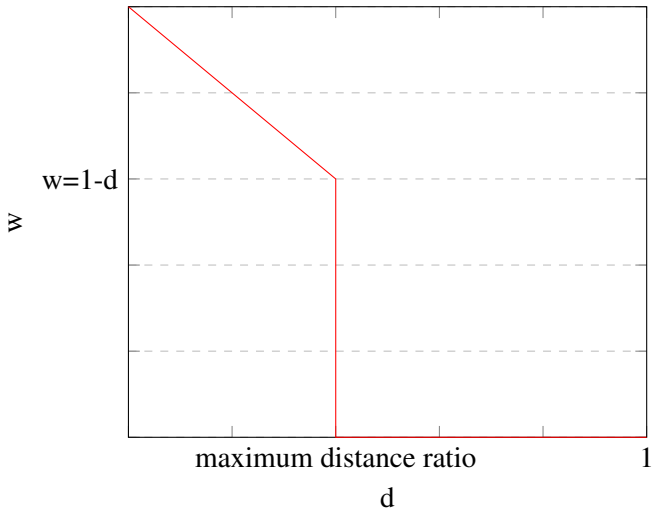


Figure 5.4: Smoothing function type 1

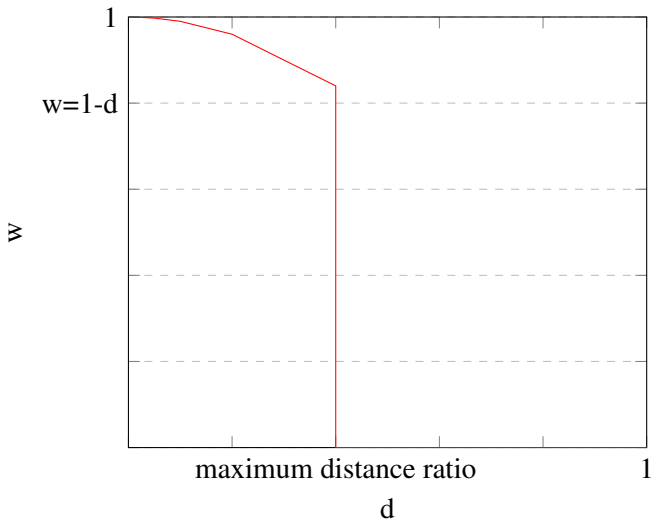


Figure 5.5: Smoothing function type 2

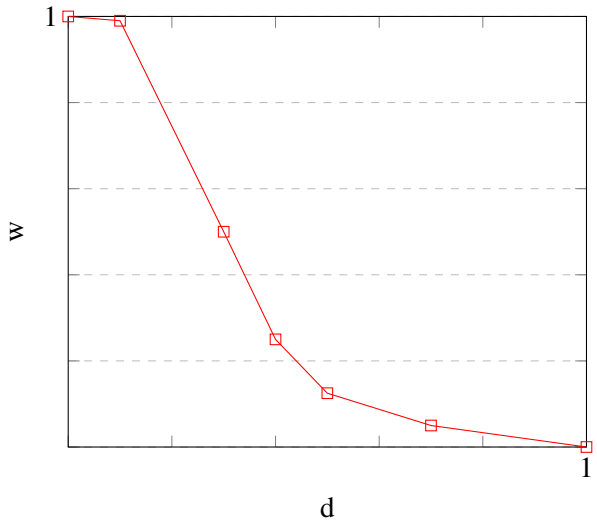


Figure 5.6: Smoothing function type 3

5.3.3 Slicing software

The last step before printing is the development of the g-code file obtained through the slicing software. In the step list mentioned in the beginning of this chapter, this corresponds to step 7.

The chosen slicing software was Prusa Slicer by Prusa (Prusa, 2020) which is an *open-source* software (version 2.1.1). Each of the solids in the form of an *.stl* file are added to the slicer and individual infill is applied to each one.

Due to the fact that all solids are in the same coordinate system (that of FEMAS), one of the solids is imported to the *slicer*. Then, there is the possibility to *add part*. That option is selected and the two remaining solids are imported in their correct place relatively to the first solid. This makes it possible to act upon the three solids as one single solid.

The value of infill percentage, present is the name of the part, must be altered in order to correspond to the actual percentage. This calibration is explained in 5.5.

Each solid name is written as *dens_aaaa_bbbb.stl* where *aaaa* is the true average density value that solid must present and *bbbb* is equal to $aaaa/1.25$ which corresponds to the infill density. Figure 5.7 shows the process of creating the *g-code*. It is very important to guarantee geometrical dimensions when printing solids with no perimeters. Often, slicing software will subtract the perimeter when printing only the infill which causes fragility and poor adhesion between the solids. It is therefore crucial to make sure that when adding the infill to each of the solids, than the perimeter zone will also be considered for infill. Using version 2.1.1 without updating when installing version 2.2.0 guaranteed that infill was done correctly with good adhesion between the solids.

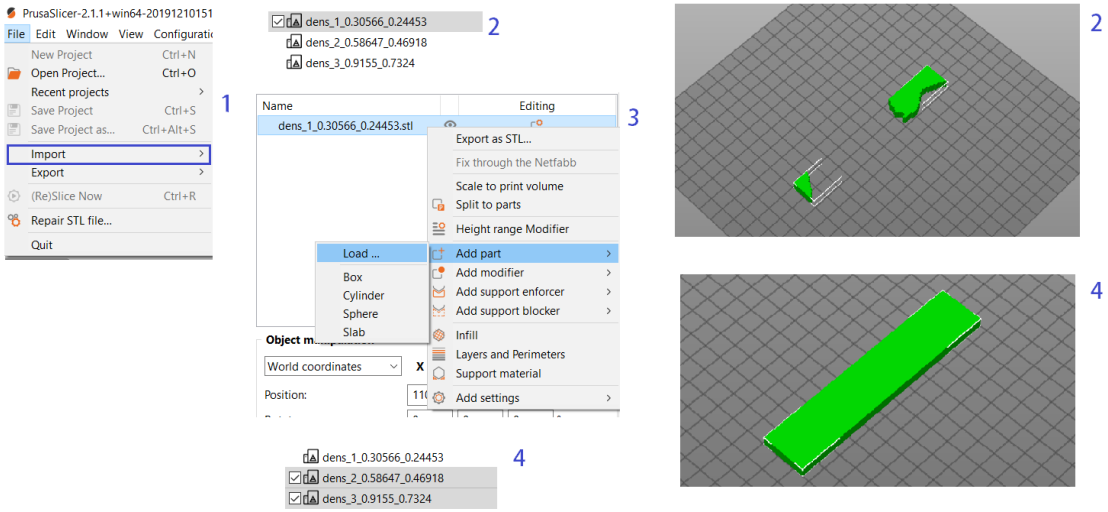


Figure 5.7: Slicing software

5.4 Printing parameters

The definition of printing parameters is included in procedural step 8 which belongs to stage 4 - printing. Due to the fact that the definition and optimization of printing parameters is already a very broad subject in itself, only a theoretical study instead of an empirical study was conducted. The main parameters to be defined are listed as following:

1. **Bed Temperature** defined as 60^{o}C which is a standard value. This parameter is important to control adhesion of the extruded filament to the bed, especially in the first layer.

2. **Extruder Temperature** defined as 210^{o}C. The higher the temperature, the better the mechanical properties (Afonso, 2019), as it adheres better to other layers. However if this temperature is too high, overhang problems are exaggerated as well as stringing and oozing problems.

3. **Layer height** defined as 0.20mm for the first layer as well as for the subsequent layers. The surface quality is as better as lower the value of this parameter is. On the other hand, printing time is compromised.

4. **Printing Speed** defined as 60mm/s which is a standard value obtained as a compromise between printing quality and speed.

Other configuration aspects are also mentioned such as the definition of the extrusion multiplier.

Extrusion Multiplier: This parameter is obtained as a first calibration. A hollow cube with one layer thickness is printed and thickness is carefully measured with a caliper. This should be around the same thickness as the nozzle diameter. The multiplier is obtained dividing the nozzle diameter by the obtained thickness and repeated until the thickness is the same as the nozzle diameter. The value used was 1.08.

Moreover, as the first layer had very little surface area to adhere to the printing surface, it was defined that first layer speed would be 30 mm/s which is half of the speed of the subsequent layers, and for the first layer, extrusion would be doubled in order to try to maximize contact area with the heated bed.

5.5 Calibration of infill densities

Calibration of infill densities belongs to Stage 1 - Preparation, namely, step 2.

The output of the bone remodelling numerical simulation is an array of densities. These densities are going to be translated into the printed specimen through its infill density. Since the simulation does not consider the unavoidable errors in FDM, it is necessary to make sure that the infill density (in percentage) corresponds to that same percentage of PLA density which was considered the simulation. In order to control this, three specimens of each gyroid infill density from an array of densities were printed and then weighted. The specimens were cubic - 25x25x25mm^3. Density was obtained dividing mass by volume. The mass of each specimen was measured with an HLD 300 scale.

Calibration results The results of the mass measurements were taken and are shown in Table 5.2.

Table 5.2: Results of the measurements for the infill density calibration

Infill	Measured mass (g)	Average (g)	Standard. Dev (g)
10%	2.140 2.135 2.125	2.133	0.008
15%	3.045 3.070 3.050	3.055	0.013
30%	5.855 5.890 5.880	5.875	0.018
40%	7.750 7.710 7.690	7.717	0.031
50%	9.585 9.580 9.560	9.575	0.013
70%	12.990 12.955 13.105	13.017	0.078
90%	16.660 16.620 16.555	16.612	0.053

From this, an interpolation table was calculated. This interpolation table is to be used as a guide when applying the infill to the *.stl* files in the *Slicing* software. The values shown in Table 5.3 are the true values, which were measured. If other densities are necessary, interpolation should be able to give a reasonable approximation.

The true infill density values were calculated as:

$$\rho_{\text{true val}}[\%] = \frac{mass_{\text{average}}[g]/V_{\text{cube}}}{\rho_{\text{PLA}}} \times 100\% \tag{5.2}$$

Table 5.3: Interpolation table from the infill density calibration procedure

True infill density	Slicing software input
11%	10%
16%	15%
30%	30%
40%	40%
49%	50%
67%	70%
85%	90%

5.6 Gyroid law

This section goes through all steps accomplished on the course of Stage 2 of the methodology shown in Figure 5.1, namely, steps 3 and 4.

A gyroid remodelling law was developed in order to conduct remodelling simulations. This required the conduction of tensile tests whose results are exposed in Figure 5.8 to specimens of three different infill density levels, namely, 20% infill - Table 5.4, 50% infill - Table 5.5 and 80% infill - Table 5.6. The specimens were prismatic in order to fit the testing machine with minimal slippage of the grips. Figure 5.9 shows a schematic representation of the tensile specimens which were printed with the largest face placed on the building surface. This way, tensile direction is the same as fiber alignment.

Grip distance was carefully measured with a digital caliper with 0.01 mm resolution to obtain the initial length.

In addition to this, the results from compression tests of specimens printed at the same density levels, were taken from the work of Silva (2019). Since it was not possible to obtain the ultimate compression strength, as is seen in the works of Belinha et al. (2013d, 2012); Lotz et al. (1991), compression stress at yield was used instead as an approximation. It is important to conduct a compression study as bone tissue works under compression. The compression tests conducted by Silva (2019) are shown in Figure 5.10 which justify the approximation of the yield stress for the ultimate compression strength.

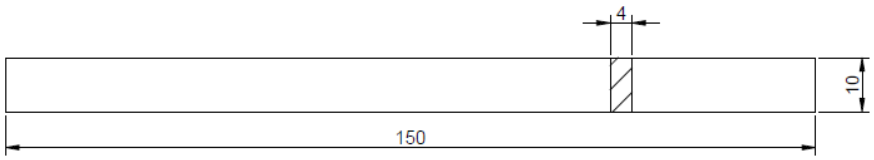
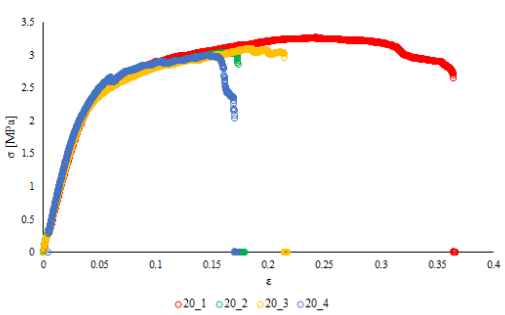
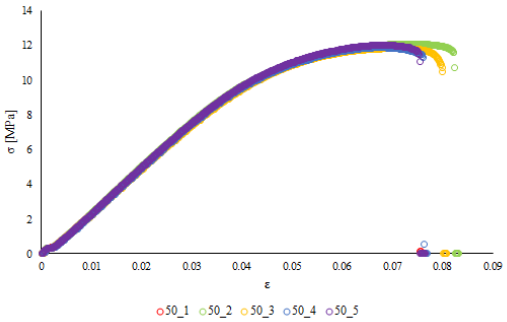


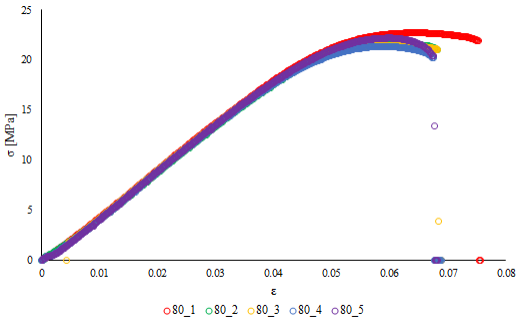
Figure 5.9: Tensile specimen



(a) 20% nominal infill



(b) 50% nominal infill



(c) 80% nominal infill

Figure 5.8: Tensile test results

Table 5.4: Tensile test results for the specimens with 20% nominal infill

	E [MPa]	σ_y[MPa]	σ_{rot}[MPa]	ε_{max}	ε_y
20_1	59.614	2.50	2.65544	0.36476	0.050
20_2	61.456	2.05	2.85683	0.17902	0.035
20_3	60.789	2.00	2.96339	0.21408	0.050
20_4	63.958	2.00	2.04253	0.17001	0.037
avg	61.454	2.14	2.62955	0.23197	0.043

Table 5.5: Tensile test results for the specimens with 50% nominal infill

	E [MPa]	σ_y[MPa]	σ_{rot}[MPa]	ε_{max}	ε_y
50_1	258.05	8	11.75126	0.07542	0.03
50_2	260.97	8	11.58940	0.08224	0.03
50_3	253.27	8	10.49918	0.08000	0.03
50_4	258.40	8	11.32142	0.07613	0.03
50_5	259.71	8	11.47735	0.07531	0.03
avg	258.08	8	11.32772	0.07782	0.03

Table 5.6: Tensile test results for the specimens with 80% nominal infill

	E [MPa]	σ_y[MPa]	σ_{rot}[MPa]	ε_{max}	ε_y
80_1	466.00	18	21.93947	0.07528	0.04
80_2	451.71	18	21.02301	0.06816	0.04
80_3	459.45	18	20.97090	0.06830	0.04
80_4	457.05	18	20.21489	0.06752	0.04
80_5	462.51	18	20.44293	0.06754	0.04
avg	459.34	18	20.91824	0.06936	0.04

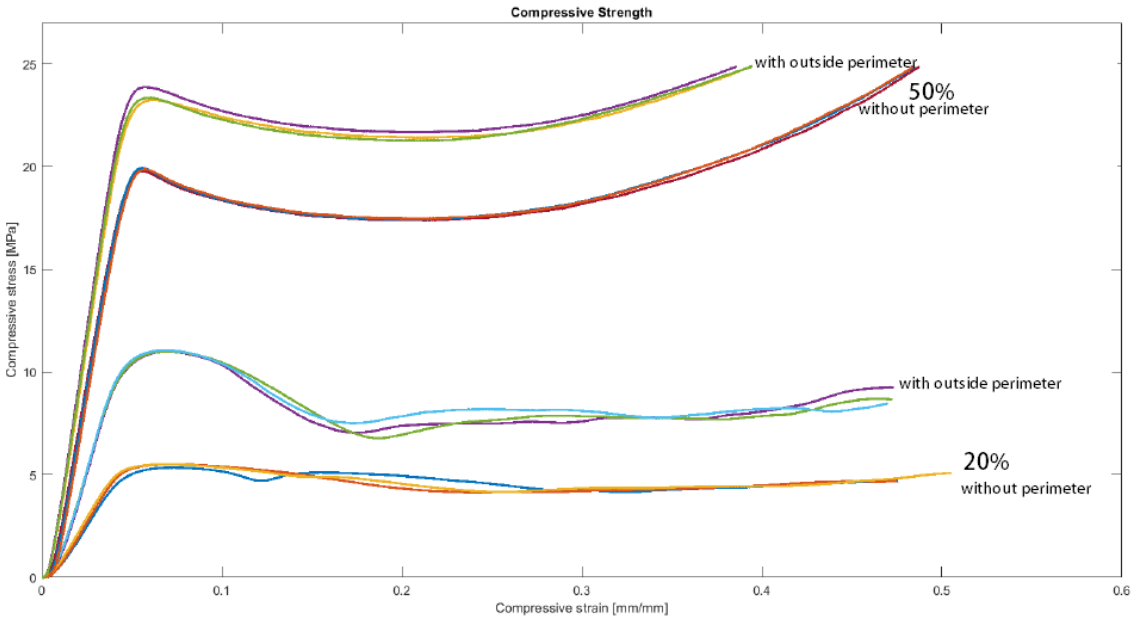


Figure 5.10: Compression test results for the gyroid infill at 20% and 50% nominal infill density. Adapted from (Silva, 2019)

Correcting the nominal infill density into an actual density through the data in Table 5.3, the curves in Figure 5.11 were obtained for maximum stress and elasticity modulus and then adjusted to a third-degree polynomial function. Equation 5.3 refers to the elasticity modulus as a function of density and Equation 5.4 refers to the maximum stress.

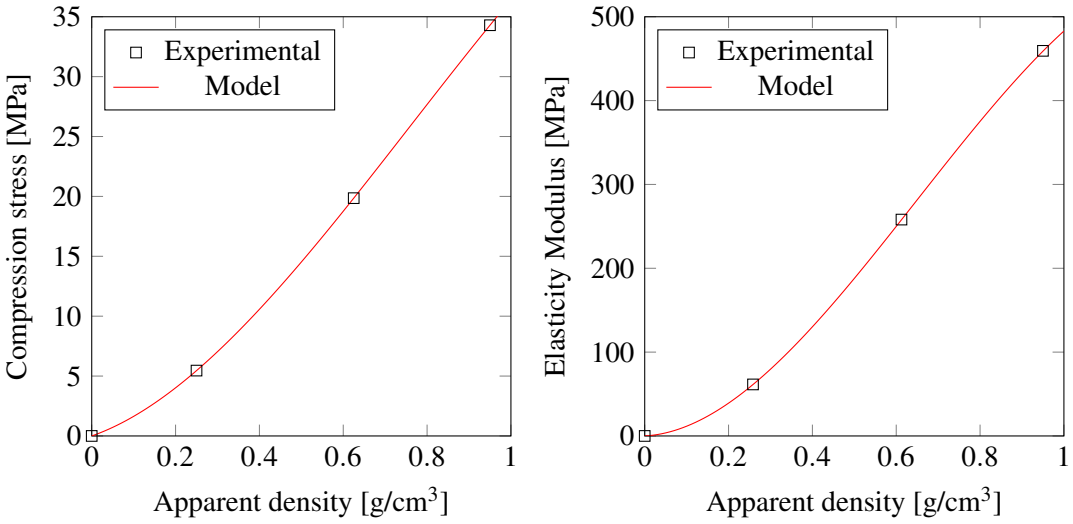


Figure 5.11: Gyroid remodelling law results

From this point forward in the course of this document, this law is referred to as Gyroid remodelling law 1, or simply law 1.

$$E = -482.65\rho_{app}^3 + 938.34\rho_{app}^2 + 27.693\rho_{app} \tag{5.3}$$

$$\sigma_{law1}^c = -18.853\rho_{app}^3 + 43.021\rho_{app}^2 + 12.242\rho_{app} \tag{5.4}$$

Further considerations consist on the fact that unlike bone there is no cortical/trabecular transition, being that the material is characterized by a single law. In addition to this, due to the periodicity of the gyroid shape it is considered that E_{11} and E_{22} are equal as well as σ_{11} and σ_{22}. This means that it is assumed that the material behaves similarly both in axial and transverse directions. This is justified by the fact that the gyroid shape in itself is periodic in the three principal directions. However, due to the fabrication process there is some anisotropy associated which is not considered for this purpose.

In addition, another law was tested where the expression for the elastic modulus is the same but the compressive stress is assumed from the tensile tests which were conducted. Assuming a traction/compression ratio of 0.5 the following expression was obtained. The difference between both laws for the compression stress is shown in Figure 5.12. From this point forward on the course of this document, this law shall be mentioned as gyroid remodelling law 2, or simply, law 2. The development of a second law is an attempt to refine the accuracy of the descriptive law for the gyroid material. However, from Figure 5.12 it is visible that both laws are very similar.

$$\sigma_{law2}^c = -31.39\rho_{app}^3 + 67.78\rho_{app}^2 + 8.052\rho_{app} \tag{5.5}$$

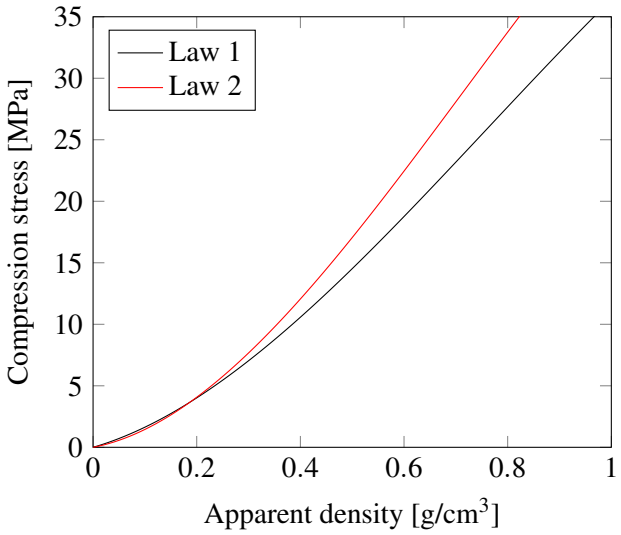


Figure 5.12: Compression stress approximation for both cases

5.7 Stiffness evaluation

For every simulation, stiffness must be calculated in order to be compared with experimental data. Stiffness is given by:

$$K = \frac{force}{displacement} \tag{5.6}$$

where the force F is the sum of all nodal forces and displacement d is the displacement measured at the point of interest. Force F changes for every iteration so that the variables are at the elastic limit and is calculated through:

$$f = \left[\int \varepsilon^T \sigma d\Omega \right] u \tag{5.7}$$

where ε is the strain vector, σ is the stress vector, u is the displacement vector for a design domain Ω. By the principle of virtual displacement, f can be given by:

$$f = \int [B]^T \sigma d\Omega \tag{5.8}$$

where $[B]$ is the matrix of the shape functions derivatives.

This is calculated in different ways for the FEM and meshless simulations. For the FEM the code is as following:

```
F_tot = zeros(3*num_nodes,1); %nodal force vector
    for ii = 1:num_gp
    dn = 8 %number of nodes per element
    gp_elem = gp_elem(ii,1); %element of the Gauss point of interest
    nii = e_nod(1:dn,gp_elem); %the nodes of the element of interest
        for jj = 1:dn
```

```
7             B(1:6,3*jj-2:3*jj) = [dFix(ii,jj) 0 0;0 dFiy(ii,jj) 0;0 0 dFiz(ii,jj);
                  dFiy(ii,jj) dFix(ii,jj) 0;0 dFiz(ii,jj) dFiy(ii,jj);dFiz(ii,jj) 0
                  dFix(ii,jj)]
8         end %horizontally concatenates the shape function derivative matrix for
              that node and Gauss point
9     end
10    gp_w = gp(4,ii); %weight of the Gauss point
11    stress_gp_ii = stress(1:6,ii); %stress in each Gauss point
12    f_local = B'*stress_gp_ii*gp_w; local force for each of the nodes of the
          element of interest
13    for jj = 1:dn
14    ii_r = nii(jj); %node at question
15    F_tot(3*ii_r-2,1) = F_tot(3*ii_r-2,ii) + f_local(3*jj-2,1); %  x component of
          the force vector for that node
16    F_tot(3*ii_r-1,1) = F_tot(3*ii_r-1,ii) + f_local(3*jj-1,1); %  y component of
          the force vector for that node
17    F_tot(3*ii_r,1) = F_tot(3*ii_r,ii) + f_local(3*jj,1); %  z component of the
          force vector for that node
18    end
```

For the meshless methods, RPIM and NNRPIM, the code is the same except that instead of dealing with the nodes of an element, each Gauss point is connected to the nodes in the influence domain as such:

```
1     for ii = 1:num_gp
2     dn = dom_num(ii,1) %number of nodes in the influence domain of the Gauss point
          of interest
3     dii = dom_inf(ii,1); %index of the nodes inside the influence of the Gauss
          point of interest
```

For the experimental data, stiffness is given by the slope of the force-displacement curve.

In order to compare the stiffness from the numerical simulations where the plate is 1mm thick with the experimental specimens which are 5mm thick the following ratio should be calculated. For a three-point bending load case for example, the maximum displacement is given by:

$$f_{max} = \frac{Pl^3}{48EI} \tag{5.9}$$

Being that $K = force/displacement$ then:

$$\frac{K_{1mm}}{K_{5mm}} = \frac{\frac{P}{\frac{Pl^3}{48EI_{1mm}}}}{\frac{P}{\frac{Pl^3}{48EI_{5mm}}}} \tag{5.10}$$

where for a same load P, this ratio is given by:

$$\frac{K_{1mm}}{K_{5mm}} = \frac{I_{1mm}}{I_{5mm}} = \frac{t_{1mm}}{t_{5mm}} = \frac{1}{5} \tag{5.11}$$

This relation is valid for any of the other two load cases which are being tested.

Specific stiffness

A specific stiffness parameter is defined along the course of chapter 6. It is defined as:

$$K_{specific} = \frac{K_i}{\frac{\rho_i}{\rho_0}} \tag{5.12}$$

and the purpose of this parameter is to assess whether one solution is better than its previous solution in terms of stiffness-to-weight ratio.

Chapter 6

Numerical Simulation Results

The results shown in this chapter are integrated in Stage 3 of the methodology flowchart referred in Chapter 5, more specifically, procedure step 6. Numerical Simulation was done using the FEMAS software. The aim of the simulations was to obtain the density value for each point. Three different remodelling approaches were taken, namely, structural optimization, bone remodeling analysis using a gyroid material law and bone remodelling analysis with a bone remodelling law which served as a comparison term with gyroid remodelling.

For the gyroid remodelling law, the results are compared with bone remodelling results using a bone material law (Belinha, 2014) in order to evaluate the possibility of obtaining bone scaffold based on the gyroid shape.

The gyroid remodelling law constructed in 5.6 was implemented in FEMAS and simulations were conducted.

Due to the fact that the Matlab script to create the *.stl* file requires solid elements, these simulations are 3D simulations even though, in order to obtain a density distribution, 2D simulations with square plane stress elements or shell elements could have been used with the advantage of possessing a lower computational cost.

A schematic diagram of the numerical study which was conducted in this chapter is shown in Figure 6.1.

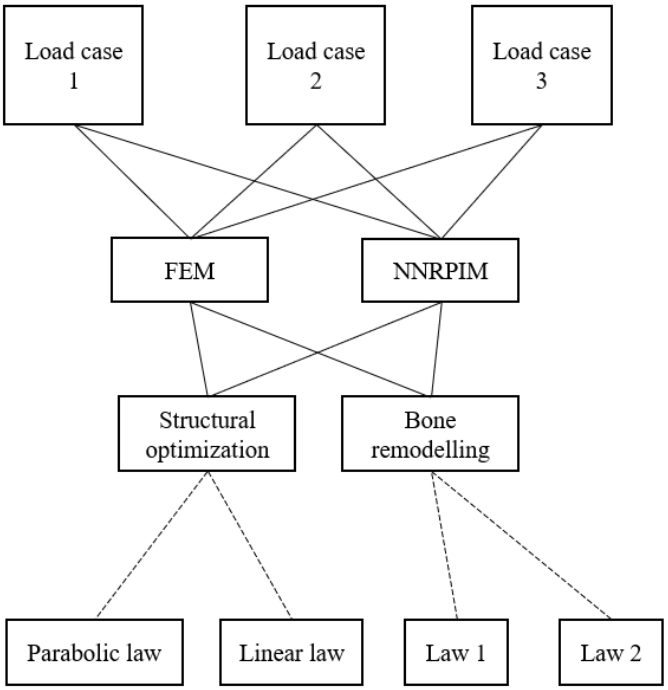


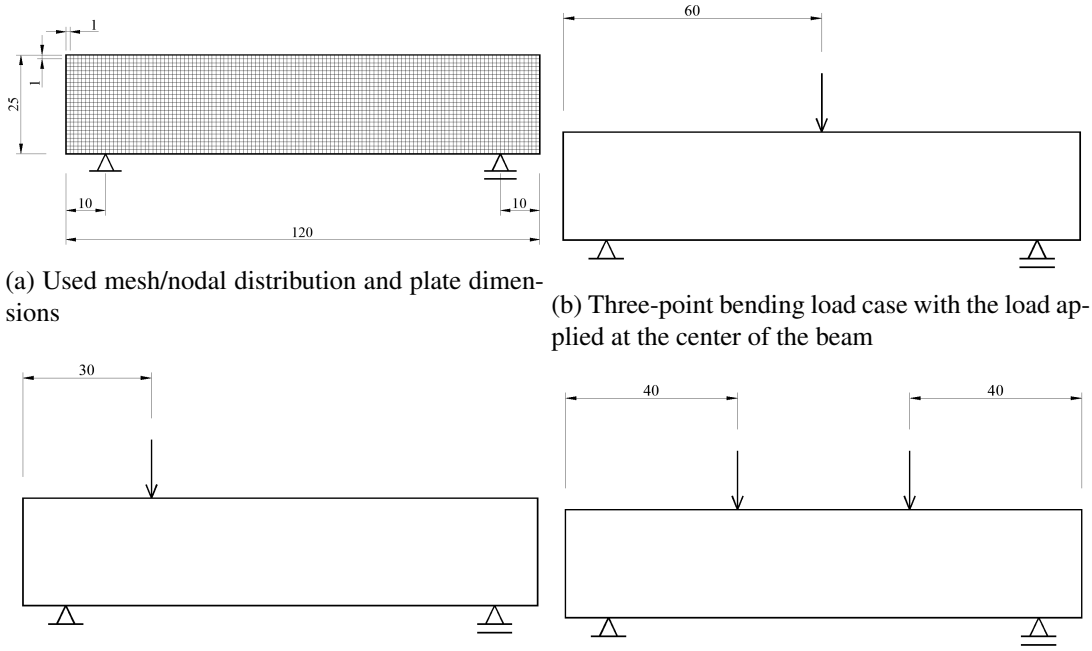
Figure 6.1: Schematic diagram of the numerical study present in this work

6.1 Load cases

Three load cases were tested (Figure 6.2). A three-point bending situation (Figure 6.2b), a three-point bending case with the load applied not at the center of the beam (Figure 6.2c), and a four-point bending situation (Figure 6.2d). Plate dimension is also indicated. The choice of the load cases was due to simplicity in experimental replication.

6.2 Discretization

The model at study was a 1mm thickness plate with 120mm length and 25mm height as it can be seen in Figure 6.2. The chosen discretization (Figure 6.2a) took into consideration not only the accuracy of results as well as the methodology being proposed. Given that the gradients are created by applying an infill to each voxel, element size should be in agreement with the precision of the machine. Moreover, nodal distribution for the NNRPIM took into consideration the fact that the nodes must not be too unevenly spaced in the three directions due to natural neighbour research. A short convergence study was conducted and the results are shown in Figure 6.3. Relative error is referent to the relative difference between theoretical displacement and the displacement obtained in the simulations at the point of load application. Analytical solution for the cantilever thick beam was obtained using a fine mesh in Abaqus of 3D shell 8 node elements. Length of the beam was twice the thickness of the beam. The mesh being used in these remodelling analyses corresponds to 25 nodes per unit length and therefore, convergence was guaranteed.



(a) Used mesh/nodal distribution and plate dimensions

(b) Three-point bending load case with the load applied at the center of the beam

(c) Three-point bending load case with a deviated load applied on the left side of the beam

(d) Four-point bending load case

Figure 6.2: Load cases at study

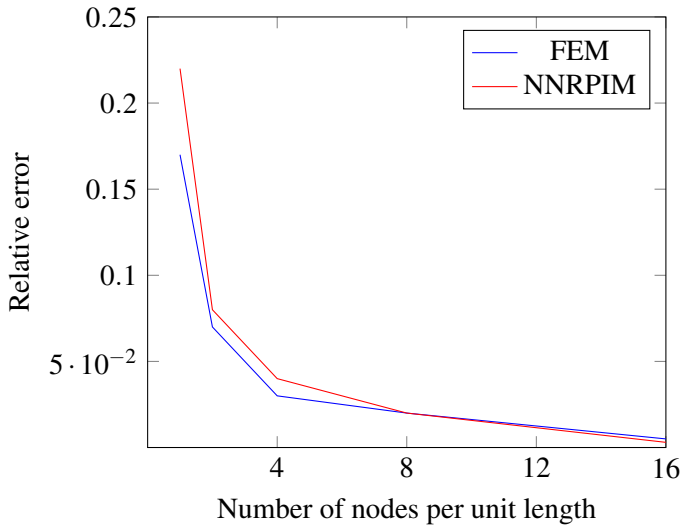


Figure 6.3: Convergence study results

6.2.1 FEM

The plate was discretized into hexahedral elements, 3DH8 with 1mmx1mmx1mm. The final model had 3000 elements and 6292 nodes. The element type is shown in Figure 6.4. The number of integration points summed up to 24000.

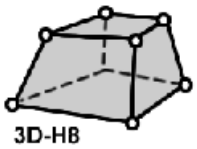


Figure 6.4: Element type used in the FEM analysis

6.2.2 NNRPIM

The NNRPIM simulation consisted of a regular distribution of 6292 nodes all equally spaced of 1mm in x, y and z directions. This summed up to a total of 144000 integration points. A first order influence cell was used. The c and p parameters of the Multi-Quadrics radial basis function were 0.0001 and 0.9999 respectively and the polynomial basis was constant with the value of 1. Lastly, a full integration scheme was used (Figure 6.5).



Figure 6.5: Full integration scheme

6.3 Structural optimization - Parabolic law

Structural optimization in the FEMAS software uses the BESO methodology. This analysis requires the following parameters to be input:

- Maximum density
- Transition density
- Minimum density
- Density increase ratio (IR)
- Density decrease ratio (RR)
- Maximum number of times that a point can remodel

Structural optimization was conducted between density values of 1.06 (maximum density allowed for the 3D printing) and $1x10^{-6}$. Since the maximum density is bellow the density of PLA, some stiffness reduction is expected. The transition density value was 0.30 because the final average density cannot be bellow that transition density. The chosen material law was a parabolic law. In addition, the material was analysed as being isotropic.

An effective Von-Mises stress was used as a remodelling criterion.

Material laws in structural optimization are shown in Figure 6.6 with a generic plot.

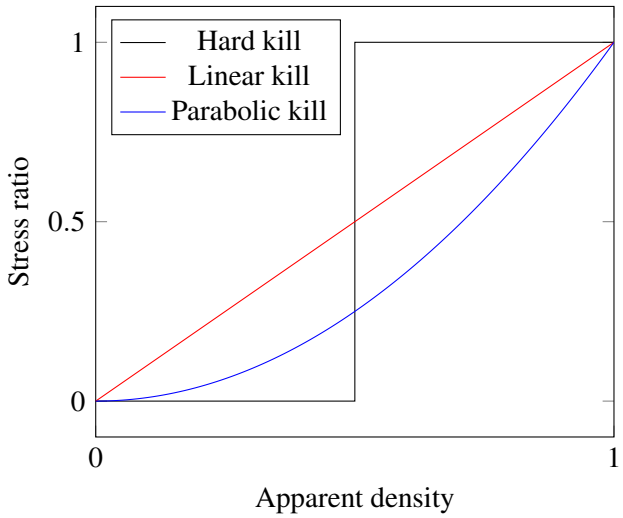
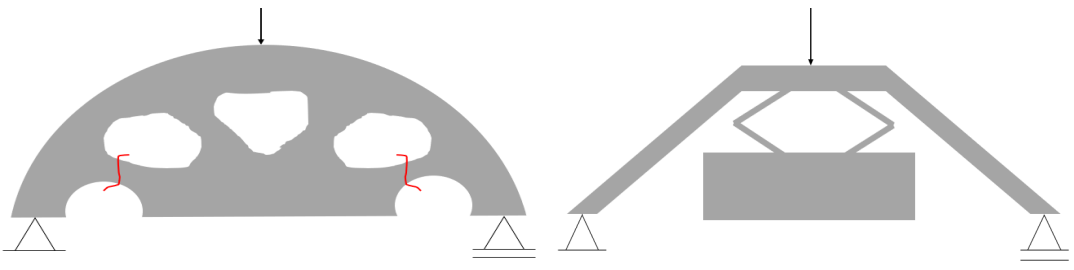


Figure 6.6: Remodelling laws in structural optimization

6.3.1 Load case 1

Load case 1 is referent to the load case depicted in Figure 6.2b. Both methods, FEM and NNRPIM were able to obtain a solution at the aimed density which is 0.7 g/cm^3. For this load case, both the FEM and NNRPIM would try to converge to a structure like the one in Figure 6.7a for the remodelling criteria of IR = 0.05 and RR = 0.10 with a maximum number of times that a point can remodel of 3. The red lines indicate where the structure separated during the optimization. It should also be noted that NNRPIM got much more approximate to this structure than FEM. As iterations would progress, the structure would evolve into a structure similar to the one depicted in Figure 6.7b.

These structures appear to be quite ineffective in the way that, since the main body of the structure is not connected to the upper arch, it is only increasing mass without reinforcing the structure. Had the simulations approached the result depicted in Figure 6.7a, efficiency would be better. Figure 6.8 shows the evolution of the density for the structures for both the FEM and NNRPIM analyses.



(a) Structure configuration for an average apparent density of $\rho = 0.7$

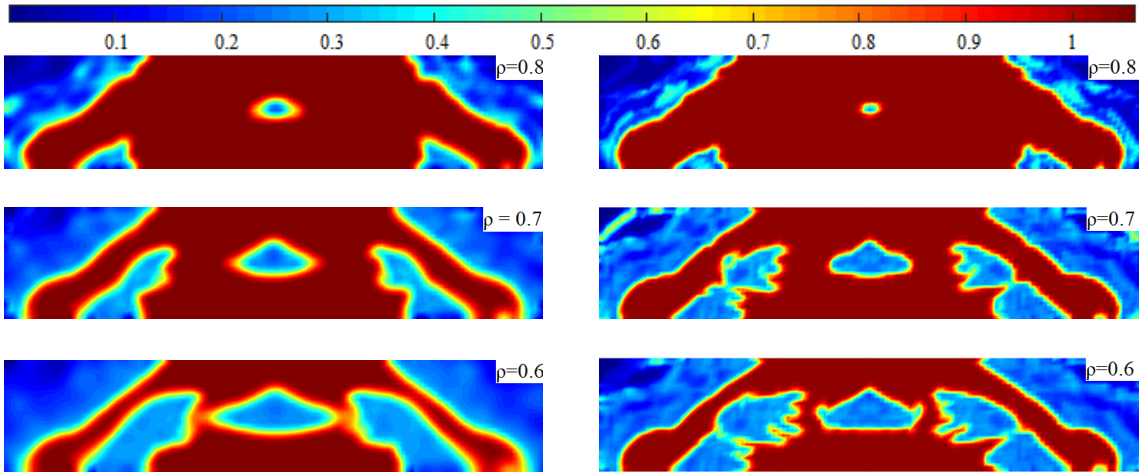
(b) Structure configuration for an average apparent density of $\rho = 0.5$

Figure 6.7: Schematic representation of the truss structure obtained with the structural optimization remodelling with a parabolic material law

FEM

The results for this simulation are shown in Figure 6.8a.

One of the greatest difficulties was to obtain a continuous structure, that is, with all "bars" connecting to each other. Moreover, it is possible to see that from a threshold level of 0.6 g/cm^3, the upper and lower arches of the structure start to separate since the middle section is at a lower density. For this simulation, however, a more continuous configuration was obtained with IR = 0.05 and RR = 0.05 but these parameters could not obtain a solution for the NNRPIM.



(a) FEM (b) NNRPIM

Figure 6.8: Density distribution obtained with the structural optimization with a parabolic law using the FEM and the NNRPIM for the load case of Figure 6.2b

NNRPIM

The remodelling results for the NNRPIM are shown in Figure 6.8b. It is visible from the referred figure that the structure is much more well defined than in the FEM (Figure 6.8a) as well as being closer to the ideal result schematically represented in Figure 6.7a. Nonetheless, even though the structure is closer to a better solution, the separation which occurs, means that there is a larger amount of mass being inefficient in the structure suggesting a smaller stiffness-to-weight ratio.

Stiffness evaluation

In order to assess the quality of the optimization, stiffness is calculated along the iterations. The FEM structures appear to present lower stiffness and higher displacements even if only slightly. Figure 6.9 presents a summarized collection of graphics with said evolution. Specific stiffness [1] has similar values for both the FEM and NNRPIM simulations.

[1] specific stiffness = stiffness$/(\frac{\rho_i}{\rho_0})$

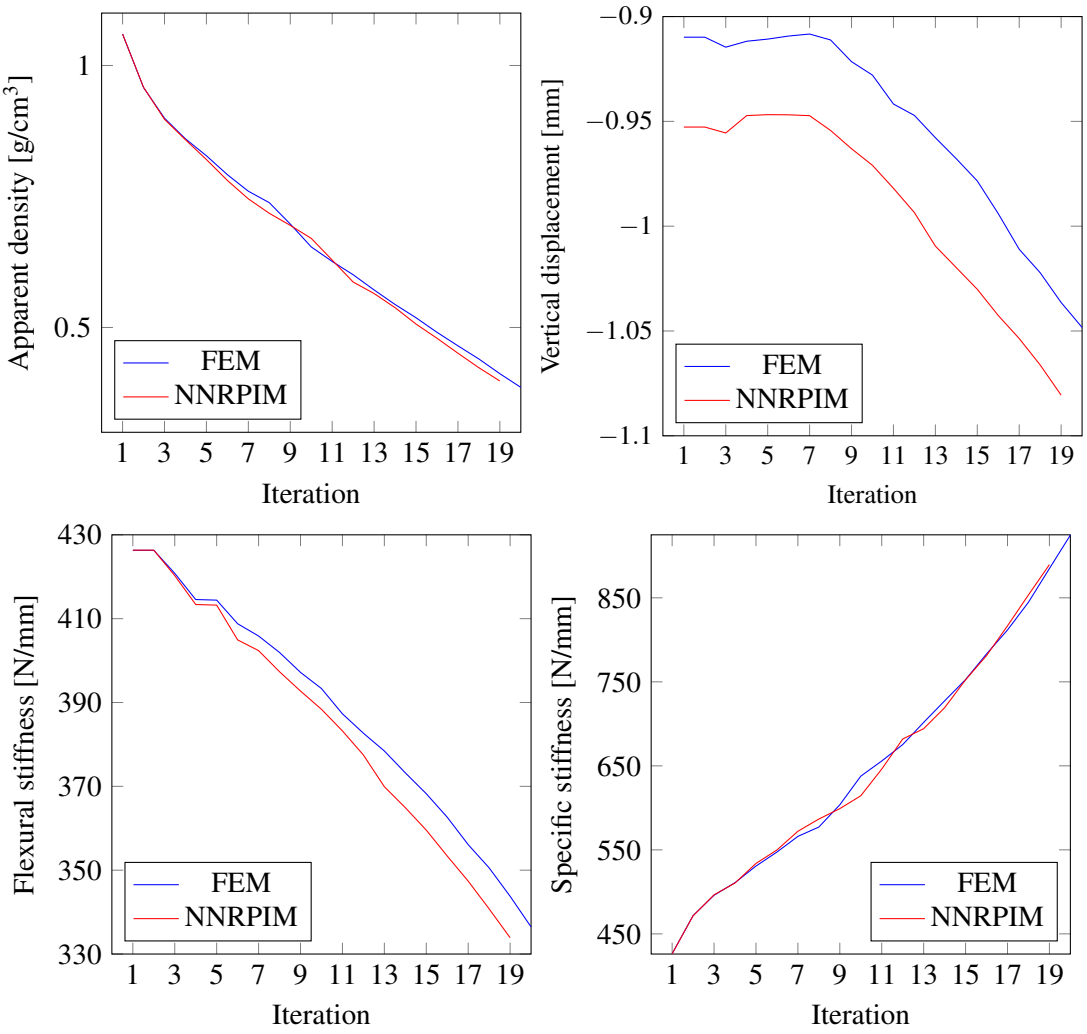


Figure 6.9: Stiffness evaluation for load case 1 using a structural optimization analysis with a parabolic law using the the FEM and the NNRPIM

6.3.2 Load case 2

For the both analyses, the used remodelling parameters were IR = 0.05, RR = 0.10 and the maximum number of times that a point can be remodeled is 3. In this load case, depicted in Figure 6.2c, obtaining a continuous structure, that is, with connection between all parts was not possible as the part of the structure which connects to the support on the right side presents lower density than the rest as is indicated in Figure 6.10 through the red lines. The density evolution results for the truss-like structures are shown in Figure 6.11.

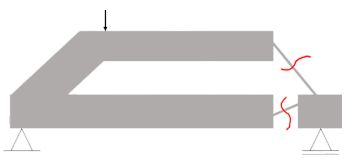
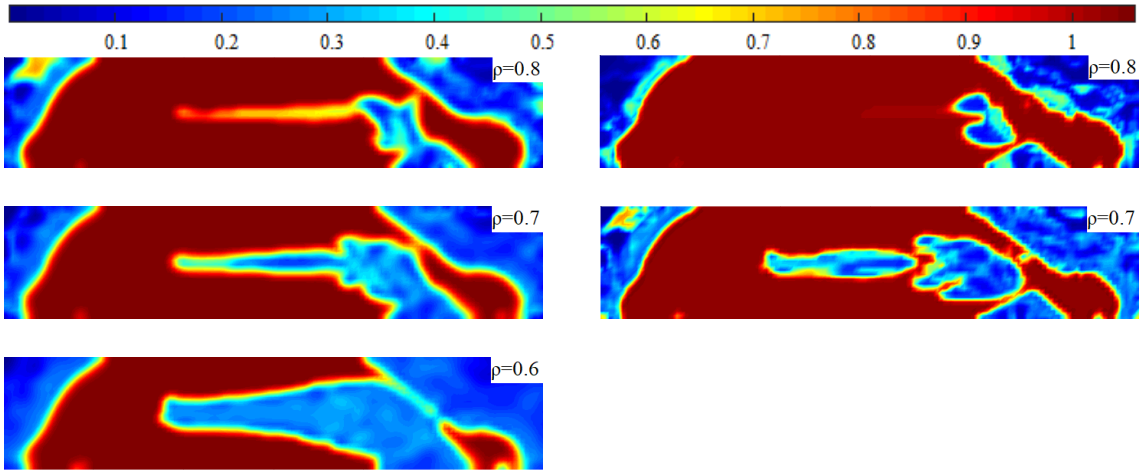


Figure 6.10: Structure into which the structural optimization for load case 2 evolves



(a) FEM (b) NNRPIM

Figure 6.11: Density distribution obtained with the structural optimization with a parabolic law using the FEM and the NNRPIM for the load case of Figure 6.2c

FEM

Figure 6.11a shows the results of the density distribution for the structural optimization analysis at question. It is visible, especially for a density level of 0.6 g/cm^3 how the structure splits. The thin section in the arm which connects the main structure to the support on the right side exhibits how the structure in itself would most likely not possess the structural integrity to endure the loads being applied. Moreover, the absence of connection between the main body of the structure and the right arm on the lower part of the structure permits high a higher displacement which also affects the behaviour of the structure.

NNRPIM

First of all, this analysis could not achieve a density level of 0.6 g/cm^3 since at iteration 10, the BESO algorithm considered that the part was near rupture and reinforced the entire structure, being the optimization results depicted in Figure 6.11b. Nonetheless, the structure is more well defined than the FEM similar to what occurred in the simulations for load case 1 as well as seeming to approximate more to an efficient solution if not for the thin section in the upper arch which led to rupture and reinforcement of the entire structure. In addition, the NNRPIM solution presents a thin reinforcement on the lower part of the structure, connecting the main body to the right arm, also implying a more efficient structure.

Stiffness evaluation

As it was mentioned previously, for the NNRPIM analysis, the structure was reinforced as the algorithm considered it to be near rupture and for that reason, the curves for the NNRPIM model

are cut shorter. Throughout the optimization process, FEM and NNRPIM present similar performance. These results are summarized in Figure 6.12.

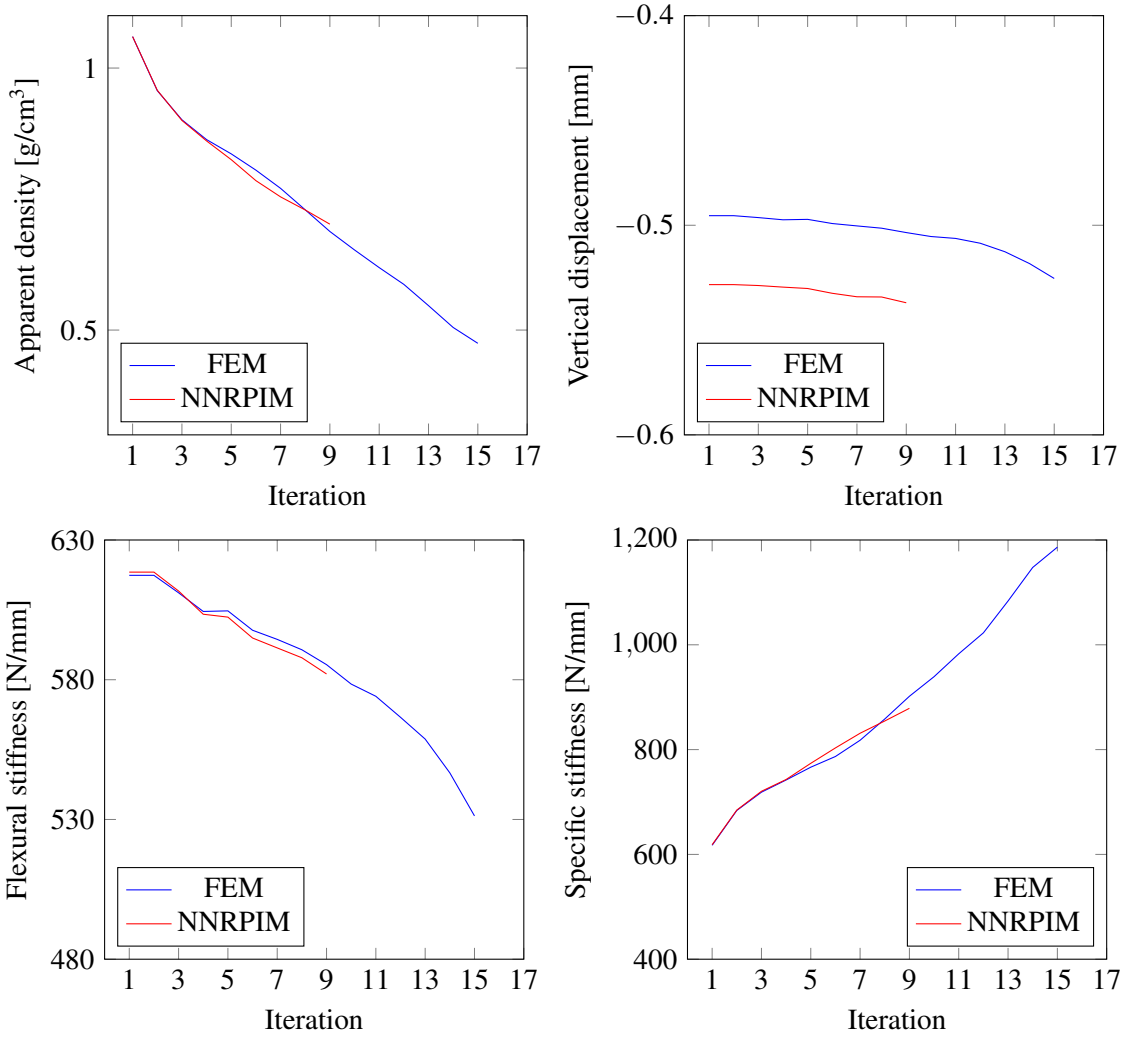
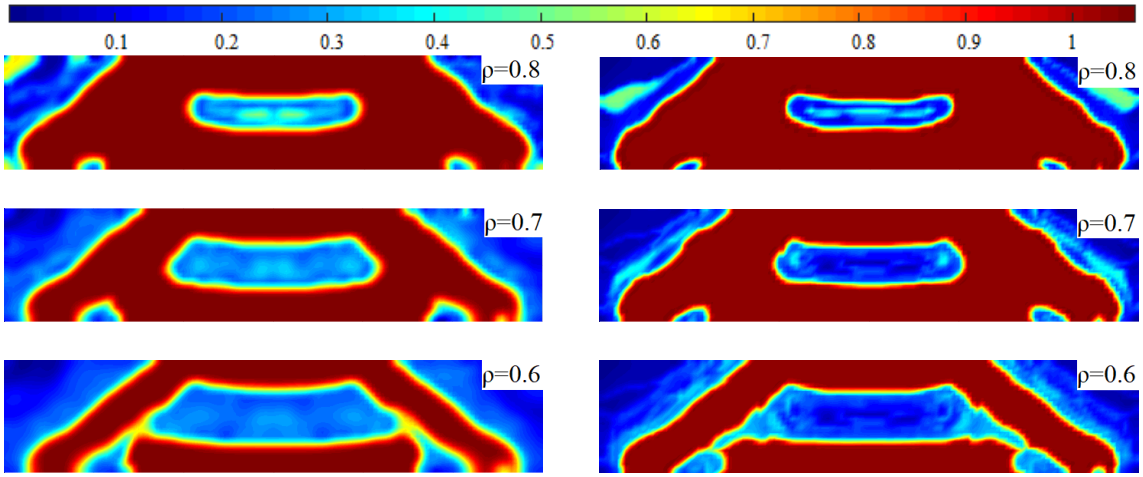


Figure 6.12: Stiffness evaluation for load case 2 using a structural optimization analysis with a parabolic law using the FEM and the NNRPIM

6.3.3 Load case 3

For load case 3, the same remodelling parameters could not be used for both the FEM and NNRPIM analyses. Only the maximum number of times that a point can remodel has kept the same value of 3. The NNRPIM required a higher rejection ratio and for that reason some possible solutions between density levels disappear. The final structure was very similar for both methods and more efficient than the structure obtained for other load cases. Figure 6.13 presents the structure evolution results in the form of the density field for the FEM and NNRPIM analyses.



(a) FEM (b) NNRPIM

Figure 6.13: Density distribution obtained with the structural optimization using a parabolic law using the FEM and the NNRPIM for the load case of Figure 6.2d

FEM

The remodelling parameters used for the NNRPIM simulation were IR = 0.05 and RR = 0.10. Analysing the plots displayed in Figure 6.13a it is visible that the structure is not connected at a density level of 0.6 g/cm^3 which is consistent with what occurred in load case 1. However, a simple and effective structure was obtained for a density level of 0.7 where there are no areas at a lower density nor any thin sections prone to rupture.

NNRPIM

The remodelling parameters used for the NNRPIM simulation were IR = 0.05 and RR = 0.15 since an RR of 0.10 would not converge. Results of this optimization are shown in Figure 6.13b presenting a similar configuration to that of the truss structure achieved with the FEM analysis.

Stiffness evaluation

Analysing the graphics in Figure 6.14 it is visible that the NNRPIM simulation achieved a final structure with lower stiffness in comparison to the FEM simulation. Some accuracy may have been lost due to the higher ratios in the NNRPIM analysis as well as some possible solutions.

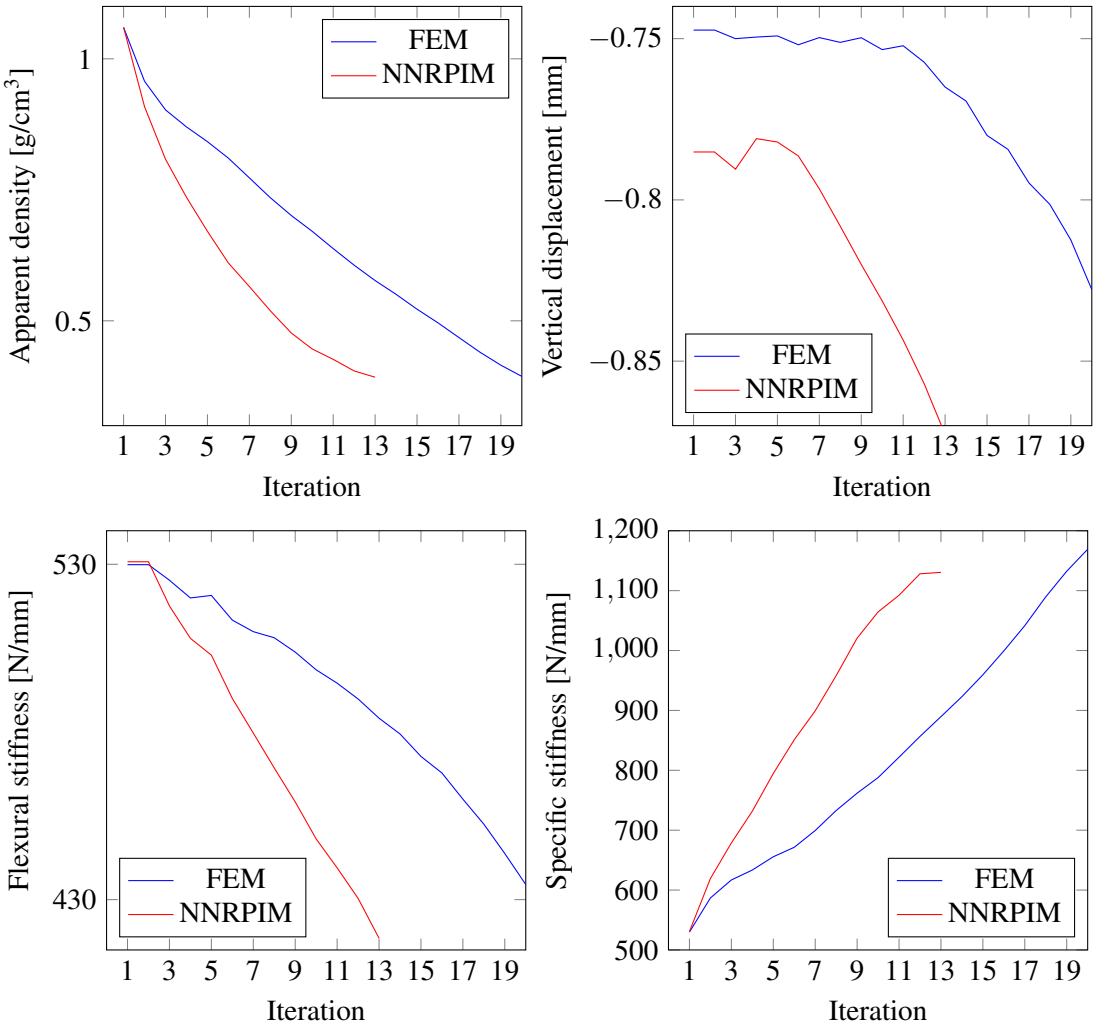


Figure 6.14: Stiffness evaluation for load case 3 using a structural optimization analysis with a parabolic law using the FEM and the NNRPIM

6.4 Structural optimization - Linear law

For the present analysis, a linear law was used and two remodelling parameters were used:

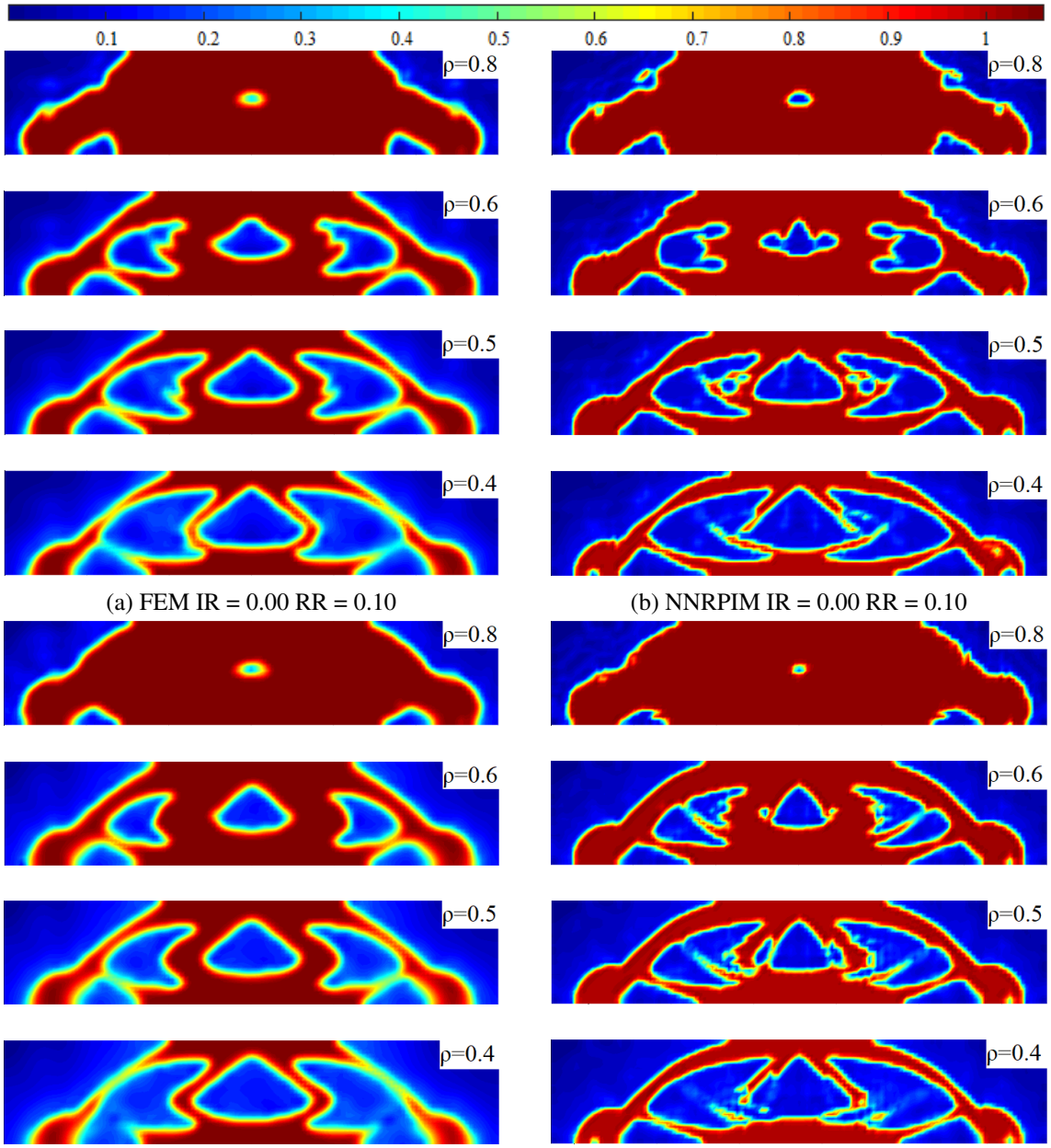
1. IR = 0, RR = 0.1;

2. IR = 0, RR = 0.05.

For both combinations, the maximum number of times that a point could remodel was defined as 3. All load cases (Figures 6.2b, 6.2c and 6.2d) were tested with the same parameters. The aim of this analysis is validating whether the transition density chosen for the parabolic law presents good results, as well conducting a small study on the influence of remodelling parameters. Moreover, a Von-Mises effective stress was employed as a remodelling criteria.

6.4.1 Load case 1

Comparing with the results for the parabolic law, it is visible in Figure 6.15 that for both parameter combinations, the structures which were obtained with the linear law present higher connectivity which means that the efficiency problems detected previously are improved. Moreover, for a density level of 0.6 g/cm^3, which is chosen for the experimental analysis, all analyses obtained a structure with connected upper and lower arches.



(a) FEM IR = 0.00 RR = 0.10

(b) NNRPIM IR = 0.00 RR = 0.10

(c) FEM IR = 0.00 RR = 0.05

(d) NNRPIM IR = 0.00 RR = 0.05

Figure 6.15: Density distribution obtained with the structural optimization with a linear material law using the FEM and NNRPIM for the load case of Figure 6.2b

FEM

The results for the FEM analysis are shown in Figure 6.15a for IR = 0.00 and RR = 0.10, and in Figure 6.15c for IR = 0.00 and RR = 0.05. The higher rejection ratio presents, for each density level, higher connectivity meaning that the structure is probably more efficient. Comparing both sets of remodelling parameters, a higher connectivity, that is, less thin sections, was achieved when using a higher rejection ratio well as presenting structures in the central part of the structure which could evolve into reinforcement trabeculae.

NNRPIM

For the NNRPIM analysis, the lower rejection ratio obtained a more well defined structure. Regarding connectivity, the higher rejection ration presented slightly less thin sections, visible in Figures 6.15b and 6.15d for a density level of 0.5 g/cm^3. Nonetheless, the using a lower rejection ratio, the simulation seemed to evolve in the sense of creating more reinforcement structures which, due to failure to fully connect to the upper arch, constitute inefficiency. In addition, similar to the FEM, the simulations with a lower rejection ratio form more thin sections, which is visible for a density level of 0.5 g/cm^3 and 0.4 g/cm^3 where the lower arch would join the upper arch.

Stiffness evaluation

Comparing both sets of parameters, the higher rejection ratio presents higher stiffness, both for the FEM and the NNRPIM (Figure 6.16), which is expected since the structure does not form the same type of thin sections. Evolution results for each set of parameters are shown in Figure 6.17 and Figure 6.18 for RR = 0.01 and RR = 0.05 respectively. For both sets of remodelling parameters, the NNRPIM presents slightly lower stiffness which goes as according to the results with the parabolic law. For the analysis with the lower rejection ratio, the FEM analysis presents a slight adjustment in vertical displacement, around iteration 11.

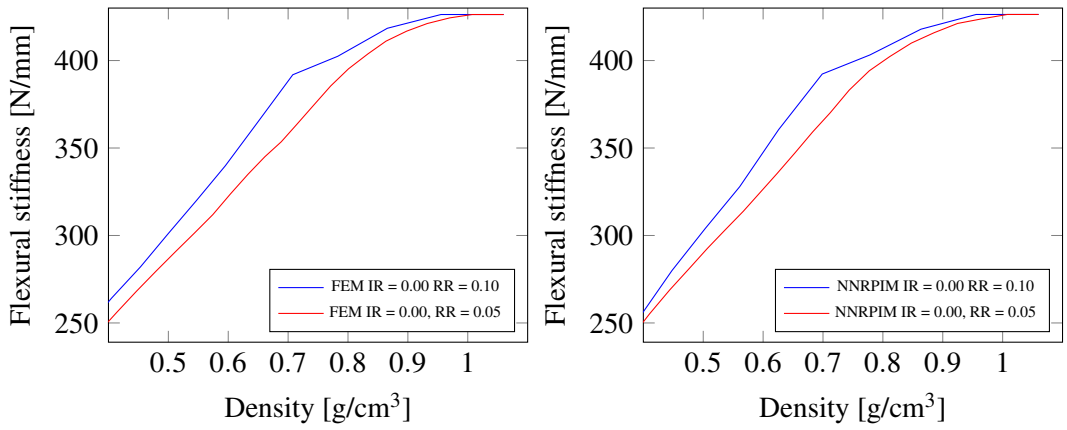


Figure 6.16: Comparison of the behaviour of different sets of remodelling parameters for the structural optimization analysis with a linear law using the FEM and the NNRPIM in load case 1

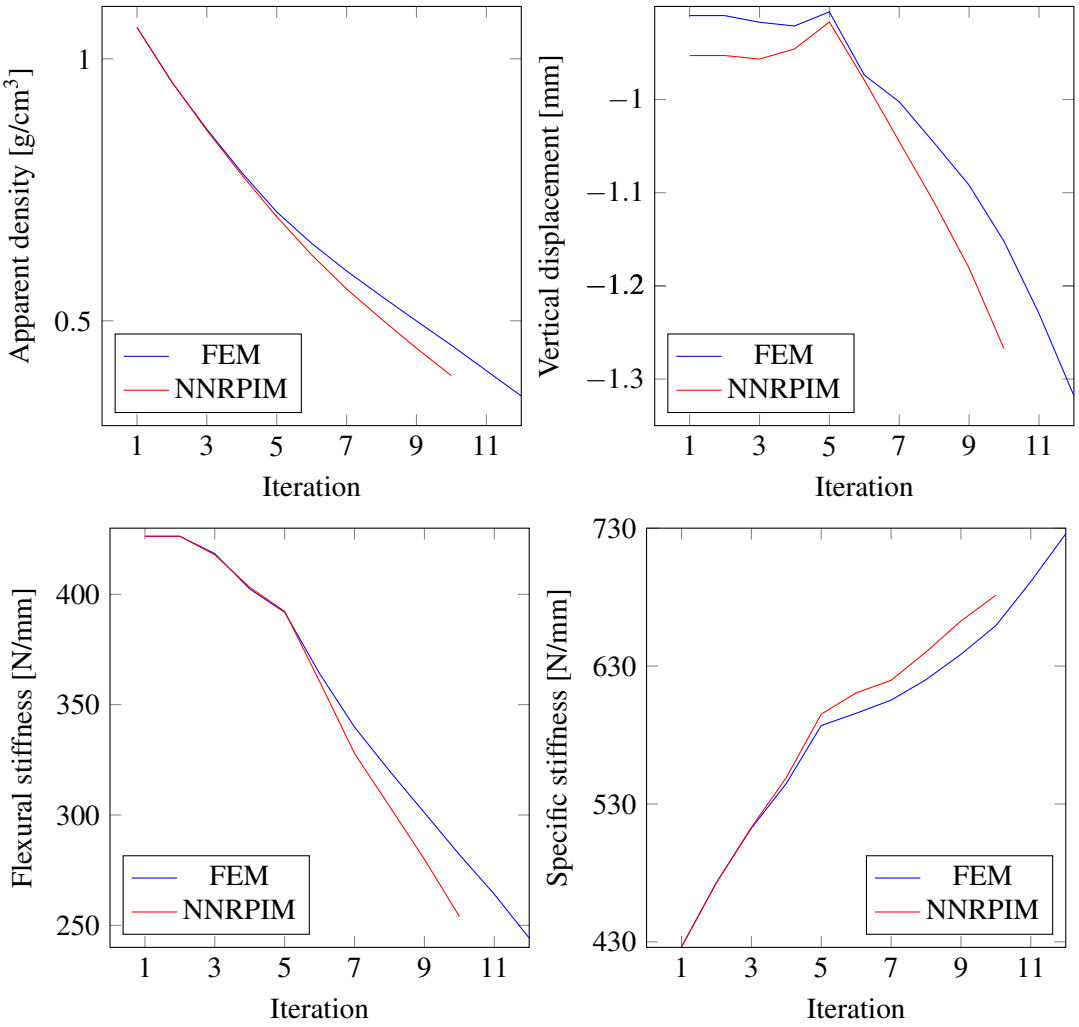


Figure 6.17: Stiffness evaluation for load case 1 using a structural optimization analysis with a linear law (IR = 0.00 and RR = 0.10) using the FEM and the NNRPIM

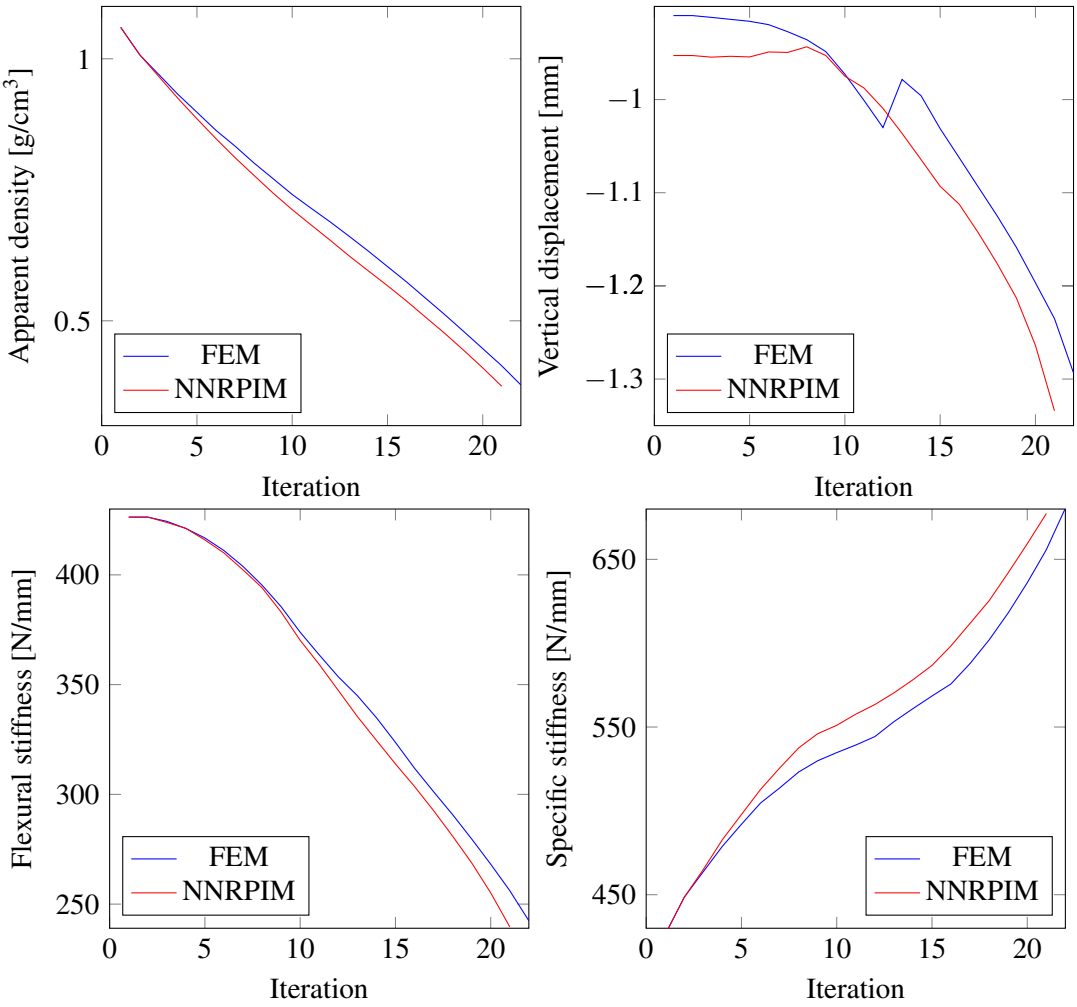
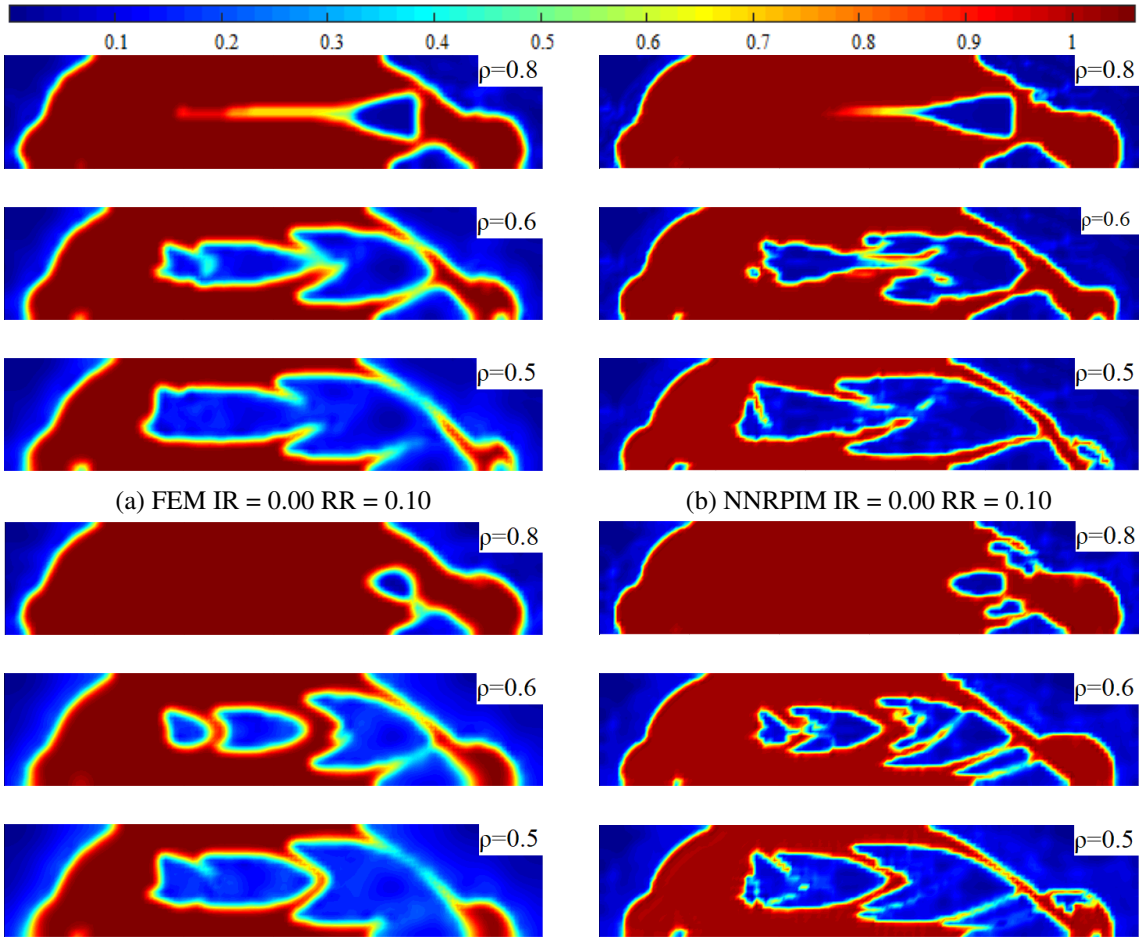


Figure 6.18: Stiffness evaluation for load case 1 using a structural optimization analysis with a linear law (IR = 0.00 and RR = 0.05) using the FEM and the NNRPIM

6.4.2 Load case 2

The connectivity issues detected with the parabolic law are minimized with the linear law even though these are still present using the FEM. When conducting the NNRPIM analysis, these occurrences were even further minimized. For both methods, the difference in using an RR of 0.1 or an RR of 0.05 is visible (more than in load case 1) especially for the NNRPIM. Similarly to what was observed in load case 1, a higher rejection ratio gives place to less thin structures, visible in the right arm which connects the main body to the support on the right side. However, for both load cases, when using a lower rejection ratio, the central reinforcement structures maintained connected which increases efficiency. Figure 6.19 shows the evolution results for the FEM and NNRPIM and both sets of remodelling parameters.



(a) FEM IR = 0.00 RR = 0.10

(b) NNRPIM IR = 0.00 RR = 0.10

(c) FEM IR = 0.00 RR = 0.05

(d) NNRPIM IR = 0.00 RR = 0.05

Figure 6.19: Density distribution obtained with the structural optimization with a linear material law using the FEM and NNRPIM for the load case of Figure 6.2c

FEM

The simulations with a higher rejection ratio seem to be less efficient than the simulations with the lower rejection ratio, being that this is more visible when comparing the structures at a density level of 0.6 g/cm^3, where the central reinforcement structures are present for the lower rejection ratio and disconnected for the higher rejection ratio, thus being inefficient. Moreover, these central structures are present even for lower density levels.

NNRPIM

The simulations with a higher rejection ratio present the same connectivity issues with the reinforcement structures which were found in the FEM, but however, the upper arch maintains at a high density even for lower density levels. The simulations with a lower rejection ratio present plenty of reinforcement arches between the upper and lower arch for a density level of 0.6g/cm^3.

The connectivity problem due to a low density value in this reinforcement structures is recurrent, even though the remodelling creates some sort of reinforcement, its density is lower than the maximum density allowed in the analysis.

Stiffness evaluation

When comparing both sets of remodelling parameters (Figure 6.20), in the FEM, similarly to what had already happened in Load case 1, the lower rejection ratio presents lower stiffness. However, for the NNRPIM, the structures obtained with a lower rejection ratio start presenting higher stiffness and then, lower stiffness than with the higher rejection ratio. Still, the difference in stiffness is quite small.

Stiffness evaluation results are shown in more detail in Figure 6.21 for IR = 0.00 and RR = 0.10 and in Figure 6.22 for IR = 0.00 and RR = 0.05. For the analysis with the lower rejection ratio, the NNRPIM presented slightly greater stiffness than the FEM and vertical displacements get closer to those obtained in FEM. The results were expected due to the appearance of reinforcement structures with the lowest rejection ratio in NNRPIM.

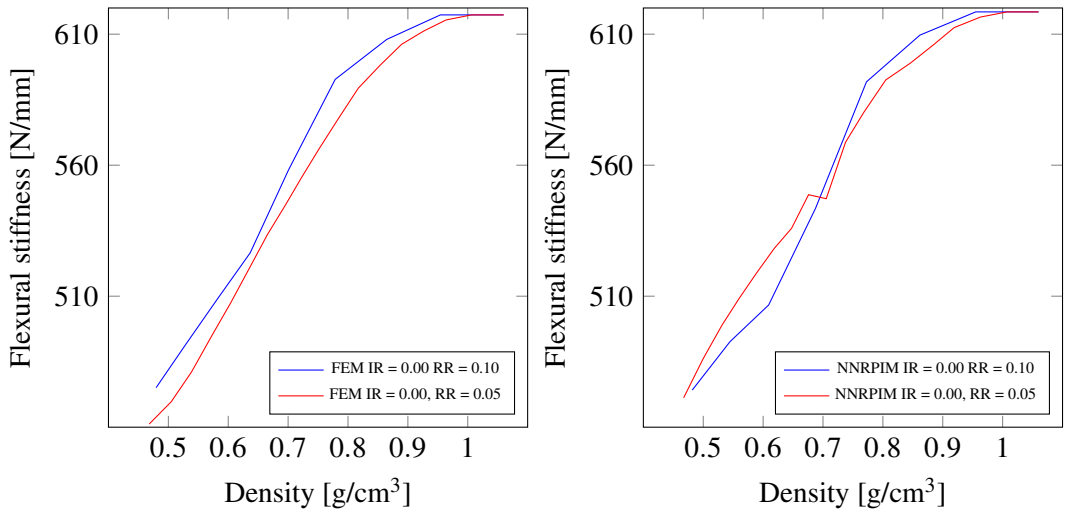


Figure 6.20: Comparison of the behaviour of different sets of remodelling parameters for the structural optimization analysis with a linear law using the FEM and NNRPIM in load case 2

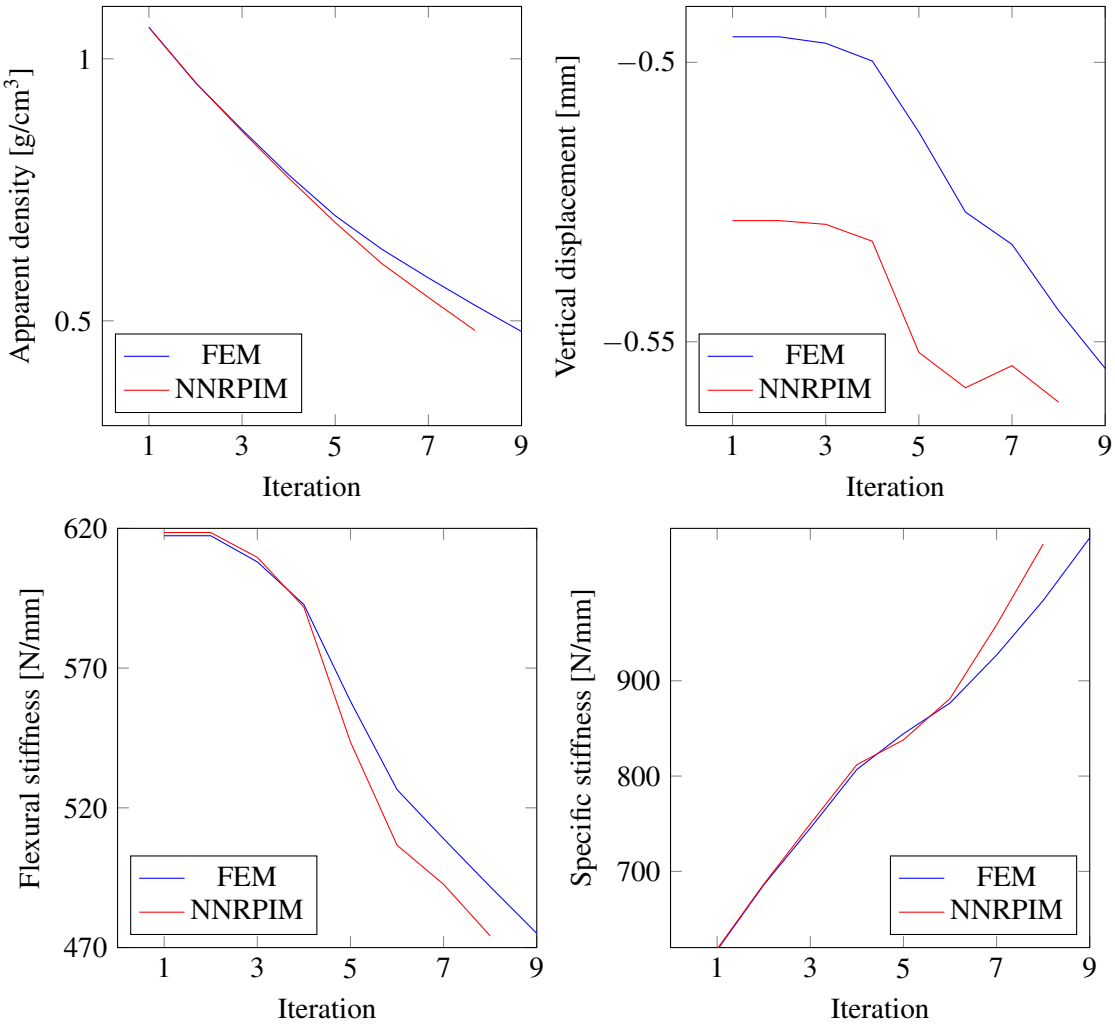


Figure 6.21: Stiffness evaluation for load case 2 using a structural optimization analysis with a linear law (IR = 0.00 and RR = 0.10) using the FEM and the NNRPIM

6.4.3 Load case 3

In load case 3, the differences between the parabolic law and the linear law were the least blatant as well as presenting the most similarities between both methods, as the structure which was obtained with the parabolic law was already quite. The differences when using a higher or lower rejection ratio were also very minimal in terms of structure configuration. The main difference was the fact that when using a lower rejection ratio the structure achieved lower density levels for the FEM. In addition, the NNRPIM simulation adjusted the structure during the simulation meaning that after achieving a density level of 0.6g/cm^3, the stress level in the structure approximated the elastic limit.

For this particular load case, the FEM achieved a more efficient and smooth structure. These results are shown in Figure 6.23.

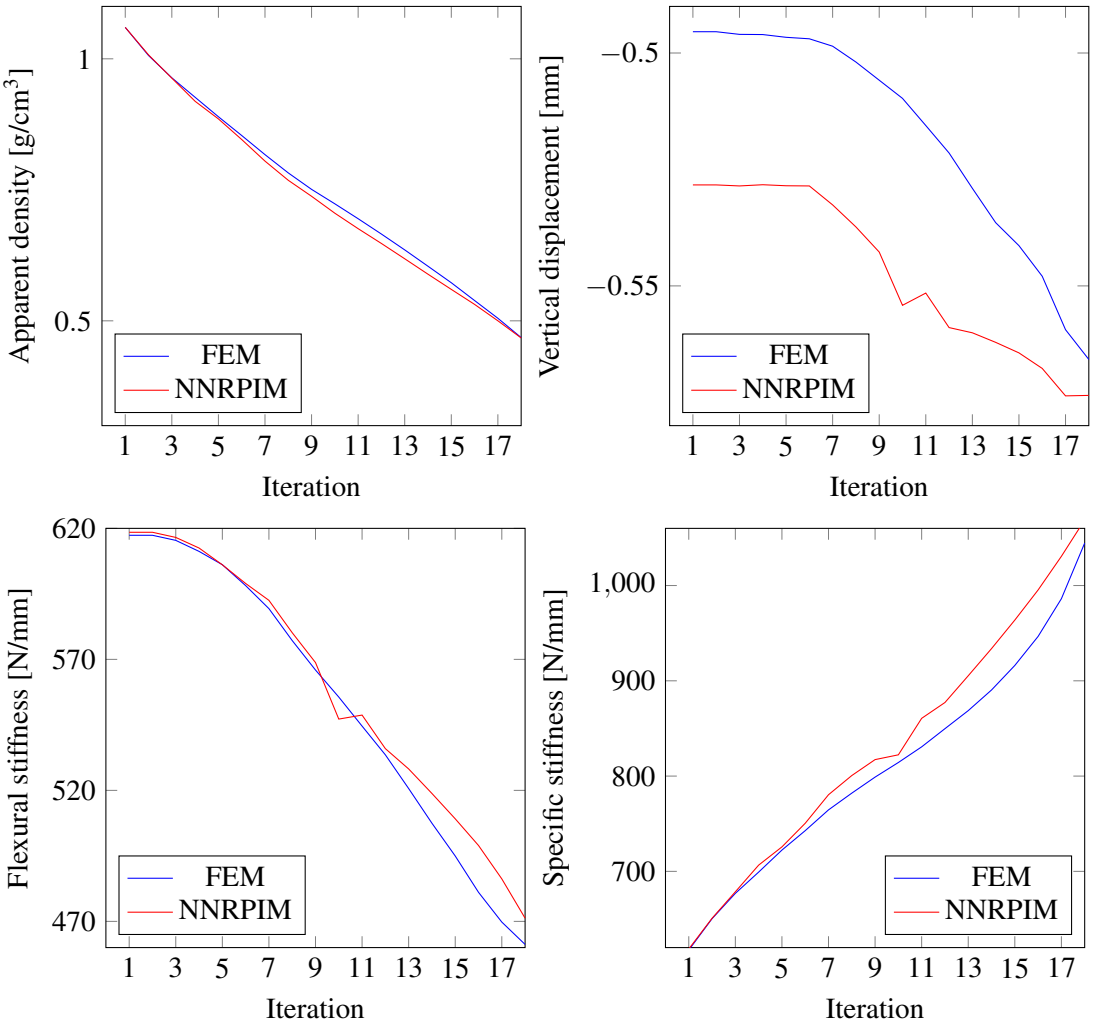
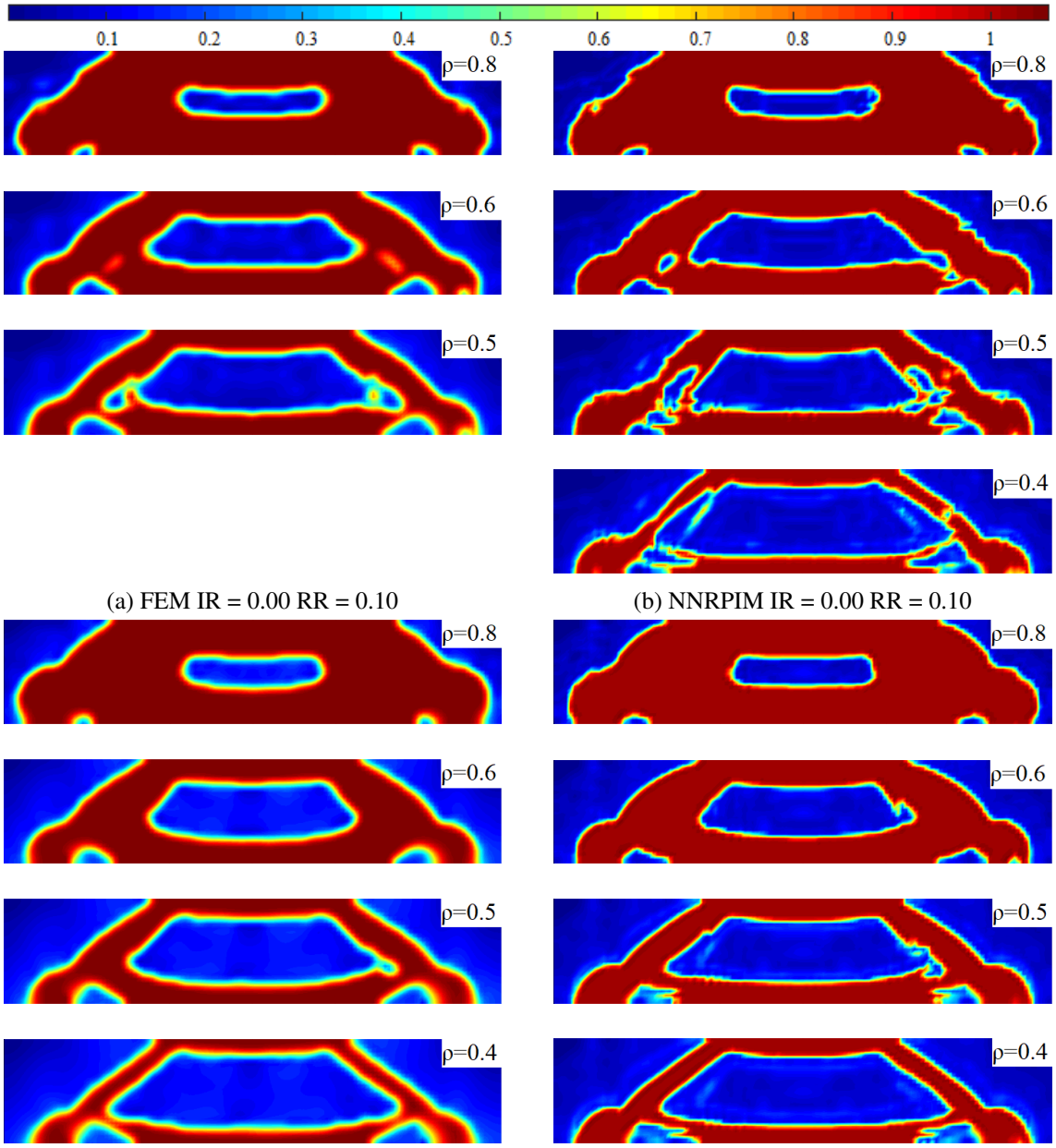


Figure 6.22: Stiffness evaluation for load case 2 using a structural optimization analysis with a linear law (IR = 0.00 and RR = 0.05) using the FEM and the NNRPIM



(a) FEM IR = 0.00 RR = 0.10

(b) NNRPIM IR = 0.00 RR = 0.10

(c) FEM IR = 0.00 RR = 0.05

(d) NNRPIM IR = 0.00 RR = 0.05

Figure 6.23: Density distribution obtained with the structural optimization with a linear material law using the FEM and NNRPIM for the load case of Figure 6.2d

FEM

Both sets of remodelling parameters showed similar results and a very stable structure. Connectivity issues are not present as there are no thin sections in the structure. For the case with a rejection ratio of 0.10, in Figure 6.23a, it was not possible to achieve an apparent density lower than 0.5 g/cm^3, in addition to the small indentations which appeared that can cause stress concentration. However, as it is seen in Figure 6.23c where a rejection ratio of 0.05 was used, the obtained structure seems to present no major issues.

NNRPIM

For the NNRPIM analysis, it is visible that the structure with the higher rejection ratio in Figure 6.23b is not as well defined as the structure in Figure 6.23d obtained with a lower rejection ratio where, even for lower density levels, the structure stays connected to all parts. This could be due to the fact that, since with a higher RR more elements are removed for each iteration, some instability areas could have surged *i.e.* removing too many points from an area of the structure where those should not have been removed.

It is important to denote that evolutionary topology algorithms, such as ESO and BESO are not optimal methods (Tanskanen, 2002; Xie and Steven, 1993) but most times present good solutions at a lower computational cost.

Stiffness evaluation

Comparing both sets of remodelling parameters (Figure 6.24), stiffness as a function of density was very similar for both cases. It is immediately visible in both Figure 6.25 referent to RR = 0.10 and Figure 6.26 referent to RR = 0.05 that the NNRPIM simulations would readjust near an apparent density of 0.6 g/cm^3 being that for both methods, a similar flexural stiffness is predicted where a slightly higher stiffness is found for the structures obtained with a higher rejection ratio.

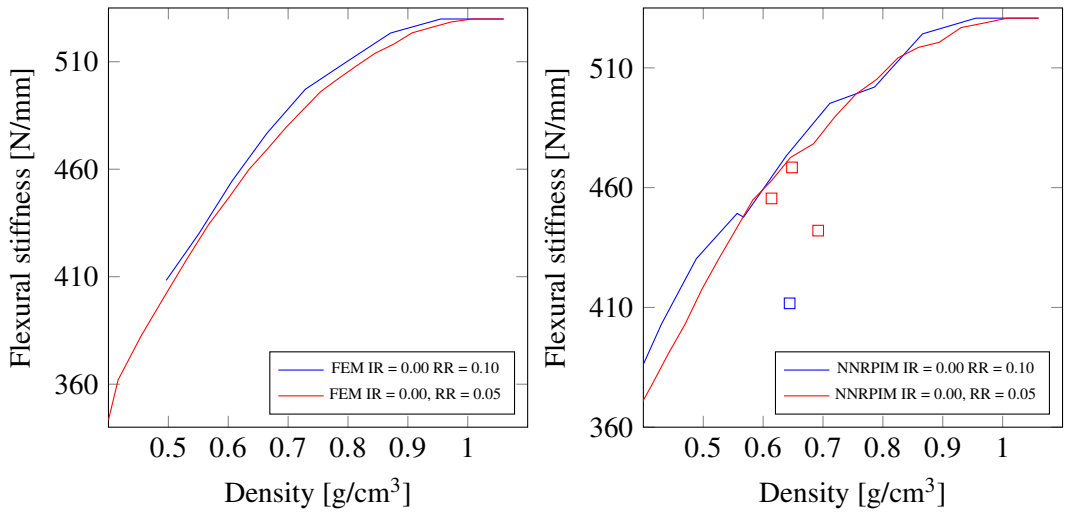


Figure 6.24: Comparison of the behaviour of different sets of remodelling parameters for the structural optimization analysis with a linear law using the FEM and NNRPIM in load case 3

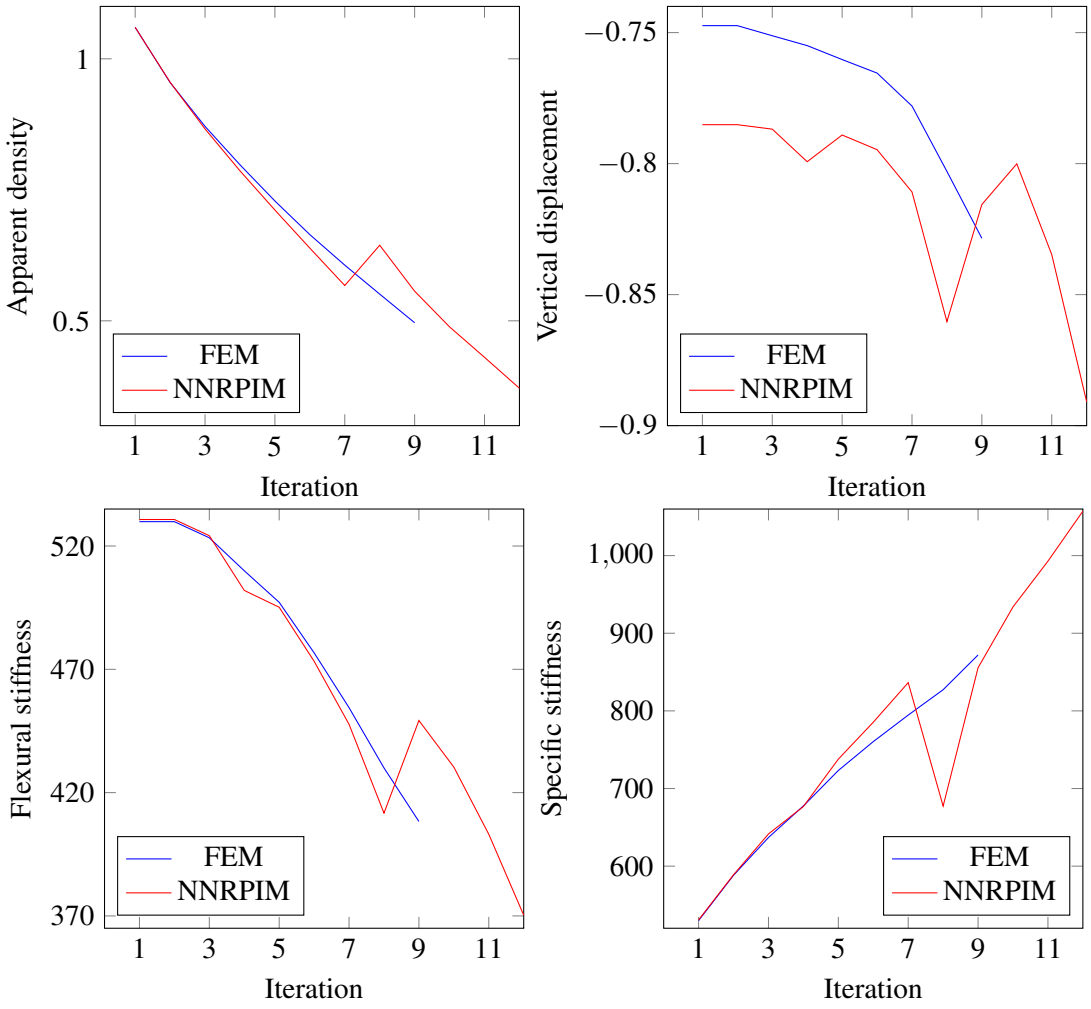


Figure 6.25: Stiffness evaluation for load case 3 using a structural optimization analysis with a linear law (IR = 0.00 and RR = 0.10) using the FEM and the NNRPIM

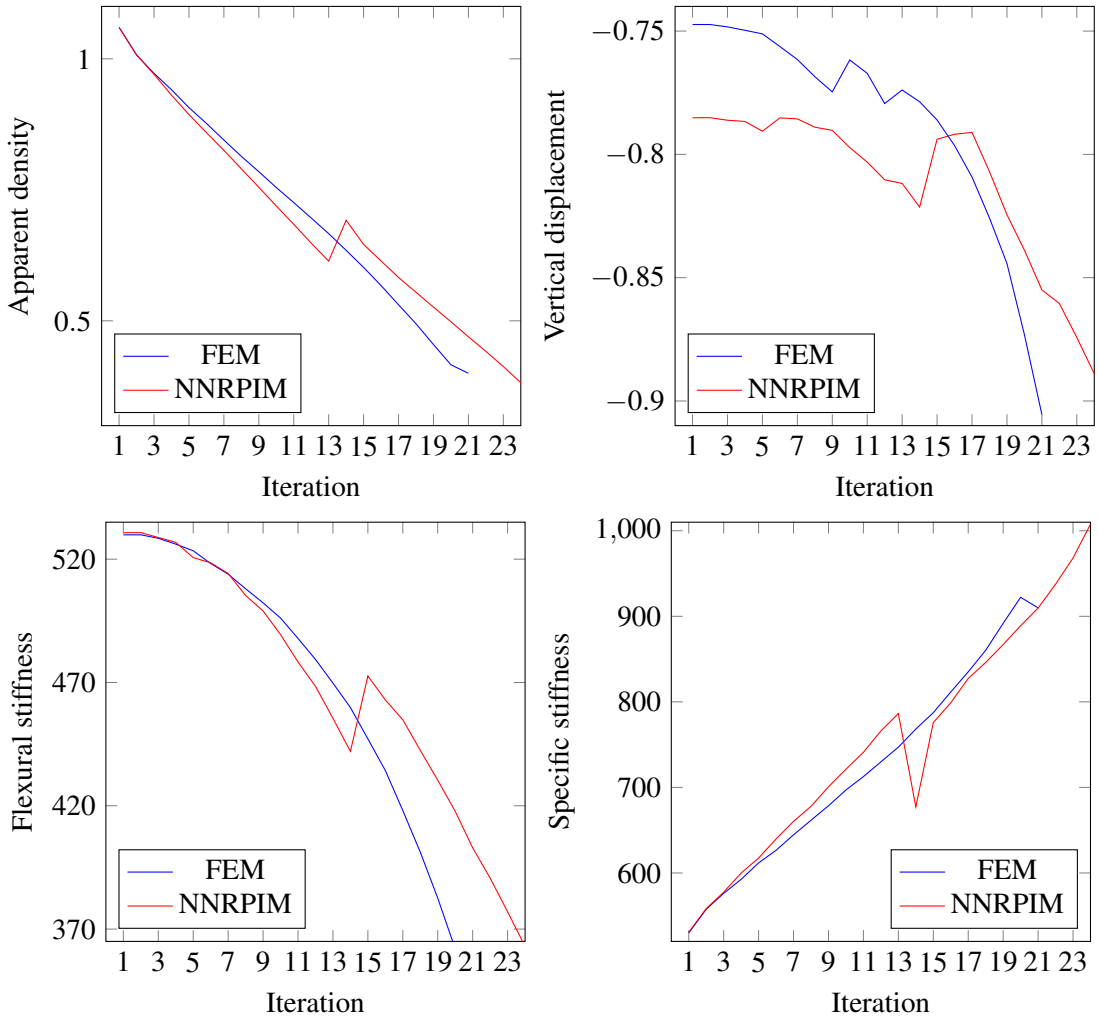


Figure 6.26: Stiffness evaluation for load case 3 using a structural optimization analysis with a linear law (IR = 0.00 and RR = 0.05) using the FEM and the NNRPIM

6.5 Gyroid remodelling - Law case 1

The remodelling analysis using a Gyroid law developed in 5.6 is implemented on the Bone Remodelling algorithm present in the FEMAS software. Similarly to the Structural Optimization analysis, a BESO algorithm is used where the following parameters must be defined:

- Maximum density
- Transition density
- Minimum density
- Density increase ratio (α)
- Density decrease ratio (β)
- Maximum number of times that a point can remodel

For this optimization, the transition density parameter is not relevant because the material was characterized with a single law unlike bone where, due to the differences between trabecular and

cortical bone, there are distinct expressions to characterize the behaviour of the material properties with density. In addition, an effective Von-Mises stress was used as a remodelling criterion, similarly to what was used in structural optimization analysis and the material was also considered isotropic.

Here, the stiffness results should correlate to what is verified in experimental testing as the law takes into consideration the manufacturing process and the shape of the infill.

A small study regarding the influence of the chosen rejection ratio is also conducted for load case 1 even though, no experimental verification for those specimens is conducted as these small rejection ratios could not achieve solutions with a Von-Mises remodelling criterion for all load cases.

6.5.1 Load case 1

Load case 1 (depicted in Figure 6.2b) worked with the same parameters for both the FEM and NNRPIM. The used remodelling parameters were $\alpha = 0.00$, $\beta = 0.10$ and the maximum number of times that a point can remodel is 2. It is visible how the structures obtained both with the FEM and NNRPIM evolved into truss-like structures similar to what can be seen in the literature for other optimization approaches (Chu et al., 2019; Di Cesare and Domaszewski, 2019; Gaynor et al., 2013; Jewett and Carstensen, 2019; Wu et al., 2017). Figure 6.27 shows a schematic representation of these structures found in the literature. Remodelling results for both the FEM and NNRPIM analyses are shown in Figure 6.28.

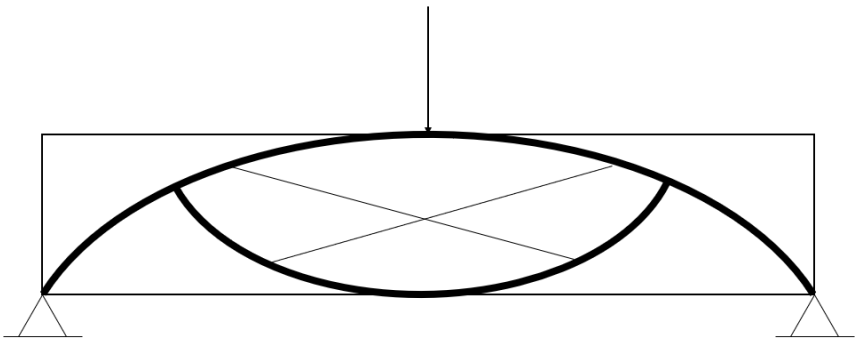
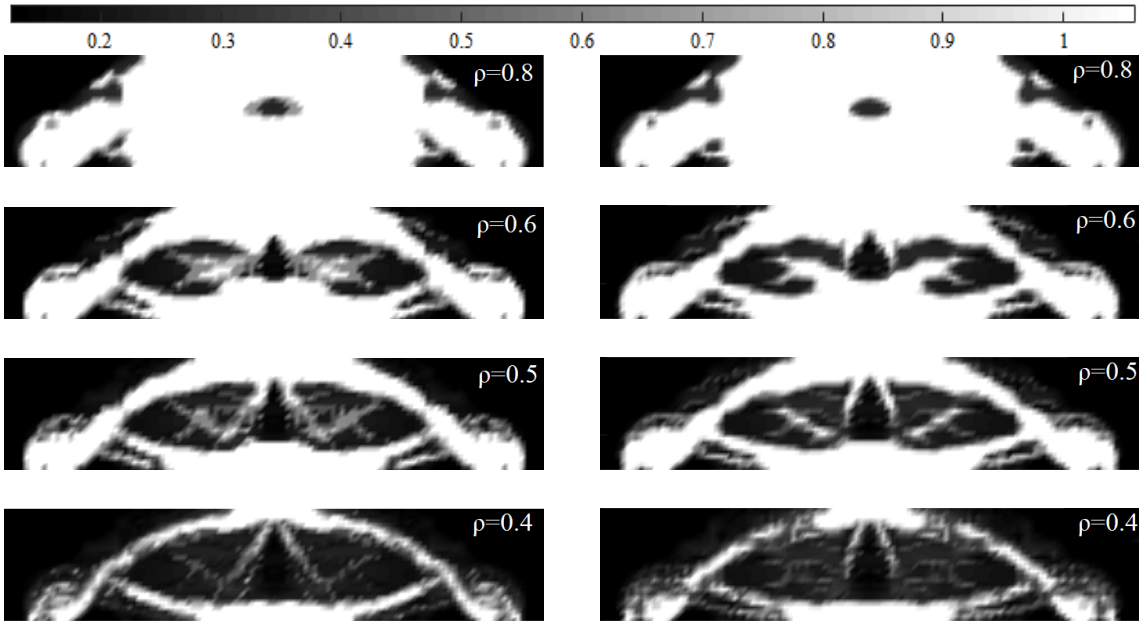


Figure 6.27: Schematic representation of a truss structure obtained with optimization techniques seen in the literature for load case 1



(a) FEM (b) NNRPIM

Figure 6.28: Density distribution obtained with the remodelling with gyroid remodelling law 1 using the FEM and the NNRPIM for the load case of Figure 6.2b

FEM

Unlike what occurred with the structural optimization analysis with a parabolic law, the structure would always present a continuous configuration allowing for it to be printed separately, that is, selecting only the higher density solid for printing. The central structure between the upper and lower arch at a density level of 0.6 g/cm^3, at a medium density, is also visible even though it is not fully connected to the arches meaning that it could represent an inefficiency. At lower density levels, this structure becomes similar to bars reinforcing the structure between the arches, being that the same problems of inter-connectivity are detected and generate inefficiencies.

NNRPIM

A similar structure to the one achieved with the FEM was obtained. It should be noted that, these results present less areas at a medium density than the FEM analysis. However the structure evolved into the same truss-like configuration and the central structure between the upper and lower arch does not fully connect to the upper arch meaning that it constitutes an inefficiency. The same evolution of the central reinforcement into bars is also verified.

Stiffness evaluation

At first sight it is immediately visible in Figure 6.29 that this remodelling evolves at a different pace than the structural optimization analysis. Here, density evolves alternating between a smaller decrease and a larger decrease. Consequently, the same sort of leaps occur for the evolution of

stiffness throughout the iterations being that for a similar density level there is an configuration with a higher and a lower density. This is amplified when looking at specific stiffness that the ratio keeps increasing and decreasing. There are no major differences in stiffness between both numerical methods. It is important to denote that for a similar density level there is always two solutions each with different stiffness values meaning that half of the possible solutions are better and correspond to the peaks in the specific stiffness plot.

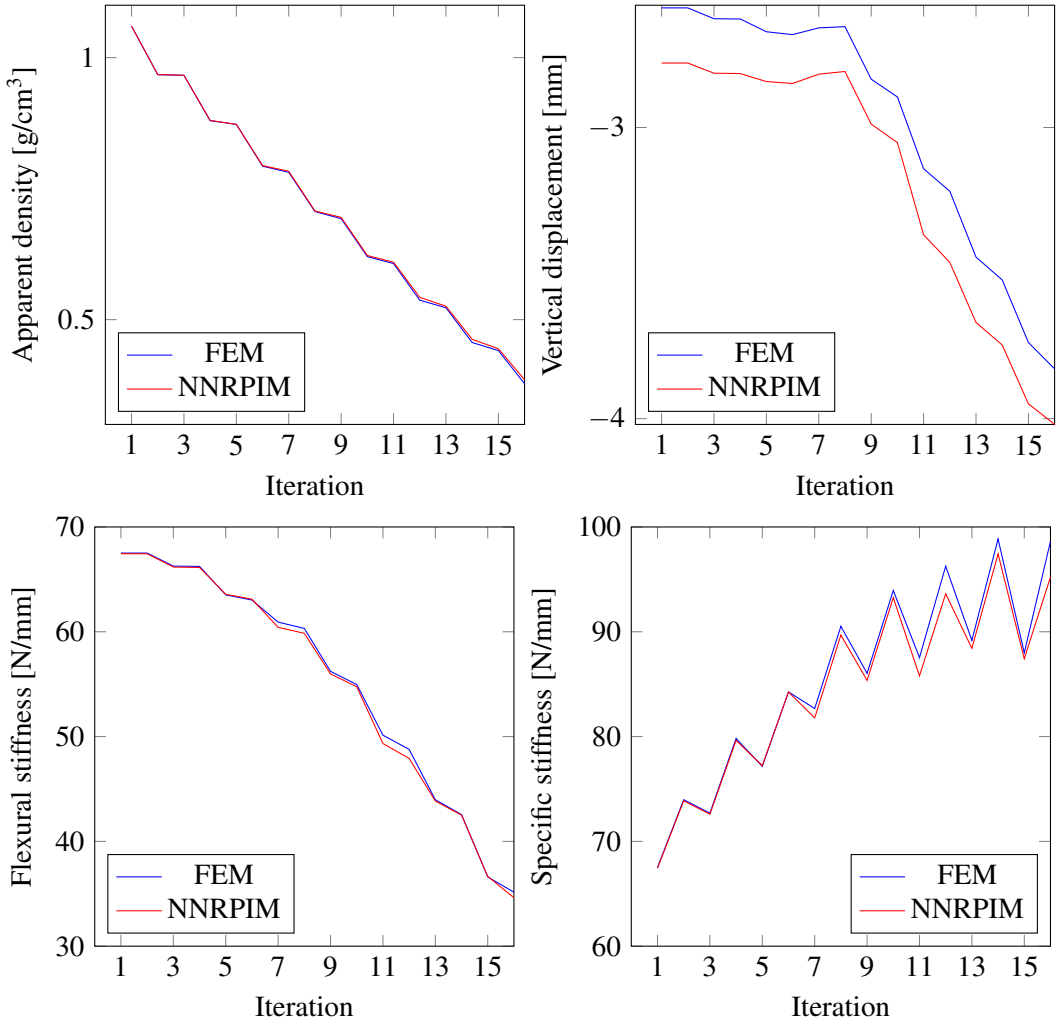
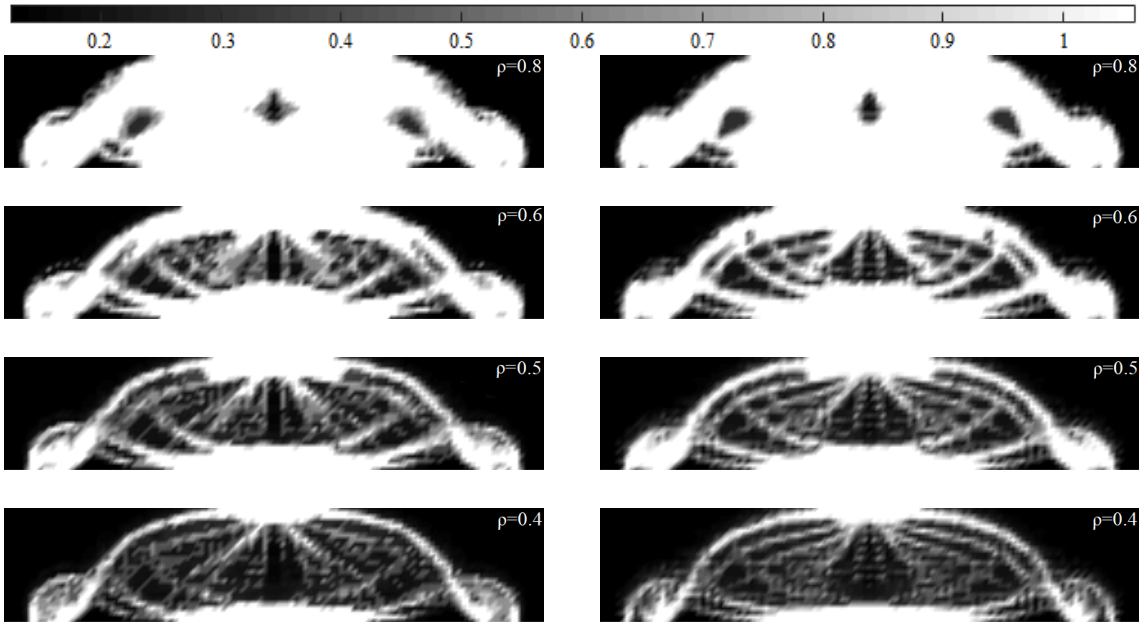


Figure 6.29: Stiffness evaluation for load case 1 with a gyroid remodelling analysis (law 1) using the FEM and the NNRPIM

Influence of remodelling parameters

These simulations have also been conducted for $\alpha = 0.00$ and $\beta = 0.05$, allowing for each point to be remodelled twice. Whereas in the FEM analysis each simulation took approximately the same amount of time per iteration, the NNRPIM analysis would consume more time for each iteration. From the previous study on structural optimization with a linear law, there is not a considerable difference in stiffness when using a lower or higher rejection ratio, being that the main difference

is the thickness of the bars of the structure - which has been seen in the literature numerous times. The results from the gyroid remodelling analysis for the FEM and NNRPIM using this new remodelling parameters are shown in Figure 6.30.



(a) FEM (b) NNRPIM

Figure 6.30: Density distribution obtained with gyroid remodelling law 1 using the FEM and the NNRPIM for the load case of Figure 6.2b with $\alpha = 0.00$, β=0.05 and a maximum number of times that a point can remodel of 2

A more defined structure was obtained using these parameters, unlike what occurred with the structural optimization where the obtained configuration was approximately the same. Whereas in the FEM there is possibly some connectivity issues between the upper and lower arches, in the NNRPIM analysis the structure is well defined and well connected. In addition, each half of the structure resembles the configuration of a Michell truss which is a common optimization result for a cantilever beam (Simonetti et al., 2019; Sokół, 2011; Yoshida, 1978).

Moreover, it is important to refer that for the asymmetrical load case of Figure 6.2c, this new set of parameters did not find a solution for the FEM, and for the load case of Figure 6.2d, the obtained structure was very similar to the structure obtained with $\alpha = 0.00$, β=0.10 only presenting a wider range of solutions and without further refining the structure. Figure 6.31 presents a comparison of the evolution of the relation between stiffness and apparent density of the structure between the two sets of remodelling parameters where it can be seen that there is no major difference between the two laws if not for a wider range of possible solutions.

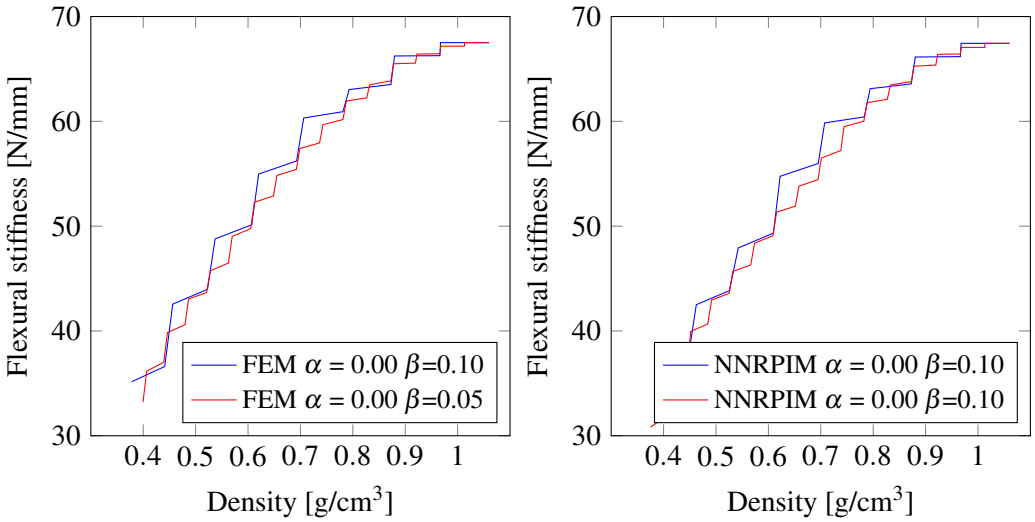
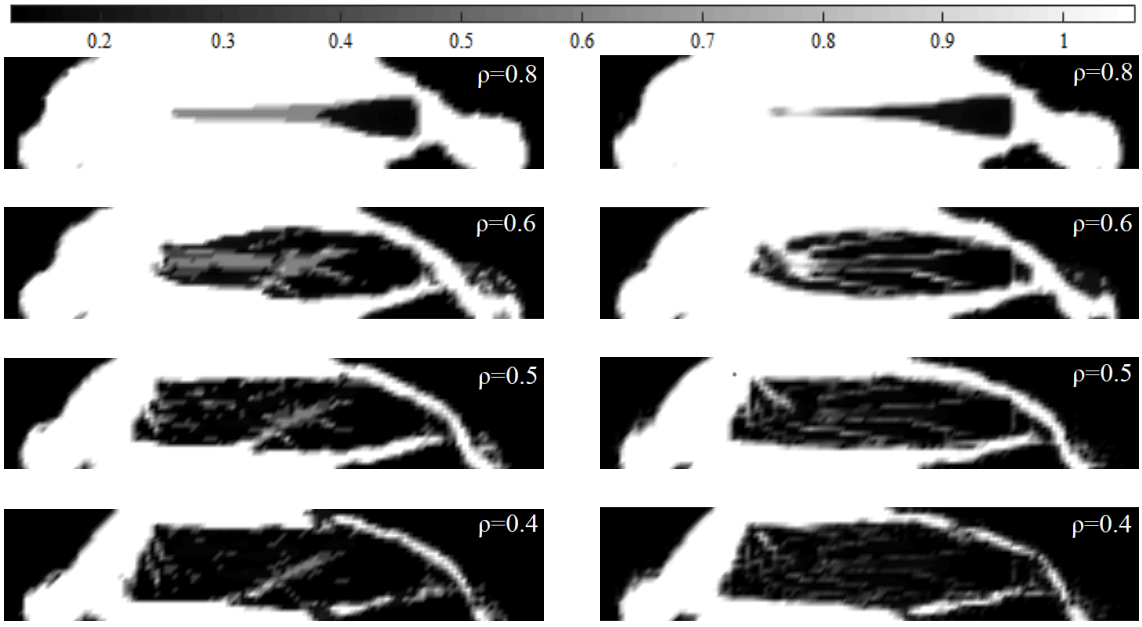


Figure 6.31: Comparison of the behaviour of different sets of remodelling parameters using the FEM and NNRPIM in load case 1 with gyroid remodelling law 1

6.5.2 Load case 2

Unlike the structural optimization analysis for the parabolic law, in this analysis, both the FEM and NNRPIM analyses obtained a continuous structure. The same parameters of Load case 1 were used (α = 0, β = 0.10), and a maximum number of times that a point can remodel of 2, both for the FEM and the NNRPIM. The structure evolved into a configuration where there is a large reinforcement near the sight of load application and an upper and lower arch which connect to the area where the part is supported on the left. Moreover, some sort of reinforcement structure appears between the upper and lower arch. The results of the evolution of the structure are shown in Figure 6.32. Once again, the FEM structures seem to present a larger number of structures at a medium density whereas the NNRPIM structure has a binary appearance and therefore more defined if the goal is to print a continuous truss structure.



(a) FEM (b) NNRPIM

Figure 6.32: Density distribution obtained with gyroid remodelling law 1 using the FEM and the NNRPIM for the load case of Figure 6.2c

FEM

It is visible that the structure separates in the lower branch at a density level of 0.5 g/cm^3. There is the presence of structures at a lower density reinforcing the whole structure between the upper and lower branch at a medium density level. Nonetheless, since there structures are not fully connected to the arches it means that these can represent an inefficiency where mass increases without any increase in stiffness.

NNRPIM

Here, it can be seen that the structure is quite similar to the one obtained with the FEM. The reinforcing structures between the upper and lower arch are more well defined than with the FEM but still seem not to be connected to the upper and lower arches.

Figure 6.33 shows the evolution results of the NNRPIM analysis when decreasing the value of β. A finer and more complex trabecular arrangement was obtained with good connectivity. The reinforcement arches present especially in the lower part of the structure also resemble the Michell truss detected in Figure 6.30.

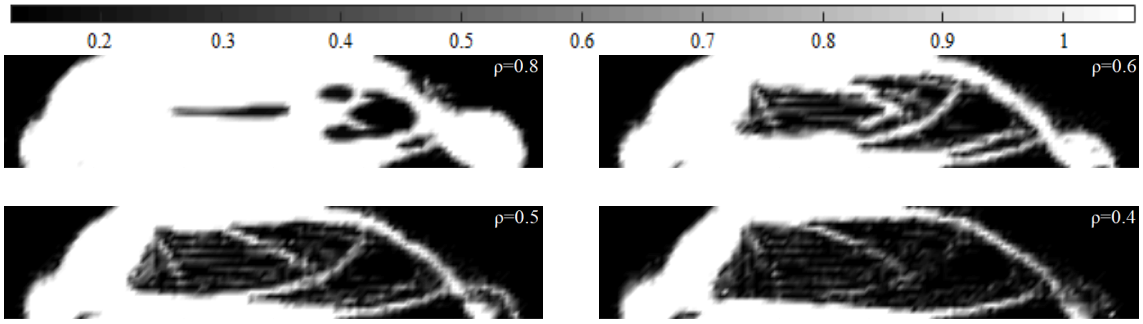


Figure 6.33: Density distribution obtained with gyroid remodelling law 1 using the NNRPIM for the load case of Figure 6.2c with $\alpha = 0.00$, $\beta = 0.05$ and a maximum number of times that a point can remodel of 2

Comparing this set of parameters with the set of parameters used for the FEM simulations ($\alpha = 0.00$ and β=0.10), the plot shown in Figure 6.34, the similarity in evolution of stiffness and density is not as similar to which was found in load case 1, being that for a lower decay rate ,β, stiffness is higher as well as presenting more possible solutions. This could be due to the reinforcement trabecular structures which were formed when using a lower β.

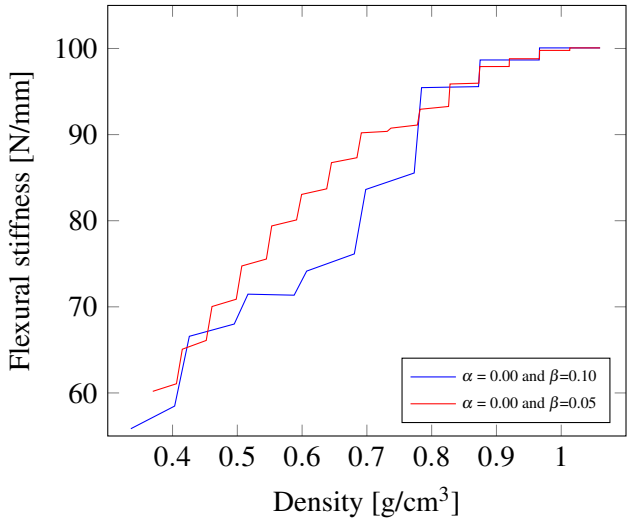


Figure 6.34: Comparison of both sets of remodelling parameters for the gyroid remodelling analysis with gyroid remodelling law 1

Stiffness evaluation

The same sort of alternating evolution seen in the results of the analyses regarding load case 1 for the same remodelling analysis is visible in Figure 6.35. The structure obtained with the NNRPIM seems to present slightly lower stiffness than the structure obtained with the FEM. Similarly, the alternating pattern "better-worst-better-worst" behaviour of the structures is seen, that is, a better solution in terms of stiffness-to-weight ratio is followed by a worse solution and so forth.

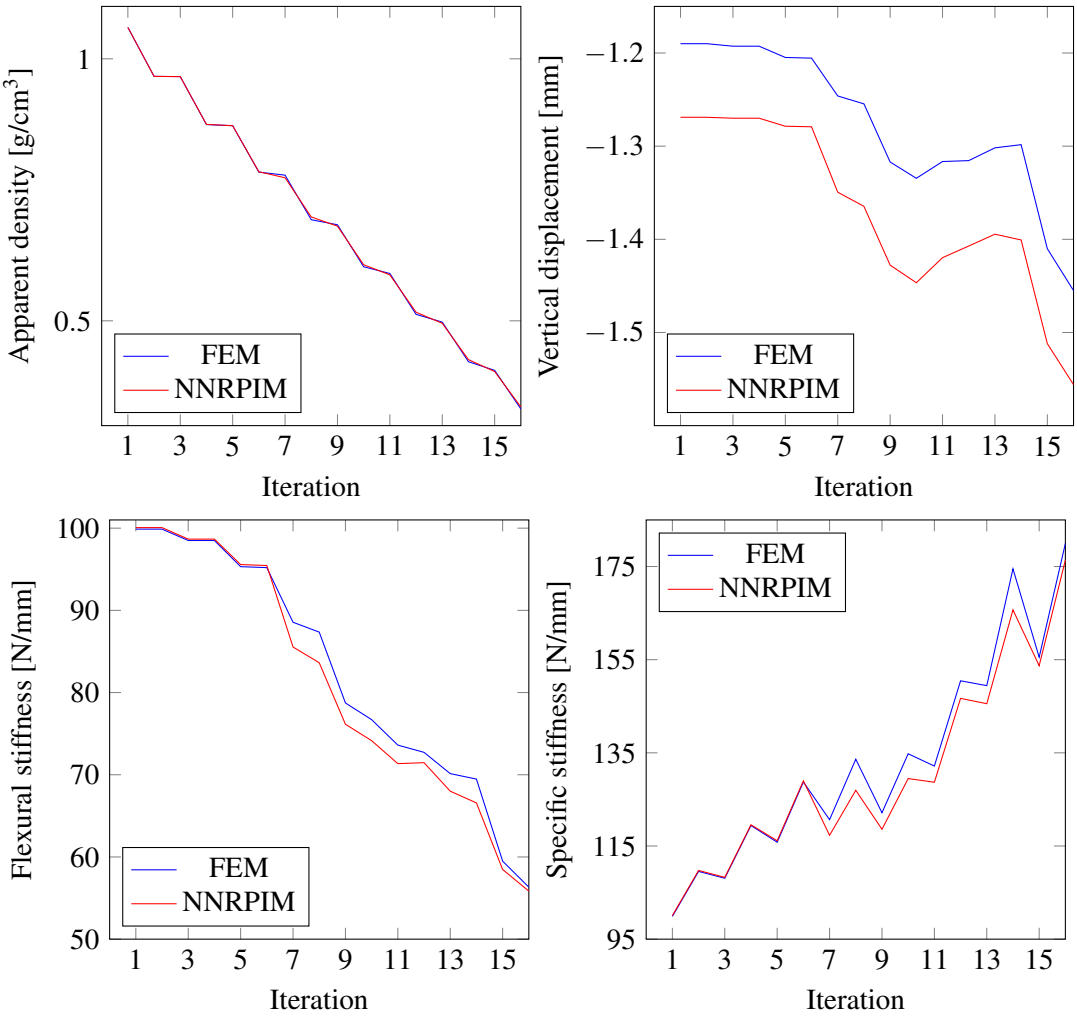
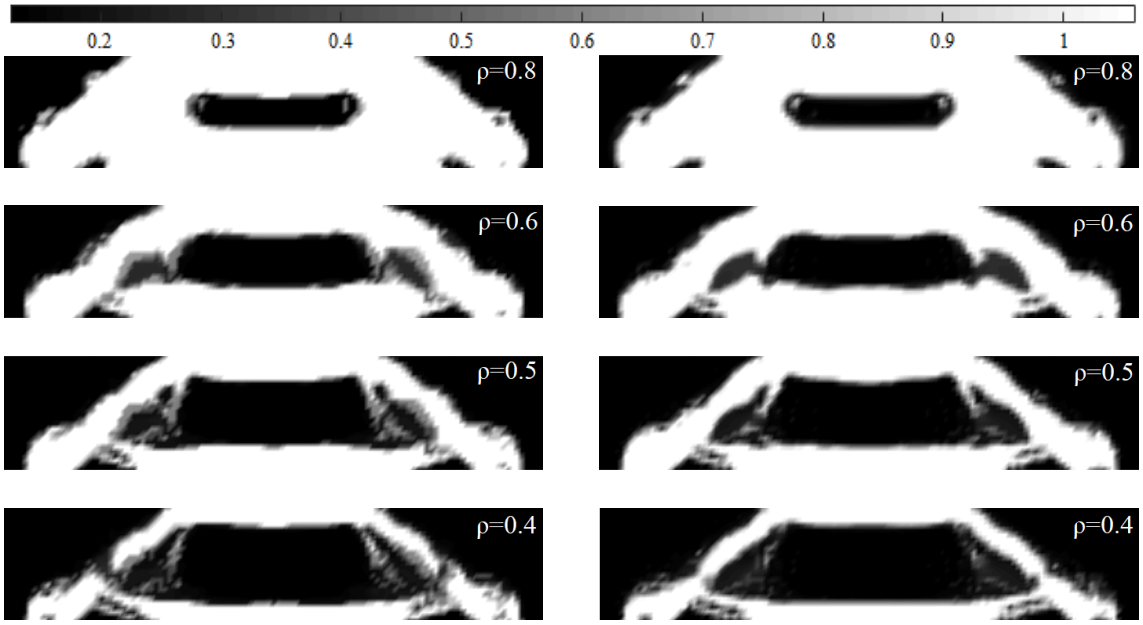


Figure 6.35: Stiffness evaluation for load case 2 with a gyroid remodelling analysis (law 1) using the FEM and the NNRPIM

6.5.3 Load case 3

For load case 3, depicted in Figure 6.2d, a more developed structure was obtained than the structure achieved with the structural optimization. The used remodelling parameters were $\alpha = 0$, $\beta = 0.10$ and the maximum number of times that a point can remodel is 2 both for the FEM analysis and the NNRPIM analysis. There are no connectivity issues to be pointed out even though the development of the structure further than the structural optimization analysis could create inefficient structures where supposed reinforcements are created which only increase mass without increasing stiffness. The structure evolution results are shown in Figure 6.36.



(a) FEM (b) NNRPIM

Figure 6.36: Density distribution obtained with gyroid remodelling law 1 using the FEM and the NNRPIM for the load case of Figure 6.2d

FEM

For the FEM analysis, even at lower density levels the structure evolves in such a way that it keeps its continuity up until a density level of 0.4 /cm^3 where the upper and lower arches split. Similarly to structural optimization analysis, a trapeze shaped truss is obtained.

NNRPIM

The structure obtained was in all similar to what was obtained with the FEM for the same remodelling law. For lower density levels, the NNRPIM structure presented higher connectivity, that is, while in the FEM the 0.4 g/cm^3 density structure split, the NNRPIM obtained a structure capable of being printed as a single solid even for a 0.4 g/cm^3 density.

Stiffness evaluation

The performance results for load case 3 using the gyroid remodelling law 1 are shown in Figure 6.37. For both the FEM and NNRPIM, there is an abrupt increase in vertical displacement from iteration 11 onward. Moreover, the same alternating pattern seen for the previous load cases is also visible here.

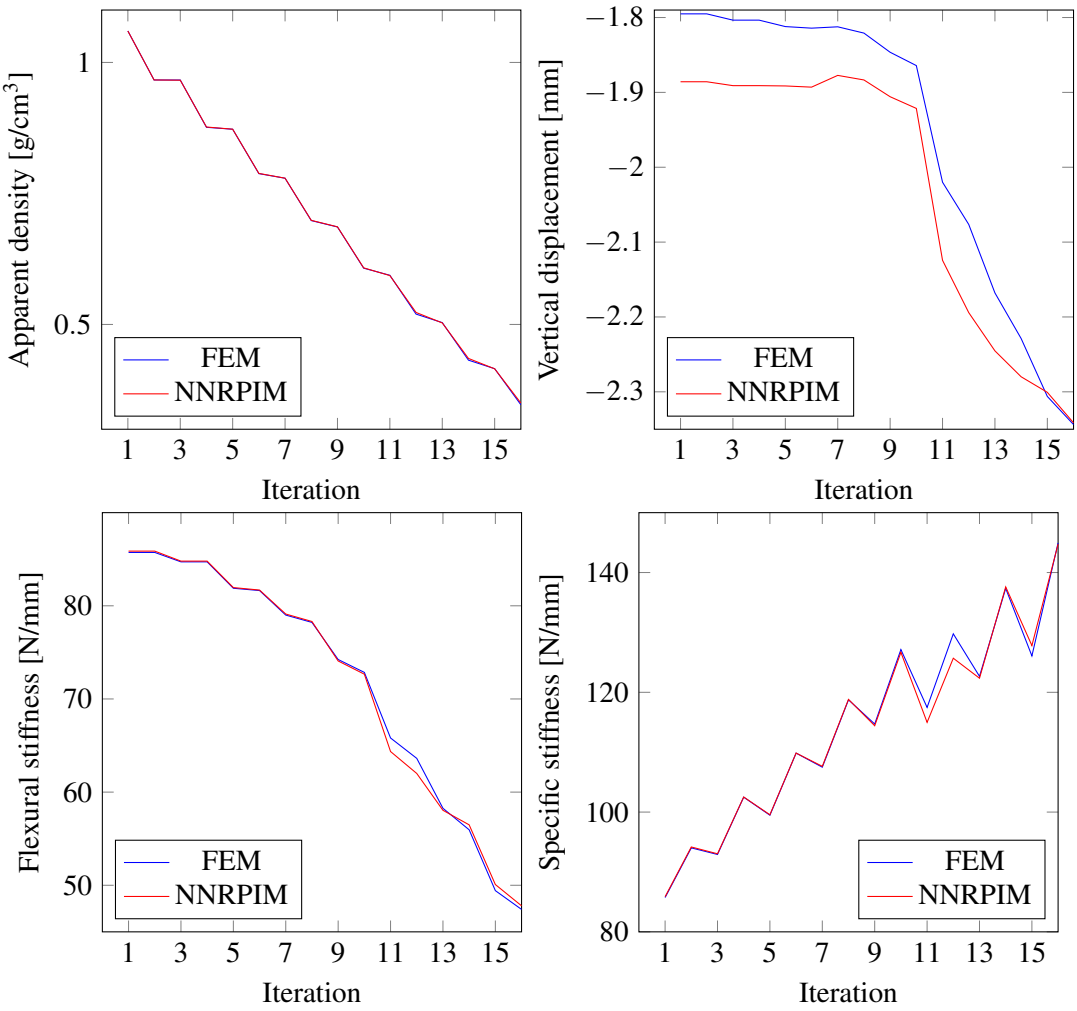
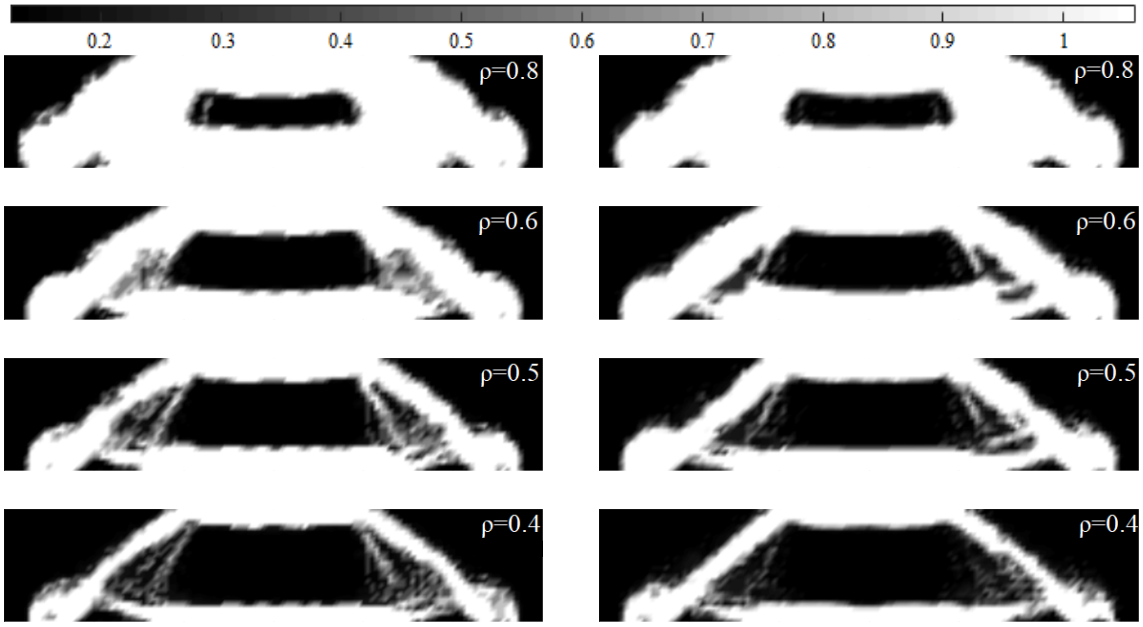


Figure 6.37: Stiffness evaluation for load case 3 with a gyroid remodelling analysis (law 1) using the FEM and the NNRPIM

Influence of remodelling parameters

Load case 3 simulations were repeated with a lower value of decay rate β. It is visible how for this load case, the solutions with a lower rejection ratio present a similar configuration being that for the NNRPIM is where the biggest similarities are found. Figure 6.38 shows the structure evolution results for this load case with a value of β of 0.05. Due to the similarities to the analysis with β = 0.10, this configuration will not be experimentally tested.



(a) FEM (b) NNRPIM

Figure 6.38: Density distribution obtained with gyroid remodelling law 1 using the FEM and the NNRPIM for the load case of Figure 6.2d with $\alpha = 0.05$, $\beta = 0.05$ and a maximum number of times that a point can remodel of 2

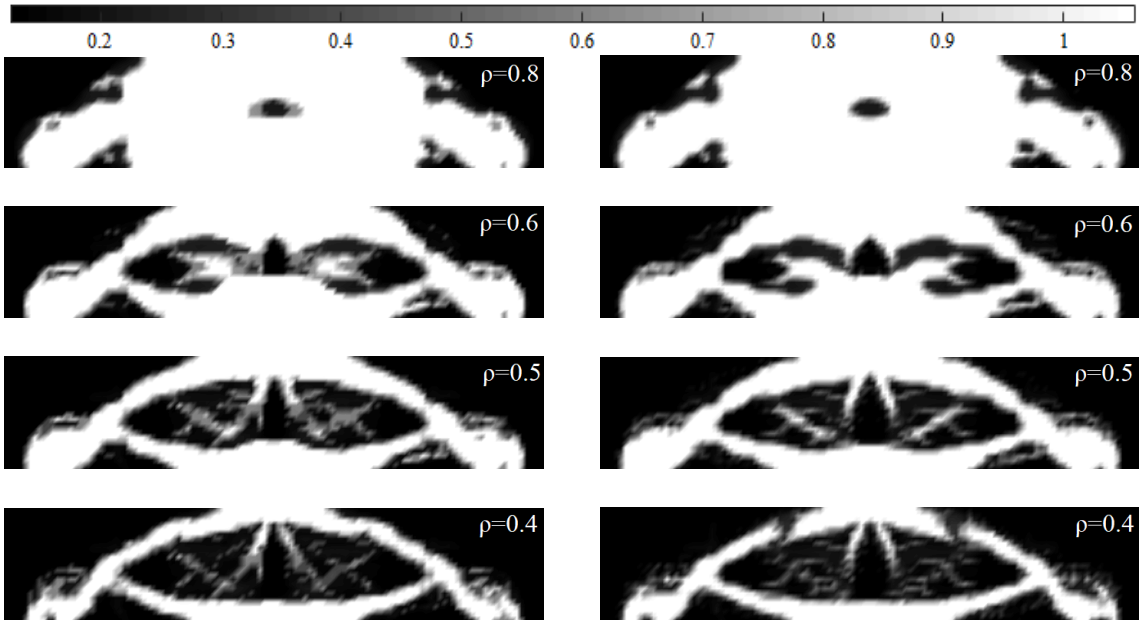
6.6 Gyroid remodelling - Law case 2

A variation of the previous gyroid law was used, maintaining the elastic modulus equation and changing the stress equation for a correlation based on experimental work using a traction/compression ratio of 0.5 for tensile tests. Comparing both equations, here, for each density, compressive stress is lower than for the previous law meaning that stiffness can be slightly lower since stress is also lower.

The remodelling parameters which were employed are the same as the ones used for the previous Gyroid Remodelling Law. The remodelling criterion was a Von-Mises equivalent stress criterion.

6.6.1 Load case 1

The remodelling parameters which were used are $\alpha = 0.00$, $\beta = 0.10$ and the maximum number of times that a point can remodel is 2. The overall structure seems quite similar to the structure obtained using gyroid remodelling law 1.



(a) FEM (b) NNRPIM

Figure 6.39: Density distribution obtained with gyroid remodelling law 2 using the FEM and the NNRPIM for the load case of Figure 6.2b

FEM

The results for Load case 1 using the FEM are shown in Figure 6.39. The central reinforcing structure between the upper and lower arch has higher density than that of load case 1 and appears to be more well connected. Nonetheless, the lack of a stronger connectivity means that this reinforcement probably constitutes an inefficiency even though this law seemed to achieve a more stable solution than law 1.

NNRPIM

The results for Load case 1 using the NNRPIM are shown in Figure 6.39. The structure is very similar to the structure which was obtained. Moreover, the connectivity of the central reinforcement seems less efficient than that of the structure obtained with the FEM analysis.

Stiffness evaluation

From the stiffness evaluation results shown in Figure 6.40 it is visible that from iteration 9, stiffness stars decreasing more abruptly and the same pattern of alternating between a smaller and a larger decrease in density and stiffness from the previous gyroid remodelling law can also be verified. This was expected due to the similarities in both laws. There is not a great difference in stiffness between the FEM and NNRPIM.

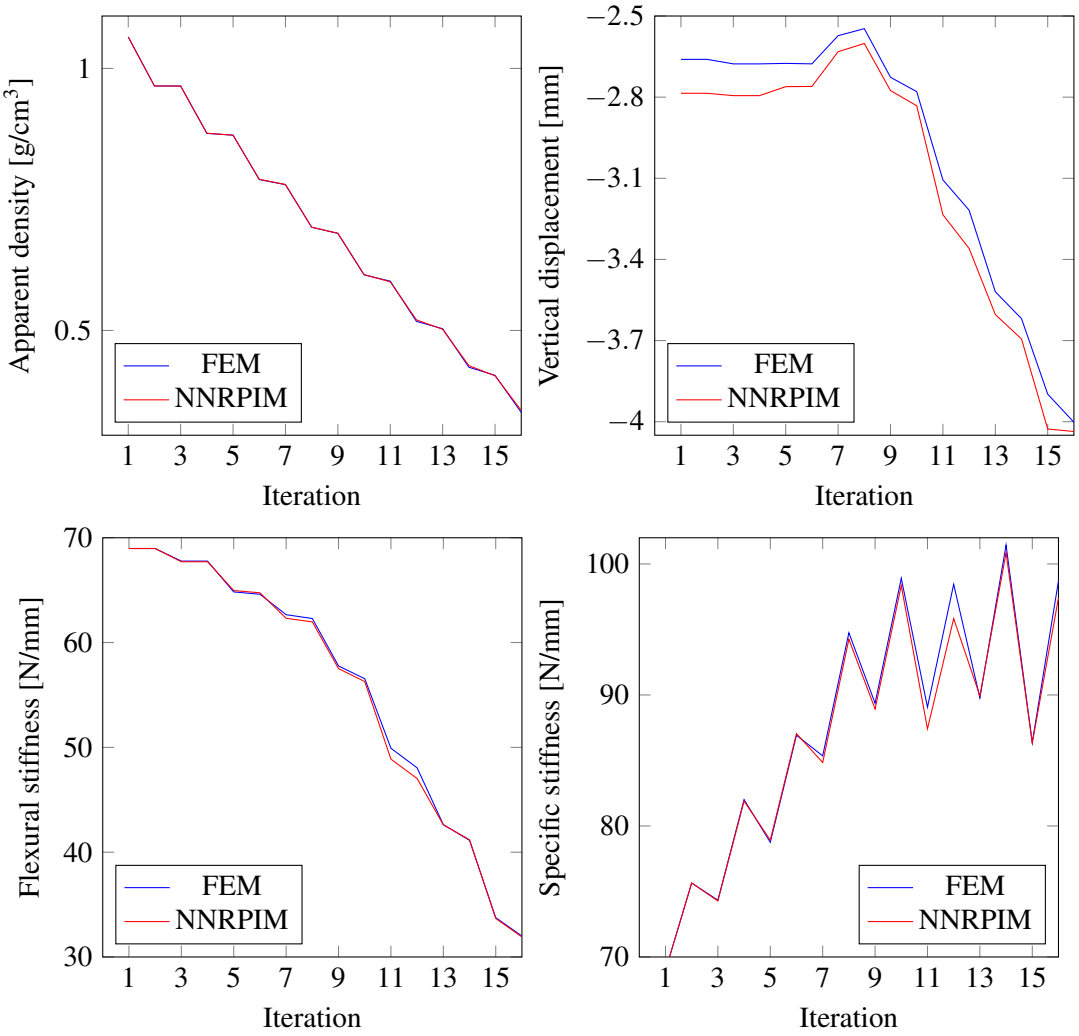
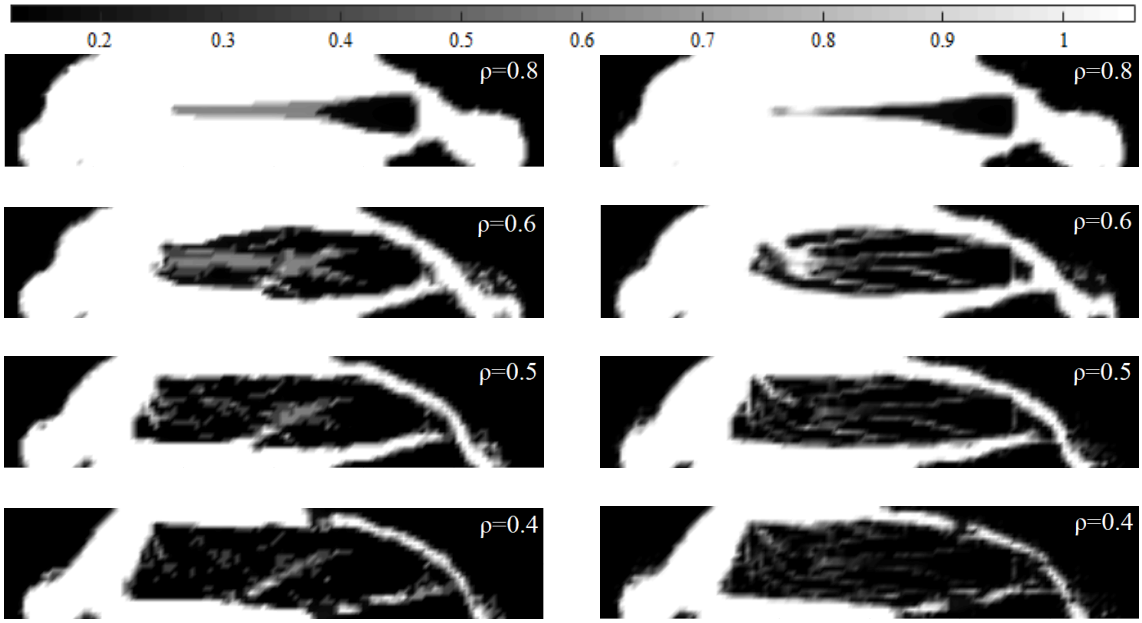


Figure 6.40: Stiffness evaluation for load case 1 obtained with a gyroid remodelling analysis (law 2) using the FEM and the NNRPIM

6.6.2 Load case 2

The remodelling parameters which were used both for the FEM and NNRPIM are $\alpha = 0$, $\beta = 0.1$ and the maximum number of times that a point can remodel was defined as 2. For both methods, the obtained structure was very similar to the equivalent structure for the gyroid remodelling law 1, presenting the same type or reinforcement at the center of the structure.



(a) FEM (b) NNRPIM

Figure 6.41: Density distribution obtained with gyroid remodelling law 2 for FEM and NNRPIM for the load case of Figure 6.2c

FEM

The obtained structures (Figure 6.41) are very similar to those referent to the gyroid remodelling law 1 where the same type of reinforcement is visible. The same remarks made previously apply here.

NNRPIM

Similarities with Figure 6.41 can be seen. The same type of reinforcing structures between the upper and lower arch can be seen as well.

Stiffness evaluation

The stiffness evaluation results are shown in Figure 6.42. The same abrupt decreases in stiffness at iterations 8 and 14 which were seen in Figure 6.35 are visible as well as the fact of the NNRPIM presenting slightly lower stiffness.

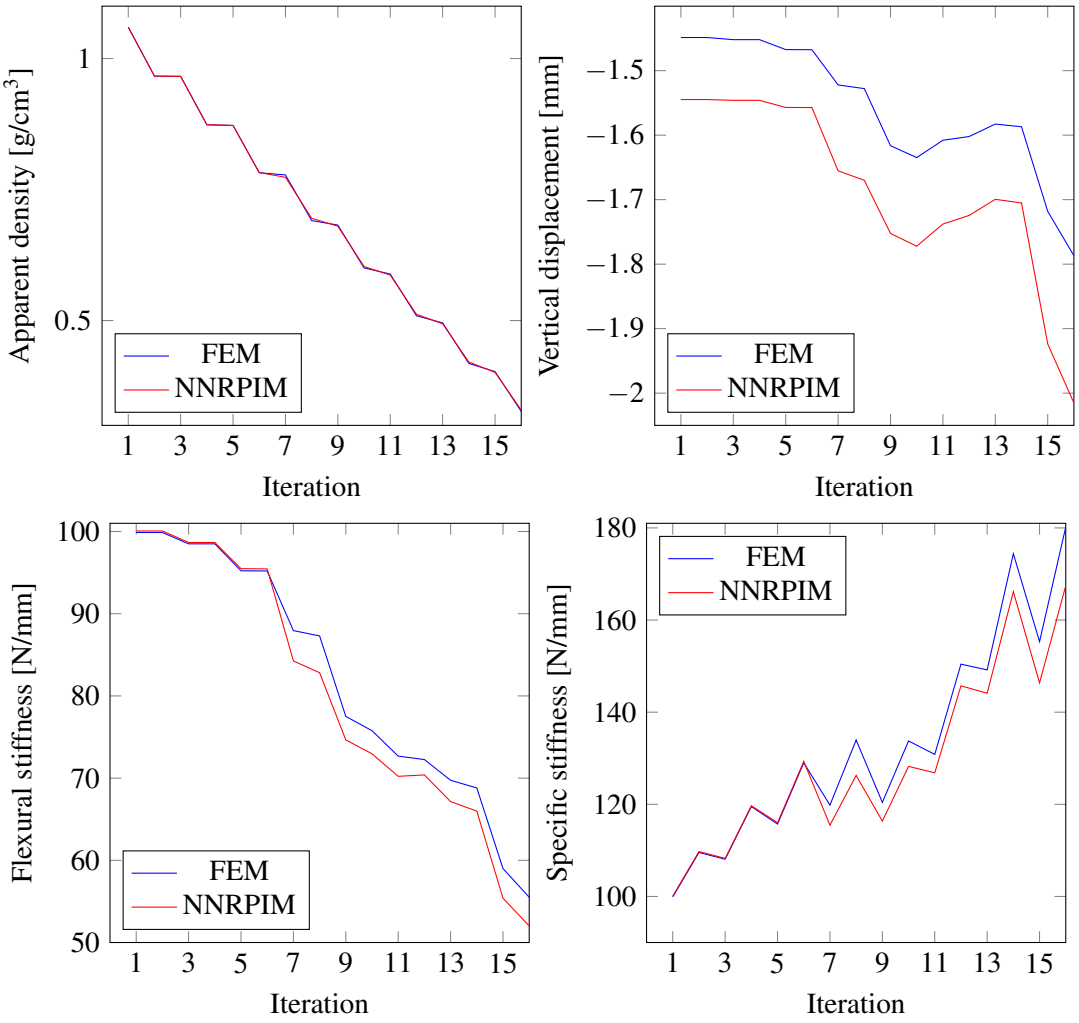
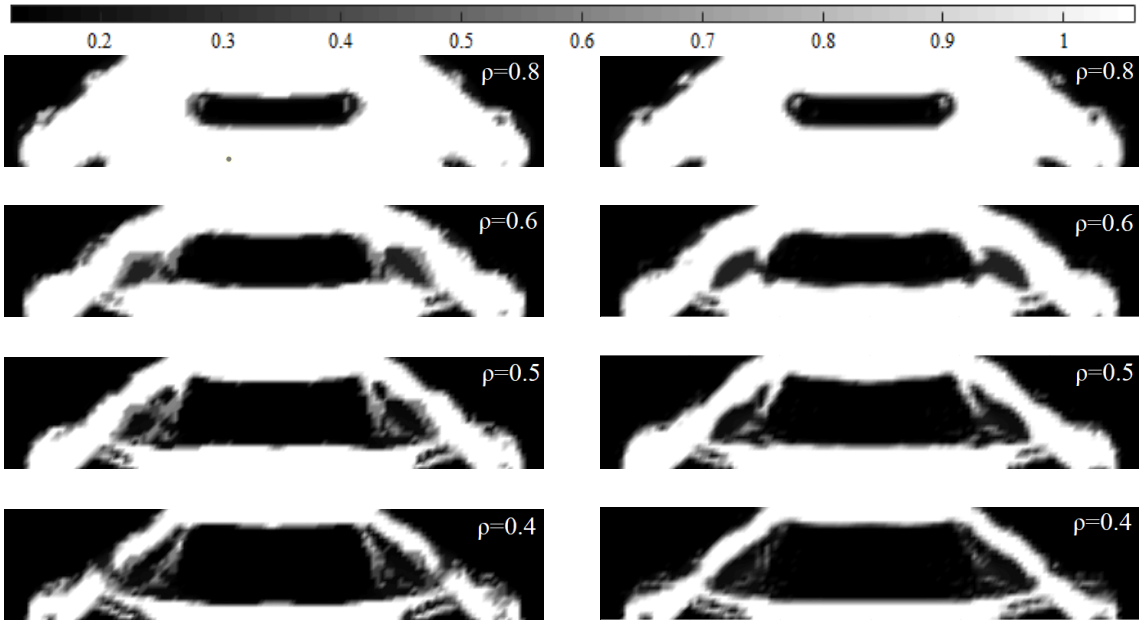


Figure 6.42: Stiffness evaluation for load case 2 obtained with a gyroid remodelling analysis (law 2) using the FEM and the NNRPIM

6.6.3 Load case 3

These results, shown in Figure 6.43, are in all similar to the results obtained with the gyroid remodelling law 1 both for the FEM and NNRPIM.



(a) FEM (b) NNRPIM

Figure 6.43: Density distribution obtained with gyroid remodelling law 2 for FEM and NNRPIM for the load case of Figure 6.2d

FEM

The same remarks made for gyroid remodelling law 1 are applicable here for the FEM analysis.

NNRPIM

The same remarks made for gyroid remodelling law 1 are applicable here for the NNRPIM analysis.

Stiffness evaluation

The same type of evolution observed for this load case with the gyroid remodelling law 1 are seen for the gyroid remodelling law 2. Results are displayed in Figure 6.44.

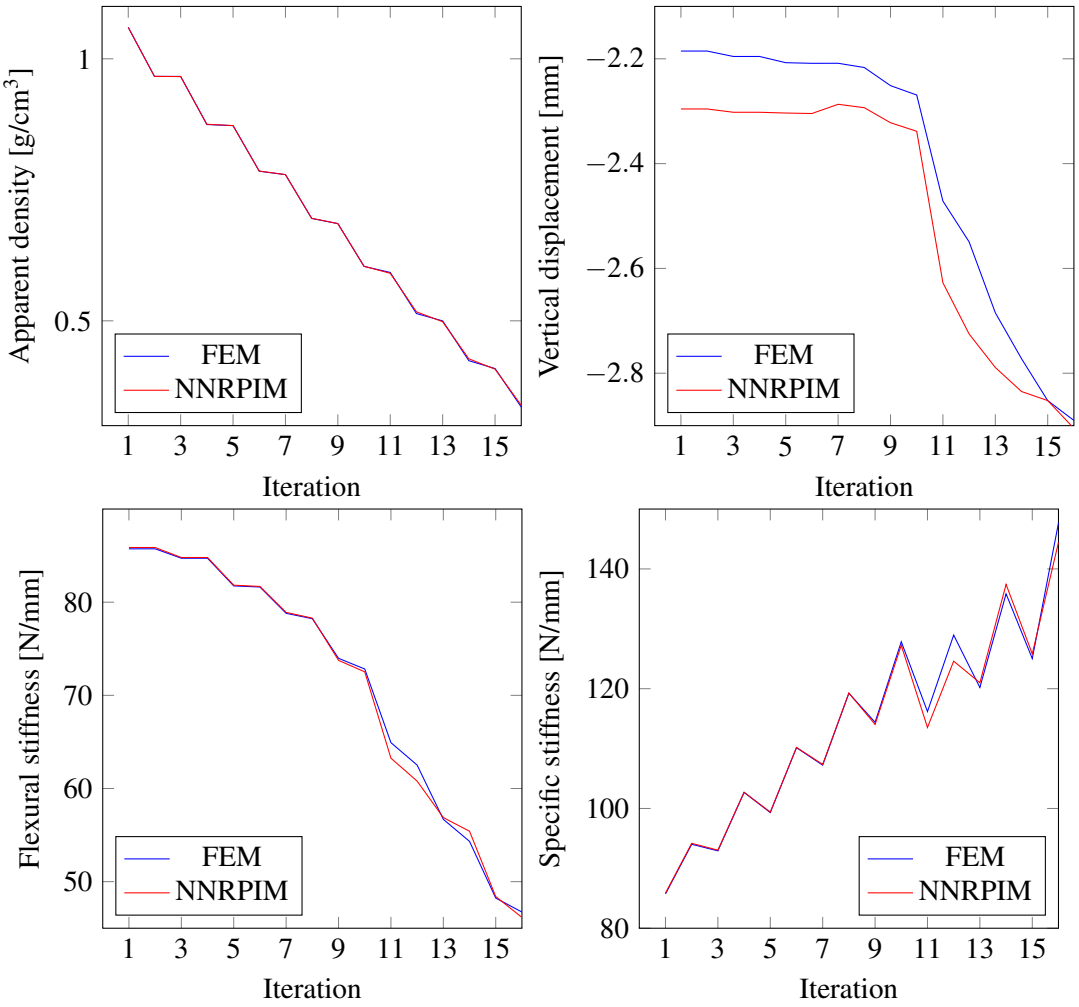


Figure 6.44: Stiffness evaluation for load case 3 obtained with a gyroid remodelling analysis (law 2) using the FEM and the NNRPIM

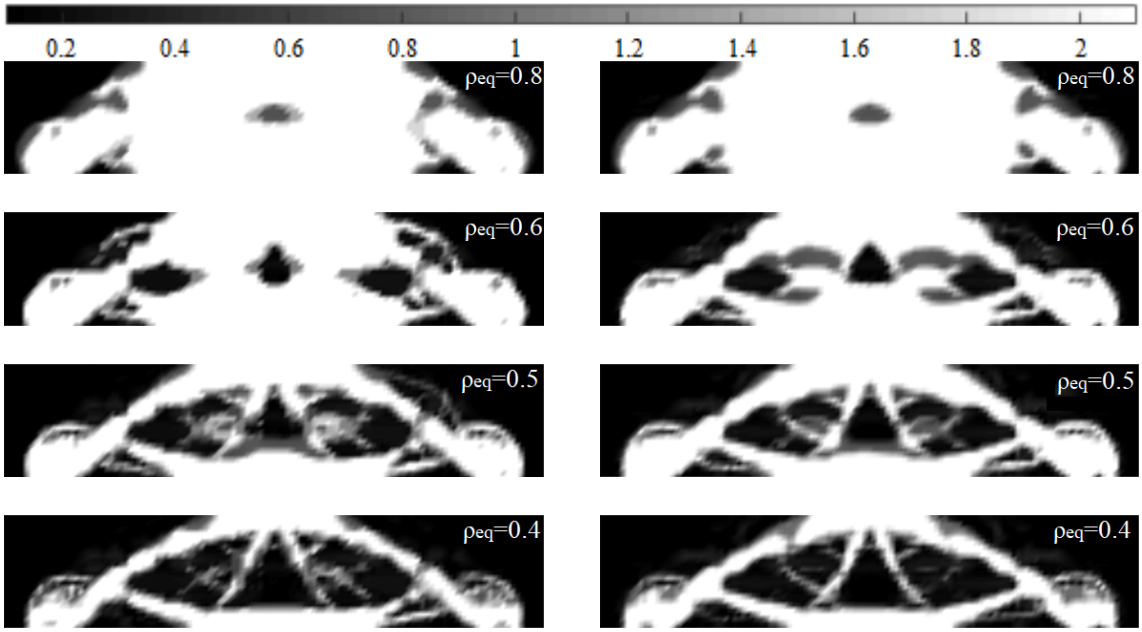
6.7 Bone remodelling

In order to attest the validity of the gyroid law remodelling results for application in bone scaffold, these structures are now compared with structures for the same load case with a bone remodelling law. Density and stiffness values are not comparable even though some proportionality can be defined as maximum bone density is about the double of PLA density. This means that the apparent density of the PLA equivalent structure can be extrapolated by dividing bone density by two. Here, differences between the FEM and NNRPIM are more visible than with the gyroid material laws since the NNRPIM will present a greater number of structures at a medium density. Nonetheless, the same kind of trabecular arrangement is somewhat achieved. For load case 1 it is visible how the NNRPIM achieves a much more well defined structure. For load case 2, the NNRPIM simulation achieved the same type of reinforcement structures between the upper and lower arch, while the FEM simulation achieved a more effective result with the bone remodellinhg.

Remodelling results for load case 1, 2 and 3 are shown in Figures 6.45, 6.46 and 6.47 respectively.

The same remodelling parameters were used ($\alpha = 0.00$, $\beta = 0.10$, maximum number of times that a point can remodel of 2) as well as using a Von-Mises remodelling criterion.

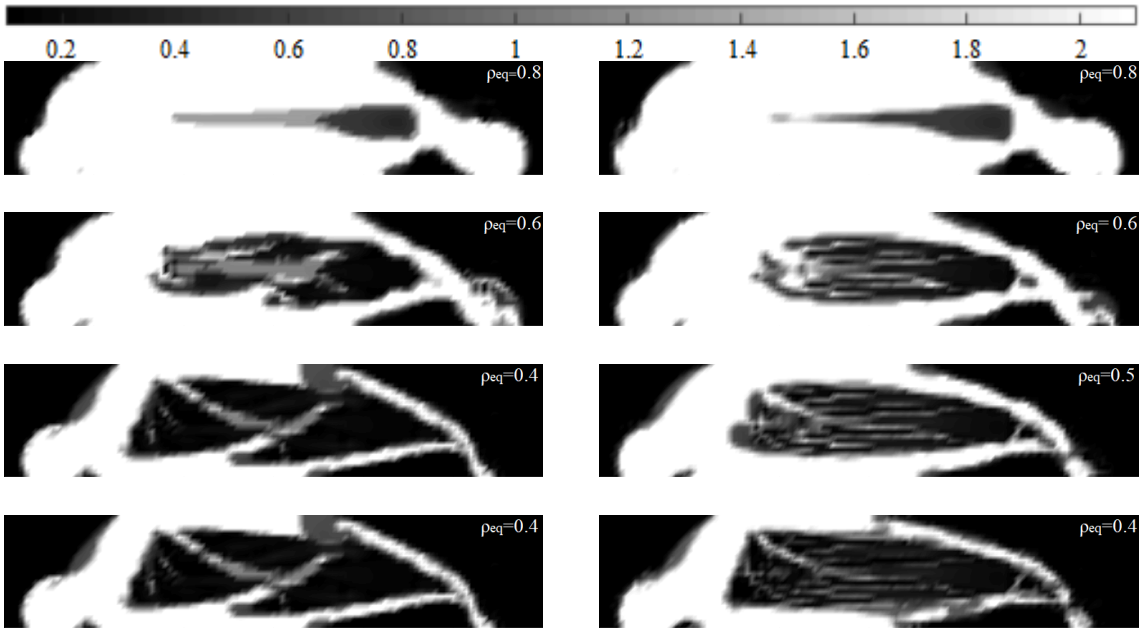
Load case 1



(a) FEM (b) NNRPIM

Figure 6.45: Density distribution obtained with the bone remodelling analysis using the FEM and NNRPIM for the load case of Figure 6.2b with $\alpha = 0.00$, β=0.10 and a maximum number of times that a point can remodel of 2

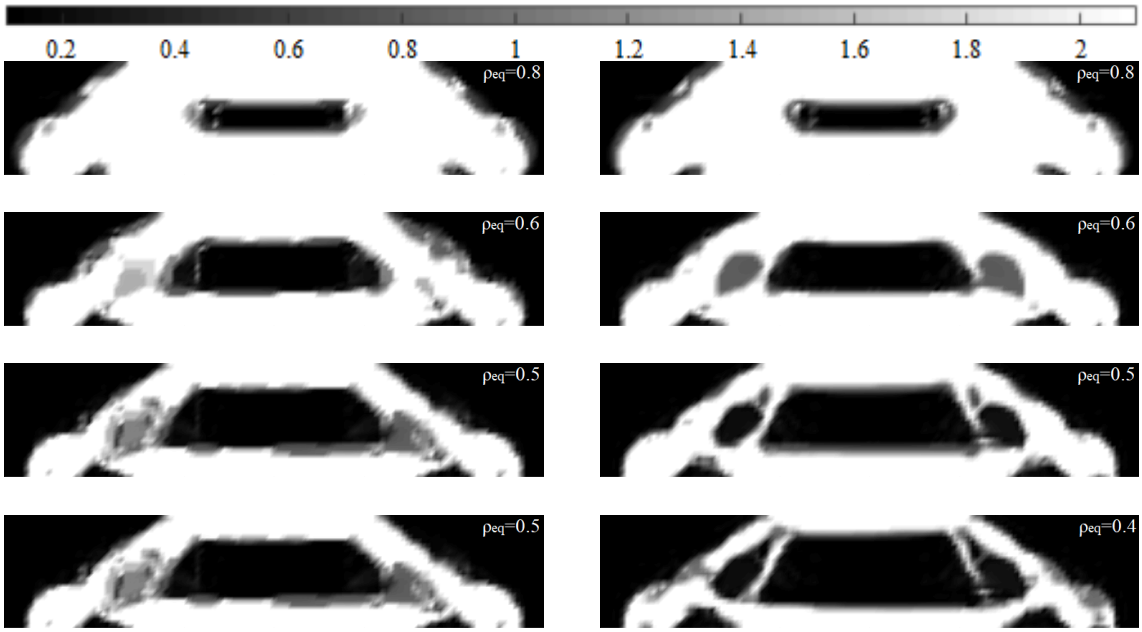
Load case 2



(a) FEM (b) NNRPIM

Figure 6.46: Density distribution obtained with the bone remodelling analysis using the FEM and NNRPIM for the load case of Figure 6.2c with $\alpha = 0.00$, β=0.10 and a maximum number of times that a point can remodel of 2

Load case 3



(a) FEM (b) NNRPIM

Figure 6.47: Density distribution obtained with the bone remodelling analysis using the FEM and NNRPIM for the load case of Figure 6.2d with $\alpha = 0.00$, β=0.10 and a maximum number of times that a point can remodel of 2

6.8 Computational effort

It is relevant to point out the computational time of these analyses. Each iteration took around 7 minutes to compute, meaning that on average, 140 minutes were required for one analysis on a computer equipped with a Intel Pentium i7 processor running at 3.4 GHz. Moreover, on average each FEM analysis would create a 300Mb comprised file and each NNRPIM analysis, due to a larger number of integration points, created a 1Gb file. This amounted to a total simulation time of 150 hours and a total size of 20Gb, regarding all analyses mentioned in this chapter.

For the analysis with a lower rejection ratio (RR or β), a larger number of iterations increased heavily the time spent computing as well as it was aforementioned, for the NNRPIM analysis, each iteration would take a longer time than the previous iteration.

6.9 Result discussion

Comparing the remodelling results it is clear that structural optimization will not predict the behaviour of the 3D printed structure as well as the gyroid remodelling, starting with the fact that predicted stiffness with the structural optimization is much higher since the elastic modulus and yield stress for the material law are those of the bulk material and more applicable to other manufacturing process such as injection molding. Nonetheless, even if stiffness prediction is poor, the

proposed structure configuration could still present better results than the gyroid remodelling laws. Two material laws for structural optimization were tested, a parabolic law with a transition density of 0.3 g/cm^3 (in order to allow for a defined structure to appear at a density level of 0.5 g/cm^3 and under), and a linear law. While many inter-connectivity problems were detected with the parabolic law and overall inefficiency of the structures, when the linear material law was employed, those problems seemed to be resolved, or, at least, minimized. For load case 2 however, connectivity issues were found for both load cases where the main body on the left size of the structure separated from the area on the right size of the structure, meaning that, without any reinforcement, these structures could not be materialized for experimental validation. More should be added that, when studying the influence of the evolutionary parameters, namely, rejection ratio RR (or density decrease ratio), that the structure configuration remained similar, differing only in thickness of the structure, where a higher rejection ratio presents thicker bars and a lower rejection ratio presents thinner bars.

Regarding the gyroid infill optimization analysis, both gyroid remodelling laws being tested presented almost similar results for load cases 2 and 3 being that load case 1 presented some slight differences. This means that the approximation for a traction/compression ratio of 0.5 which was used in order to predict the compressive behaviour from tensile tests constitutes a valid assumption. The conclusion about which law more accurately describes the gyroid behaviour can only be obtained with experimental testing. In addition, these remodelling analysis converged into well known truss-like structures present in the literature. These structures become more well defined when decreasing the density decrease ratio parameters, β. When a β value of 0.05 instead of 0.10 was used, especially with the NNRPIM analysis, a well defined Michell truss-like structure was obtained, however, presenting a much more significant computational cost.

Regarding the similarities between the gyroid remodelling laws and bone remodelling law, for equivalent volume fractions, both laws present similar structure configurations, especially when conducting a NNRPIM analysis.

Finally, for all analyses, there are differences in structure configuration for both methods, being that for load case 3 these are less prominent for the structural optimization analysis.

Chapter 7

Experimental Study

This section presents the results of the experimental tests which were conducted to the specimens based on the numerical simulations, corresponding to Stage 5 of the methodology shown in Figure 5.1, more specifically, procedure step 9 of the list which was presented in Chapter 5. The experimental results were compared to the numerical simulation results in terms of stiffness.

7.1 Printed specimens

To each conducted simulation, some smoothing functions are applied and the specimens are printed. Regarding the smoothing types, the first printed specimens revealed that the difference between Smoothing Type 1 and Smoothing Type 2 was not very visible and for that reason, due to time constraints, Smoothing Type 2 specimens were not printed. In addition, also due to time constraints, a "full factorial" was substituted by a "reduced factorial", that is, the effect of each Smoothing Type will be tested for some simulations and extrapolated for other simulations. Tables 7.1, 7.2, 7.3 and 7.4 show the number of specimens printed for each load case/method/smoothing combination, namely for: structural optimization with a parabolic law and linear law, gyroid remodelling law 1 and gyroid remodelling law 2.

Regarding the influence of printing direction, some of the specimens corresponding to smoothing type 1 with a maximum distance ratio of 0.1 were printed also vertically according to the scheme in Figure 7.1. It is expected that vertically printed specimens present better mechanical properties (Afonso, 2019).

The total amount of specimens summed up to 252 corresponding to nearly 400h of printing. Wear of the machine as well as slight environmental variations that may occur are not considered since the environment was made to be as stable as possible in terms of temperature and humidity. Moreover, the FFF equipment was placed in a rigid surface to minimize any vibration.

Figures 7.2, 7.3, and 7.4 show a representative specimen configuration for each load case/smoothing function combination where the geometry maintenance is visible.

Table 7.1: Printed specimens for the Structural Optimization analysis with a parabolic material law

Method	Load case	Smoothing type	Number of specimens
FEM	1	No smoothing	3
		Type 1 MDR 0.1	3 + 3 vertical
		Type 1 MDR 0.2	3
		Type 3	3
NNRPIM	1	No smoothing	3
		Type 1 MDR 0.1	3 + 3 vertical
		Type 1 MDR 0.2	3
		Type 3	3
FEM	2	Type 1 MDR 0.1	3 + 3 vertical
		Type 1 MDR 0.2	3
		Type 3	3
NNRPIM	2	Type 1 MDR 0.1	3 + 3 vertical
		Type 1 MDR 0.2	3
		Type 3	3
FEM	3	No smoothing	3
		Type 1 MDR 0.1	3 + 3 vertical
		Type 1 MDR 0.2	3
		Type 3	3
NNRPIM	3	No smoothing	3
		Type 1 MDR 0.1	3 + 3 vertical
		Type 1 MDR 0.2	3
		Type 3	3

Table 7.2: Printed specimens for the analysis of structural optimization with a linear material law

Method	Load case	Smoothing type	Number of specimens
FEM	1	No smoothing	3
	1	Type 1 MDR 0.1	3
NNRPIM	1	No smoothing	3
	1	Type 1 MDR 0.1	3
FEM	2	No smoothing	3
	2	Type 1 MDR 0.1	3
NNRPIM	2	No smoothing	3
	2	Type 1 MDR 0.1	3
FEM	3	No smoothing	3
	3	Type 1 MDR 0.1	3
NNRPIM	3	No smoothing	3
	3	Type 1 MDR 0.1	3

Table 7.3: Printed specimens for the Gyroid Remodelling analysis with law 1

Method	Load case	Smoothing type	Number of specimens
FEM	1	No smoothing	3 + 3 $\rightarrow \beta = 0.05$
		Type 1 MDR 0.1	3 + 3 vertical
		Type 1 MDR 0.2	3
		Type 3	3
NNRPIM	1	No smoothing	3 + 6 $\rightarrow \beta = 0.05$
		Type 1 MDR 0.1	3 + 3 vertical
		Type 1 MDR 0.2	3
		Type 3	3
FEM	2	No smoothing	3
		Type 1 MDR 0.1	3 + 3 vertical
		Type 1 MDR 0.2	3
		Type 3	3
NNRPIM	2	No smoothing	3
		Type 1 MDR 0.1	3 + 3 vertical
		Type 1 MDR 0.2	3
		Type 3	3
FEM	3	No smoothing	3
		Type 1 MDR 0.1	3 + 3 vertical
		Type 1 MDR 0.2	3
		Type 3	3
NNRPIM	3	No smoothing	3
		Type 1 MDR 0.1	3 + 3 vertical
		Type 1 MDR 0.2	3
		Type 3	3

Table 7.4: Printed specimens for the Gyroid Remodelling analysis with law 2

Method	Load case	Smoothing type	Number of specimens
FEM	1	No smoothing Type 1 MDR 0.1	3 3
NNRPIM	1	No smoothing Type 1 MDR 0.1	3 3
FEM	2	No smoothing Type 1 MDR 0.1	3 3
NNRPIM	2	No smoothing Type 1 MDR 0.1	3 3
FEM	3	No smoothing Type 1 MDR 0.1	3 3
NNRPIM	3	No smoothing Type 1 MDR 0.1	3 3

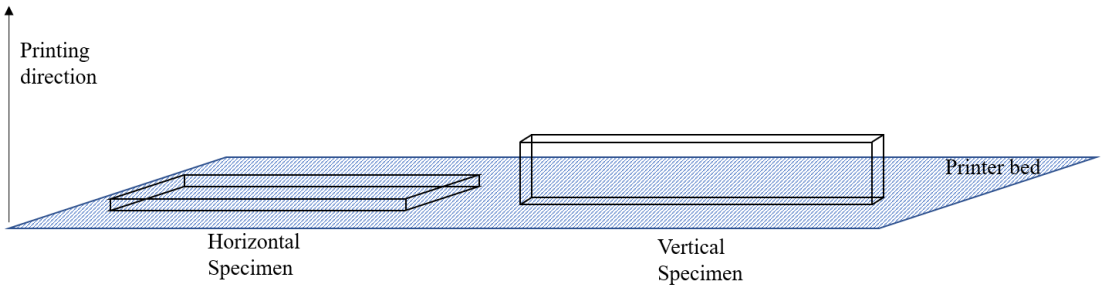


Figure 7.1: Schematic representation of printing direction and respective placement of parts on the printing bed

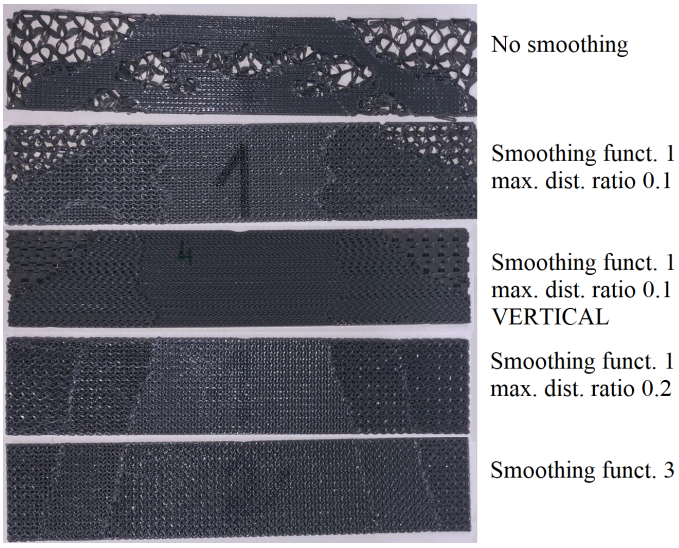


Figure 7.2: Printed specimens example - Load case 1

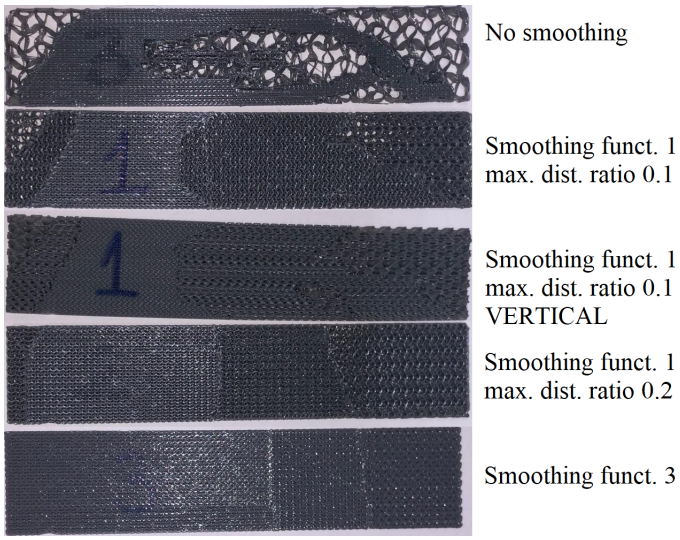


Figure 7.3: Printed specimens example - Load case 2

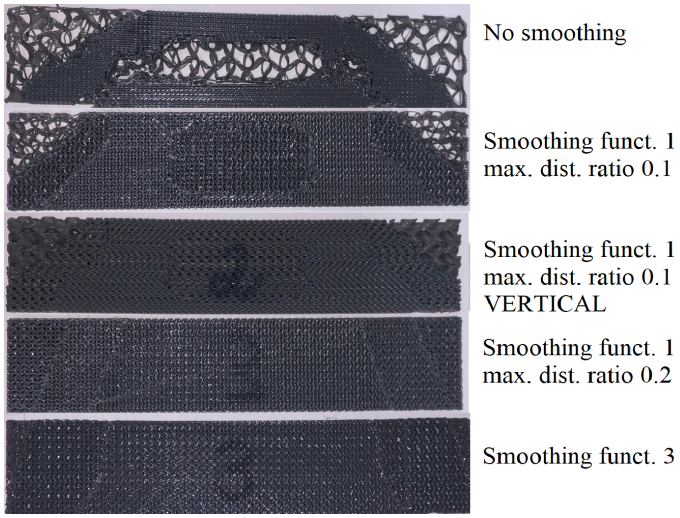


Figure 7.4: Printed specimens example - Load case 3

This information regarding specimen configuration is available, with more detail in Appendix C, where a specimen from each load case/method/material law/smoothing function combination printed and tested is shown. For logistic reasons, these images are relative to the already tested specimens, and for that reason, some may appear heavily deformed or fractured.

7.2 Common issues

Poor layer adhesion and layer delamination is the biggest challenge of materials obtained through FFF (Dizon et al., 2018). These specimens present the particularity of being printed without top or bottom layer as well as no perimeters. This means that the surface area in contact with the heated surface is much lower than that which would be if a bottom layer or *raft* is used. Therefore,

adhesion problems were quite common especially in the specimens without any smoothing applied as the geometry is much more intricate and complex. The main problems being detected were an uneven first layer and warping - Figure 7.5.



(a) Uneven first layer (b) Warping

Figure 7.5: Common defects in printed parts due to bad adhesion of the first layer to the building surface

Due to these defects, which might not be immediately visible, there is often dimensional variation within the same specimen and between specimens. This is caused both by the complexity of the geometry and the simplicity of the equipment which is used.

Frequency of small defects was quite elevated and therefore, acceptance criteria had to be defined so as to avoid excessive *re-printing* of parts. Every specimen passed through visual inspection to check for any of these defects and if present, to decide whether these are acceptable. An acceptable defect was considered to be any defect occurring in the area left of where the left support is placed and/or right to the area where the right support is placed. This means that, if small defects occur in areas which do not suffer any loading, that the specimen would be considered acceptable for experimental testing.

7.3 Necessary accessories for testing

The available testing machine already presented all the accessories for load cases 1 and 2. However, for load case 3 it was necessary to build another tool which is shown in Figure 7.6. In addition to this, it was necessary to build a support so as to avoid tumbling while testing. This support is also to be printed in FFF with PLA as its only function does not require strength (Figure 7.7). Moreover, a positioning tool was printed in order to easily guarantee that the specimen is placed symmetrically with regard to positioning of the supports (Figure 7.8). All technical drawings are annexed in Appendix.

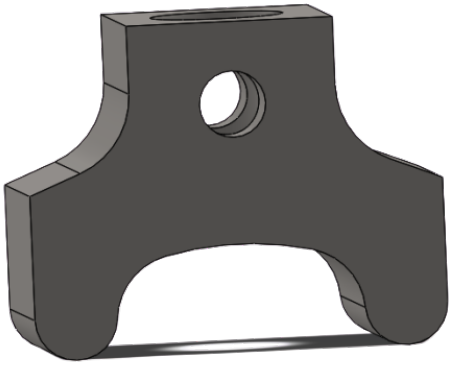


Figure 7.6: Four point bending tool - technical drawing in Annex B

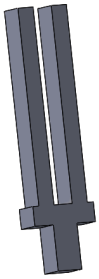


Figure 7.7: Support to prevent the specimens from falling during testing - technical drawing in Annex B

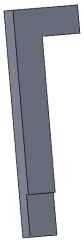


Figure 7.8: Positioning tool - technical drawing in Annex B

7.4 Flexural testing

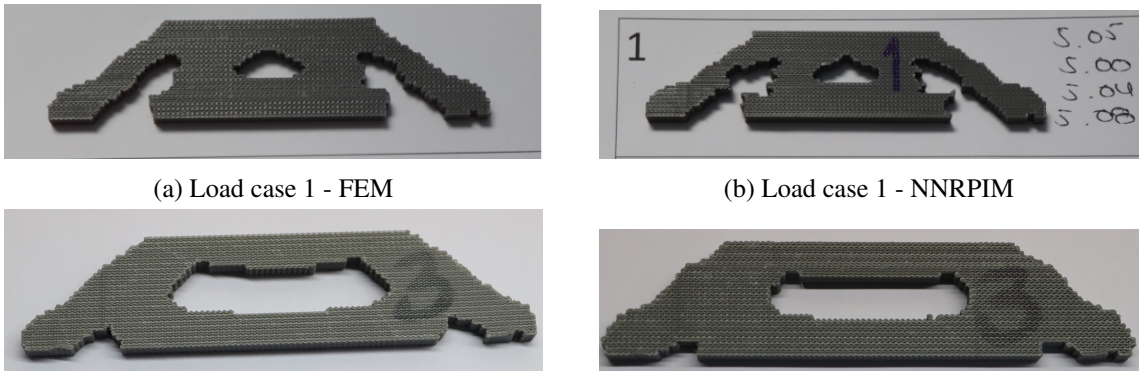
All tests were performed on a MultiTest-dV equipment (MecMesin, 2020a) with a maximum force of 2500N. Since plasticity is not being evaluated and linear elasto-static simulations are only valid for small displacements, it is not relevant whether the equipment is capable of applying a force high enough to cause fracture. The machine was connected with VectorPro software (MecMesin, 2020b) for data acquisition.

The results which are now being exposed are organized first by simulation and then, for each simulation, each load case is explored where the effect of different smoothing functions is evaluated. In addition, the Force-Displacement plot is referent to the average stiffness of all three tested specimens.

7.4.1 Structural optimization - Parabolic law

The summary of the structural optimization results with a parabolic law is shown next. Stiffness is compared for the both methods with the different smoothing functions. All specimens were printed at an average apparent density of 0.7g/cm^3. The specimens which did not undergo any smoothing were printed only for the maximum density corresponding to the truss structure (Figure 7.9).

For all load cases, a tendency of stiffness reduction as the amount of elements considered for the smoothing function was verified except for the "*no smoothing*" specimens in load case 1 where a possible lack of structural integrity had already been detected when analysing the numerical simulation results. When comparing the stiffness-to-weight ratio of specimens based on FEM and NNRPIM simulations, the latter present a slightly greater behaviour for smoothed specimens in load cases 1 and 3.



(a) Load case 1 - FEM

(b) Load case 1 - NNRPIM

(c) Load case 3 - FEM

(d) Load case 3 - NNRPIM

Figure 7.9: Structural optimization specimens which did not undergo any smoothing

Load Case 1

Load case 1 is schematically expressed in Figure 6.2b. Regarding stiffness, is it immediately visible that the specimens which were not smoothed present much lower stiffness than the smooth specimens. The smoothing function type 1 with a maximum distance ratio of 0.1 seems to present slightly better results than the other smoothed specimens both considering stiffness and stiffness ratio. Figure 7.10 shows what was now just mentioned being that the results are summarized in Table 7.5. The lack of stiffness in the specimens without smoothing is due to the lack of reinforcement between the central part of the structure and the bars which connect to the support. This lack of support between the upper and lower arch of the structure does not contribute to strength but increases the overall mass. Figure 7.9a and 7.9b show how the specimens present lack of reinforcement between the upper and lower arch.

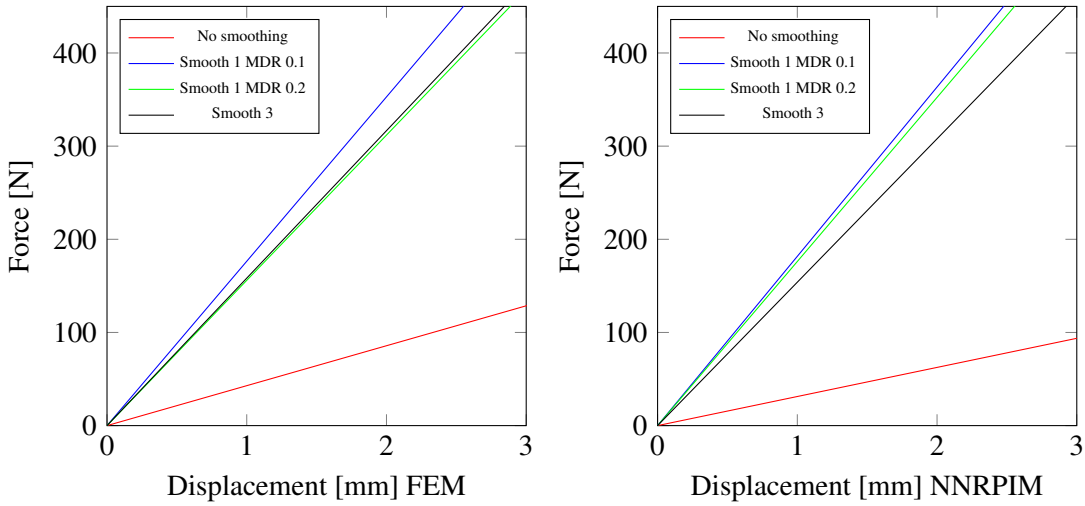


Figure 7.10: Experimental results for the structural optimization (parabolic law) specimens subject to load case 1

Table 7.5: Summary of results for the structural optimization specimens (parabolic law) subject to load case 1 created with FEM and NNRPIM

		Mass [g]	K [N/mm]	Ratio [N/(g*mm)]
FEM	No Smoothing	8.57 ± 0.02	42.87 ± 2.04	5.00 ± 0.23
	Smoothing Type 1 MDR 0.1	10.49 ± 0.04	176.42 ± 2.03	16.81 ± 0.18
	Smoothing Type 1 MDR 0.2	10.58 ± 0.10	155.92 ± 3.28	14.74 ± 0.28
	Smoothing Type 3	10.88 ± 0.04	158.29 ± 2.06	14.55 ± 0.18
NNRPIM	No Smoothing	8.18 ± 0.02	31.24 ± 0.38	3.82 ± 0.04
	Smoothing Type 1 MDR 0.1	10.4 ± 0.05	181.72 ± 3.31	17.53 ± 0.42
	Smoothing Type 1 MDR 0.2	10.56 ± 0.03	176.16 ± 4.48	16.68 ± 0.40
	Smoothing Type 3	10.82 ± 0.05	153.94 ± 4.24	14.23 ± 0.33

Regarding printing direction, the vertically printed specimens displayed better properties, which was as expected. Figure 7.11 and Table 7.6 compare the stiffness and ratio results for both specimens. Moreover, the vertically printed specimens present higher mass and a higher stiffness-to-weight ratio.

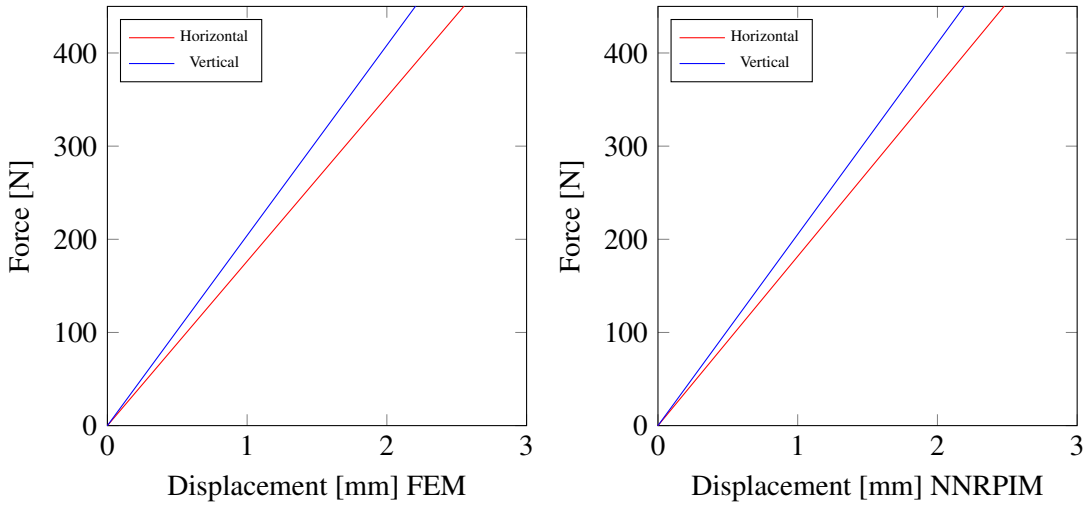


Figure 7.11: Comparison of horizontally and vertically printed specimens for load case 1, smoothing type 1 with a maximum distance ratio of 0.1, both for FEM and NNRPIM

Table 7.6: Summary results of the comparative analysis of horizontally and vertical printed specimens for load case 1, smoothing type 1 with a maximum distance ratio of 0.1, both for FEM and NNRPIM

		Mass [g]	K [N/mm]	Ratio [N/(g*mm)]
FEM	Horizontal	10.49 ± 0.04	176.42 ± 2.03	16.81 ± 0.18
	Vertical	10.65 ± 0.04	204.15 ± 2.07	19.17 ± 0.26
NNRPIM	Horizontal	10.4 ± 0.05	181.72 ± 3.31	17.53 ± 0.42
	Vertical	10.62 ± 0.004	205.32 ± 2.85	19.34 ± 0.25

Load case 2

The structural optimization specimens were not printed in the non-smoothed form due to the issues presented in 6.3.2 of not being able to form a continuous truss-structure. Therefore, only smoothed specimens were printed and tested. The results are shown in Figure 7.12 and Table 7.7. Here, a tendency of decreased stiffness when increasing the amount of elements weighting for the smoothing function is verified both for the FEM and NNRPIM except with the smoothing function 3 for the latter method.

Regarding the influence of printing direction, the obtained results are shown in Figure 7.13 and Table 7.8 where the results correspond to what was expected and stiffness is enhanced when printing the specimens vertically.

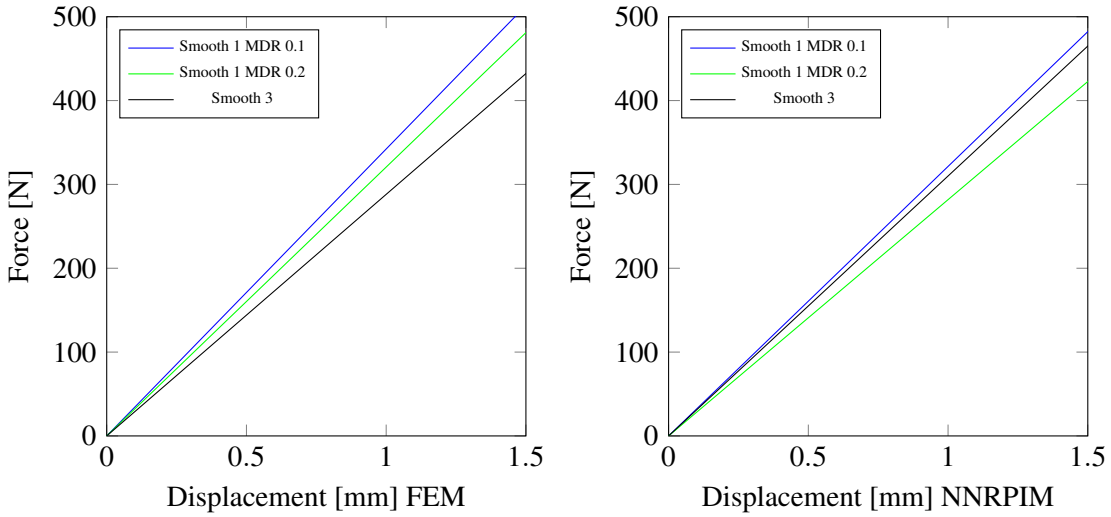


Figure 7.12: Experimental results for the structural optimization (parabolic law) specimens subject to load case 2

Table 7.7: Summary of results for the structural optimization specimens subject to load case 2 created with FEM and NNRPIM

		Mass [g]	K [N/mm]	Ratio [N/(g*mm)]
FEM	Smoothing Type 1 MDR 0.1	10.97 ± 0.04	342.23 ± 3.44	31.21 ± 0.31
	Smoothing Type 1 MDR 0.2	11.18 ± 0.06	320.66 ± 6.60	28.56 ± 0.47
	Smoothing Type 3	11.41 ± 0.02	288.13 ± 2.90	25.26 ± 0.20
NNRPIM	Smoothing Type 1 MDR 0.1	10.78 ± 0.12	321.45 ± 10.88	29.81 ± 0.68
	Smoothing Type 1 MDR 0.2	10.98 ± 0.02	281.81 ± 5.90	25.67 ± 0.52
	Smoothing Type 3	11.29 ± 0.02	310.01 ± 6.27	27.84 ± 0.39

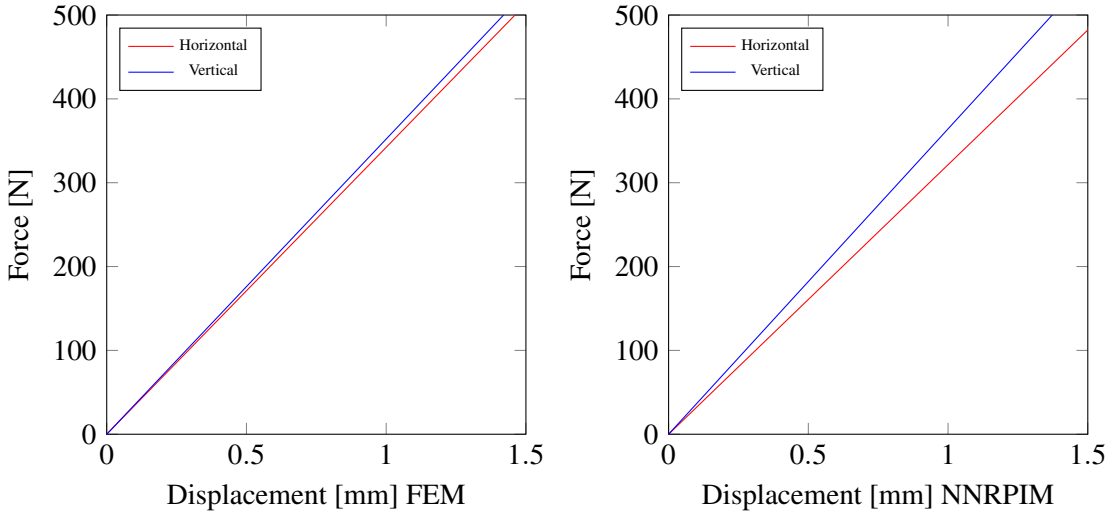


Figure 7.13: Comparison of horizontally and vertical printed specimens for load case 2, smoothing type 1 with a maximum distance ratio of 0.1, both for FEM and NNRPIM

Table 7.8: Summary results of the comparative analysis of horizontally and vertical printed specimens for load case 2, smoothing type 1 with a maximum distance ratio of 0.1, both for FEM and NNRPIM

		Mass [g]	K [N/mm]	Ratio [N/(g*mm)]
FEM	Horizontal	10.97 ± 0.04	342.23 ± 3.44	31.21 ± 0.31
	Vertical	11.21 ± 0.02	352.08 ± 4.91	31.40 ± 0.42
NNRPIM	Horizontal	10.78 ± 0.12	321.45 ± 10.88	29.81 ± 0.68
	Vertical	10.90 ± 0.07	364.22 ± 4.88	33.41 ± 0.33

Load case 3

Unlike the specimens subjected to load case 1, these truss structures presented the necessary connectivity between the upper and lower arch - Figures 7.9c and 7.9d, being that this was already expected from the simulations. For that reason, the stiffness and the stiffness-to-weight ratio are greater for these specimens than for the specimens which did not undergo any smoothing function.

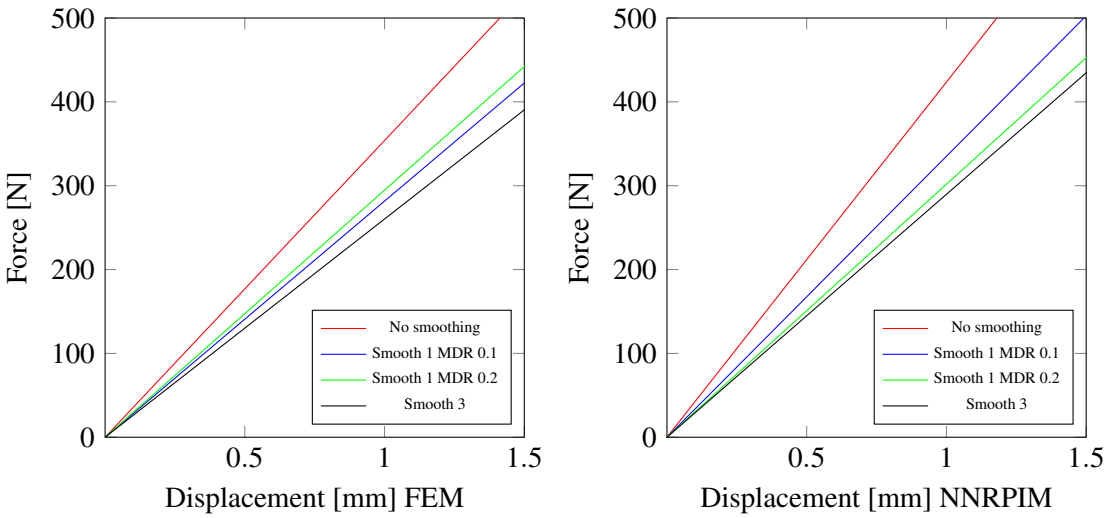


Figure 7.14: Experimental results for the structural optimization (parabolic law) specimens subject to load case 3

Table 7.9: Summary of results for the structural optimization (parabolic law) specimens subject to load case 3 created with FEM and NNRPIM

		Mass [g]	K [N/mm]	Ratio [N/(g*mm)]
FEM	No Smoothing	8.72 ± 0.02	353.92 ± 5.11	40.58 ± 0.53
	Smoothing Type 1 MDR 0.1	9.87 ± 0.07	281.64 ± 4.08	28.54 ± 0.36
	Smoothing Type 1 MDR 0.2	10.85 ± 0.05	294.72 ± 6.63	27.17 ± 0.51
	Smoothing Type 3	10.53 ± 0.05	260.29 ± 3.93	24.72 ± 0.40
NNRPIM	No Smoothing	9.93 ± 0.01	423.58 ± 0.14	42.65 ± 0.02
	Smoothing Type 1 MDR 0.1	10.47 ± 0.03	335.08 ± 4.43	32.02 ± 0.33
	Smoothing Type 1 MDR 0.2	11.15 ± 0.03	301.80 ± 0.03	27.03 ± 0.06
	Smoothing Type 3	11.30 ± 0.05	289.73 ± 4.93	25.63 ± 0.37

Regarding the influence of printing direction, the results are shown in Figure 7.15 and Table 7.10.

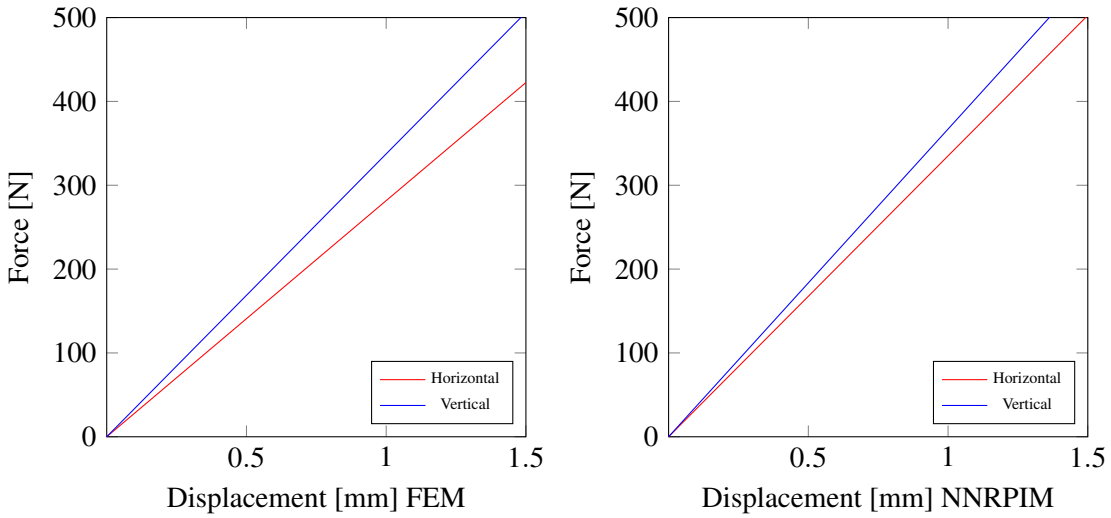


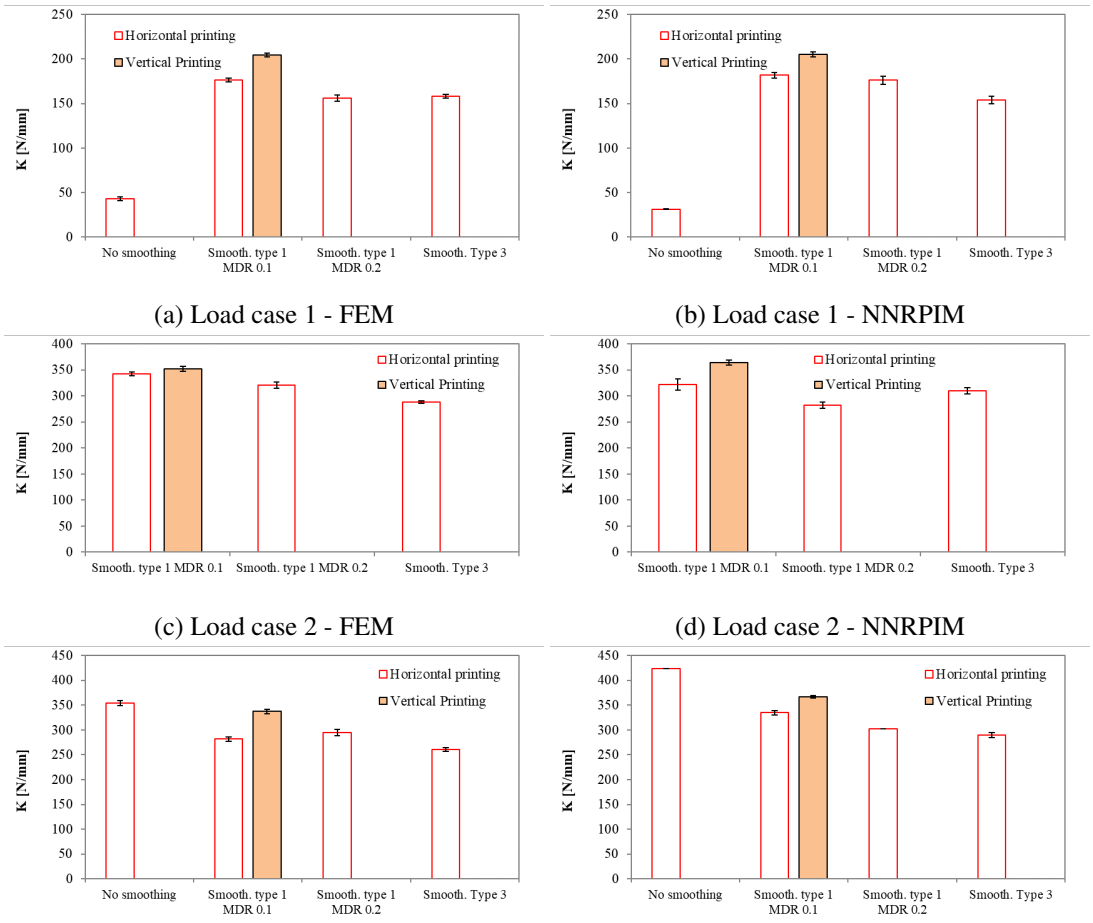
Figure 7.15: Comparison of horizontally and vertical printed specimens for load case 3, smoothing type 1 with a maximum distance ratio of 0.1, both for FEM and NNRPIM

Table 7.10: Summary results of the comparative analysis of horizontally and vertical printed specimens for load case 3, smoothing type 1 with a maximum distance ratio of 0.1, both for FEM and NNRPIM

		Mass [g]	K [N/mm]	Ratio [N/(g*mm)]
FEM	Horizontal	9.87 ± 0.07	281.64 ± 4.08	28.54 ± 0.36
	Vertical	10.67 ± 0.04	337.40 ± 4.20	31.62 ± 0.28
NNRPIM	Horizontal	10.47 ± 0.03	335.05 ± 4.43	32.02 ± 0.33
	Vertical	11.11± 0.01	367.03 ± 2.30	33.05 ± 0.23

Summary

In summation, it was seen that for this particular material law (parabolic), the inefficiency of the structures was verified and that the smoothing functions presented a positive result being difficult to point out which smoothing function is more efficient at doing so. There is reason to believe that smoothing function 1 with and MDR of 0.1 presents structures with higher stiffness. On the other had, when the structure is very stable and efficient, as was verified in Chapter 6 for the structures obtained with load case 3, the smoothing functions present the opposite effect. Figure 7.16 shows the stiffness comparison between methods for all load cases. Stiffness-to-weight ratio follows a similar trend as the trend visualized for flexural stiffness (Figure 7.17).



(a) Load case 1 - FEM

(b) Load case 1 - NNRPIM

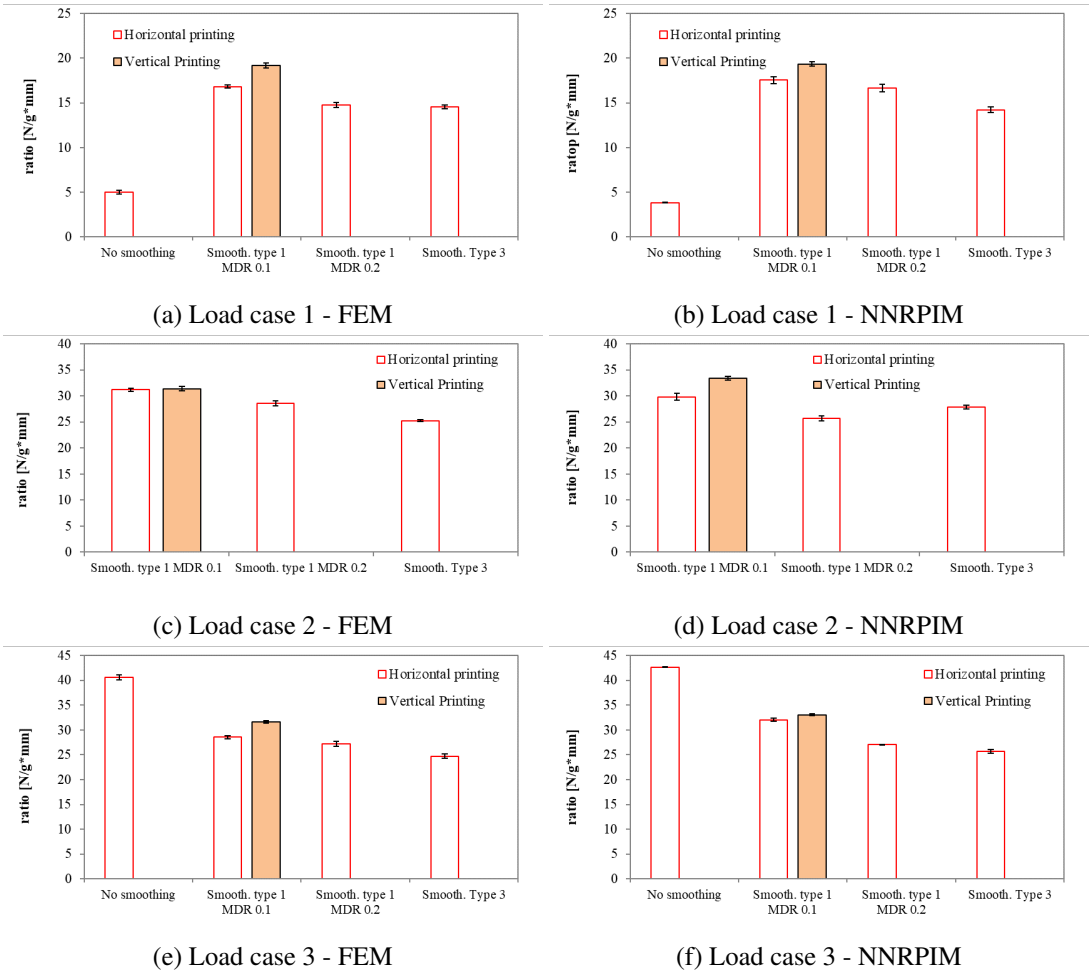
(c) Load case 2 - FEM

(d) Load case 2 - NNRPIM

(e) Load case 3 - FEM

(f) Load case 3 - NNRPIM

Figure 7.16: Stiffness comparison between methods (FEM and NNRPIM) for all load cases using structural optimization with a parabolic law



(a) Load case 1 - FEM

(b) Load case 1 - NNRPIM

(c) Load case 2 - FEM

(d) Load case 2 - NNRPIM

(e) Load case 3 - FEM

(f) Load case 3 - NNRPIM

Figure 7.17: Stiffness-to-weight ratio comparison between methods (FEM and NNRPIM) for all load cases using structural optimization with a parabolic law

7.4.2 Structural optimization - Linear law

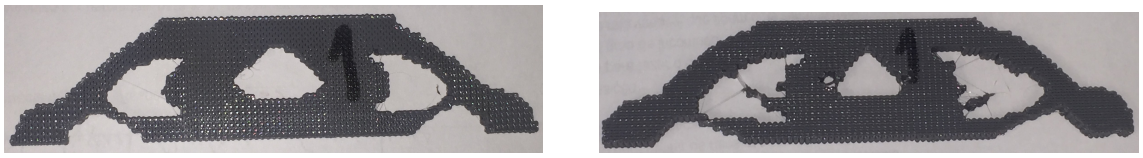
The specimens based on simulations with a linear material law for structural optimizations are tested and compared with the parabolic law specimens for all load cases. For these simulations, only two types of smoothing functions are tested: smoothing function type 1 with a maximum distance ratio of 0.1 and the non-application of a smoothing function. In addition, vertical printing direction is not tested at this stage. According to numerical simulations, it is expected that the specimens based on linear law simulations have a more optimized behaviour. Unlike the previous analysis of structural optimization, where the specimens were printed at a density level of 0.7 g/cm^3, here, a density level of 0.6 g/cm^3 was employed.

Load case 1

The results of three point bending test are shown in Figure 7.19 where the results of the specimens with a parabolic law are also shown for comparison. Due to the difference in mass for both cases,

the specimens based on the parabolic law present higher stiffness when the smoothing function is applied. However, when analysing Table 7.11 it is visible that the ratio for both material laws when applying smoothing function type 1 with an MDR of 0.1, is very similar with only a difference of about 0.5N/(g*mm), when the FEM was used. Using the NNRPIM, the ratio is greater for the specimens based on the parabolic law when using a smoothing function. Also, comparing the truss structures obtained with both laws using the FEM or NNRPIM ("*No smoothing*" specimens), the ratio of the specimens printed with the linear law is much higher than with the parabolic law, confirming the assumption made about the efficiency of the structures. Figure 7.18 presents examples of the specimens without any smoothing function.

It is verifiable in Figure 7.18 that especially the structure based on NNRPIM simulations could be improved. For that reason, the structure was rebuilt in order to include the areas at a transition density. The printed specimen is shown in Figure 7.20 as well as the force displacement plot for both structures. Table 7.12 further specifies the results, comparing both types of specimens.



(a) FEM (b) NNRPIM

Figure 7.18: Truss-like specimens based on structural optimization simulations with a linear material law for load case 1

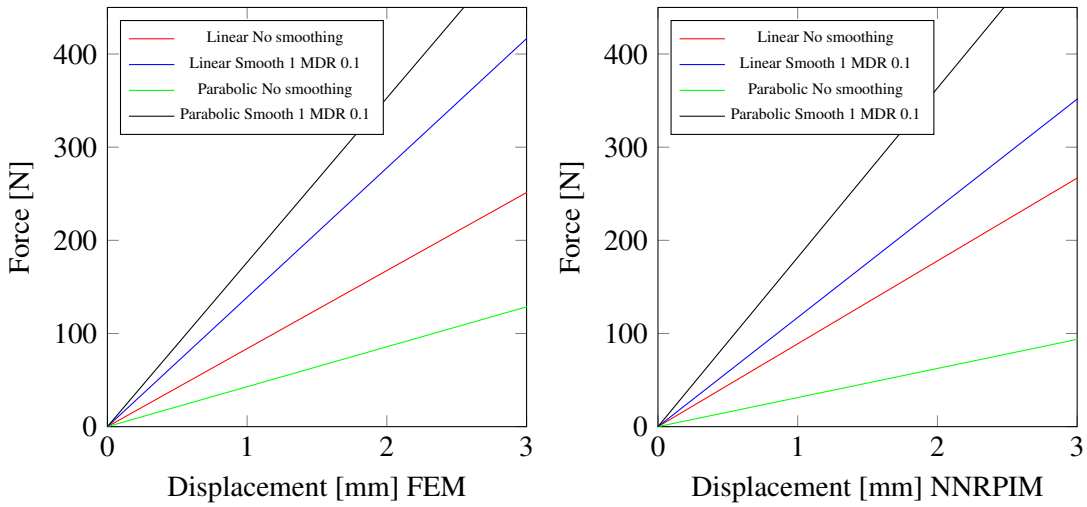
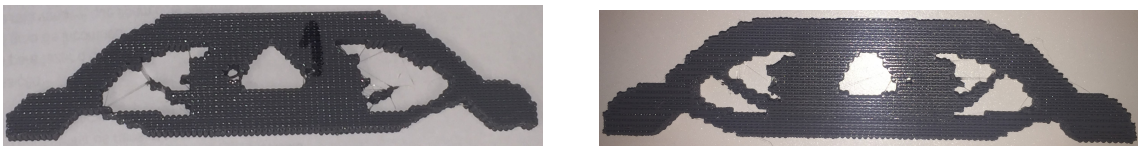


Figure 7.19: Comparisson of experimental results for the structural optimization specimens with linear and parabolic material law subject to load case 1

Table 7.11: Summary of results for the structural optimization specimens subject to load case 1 created with FEM and NNRPIM

		Mass [g]	K [N/mm]	Ratio [N/(g*mm)]
FEM	Linear No Smoothing	6.94 ± 0.03	83.77 ± 3.46	12.07 ± 0.45
	Linear Smoothing Type 1 MDR 0.1	8.50 ± 0.01	138.87 ± 1.20	16.33 ± 0.15
	Parabolic No Smoothing	8.57 ± 0.02	42.87 ± 2.04	5.00 ± 0.23
	Parabolic Smoothing Type 1 MDR 0.1	10.49 ± 0.04	176.42 ± 2.03	16.81 ± 0.18
NNRPIM	Linear No Smoothing	6.64 ± 0.03	88.94 ± 2.33	13.41 ± 0.38
	Linear Smoothing Type 1 MDR 0.1	8.33 ± 0.22	117.2 ± 0.05	13.94 ± 0.39
	Parabolic No Smoothing	8.18 ± 0.02	31.24 ± 0.38	3.82 ± 0.04
	Parabolic Smoothing Type 1 MDR 0.1	10.4 ± 0.05	181.72 ± 3.31	17.53 ± 0.42



(a) Original (b) Reinforced

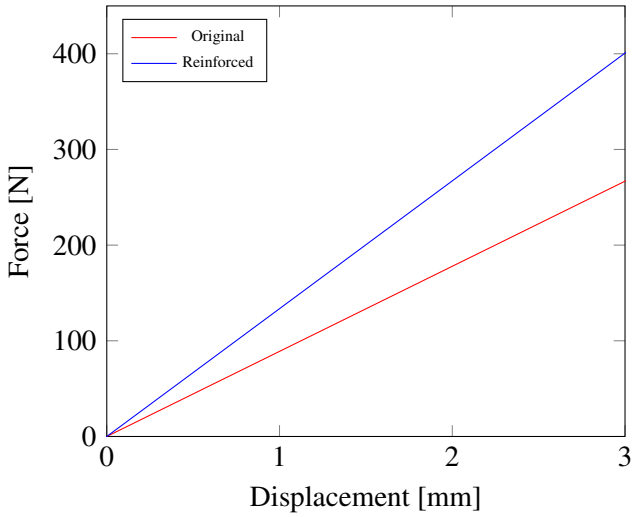


Figure 7.20: Comparison between an original and reinforced structure in order to show that the inclusion of the areas at a transition density may bring benefit to the structure despite the increase in mass

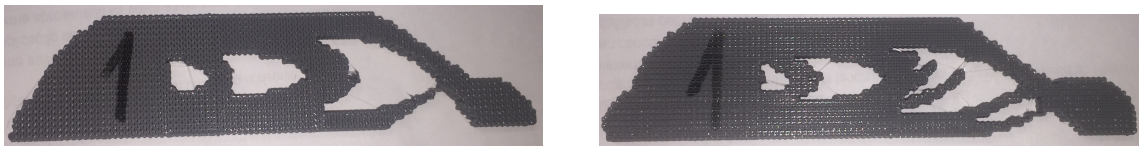
Table 7.12: Comparison between an original and reinforced structure for the specimens based on NNRPIM structural optimization simulations using a linear material law

	Mass [g]	K [N/mm]	Ratio [N/(g*mm)]
Original	6.64 ± 0.03	88.94 ± 2.33	13.41 ± 0.38
Reinforced	7.61 ± 0.14	133.57 ± 1.24	17.57 ± 0.49

Load case 2

For load case 2, the *no-smoothing* specimens could only be printed when reinforced, meaning that the areas which correspond to the transition density included and infilled at the same density as the main part of the structure. Figure 7.21 shows examples of the *no-smoothing* specimens for load case 2, based on FEM and NNRPIM simulations. Had these specimens not been reinforced, and it would not be possible to print the structures as one single body. Figure 7.22 and Table 7.13 show a comparison between these specimens based on a linear material law and the specimens based on a parabolic material law. The results of the tests conducted on the reinforced truss-like structures are also included in Figure 7.22 and Table 7.13. Since the structures obtained with a parabolic material law were printed from a higher density level, stiffness is naturally higher.

The structures based on NNRPIM simulations present higher stiffness which is expected from the structure configuration where more reinforcement trabeculae are present.



(a) FEM (b) NNRPIM

Figure 7.21: Reinforced truss-like structures for based on FEM and NNRPIM structural optimization simulations with a linear material law for load case 2

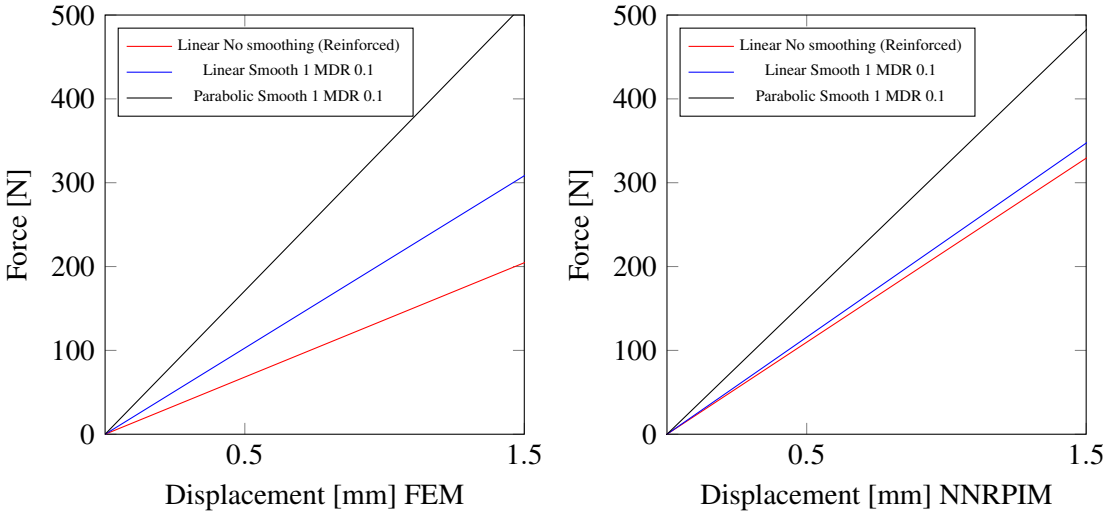


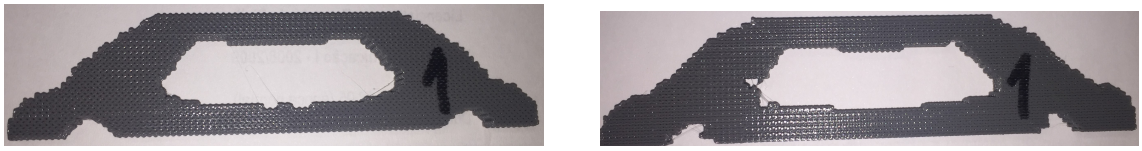
Figure 7.22: Comparisson of experimental results for the structural optimization specimens with linear and parabolic material law subject to load case 2

Table 7.13: Summary of results for the structural optimization specimens subject to load case 2 created with FEM and NNRPIM

		Mass [g]	K [N/mm]	Ratio [N/(g*mm)]
FEM	Linear No Smoothing (reinforced)	7.74 ± 0.04	136.37 ± 2.36	17.62 ± 0.41
	Linear Smoothing Type 1 MDR 0.1	8.29 ± 0.04	205.54 ± 3.72	24.59 ± 0.35
	Parabolic Smoothing Type 1 MDR 0.1	10.97 ± 0.04	342.23 ± 3.44	31.21 ± 0.31
NNRPIM	Linear No Smoothing (reinforced)	8.42 ± 0.06	219.49 ± 0.74	26.08 ± 0.28
	Linear Smoothing Type 1 MDR 0.1	8.39 ± 0.02	231.49 ± 1.15	27.60 ± 0.21
	Parabolic Smoothing Type 1 MDR 0.1	10.78 ± 0.12	321.45 ± 10.88	29.81 ± 0.68

Load case 3

Load case 3 is where the least differences between the parabolic law and linear law are found. Figure 7.23 shows the specimens which were not subject to any smoothing function based on both FEM and NNRPIM simulations. Due to robustness of the structure, no reinforcement was needed. A good performance of *no smoothing* structures was verified, similarly to what occurred for the parabolic law. Since these specimens based on the linear law were printed at a lower density level, higher stiffness is expected for the parabolic law. Results for structural optimization with a linear law and parabolic law are shown in Figure 7.24 and Table 7.14.



(a) FEM (b) NNRPIM

Figure 7.23: Truss-like structures for based on FEM and NNRPIM structural optimization simulations with a linear material law for load case 3

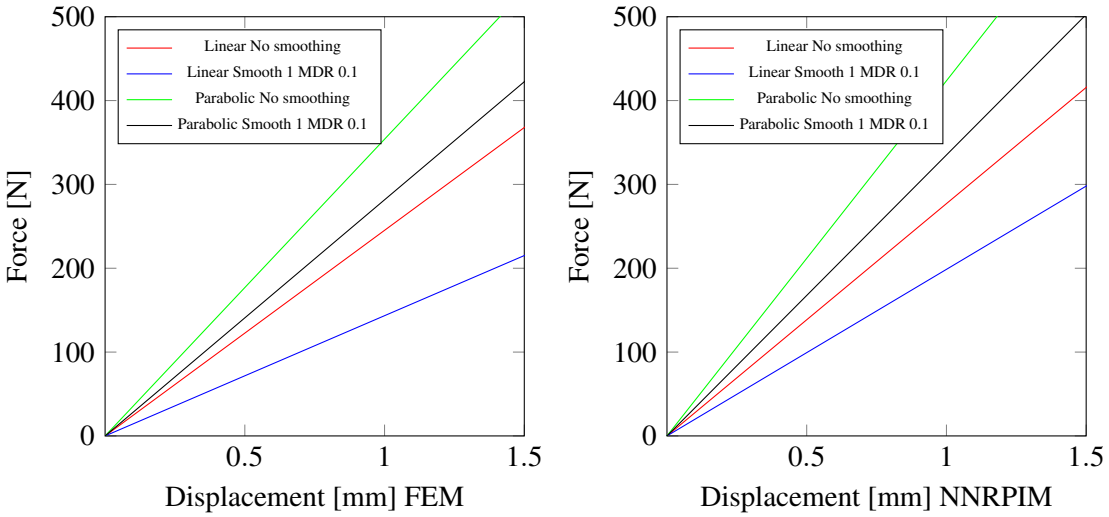


Figure 7.24: Comparisson of experimental results for the structural optimization specimens with linear and parabolic material law subject to load case 3

Table 7.14: Summary of results for the structural optimization specimens subject to load case 3 created with FEM and NNRPIM

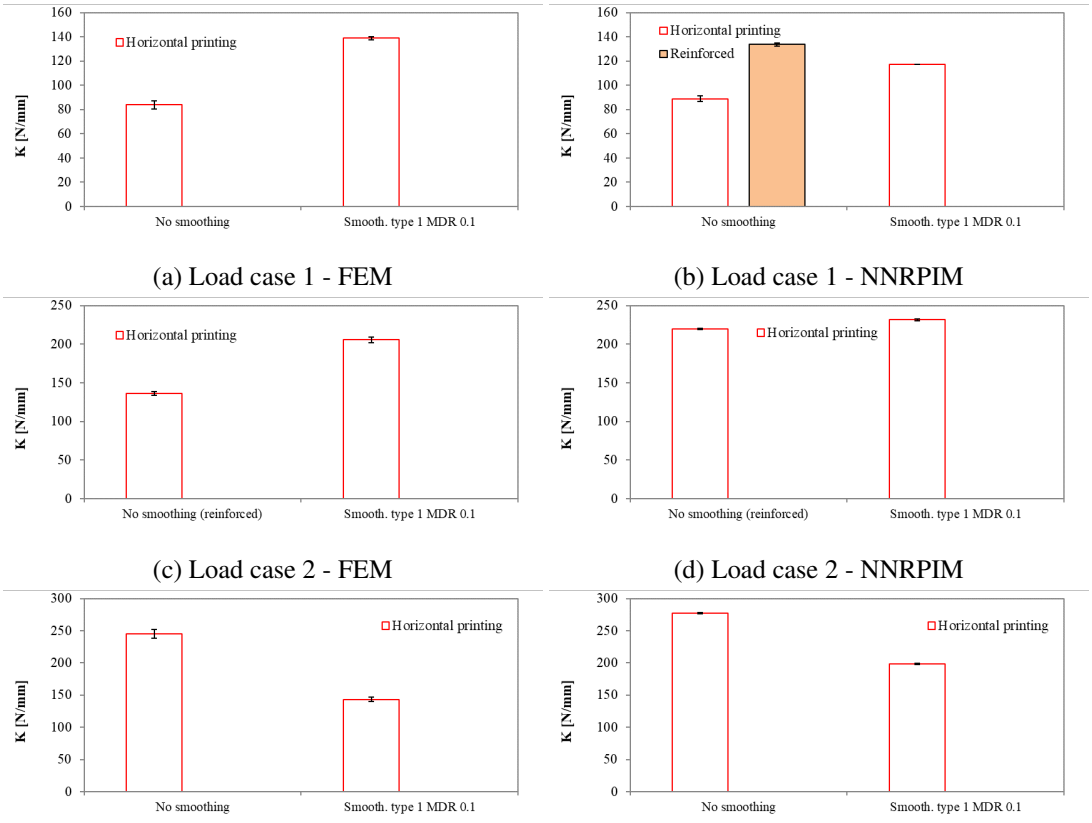
		Mass [g]	K [N/mm]	Ratio [N/(g*mm)]
FEM	Linear No Smoothing	6.69 ± 0.06	245.23 ± 6.68	36.64 ± 0.69
	Linear Smoothing Type 1 MDR 0.1	7.88 ± 0.14	143.42 ± 3.05	18.21 ± 0.47
	Parabolic No Smoothing	8.72 ± 0.02	353.92 ± 5.11	40.58 ± 0.53
	Parabolic Smoothing Type 1 MDR 0.1	9.87 ± 0.07	281.64 ± 4.08	28.54 ± 0.36
NNRPIM	Linear No Smoothing	7.46 ± 0.01	277.07 ± 0.73	37.13 ± 0.11
	Linear Smoothing Type 1 MDR 0.1	8.17 ± 0.01	198.66 ± 0.89	24.31 ± 0.11
	Parabolic No Smoothing	9.93 ± 0.01	423.58 ± 0.14	42.65 ± 0.02
	Parabolic Smoothing Type 1 MDR 0.1	10.47 ± 0.03	335.08 ± 4.43	32.02 ± 0.33

Summary

Here, the effectiveness of the structures obtained through the use of a structural optimization considering a linear material law is verified since the structures without any smoothing present a superior behaviour than the same structures with a parabolic law for load case 1. Moreover, the connectivity of structures is improved since, even though the structures obtained with a linear law needed reinforcement, it was possible to obtain a continuous structure at a lower density level. It is also concluded here how the mass of the specimens is relevant for the increase in stiffness and stiffness-to-weight ratio. It was verified that even though effectiveness of the structures obtained with a parabolic law was lower, smoothed specimens presented higher stiffness and stiffness-to-weight ratio.

The same conclusions regarding the effect of smoothing functions with a parabolic material law are valid here. When the structure is highly effective and connected (load case 3), the addition of a smoothing function does not bring any benefit. Figure 7.25 shows a comparison between

methods, for all load cases, of flexural stiffness, and stiffness-to-weight ratio is compared in Figure 7.26. It is verified in Figure 7.25b that the behaviour of structures with reinforcement is enhanced when the elements at a medium density are included, and that therefore, it is important to take a critical look when assembling the *.stl* file to be printed to minimize the presence of thin structures.



(a) Load case 1 - FEM

(b) Load case 1 - NNRPIM

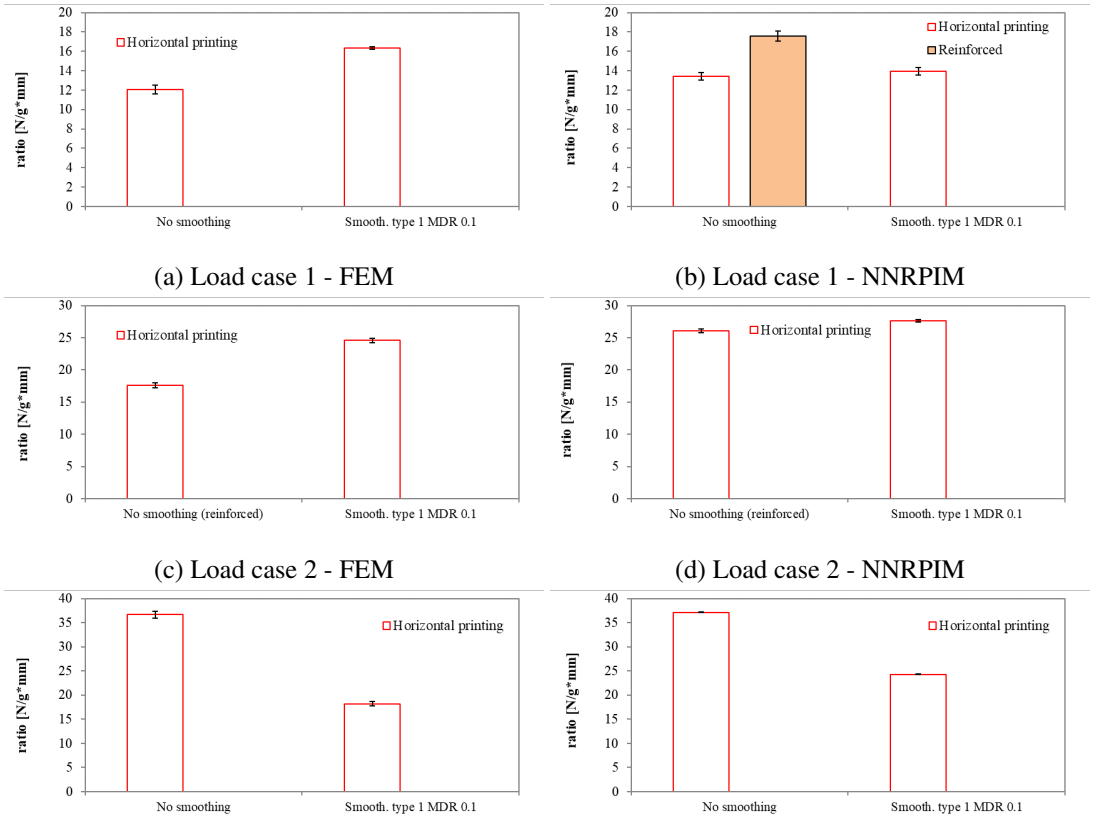
(c) Load case 2 - FEM

(d) Load case 2 - NNRPIM

(e) Load case 3 - FEM

(f) Load case 3 - NNRPIM

Figure 7.25: Stiffness comparison between methods (FEM and NNRPIM) for all load cases using structural optimization with a linear law



(a) Load case 1 - FEM

(b) Load case 1 - NNRPIM

(c) Load case 2 - FEM

(d) Load case 2 - NNRPIM

(e) Load case 3 - FEM

(f) Load case 3 - NNRPIM

Figure 7.26: Stiffness-to-weight ratio comparison between methods (FEM and NNRPIM) for all load cases using structural optimization with a linear law

7.4.3 Gyroid remodelling law 1

Unlike the specimens based on structural optimization simulations, the specimens which did not undergo any smoothing also include the minimal and transition density areas. This is because the minimal density in the numerical analysis corresponds to 10% of infill density and therefore can be printed. Accuracy between these simulation and experimental results is expected to be better than for structural optimization analyses because of the adaptive law employed here. Nevertheless, stability and robustness of the structures can be compared for both simulations.

Load case 1

Whereas the specimens based on structural optimization for load case 1, using the gyroid remodelling law, the specimens which did not undergo any smoothing function, presented higher stiffness and higher ratio, especially the specimens based on NNRPIM simulations. The results with respect to load case 1 based on gyroid remodelling simulations with law 1 are shown in Figure 7.27 and Table 7.15. The FEM simulation based specimens presented the highest stiffness employing the smoothing function 1 with a MDR of 0.1 and the NNRPIM simulation based specimens presented the highest stiffness for the specimens that did not undergo any smoothing.

For the FEM analysis, the specimens without any smoothing function presented worst behaviour than the smooth specimens whereas, for the NNRPIM, the *no smoothing* specimens presented higher stiffness and higher STW ratio than the smooth specimens.

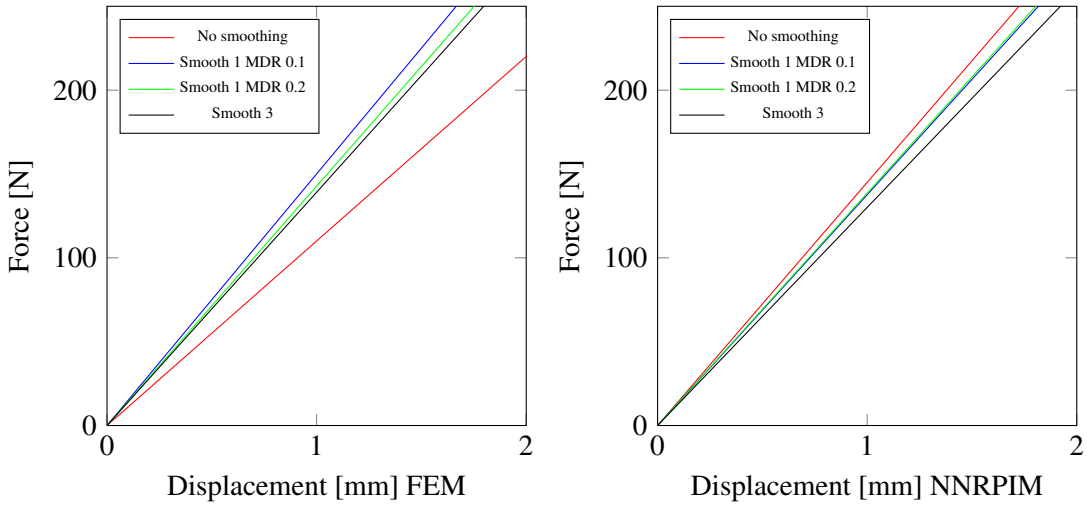


Figure 7.27: Experimental results for the gyroid remodelling law 1 specimens subject to load case 1

Table 7.15: Summary of results for the gyroid remodelling law 1 subject to load case 1 created with FEM and NNRPIM

		Mass [g]	K [N/mm]	Ratio [N/(g*mm)]
FEM	No Smoothing	8.07 ± 0.04	110.05 ± 0.48	13.64 ± 0.01
	Smoothing Type 1 MDR 0.1	8.60 ± 0.02	150.04 ± 1.70	17.44 ± 0.19
	Smoothing Type 1 MDR 0.2	9.01 ± 0.01	152.08 ± 3.00	16.89 ± 0.31
	Smoothing Type 3	9.29 ± 0.02	139.10 ± 4.89	14.97 ± 0.50
NNRPIM	No Smoothing	8.64 ± 0.00	145.00 ± 6.86	16.79 ± 0.79
	Smoothing Type 1 MDR 0.1	8.75 ± 0.02	137.62 ± 2.00	15.74 ± 0.21
	Smoothing Type 1 MDR 0.2	9.04 ± 0.01	138.56 ± 2.08	15.34 ± 0.24
	Smoothing Type 3	9.29 ± 0.04	130.08 ± 3.33	14.01 ± 0.33

Similarly to the structural optimization analysis with the parabolic law, the specimens with the smoothing function 1 using an MDR of 0.1 were printed both vertically and horizontally. Regarding the influence of printing direction, the vertically printed specimens presented higher stiffness, stiffness ratio and mass than the horizontally printed specimens. This comparison is shown in Figure 7.28 and Table 7.16.

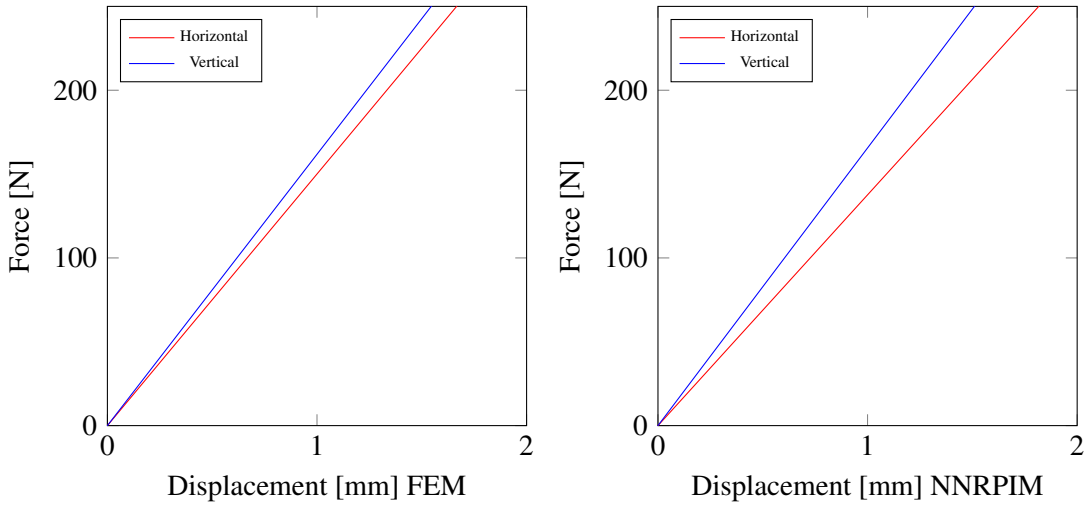


Figure 7.28: Comparison of horizontally and vertical printed specimens for load case 1, smoothing type 1 with a maximum distance ratio of 0.1 using the gyroid remodelling law 1

Table 7.16: Summary results of the comparative analysis of horizontally and vertical printed specimens for load case 1, smoothing type 1 with a maximum distance ratio of 0.1, both for FEM and NNRPIM using the gyroid remodelling law 1

		Mass [g]	K [N/mm]	Ratio [N/(g*mm)]
FEM	Horizontal	8.60 ± 0.02	150.04 ± 1.70	17.44 ± 0.19
	Vertical	9.06 ± 0.05	161.80 ± 1.46	17.87 ± 0.20
NNRPIM	Horizontal	8.75 ± 0.02	137.62 ± 2.00	15.74 ± 0.21
	Vertical	9.13 ± 0.01	165.59 ± 1.16	18.14 ± 0.09

Influence of remodelling parameters It was previously mentioned that using a lower density decrease ratio β for the analysis could obtain better defined structures, especially for the NNRPIM analysis, with the disadvantage of carrying a much higher computational time. The structures based on the FEM analysis were printed with a low density reinforcement and the structures based on the NNRPIM analysis were printed with a low density reinforcement and only the truss structure in order to conclude about the benefit of adding this low density reinforcement.

The FEM structures presented a higher modulus for the simulations with a lower density decrease ratio, even though these structures are not as well defined as the structures based on the NNRPIM analysis. On the other hand, the structures based on NNRPIM simulations presented slightly lower STW ratio with the lower value of β, which could indicate that the higher computational cost of these simulations could not be worth it in terms of final stiffness, maybe due to manufacturing limitations where small details are not possible to be fully replicated. Finally, the outer reinforcement proved to enhance performance of the specimens.

These results are summarized in Figure 7.29 and Table 7.17.

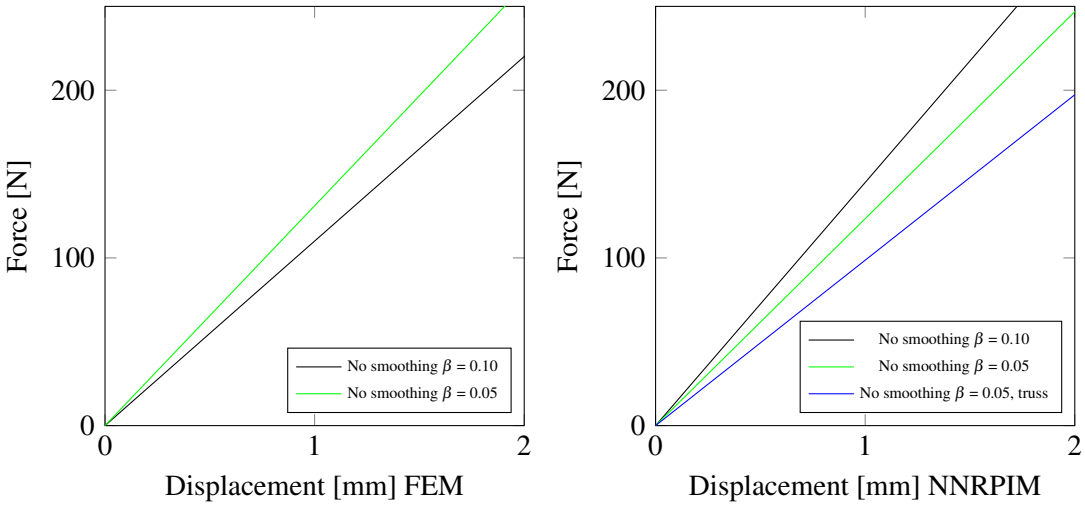


Figure 7.29: Influence of parameter β in the performance of structures obtained with gyroid remodelling law 1, for load case 1

Table 7.17: Influence of parameter β in the performance of structures obtained with gyroid remodelling law 1, for load case 1

	β	m [g]	K[K/mm]	ratio [N/(g*mm)]
FEM	0.10	8.07±0.04	110.05±0.48	13.64± 0.01
	0.05	7.94±0.04	131.12±2.35	16.52±0.21
NNRPIM	0.10	8.64±0.00	145.00±6.86	16.79±0.79
	0.05	8.01±0.00	123.42±1.17	15.42±0.15
	0.05 truss	6.89±0.02	98.65±0.64	14.32±0.13

Load case 2

For these specimens it was possible to obtain continuous enough structures even when no smoothing function was employed although, continuity was not key for this analysis since the areas at a minimum and transition density are also printed. The results for the horizontally printed specimens are shown in Figure 7.30 and summarized in Table 7.18. The specimens based on the results of NNRPIM simulations presented very similar stiffness values between themselves.

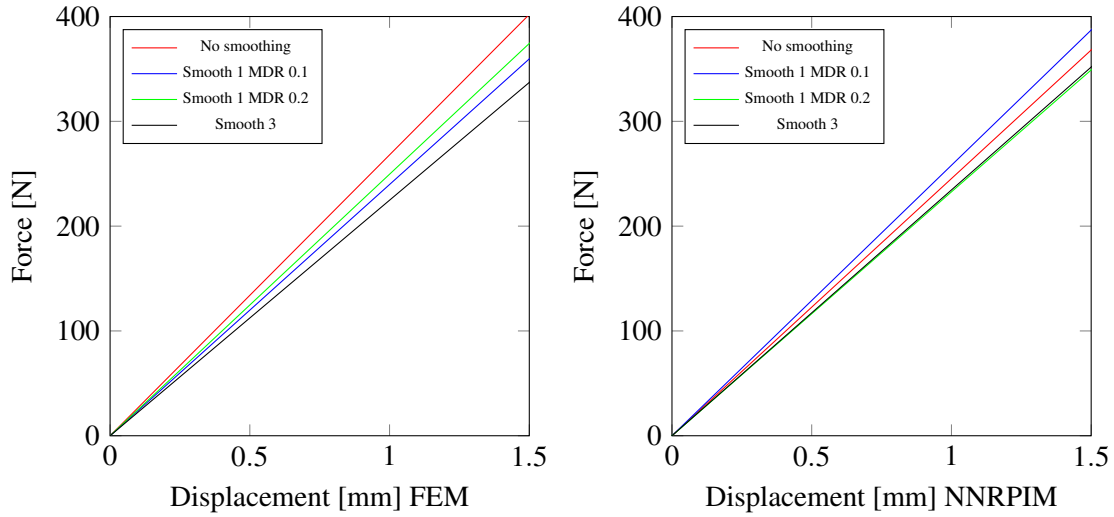


Figure 7.30: Experimental results for the gyroid remodelling law 1 specimens subject to load case 2

Table 7.18: Summary of results for the gyroid remodelling law 1 subject to load case 2 created with FEM and NNRPIM

		Mass [g]	K [N/mm]	Ratio [N/(g*mm)]
FEM	No Smoothing	8.57 ± 0.05	267.99 ± 3.16	31.26 ± 0.26
	Smoothing Type 1 MDR 0.1	8.52 ± 0.01	239.72 ± 5.02	28.15 ± 0.55
	Smoothing Type 1 MDR 0.2	9.03 ± 0.06	249.53 ± 6.81	27.63 ± 0.72
	Smoothing Type 3	9.16 ± 0.04	224.74 ± 7.05	24.55 ± 0.88
NNRPIM	No Smoothing	8.56 ± 0.00	245.36 ± 3.35	28.67 ± 0.40
	Smoothing Type 1 MDR 0.1	8.73 ± 0.05	258.05 ± 0.60	29.57 ± 0.23
	Smoothing Type 1 MDR 0.2	8.88 ± 0.03	232.67 ± 1.81	26.19 ± 0.12
	Smoothing Type 3	9.14 ± 0.01	234.52 ± 4.30	25.67 ± 0.48

The specimens to which the smoothing function 1 was applied with a maximum distance ratio of 0.1 were printed also in the vertical direction. The specimens printed in the vertical direction presented greater mass, stiffness and stiffness ratio. The results of the comparison between vertical and horizontal specimens are shown in Figure 7.31 and Table 7.19.

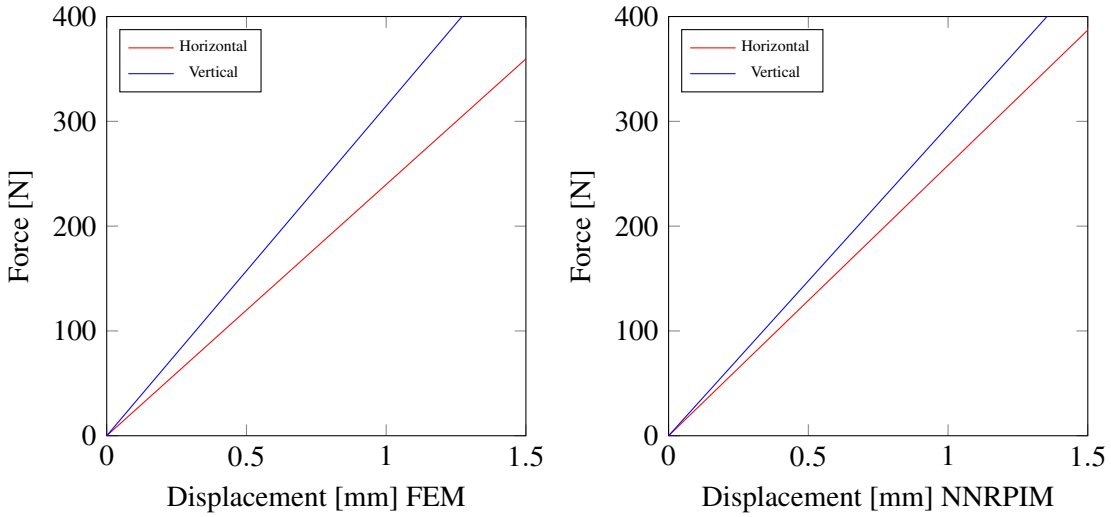


Figure 7.31: Comparison of horizontally and vertical printed specimens for load case 2, smoothing type 1 with a maximum distance ratio of 0.1 using the gyroid remodelling law 1

Table 7.19: Summary results of the comparative analysis of horizontally and vertical printed specimens for load case 2, smoothing type 1 with a maximum distance ratio of 0.1, both for FEM and NNRPIM using the gyroid remodelling law 1

		Mass [g]	K [N/mm]	Ratio [N/(g*mm)]
FEM	Horizontal	8.52 ± 0.01	239.72 ± 5.02	28.15 ± 0.55
	Vertical	9.09 ± 0.02	314.69 ± 1.66	34.63 ± 0.19
NNRPIM	Horizontal	8.73 ± 0.05	258.05 ± 0.60	29.57 ± 0.23
	Vertical	8.89 ± 0.03	295.38 ± 3.10	33.24 ± 0.26

Load case 3

Similarly to the specimens subject to the same load case in the structural optimization analysis, the ones without any smoothing function presented greater stiffness. The results from all tests are shown in Figure 7.32 and Table 7.20. The verified tendency of decreased stiffness when increasing the number of elements considered for the smoothing function is verified for the specimens based on FEM analysis.

Moreover, the vertically printed specimens presented greater stiffness than their horizontally printed counterparts. The results are summarized in Figure 7.33 and Table 7.21.

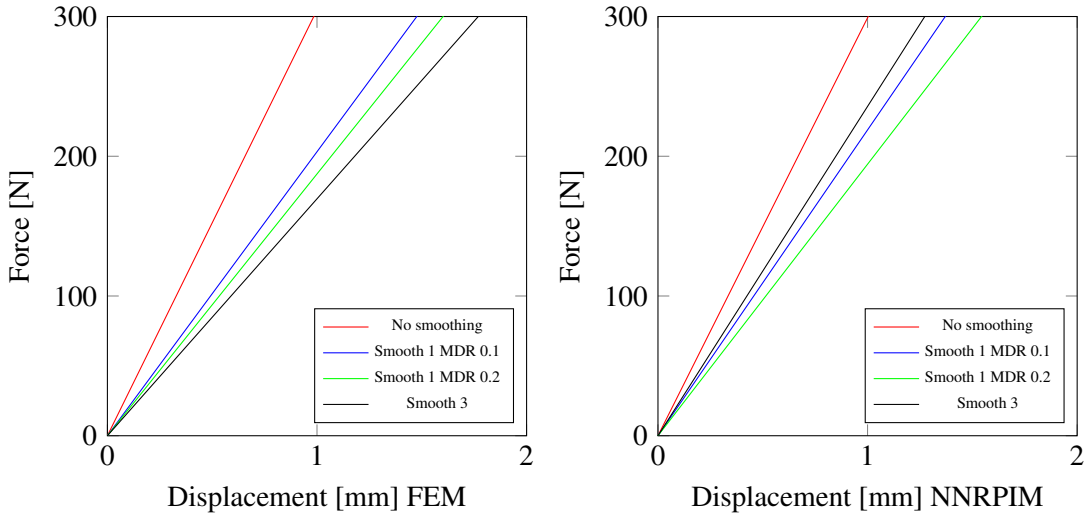


Figure 7.32: Experimental results for the gyroid remodelling law 1 specimens subject to load case 3

Table 7.20: Summary of results for the gyroid remodelling law 1 subject to load case 3 created with FEM and NNRPIM

		Mass [g]	K [N/mm]	Ratio [N/(g*mm)]
FEM	No Smoothing	8.54 ± 0.01	304.65 ± 0.48	35.67 ± 0.04
	Smoothing Type 1 MDR 0.1	8.29 ± 0.05	203.22 ± 3.97	24.52 ± 0.62
	Smoothing Type 1 MDR 0.2	8.66 ± 0.04	187.33 ± 3.85	21.63 ± 0.35
	Smoothing Type 3	8.95 ± 0.02	169.54 ± 1.57	18.94 ± 0.13
NNRPIM	No Smoothing	8.67 ± 0.01	299.09 ± 4.28	34.50 ± 0.46
	Smoothing Type 1 MDR 0.1	8.37 ± 0.03	218.85 ± 0.15	26.15 ± 0.10
	Smoothing Type 1 MDR 0.2	8.90 ± 0.01	194.32 ± 4.42	21.83 ± 0.51
	Smoothing Type 3	9.09 ± 0.00	235.68 ± 4.54	25.93 ± 0.49

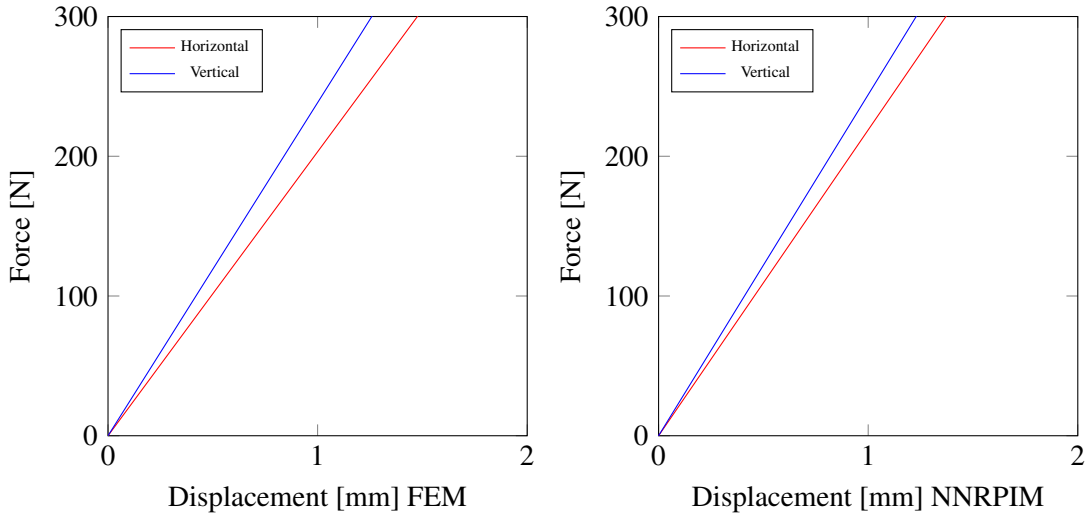


Figure 7.33: Comparison of horizontally and vertical printed specimens for load case 3, smoothing type 1 with a maximum distance ratio of 0.1 using the gyroid remodelling law 1

Table 7.21: Summary results of the comparative analysis of horizontally and vertical printed specimens for load case 3, smoothing type 1 with a maximum distance ratio of 0.1, both for FEM and NNRPIM using the gyroid remodelling law 1

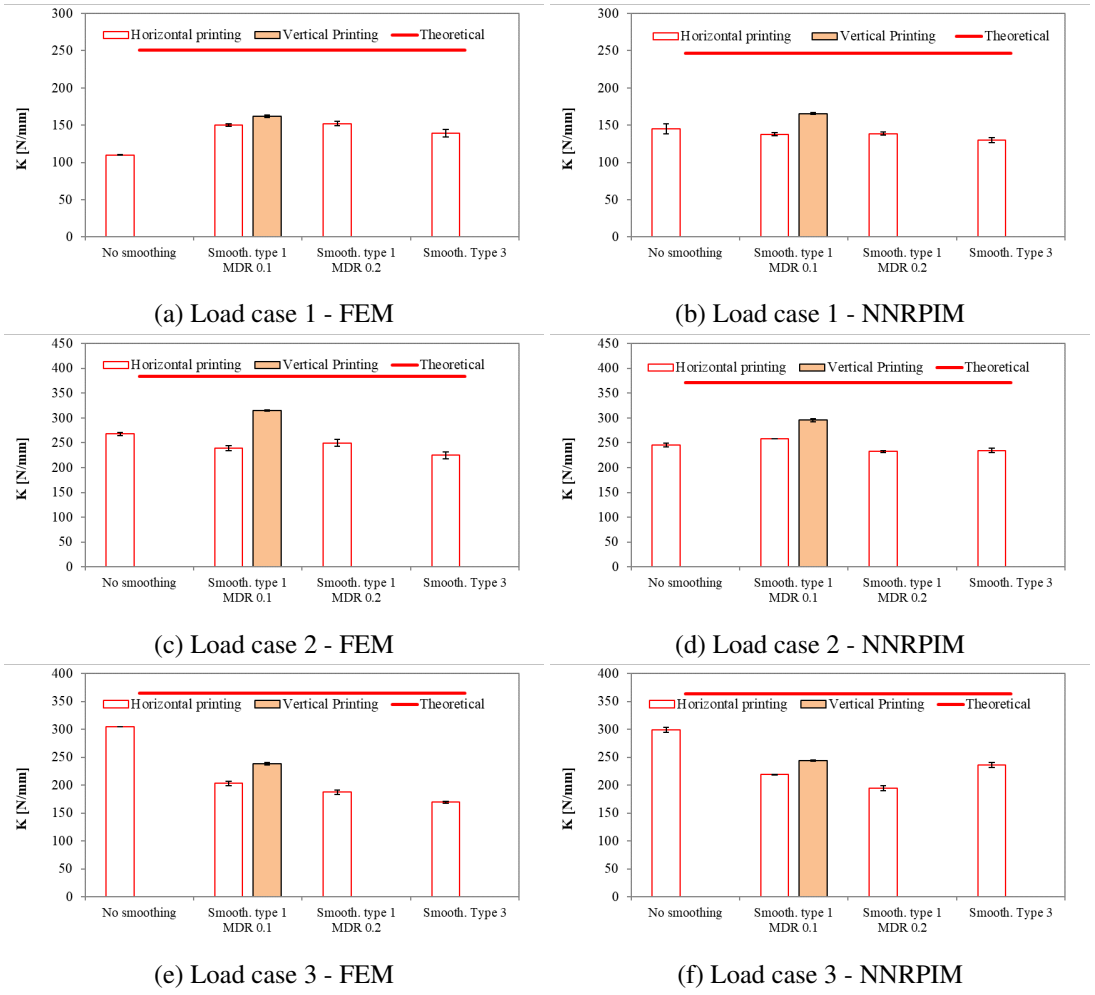
		Mass [g]	K [N/mm]	Ratio [N/(g*mm)]
FEM	Horizontal	8.29 ± 0.05	203.22 ± 3.97	24.52 ± 0.62
	Vertical	8.67 ± 0.02	238.37 ± 2.30	27.50 ± 0.20
NNRPIM	Horizontal	8.37 ± 0.03	218.85 ± 0.15	26.15 ± 0.10
	Vertical	8.77 ± 0.03	244.08 ± 0.91	27.84 ± 0.17

Summary

For this analysis, unlike the previous analyses, it was possible to compare the obtained values with the theoretical predicted stiffness from the numerical simulations. The specimens without any smoothing, subject to a four-point bending test got the closest to the predicted stiffness indicating that the distribution of the load can be relevant for the functioning of the algorithm. Accuracy regarding the numerical value was quite low for load case 1. Vertically printed specimens present the best behaviour and the specimens subject to load case 3 without any smoothing show, once again, that smoothing functions can worsen the mechanical behaviour of structures when these are very efficient by themselves.

On the influence of remodelling parameters, it was shown that it is not clear whether the refinement of structures brings any increase in behaviour when printing the structure. It is clear however that a much higher computational is required which may not compensate the obtained behaviour. In addition, it was also verified while studying the influence of remodelling parameters that the presence of the low density reinforcement on the exterior of the main truss brings a positive effect in mechanical behaviour.

Figure 7.34 and Figure 7.35 compare stiffness and stiffness-to-weight ratio, respectively, for all methods, load cases and smoothing functions. Here, it is not immediate to find a trend in effect of smoothing functions, as this effect varies with method and load case.



(a) Load case 1 - FEM

(b) Load case 1 - NNRPIM

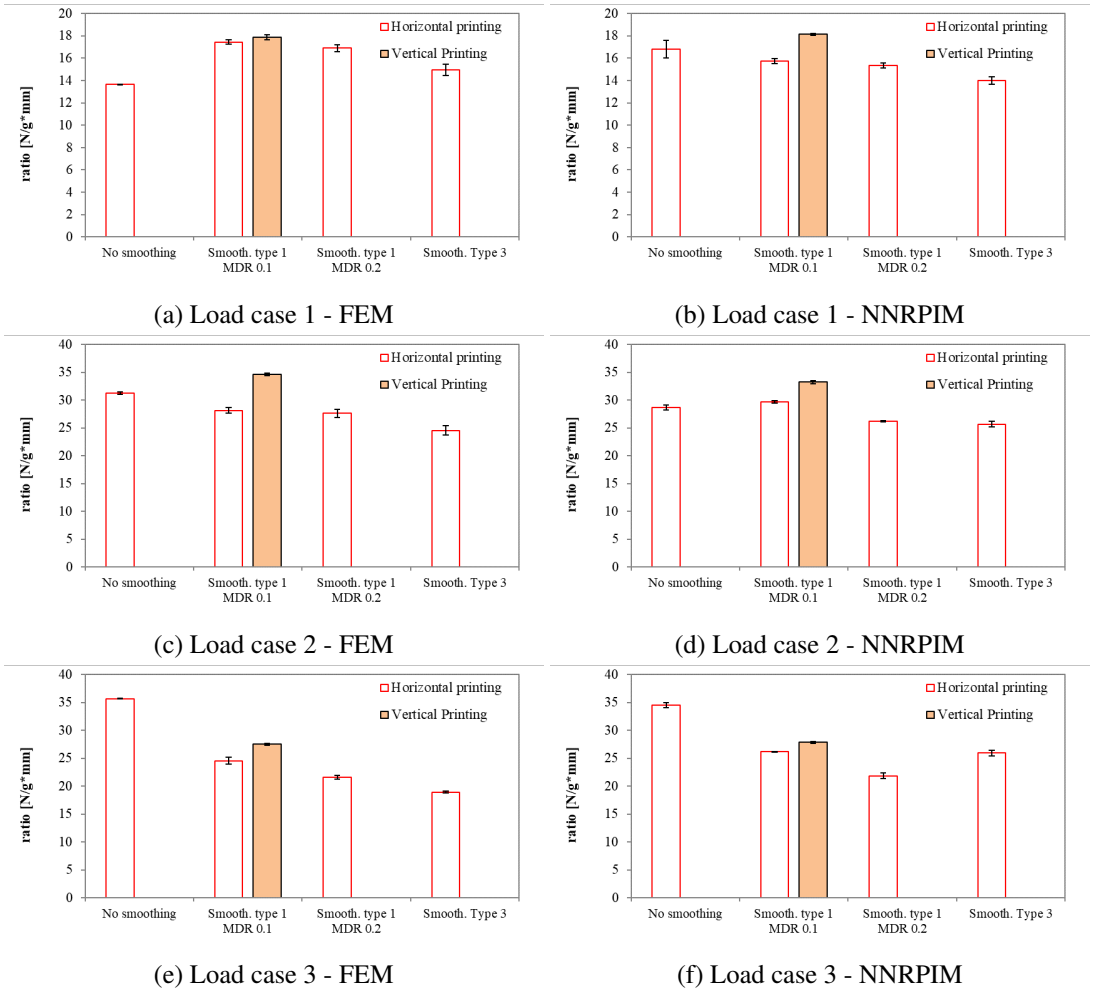
(c) Load case 2 - FEM

(d) Load case 2 - NNRPIM

(e) Load case 3 - FEM

(f) Load case 3 - NNRPIM

Figure 7.34: Stiffness comparison between methods (FEM and NNRPIM) for all load cases using gyroid remodelling law 1



(a) Load case 1 - FEM

(b) Load case 1 - NNRPIM

(c) Load case 2 - FEM

(d) Load case 2 - NNRPIM

(e) Load case 3 - FEM

(f) Load case 3 - NNRPIM

Figure 7.35: Stiffness-to-weight ratio comparison between methods (FEM and NNRPIM) for all load cases using gyroid remodelling law 1

7.4.4 Gyroid remodelling law 2

This remodelling law only differs from the first one in the stress equation which was approximated from tensile tests. Since the smoothing effect has already been studied in the previous analyses, only the specimens without any smoothing and with smoothing function type 1 are printed since the previous study showed that these perform better in stiffness and ratio for most cases. The stiffness results are to be compared to the equivalent specimens using the gyroid remodelling law 1 simulations. As it was seen in Chapter 6, both laws achieve very similar structure configuration and therefore, the main difference between specimens obtained with both laws will be the infill density applied to each of the solids, especially for higher densities where both laws differ the most.

Load case 1

The specimens based of the results from the gyroid remodeling law 2 presented higher stiffness which may indicate that the law could eventually be better at modelling the mechanical behaviour of the gyroid even though the NNRPIM results are very similar. Moreover, for all specimens except the law 1 specimens using the NNRPIM, the use of a smoothing function improved stiffness and stiffness-to-weight ratio. For both laws using a FEM analysis, the specimens presented similar stiffness for the smooth specimens. The specimens based on NNRPIM analysis presented better stiffness and STW ratio. The stiffness results for load case 1 comparing both laws are shown in Figure 7.36 and Table 7.22.

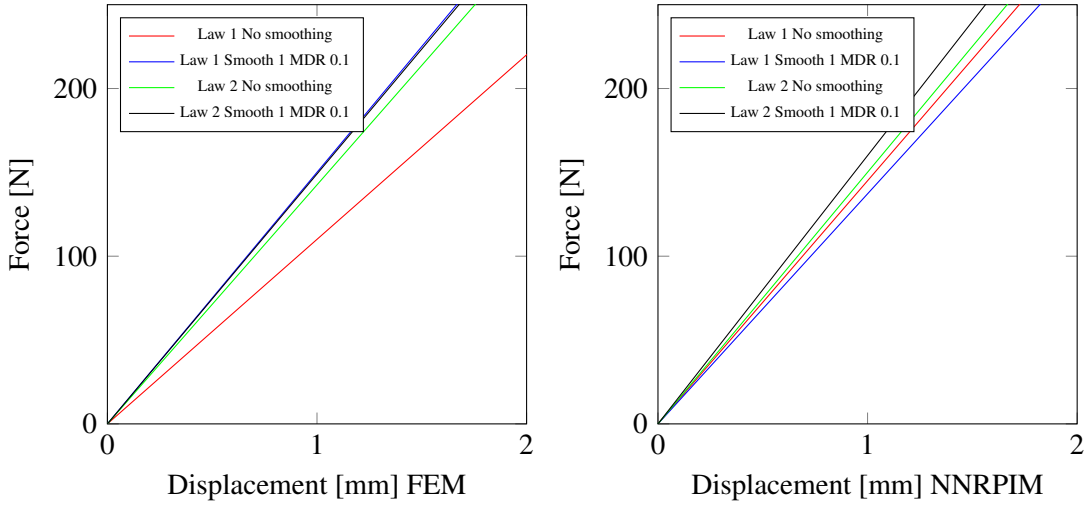


Figure 7.36: Comparison of specimens without any smoothing function applied and smoothing function type 1 for the gyroid remodelling law 1 and gyroid remodelling law 2 for load case 1

Table 7.22: Summary results of the comparative analysis of printed specimens based on the simulations using the gyroid remodelling law 1 and gyroid remodelling law 2 for for load case 1

		Mass [g]	K [N/mm]	Ratio [N/(g*mm)]
FEM	Law 1 No Smoothing	8.07 ± 0.04	110.05 ± 0.45	13.64 ± 0.01
	Law 1 Smoothing Type 1 MDR 0.1	8.60 ± 0.02	150.04 ± 1.70	17.44 ± 0.19
	Law 2 No Smoothing	8.54 ± 0.00	142.53 ± 0.63	15.77 ± 0.06
	Law 2 Smoothing Type 1 MDR 0.1	8.80 ± 0.02	149.03 ± 1.76	16.93 ± 0.17
NNRPIM	Law 1 No Smoothing	8.64 ± 0.00	145.00 ± 6.86	16.79 ± 0.79
	Law 1 Smoothing Type 1 MDR 0.1	8.75 ± 0.02	137.62 ± 2.00	15.74 ± 0.21
	Law 2 No Smoothing	8.67 ± 0.01	150.07 ± 0.43	17.30 ± 0.06
	Law 2 Smoothing Type 1 MDR 0.1	8.86 ± 0.02	160.00 ± 0.56	18.06 ± 0.10

Load case 2

For load case 2, using law 1, the specimens corresponding to smoothing type 1 presented higher stiffness both using the FEM and NNRPIM, whereas, using law 2, the specimens without any

smoothing function presented higher stiffness. Results are shown in Figure 7.37 and in Table 7.23.

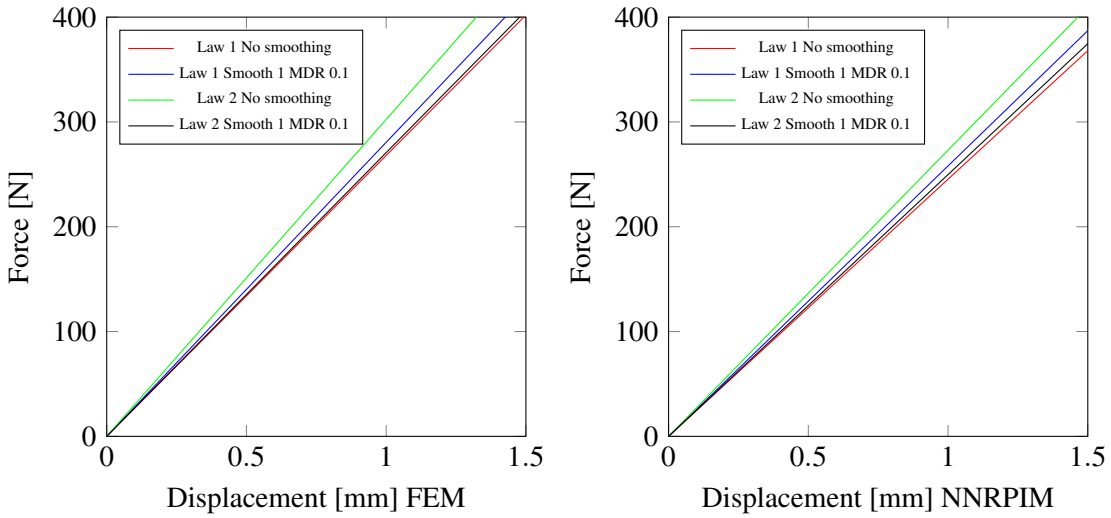


Figure 7.37: Comparison of specimens without any smoothing function applied and smoothing function type 1 for the gyroid remodelling law 1 and gyroid remodelling law 2 for load case 2

Table 7.23: Summary results of the comparative analysis of printed specimens based on the simulations using the gyroid remodelling law 1 and gyroid remodelling law 2 for for load case 2

		Mass [g]	K [N/mm]	Ratio [N/(g*mm)]
FEM	Law 1 No Smoothing	8.57 ± 0.05	267.99 ± 3.16	31.26 ± 0.26
	Law 1 Smoothing Type 1 MDR 0.1	8.80 ± 0.03	280.54 ± 8.50	31.89 ± 0.94
	Law 2 No Smoothing	8.69 ± 0.03	302.42 ± 6.38	34.79 ± 0.66
	Law 2 Smoothing Type 1 MDR 0.1	8.70 ± 0.02	270.69 ± 5.12	31.10 ± 0.52
NNRPIM	Law 1 No Smoothing	8.56 ± 0.00	245.36 ± 3.35	28.67 ± 0.40
	Law 1 Smoothing Type 1 MDR 0.1	8.73 ± 0.05	258.05 ± 0.60	29.67 ± 0.23
	Law 2 No Smoothing	8.70 ± 0.01	273.11 ± 2.19	31.40 ± 0.28
	Law 2 Smoothing Type 1 MDR 0.1	8.62 ± 0.08	249.77 ± 0.56	28.97 ± 0.43

Load case 3

Both laws presented very similar results as well as both presenting higher stiffness in specimens without any smoothing for a factor of about 1.5. Results are displayed in Figure 7.38 and Table 7.24.

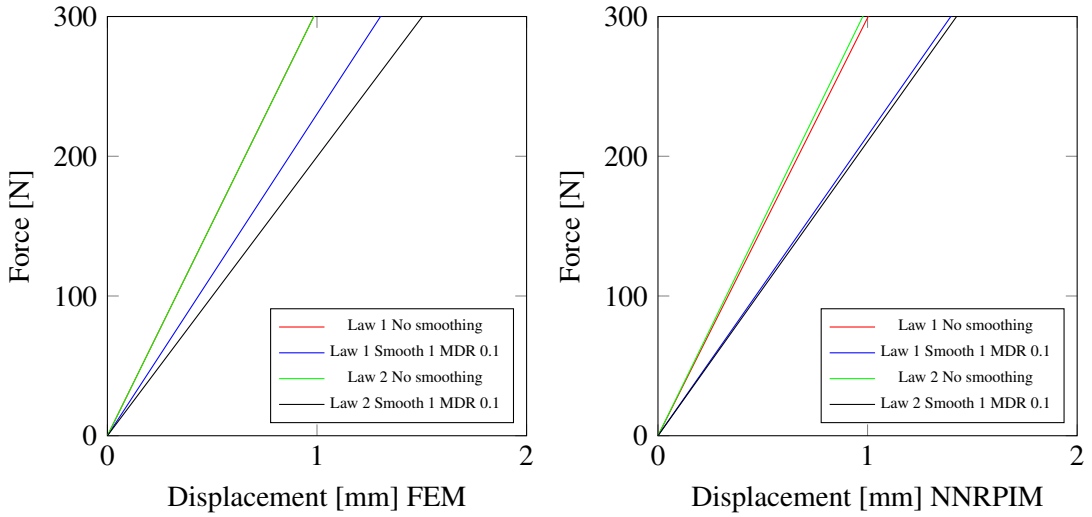


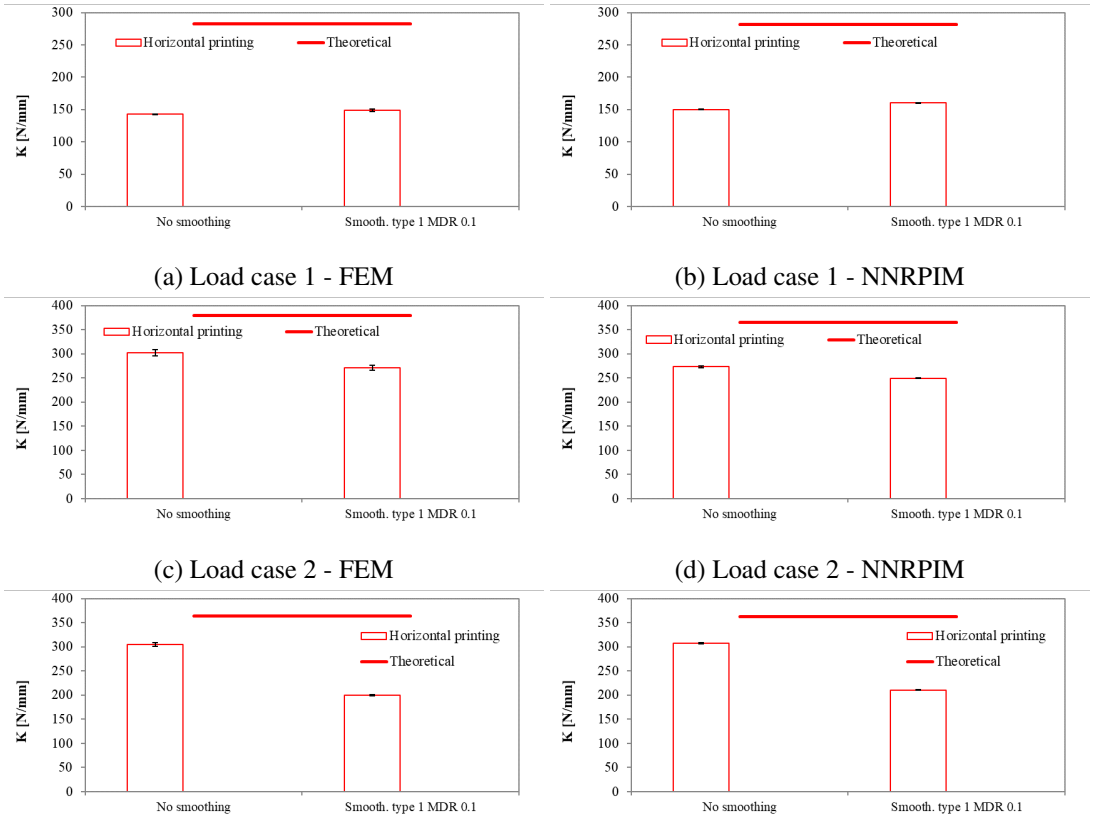
Figure 7.38: Comparison of specimens without any smoothing function applied and smoothing function type 1 for the gyroid remodelling law 1 and gyroid remodelling law 2 for load case 3

Table 7.24: Summary results of the comparative analysis of printed specimens based on the simulations using the gyroid remodelling law 2 and gyroid remodelling law 2 for for load case 3

		Mass [g]	K [N/mm]	Ratio [N/(g*mm)]
FEM	Law 1 No Smoothing	8.54 ± 0.01	304.65 ± 0.48	35.67 ± 0.04
	Law 1 Smoothing Type 1 MDR 0.1	8.29 ± 0.05	203.22 ± 3.97	24.52 ± 0.62
	Law 2 No Smoothing	8.45 ± 0.03	304.51 ± 3.61	36.04 ± 0.36
	Law 2 Smoothing Type 1 MDR 0.1	8.33 ± 0.01	199.62 ± 1.02	23.98 ± 0.15
NNRPIM	Law 1 No Smoothing	8.67 ± 0.01	299.09 ± 4.28	34.50 ± 0.46
	Law 1 Smoothing Type 1 MDR 0.1	8.41 ± 0.07	214.71 ± 3.83	25.52 ± 0.25
	Law 2 No Smoothing	8.42 ± 0.00	306.98 ± 1.29	36.46 ± 0.17
	Law 2 Smoothing Type 1 MDR 0.1	8.27 ± 0.01	210.57 ± 0.73	25.48 ± 0.04

Summary

This law obtained very similar structure to those obtained with law 1. For load case 1, a positive effect of smoothing functions was obtained for load case 1, and a negative effect of smoothing functions was obtained for load cases 2 and 3. This gyroid law proved best in stiffness prediction for load case 2 and 3 for specimens without any smoothing function. These results are shown in Figures 7.39 and 7.40 for stiffness and stiffness-to-weight ratio respectively. There is no clear tendency about the efficiency of either numerical method in obtaning structures with a better mechanical behaviour when materialized.



(a) Load case 1 - FEM

(b) Load case 1 - NNRPIM

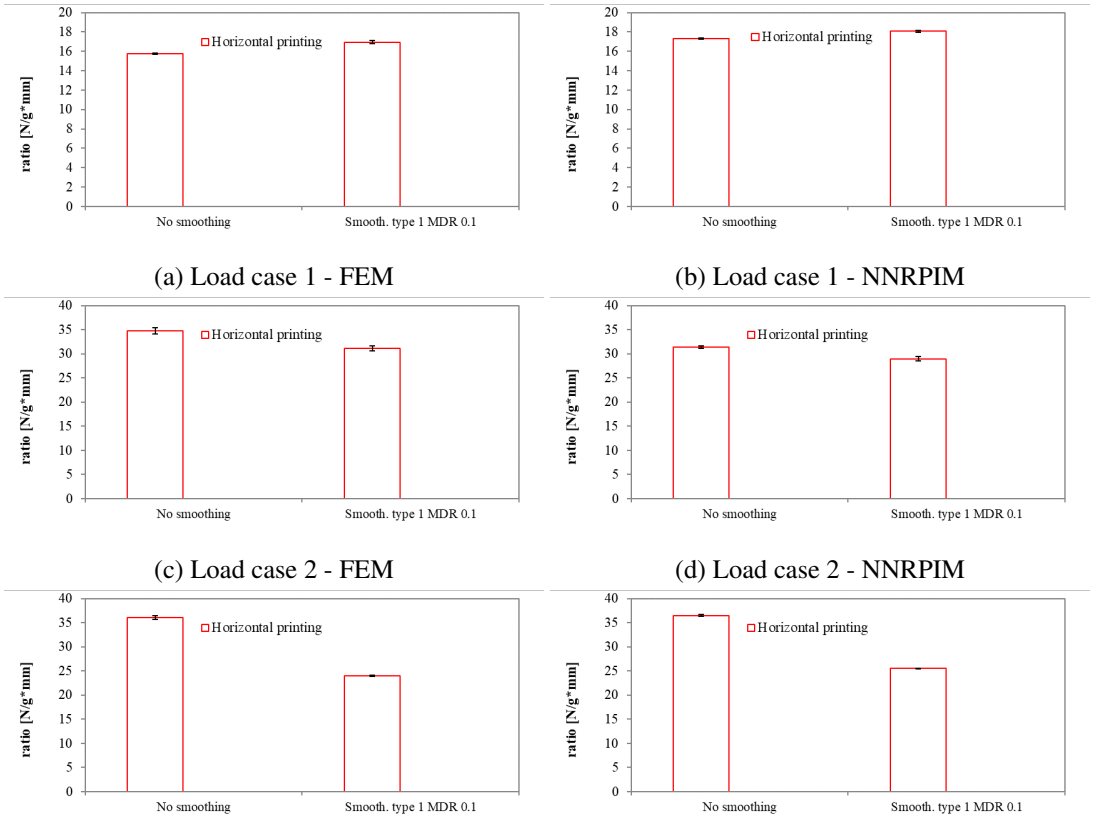
(c) Load case 2 - FEM

(d) Load case 2 - NNRPIM

(e) Load case 3 - FEM

(f) Load case 3 - NNRPIM

Figure 7.39: Stiffness comparison between methods (FEM and NNRPIM) for all load cases using gyroid remodelling law 2



(a) Load case 1 - FEM

(b) Load case 1 - NNRPIM

(c) Load case 2 - FEM

(d) Load case 2 - NNRPIM

(e) Load case 3 - FEM

(f) Load case 3 - NNRPIM

Figure 7.40: Stiffness-to-weight ratio comparison between methods (FEM and NNRPIM) for all load cases using gyroid remodelling law 2

7.5 Influence of printing direction

From all tested specimens it was possible to conclude that the vertically printed specimens present higher stiffness as well as higher stiffness-to-weight ratio than all other specimens. This is due to the fact that when the load is applied in the direction of building, the filament layers are compressed between each other whereas when the specimen is printed with the larger face placed on the table, the layers are parallel to the direction of the load. This causes for shear stress to appear between the layers. Figure 7.41 shows a schematic image of the deposition of the layers for both cases relatively to loading direction.

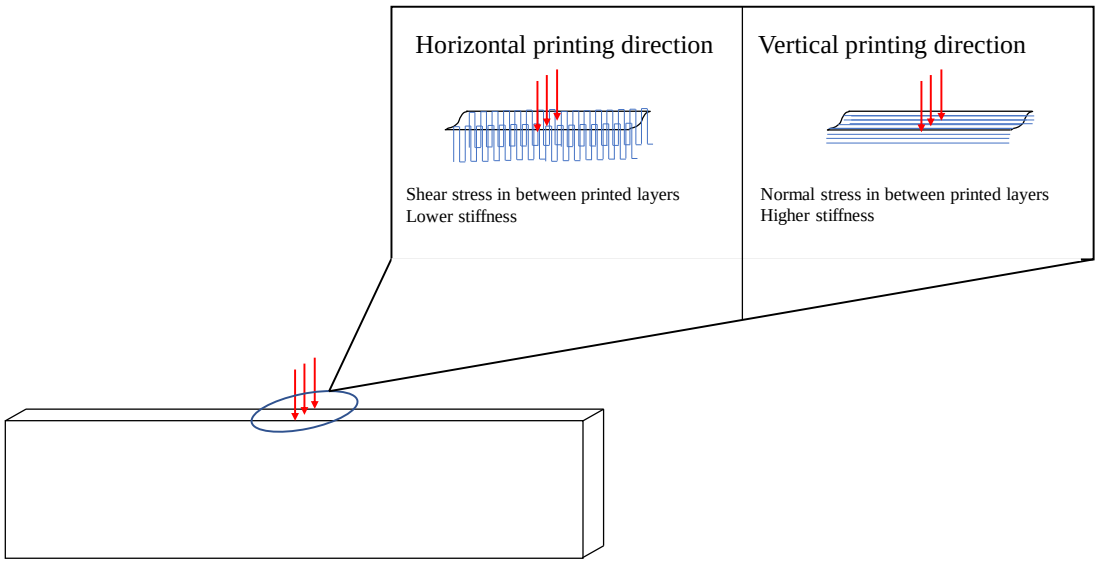


Figure 7.41: Comparison between layer position of horizontally and vertically printed specimens

Preferable printing direction is same the direction as the load is being applied, that is, the area that maximizes the cross section perpendicular to load application (Shojib Hossain et al., 2014; Torres et al., 2016).

7.6 Comparison with numerical simulations

In order to evaluate how the numerical simulations correlate to the experimental analysis, calculated stiffness is compared to measured stiffness. Simulations were conducted for a 1mm plate and it was necessary to obtain the equivalent stiffness for a 5mm plate. Table 7.25 and 7.26 display the theoretical stiffness for structural optimization analysis and gyroid remodelling analysis respectively. The gyroid remodelling analysis with law 1 and a value of β of 0.05 has its results shown in Table 7.27. All mentioned tables are in units of N/mm.

Visibly, the gyroid material based which takes into consideration the manufacturing process, predicts a much lower stiffness meaning that building any component with the gyroid shape will only present about 10 to 15% of the stiffness it would present if the material had been processed in bulk, for example, through injection molding.

Table 7.25: Predicted stiffness for a 5mm plate at a density level of 0.6 g/cm^3 - Structural optimization analysis

		Load case 1	Load case 2	Load case 3
Parabolic law	FEM	1985.918	2953.622	2519.043
	NNRPIM	1963.651	2939.302	2539.556
Linear law	FEM	1618.441	2537.322	2235.667
	NNRPIM	1623.158	2599.095	2274.29

Table 7.26: Predicted stiffness for a 5mm plate at a density level of 0.6 g/cm^3 - Gyroid remodelling analysis

		Load case 1	Load case 2	Load case 3
Remodelling law 1	FEM	250.67	383.50	364.25
	NNRPIM	246.69	370.75	363.29
Remodelling law 2	FEM	282.75	378.85	364.10
	NNRPIM	281.40	364.80	362.61

Table 7.27: Predicted stiffness for a 5mm plate at a density level of 0.6 g/cm^3 - Gyroid remodelling analysis with law 1 ($\beta = 0.05$)

	Load case 1
FEM	248.849
NNRPIM	245.442

7.6.1 Summary

Each conducted test is compared in terms of percentage of accuracy with predicted stiffness from numerical simulations. Load case 3 presented the most accuracy as well as presenting a better behaviour for structures with no smoothing. Moreover, gyroid law 2 seems to represent a more accurate behaviour of the gyroid law. Tables 7.28, 7.29, 7.30 and 7.32 present the percentage of stiffness results for all tested laws. For the remodelling analysis of load case 1 with gyroid remodelling law 1 using a density decrease ratio of 0.05 results are shown in Table 7.31.

Table 7.28: Proportion of stiffness for each set of specimens compared to the original simulation for the specimens based on structural optimization simulations with a parabolic law

		Load case 1	Load case 2	Load case 3
FEM	No Smoothing	2%	-	14%
	Smoothing Type 1 MDR 0.1 hor	9%	12%	11%
	Smoothing Type 1 MDR 0.1 vert	10%	12%	13%
	Smoothing Type 1 MDR 0.2	8%	11%	12%
	Smoothing Type 3	8%	10%	10%
NNRPIM	No Smoothing	2%	-	17%
	Smoothing Type 1 MDR 0.1 hor	9%	11%	13%
	Smoothing Type 1 MDR 0.1 vert	11%	12%	14%
	Smoothing Type 1 MDR 0.2	9%	10%	12%
	Smoothing Type 3	8%	6%	11%

Table 7.29: Proportion of stiffness for each set of specimens compared to the original simulation for the specimens based on structural optimization simulations with a linear law

		Load case 1	Load case 2	Load case 3
FEM	No Smoothing	5%	-	11%
	No Smoothing reinforced	-	5%	-
	Smoothing Type 1 MDR 0.1	9%	8%	6%
NNRPIM	No Smoothing	5%	-	12%
	No Smoothing reinforced	8%	8%	-
	Smoothing Type 1 MDR 0.1	7%	9%	9%

Table 7.30: Proportion of stiffness for each set of specimens compared to the original simulation for the specimens based on gyroid remodelling simulations with law 1

		Load case 1	Load case 2	Load case 3
FEM	No Smoothing	44%	70%	84%
	Smoothing Type 1 MDR 0.1 hor	60%	63%	56%
	Smoothing Type 1 MDR 0.1 vert	65%	82%	65%
	Smoothing Type 1 MDR 0.2	61%	65%	51%
	Smoothing Type 3	55%	59%	47%
NNRPIM	No Smoothing	51%	64%	82%
	Smoothing Type 1 MDR 0.1 hor	49%	68%	60%
	Smoothing Type 1 MDR 0.1 vert	59%	78%	67%
	Smoothing Type 1 MDR 0.2	49%	61%	53%
	Smoothing Type 3	46%	62%	65%

Table 7.31: Proportion of stiffness for each set of specimens compared to the original simulation for the specimens based on gyroid remodelling simulations with law 1 and a β value of 0.05

		Load case 1
FEM	outside reinforcement	53%
NNRPIM	outside reinforcement	50%
	truss	40%

Table 7.32: Proportion of stiffness for each set of specimens compared to the original simulation for the specimens based on gyroid remodelling simulations with law 2

		Load case 1	Load case 2	Load case 3
FEM	No Smoothing	50%	80%	84%
	Smoothing Type 1 MDR 0.1 hor	53%	71%	55%
NNRPIM	No Smoothing	53%	75%	85%
	Smoothing Type 1 MDR 0.1 hor	57%	68%	58%

7.7 Result discussion

Two types of remodelling analysis were tested, namely, structural optimization and optimization based on bone remodelling analysis using property laws from experimental characterization of the gyroid infill. For some load cases, and seldom even varying with the method, the specimens without any smoothing function applied presented higher STW ratio and stiffness than specimens to which smoothing functions were applied.

For the structural optimization analysis with a parabolic law where the structure was quite inefficient, the employment of a smoothing function, greatly enhanced stiffness. When a linear law was employed, and no minimal density area was printed, stiffness was improved but still presented lower stiffness than a smoothed specimen. The specimens obtained with a parabolic law presented higher ratio which may be due to being printed with a density of 0.7 instead of 0.6, indicating that, as the volume fraction is being reduced, stiffness and stiffness-to-weight ratio also decrease.

The gyroid remodelling law specimens, printed with minimal density area presented higher stiffness and ratio than smooth specimens. This could mean that when stiffness of the truss structure in itself is low, smoothing functions can help overcome this but not as much as the presence of a low density reinforcement around the structure.

Moreover, the more stable the load case was, the better the simulations behaved and correlated to the simulation results, that is, for load case 3 where load placement is the most distributed, *no-smoothing* specimens presented the best behaviour followed by load case 1 and finally load case 2. Comparing gyroid remodelling laws 1 and 2, for most cases, the specimens obtained with gyroid law 2 presented higher stiffness-to-weight ratio as well as a slightly higher correlation to theoretical stiffness.

The influence of printing direction proved to be extremely relevant in increasing stiffness. Although these are more complicated to print and are more prone to present the defects mentioned, the increase in section area in perpendicularly to loading direction (Torres et al., 2016) is important to optimize the behaviour of parts manufactured through an AM process with such anisotropy.

Chapter 8

Femur Scaffold Analysis: a preliminary study

In the literature, TPMS have often been used as a possibility for bone scaffold. The easily controlled density and therefore, control of elastic modulus permits to avoid stress shielding which occurs when there is a high difference in modulus (Ma et al., 2019). Moreover, gyroid scaffolds are, according to Melchels et al. (2010), more easily wetted and intruded, which results in a more homogeneous cell distribution and deeper cell colonization. Therefore, this chapter will aim at producing an optimized femur-shaped part based on the methodology proposed on this thesis. Remodelling analysis based on the gyroid remodelling laws are employed for the finite element and meshless methods. Based on the conclusions taken previously, it is important to build the specimen in same direction as the one it is being solicited so the prototypes will be built vertically. Two different density levels will be tested, 0.6 and 0.4 g/cm^3 without having any smoothing function applied.

The objective of this preliminary study is to test the capability of the gyroid remodelling laws to evolve into a structure which is similar to the one obtained with bone remodelling algorithms and to correlate with numerical results. This chapter is dedicated to the last stage of the methodology presented in Figure 5.1, that is, stage 6.

8.1 Model and boundary conditions

The femur is a long bone articulated in the hip-bone being that the body weight is directly applied to the femur head. To simulate an approximated load case, two vertical loads (which correspond to distributed loads on the femur head) are applied. The two dimensional equivalent of the load case is shown in Figure 8.1. These boundary conditions are based on what is found in the literature (Beaupré et al., 1990a,b; Belinha, 2014; Idhammad et al., 2013). The scale of the model corresponds to approximately $\frac{1}{3}$ of the size of an average bone taking into reference the length of the femoral axis (Ishii et al., 2012).

The algorithm for solid creation needs a structured hexahedral mesh/nodal distribution. This required voxelization of a Solidworks part existent online (An, 2013) (Figure 8.2). The voxelized model and the abaqus meshed part are shown in Figure 8.3.

Figure 8.4 shows the three-dimensional voxelized model with boundary conditions. This voxelization and meshing corresponds to step 10 in the list presented in Chapter 5.

After meshing the part in Abaqus, the .inp file is imported into Femap and then exported into another .inp file which is read by FEMAS. Boundary conditions are applied in FEMAS. The full model with boundary conditions is shown in Figure 8.4. It is understood that the mesh is rather course, however, refining the mesh size requires an exponentially greater amount of computational power even for the voxelization process. Unlike the fine plate case, a solid design domain with elevated thickness takes much longer to compute the nodal integration for the meshless method.

For the FE analysis, hexahedral elements with 2.5x2.5x2.5mm^3 size were used and for the NNRPIM, a regular nodal distribution was employed with a constant interpolation function and a full integration scheme. In addition, a first order influence cell was used.

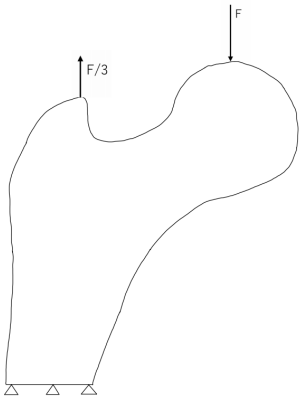
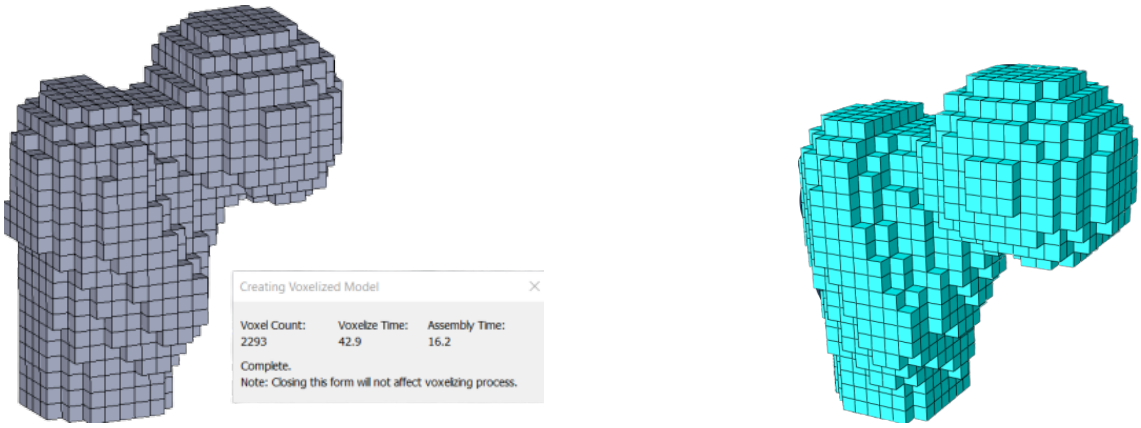


Figure 8.1: Two-dimensional approximation of the boundary conditions used for the simulations



Figure 8.2: Femur 3D model An (2013)



(a) Voxelization in Solidworks (b) Abaqus Meshing

Figure 8.3: Voxelization and meshing of the part

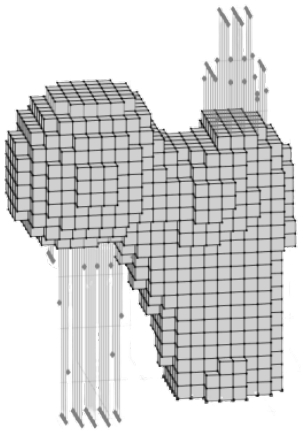


Figure 8.4: Voxelixed 3D model with boundary conditions

8.2 Analysis

8.2.1 Linear elasto-static analysis

For a real femoral bone, considering the load conditions which were used, the effective stress distribution follows a pattern where the maximum stress occurs at the thinest part of the bone as can be seen in Figure 8.5.

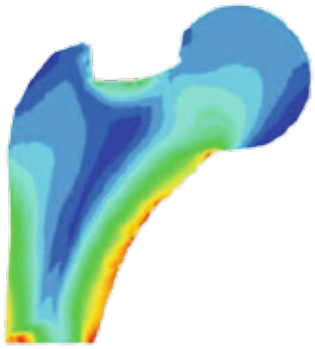
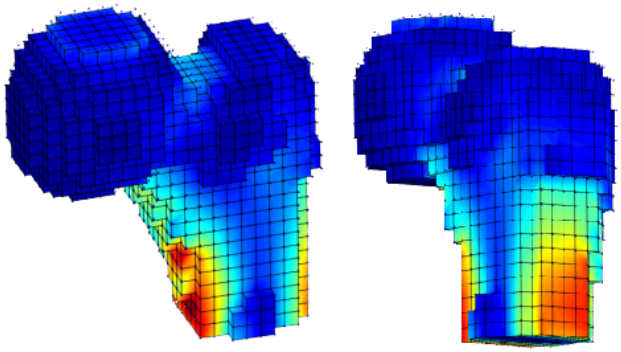
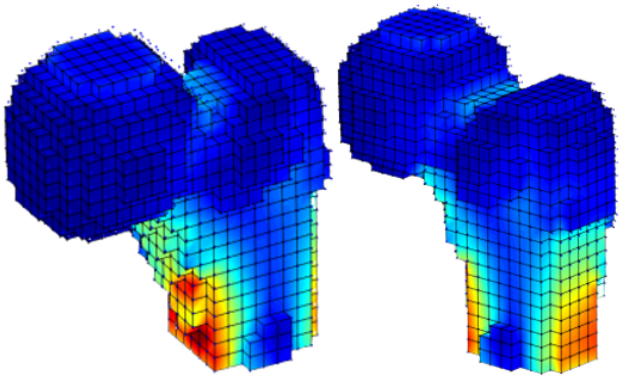


Figure 8.5: Stress distribution for the femoral bone with similar loading to that of 8.1. Adapted from Belinha (2014)

The results which were obtained with the voxelized model follow a similar pattern even with a sparse mesh as it can be seen in Figure 8.6. This validation allows to continue with the remodelling analysis [1].



(a) FEM



(b) NNRPIM

Figure 8.6: Equivalent Von-Mises Stress distribution for the elasto-static analysis

[1] As this analysis belongs to the linear regime of the material, no numerical value or colorbar is being presented since for the remodelling analysis, each variable is brought to its elastic limit and load magnitudes present in the literature are adapted to bone properties. The relevant aspect to highlight is that stress analysis follows the same pattern seen in the literature.

8.2.2 Remodelling analysis

Both gyroid laws developed in section 5.6 were employed. The remodelling parameters used were:

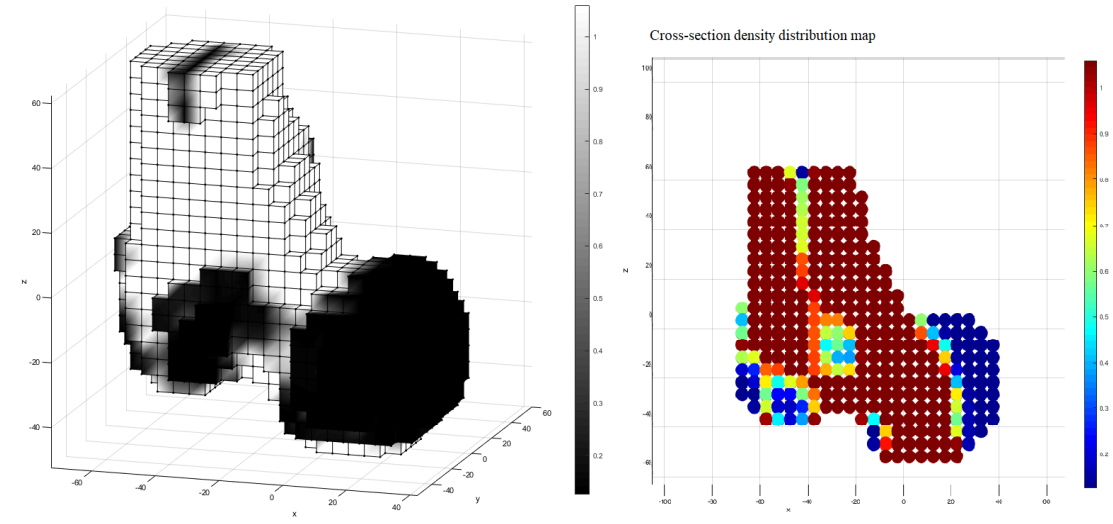
- **Maximum density** of 1.06 g/cm^3
- **Transition density** of 0.6 g/cm^3
- **Minimum density** of 0.125 g/cm^3
- **Ultimate traction/compression ratio** of 0.5
- **Density increase ratio** α of 0.0
- **Density decrease** β of 0.075
- **Maximum number of times that a point would remodel** of 2

It is expected that the density distribution follows a pattern were a higher density is verified at the thinner part of the bone. Due to the coarse mesh, the occurrence of fine trabeculae will not be as visible as two dimensional simulations found in the literature (Belinha, 2014).

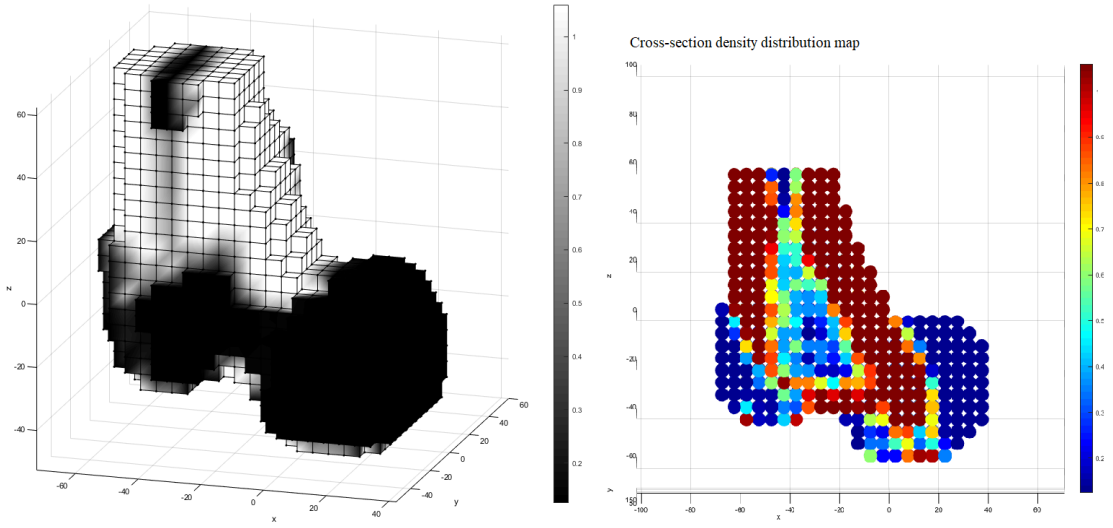
Gyroid remodelling law

The remodelling results are similar to other studies conducted on three-dimensional bone remodelling where two density levels are visible, being that the higher density zone occurs at the thinnest part of the femur. The analysis was conducted both with FEM and NNRPIM where the density distribution results were very similar. Both gyroid remodelling laws presented similar results and the same structure configuration. For gyroid remodelling law 1, density distribution results for the FEM are shown in Figure 8.7 and the density distribution for the NNRPIM is shown in Figure 8.8. For gyroid remodelling law 2, these results are shown in Figure 8.9 for the FEM and Figure 8.10 for the NNRPIM. The application of both gyroid remodelling laws corresponds to step 11 in stage 6.

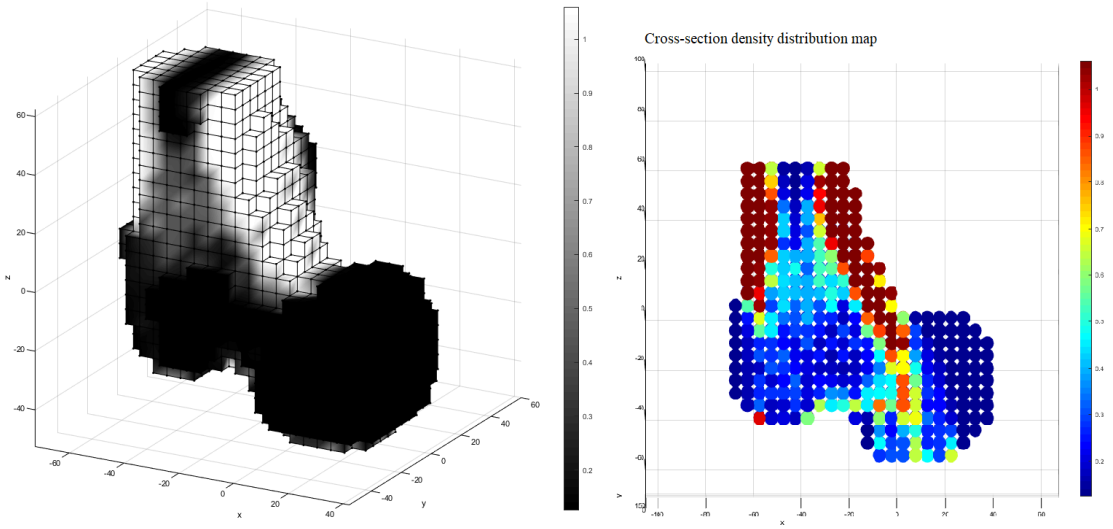
Comparing with bone remodelling results obtained with an actual bone tissue remodelling law, the respective density distribution in its medium cross section is shown in Figure 8.11 for the FEM analysis and in Figure 8.12 for the NNRPIM analysis. The density distribution map in the femur model follows the same pattern with the gyroid remodelling law and with the bone remodelling law, which validates the use of the gyroid remodelling law as a tool for building bone tissue scaffold based on TPMS.



(a) Apparent density 0.8g/cm3, volume fraction = 65%

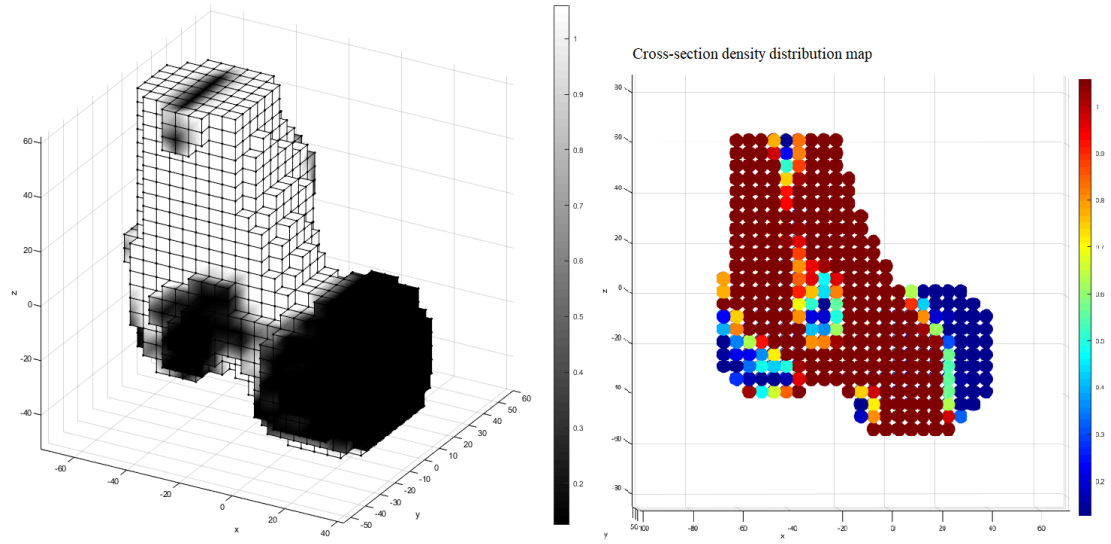


(b) Apparent density 0.6g/cm3, volume fraction = 50%

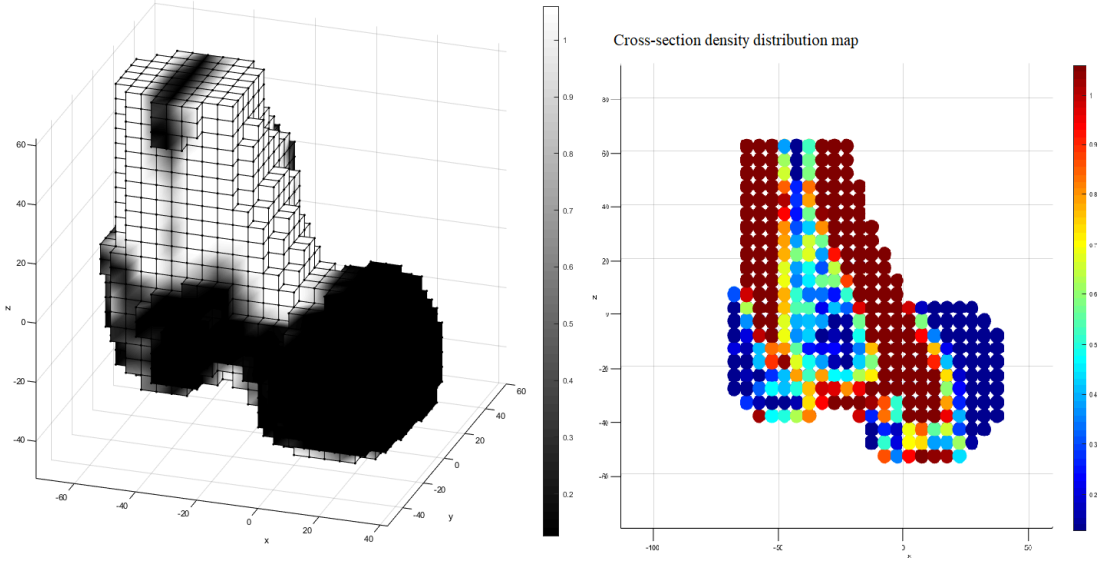


(c) Apparent density 0.4g/cm3, volume fraction = 33%

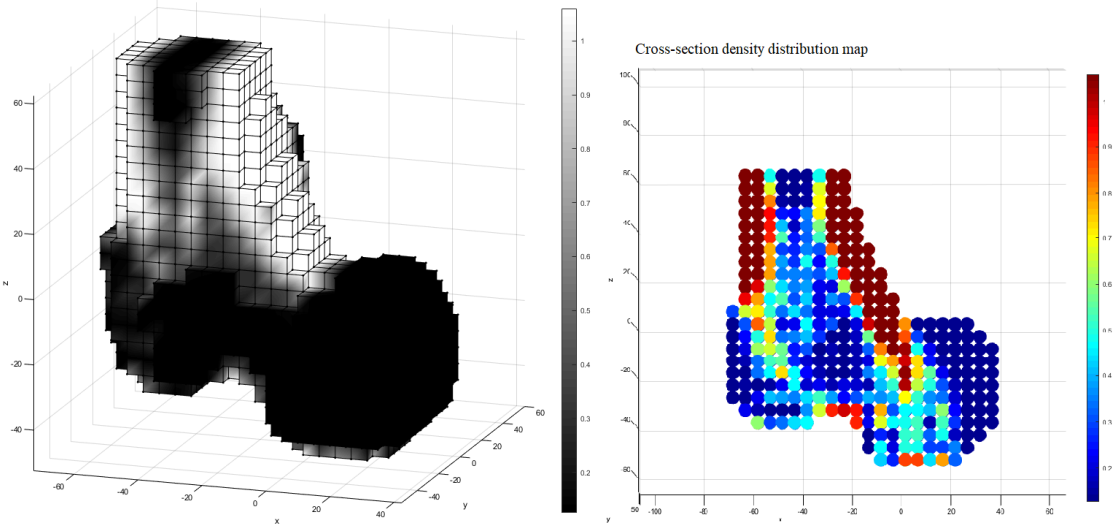
Figure 8.7: Femur remodelling with the gyroid remodelling law 1 using the FEM



(a) Apparent density 0.8g/cm3, volume fraction = 65%

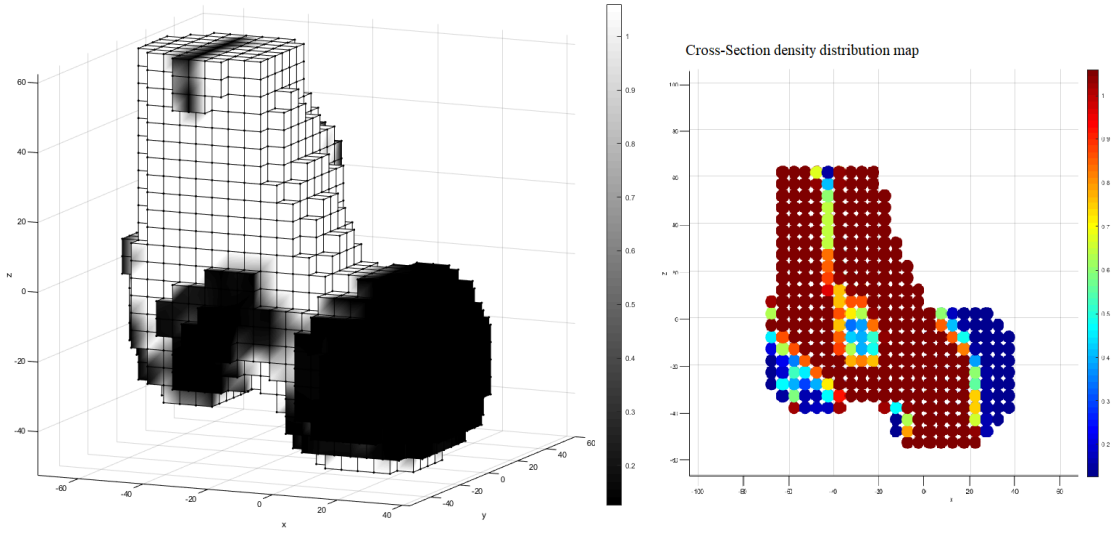


(b) Apparent density 0.6g/cm3, volume fraction = 50%

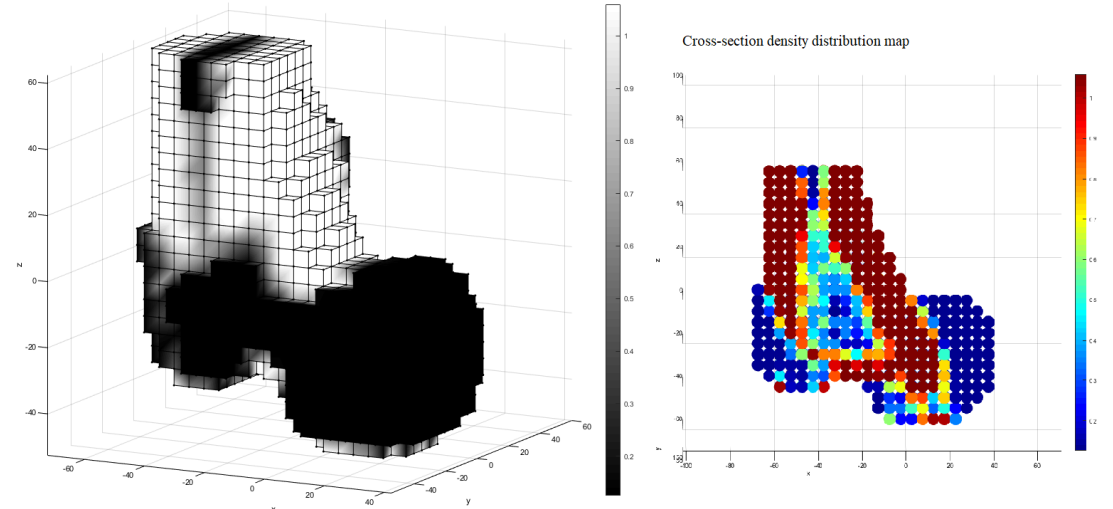


(c) Apparent density 0.4g/cm3, volume fraction = 33%

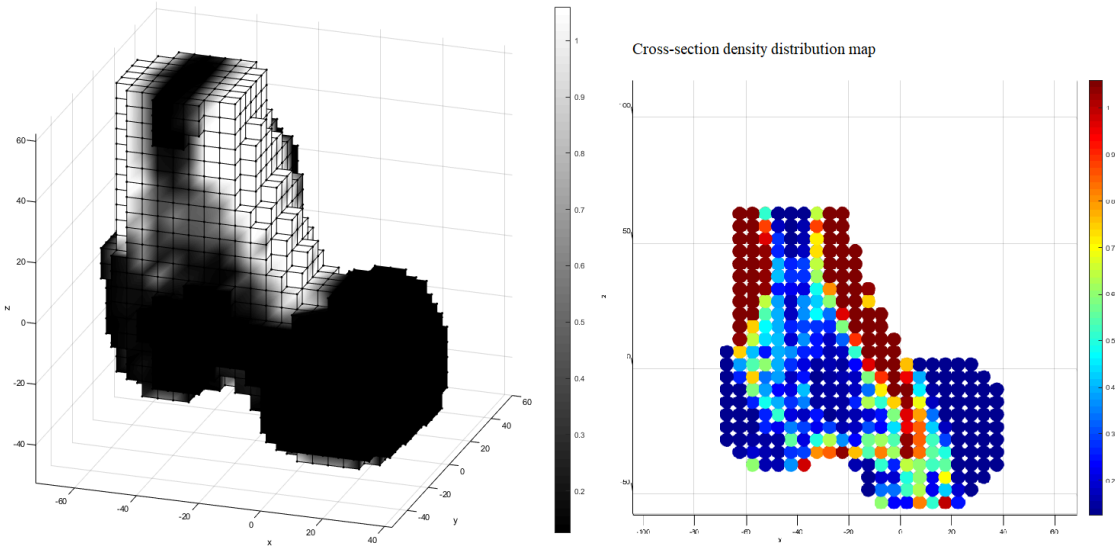
Figure 8.8: Femur remodelling with the gyroid remodelling law 1 using the NNRPIM



(a) Apparent density 0.8g/cm3, volume fraction = 65%

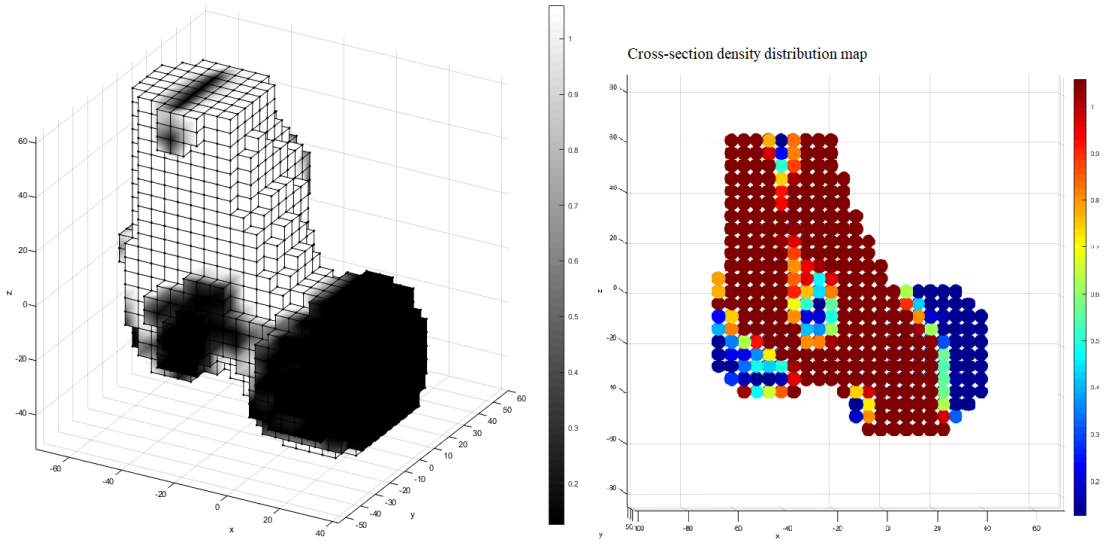


(b) Apparent density 0.6g/cm3, volume fraction = 50%

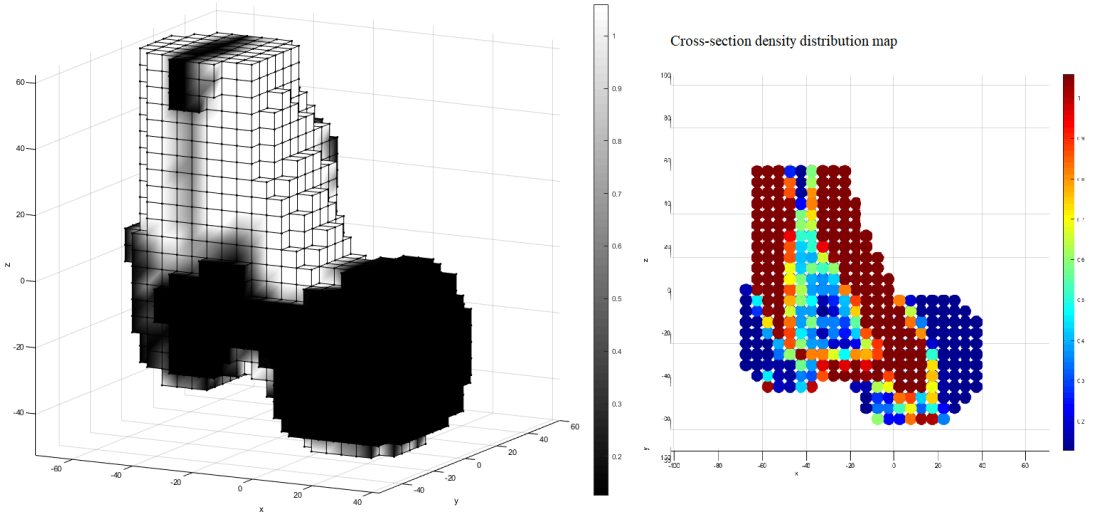


(c) Apparent density 0.4g/cm3, volume fraction = 33%

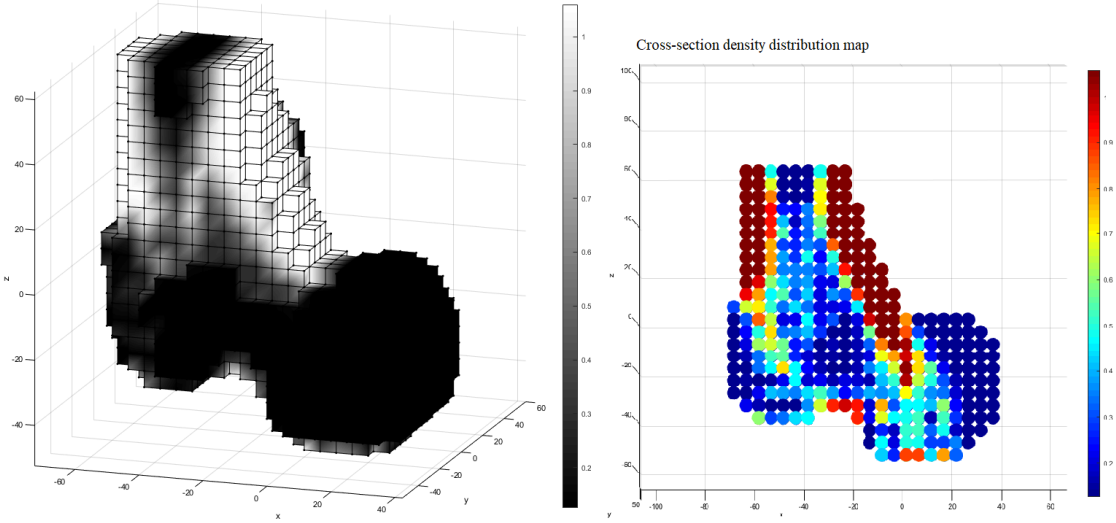
Figure 8.9: Femur remodelling with the gyroid remodelling law 2 using the FEM



(a) Apparent density 0.8g/cm3, volume fraction = 65%

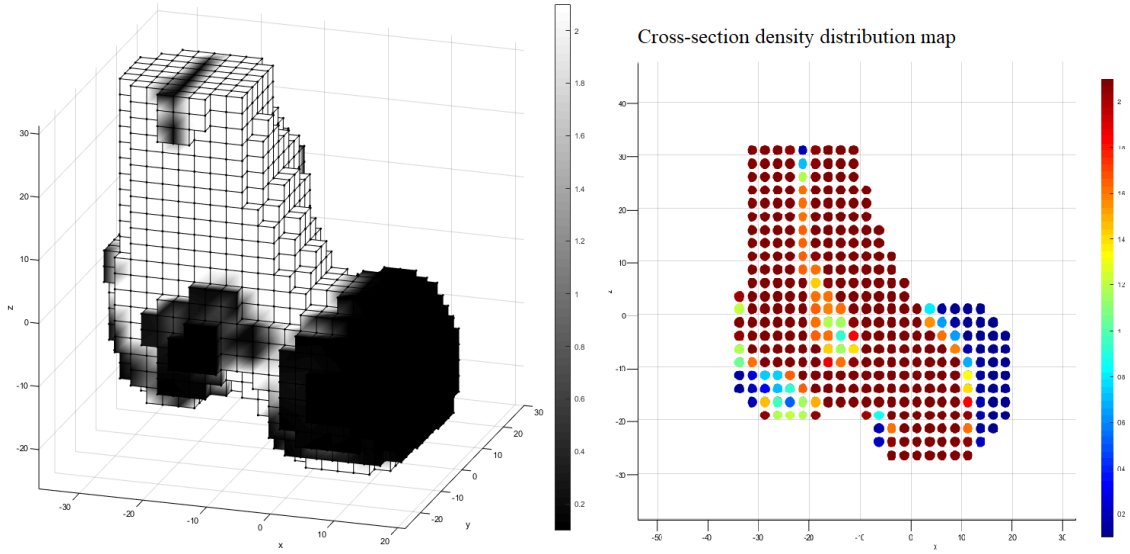


(b) Apparent density 0.6g/cm3, volume fraction = 50%

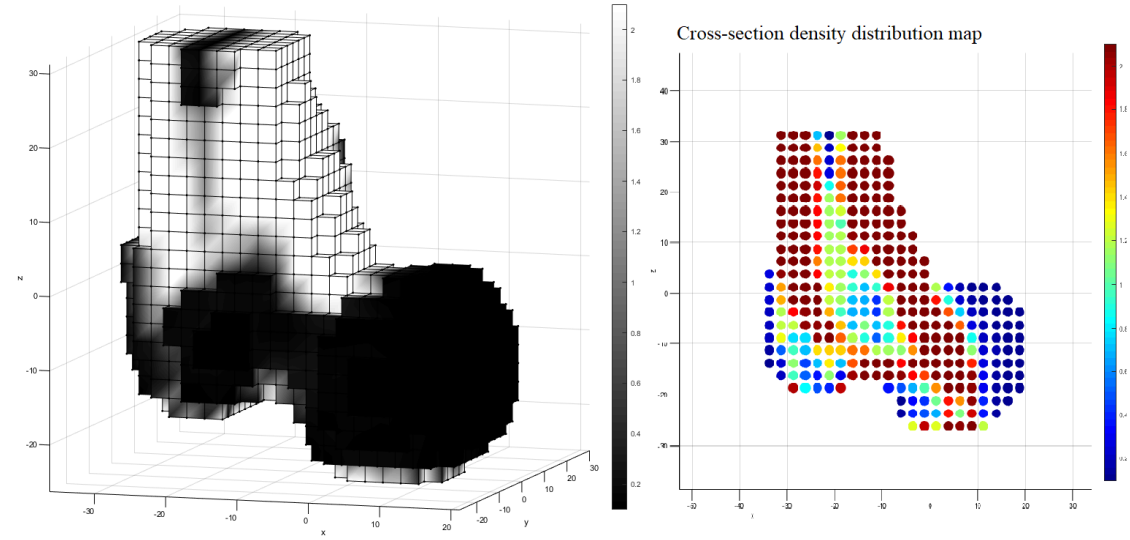


(c) Apparent density 0.4g/cm3, volume fraction = 33%

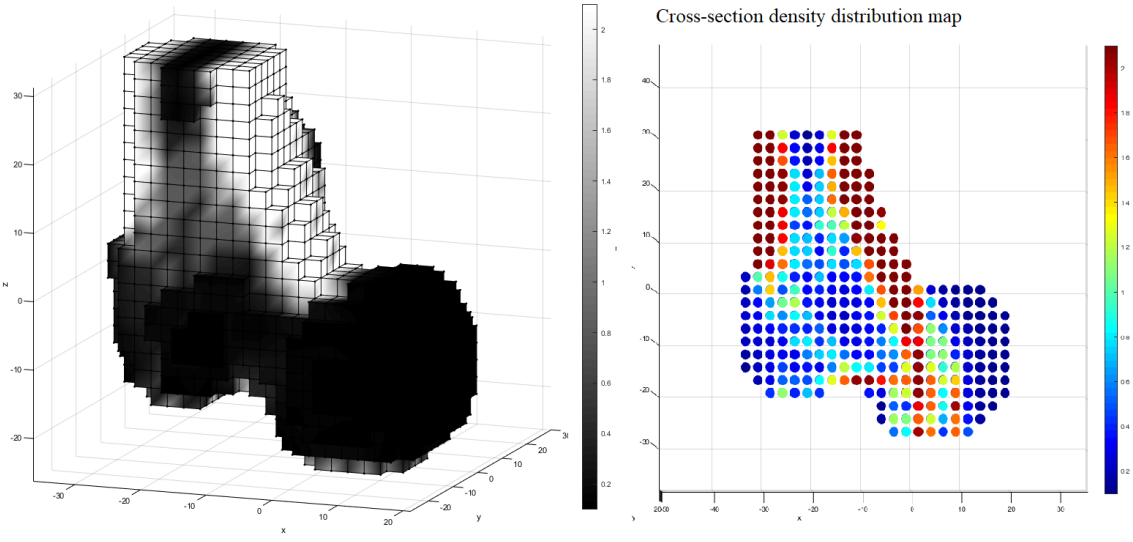
Figure 8.10: Femur remodelling with the gyroid remodelling law 2 using the NNRPIM



(a) Apparent density 1.6g/cm3, volume fraction = 65%

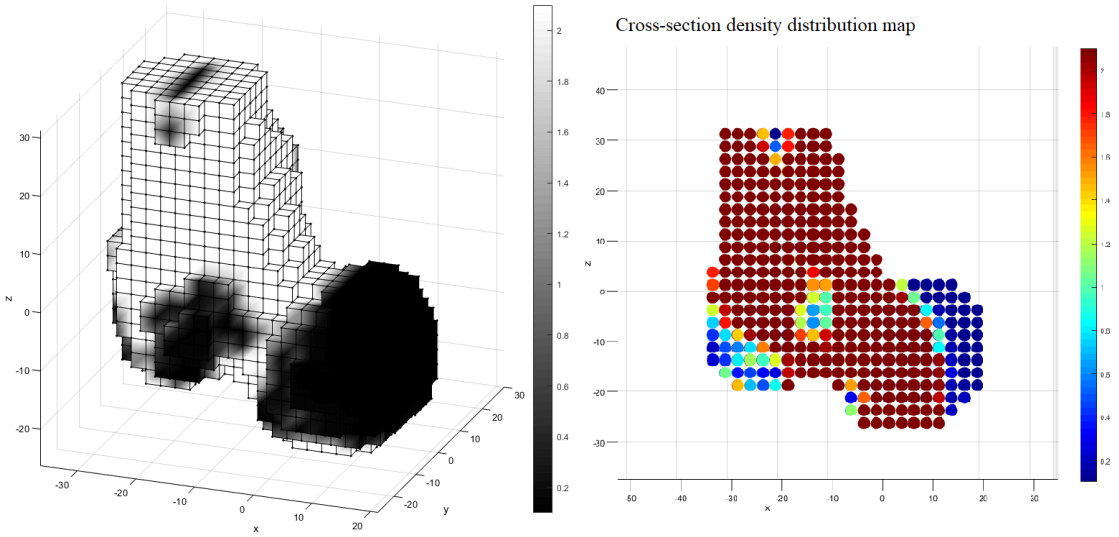


(b) Apparent density 1.2g/cm3, volume fraction = 50%

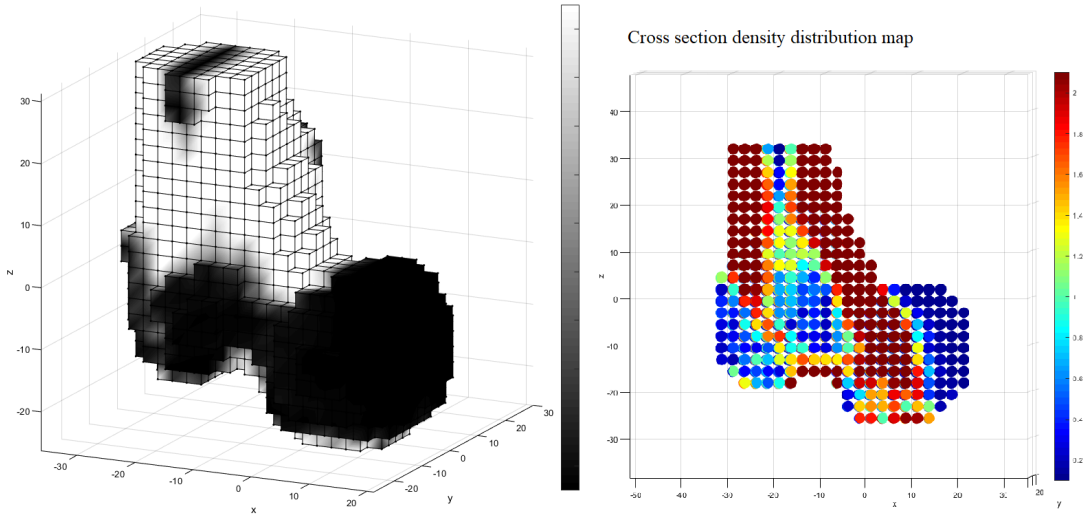


(c) Apparent density 0.8g/cm3, volume fraction = 33%

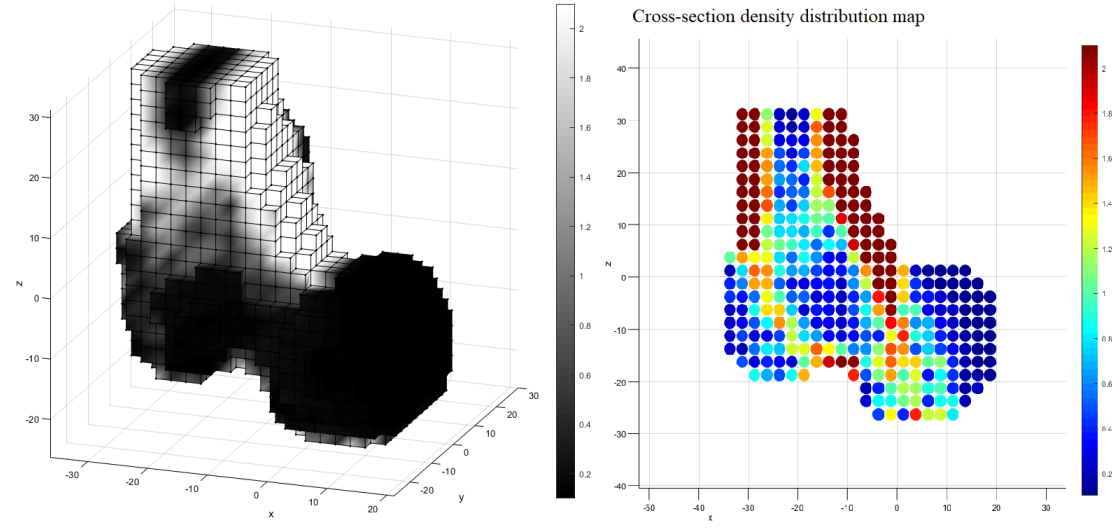
Figure 8.11: Femur remodelling with a bone remodelling law using the FEM



(a) Apparent density 1.6g/cm3, volume fraction = 65%



(b) Apparent density 1.2g/cm3, volume fraction = 50%



(c) Apparent density 0.8g/cm3, volume fraction = 33%

Figure 8.12: Femur remodelling with a bone remodelling law using the NNRPIM

Moreover, even though the used mesh is rather coarse, the obatined trabecular structure is conistent with two-dimensional solutions found in the literature, for example, the solutions shown in Figure 8.13 which includes FEM solutions as a the meshless method used in this thesis.

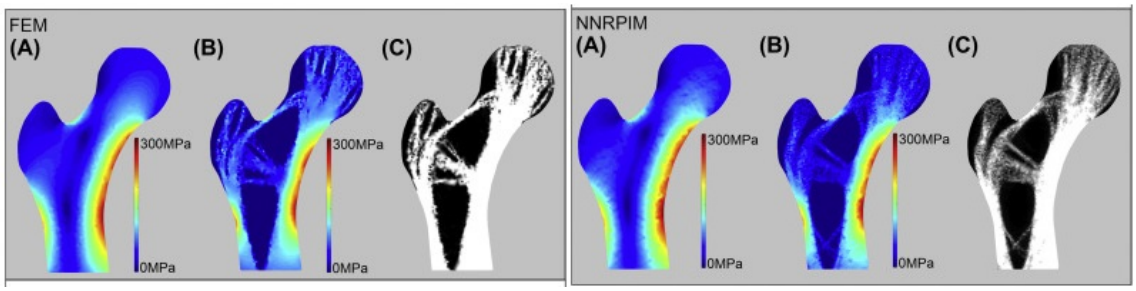


Figure 8.13: Bone remodelling displaying the trabecular structure of the femoral bone through 2D analyses using the two numerical methods employed in these thesis. Adapted from (Peyroteo et al., 2018).

Summarizing, the remodelling algorithm formed two large trabeculae aligned with the direction of load application, as well as a transversal thinner trabeculae which gets thinner and thinner at every iteration, and disappearing completely at a volume fraction of 33%. These three dimensional structures can be seen in Figure 8.14 which shows a representation of the.*stl* files obtained from the slicer.

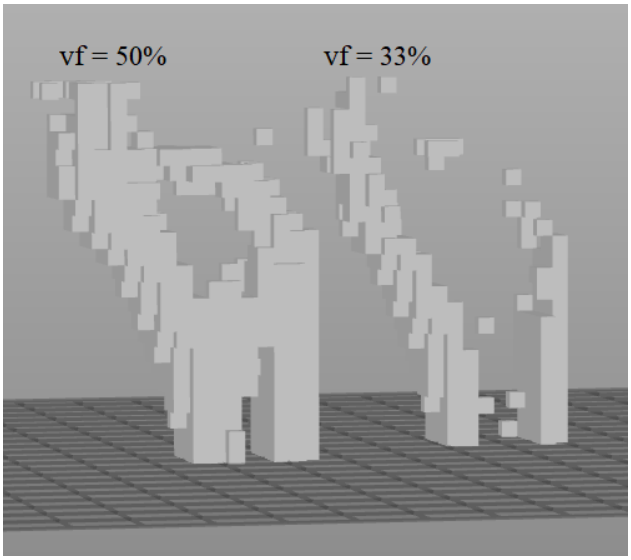


Figure 8.14: High density structures from the femur prototypes

The evolution results of stiffness with density, for both laws are shown in Figure 8.15 where the previous statements about the similarities of both laws are visible, since both plots show the same sort to "ladder effect" with the FEM showing slightly greater siffness for higher densities.

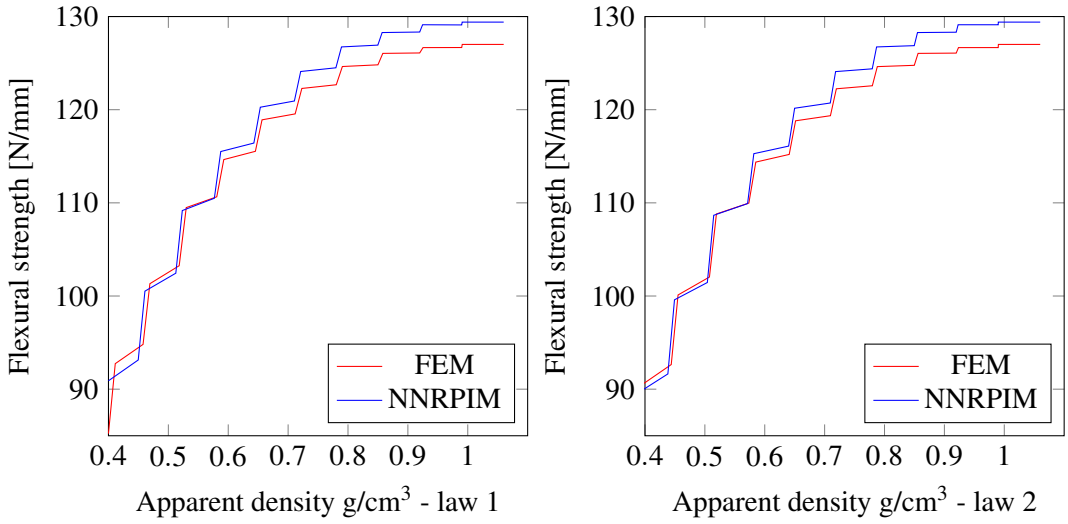


Figure 8.15: Stiffness evolution with density for the gyroid remodelling analysis applied to the femur scaffold

8.3 Printing of the prototypes

This section comprises steps 12 and 13 of the last stage menstioned in Figure 5.1 in Chapter 5. The post-processing Matlab script was run on the data from the remodelling simulations. According to the previous conclusions, the specimens did not undergo any smoothing function. In addition, it is necessary to add support structures while handling the part on the slicing software as the femur head is overhanging from the base. Having printed the parts, the final prototype has the appearance shown in Figure 8.16 - front and rear view.

The necessity for supports increased contact area with the building surface due to the *raft* which is created, and thus warping defects were not an issue. Moreover, these specimens were printed in the same direction as the direction where the load is applied. The areas at a lower density could suffer slight damage when removing the support structures. One alternative would be to print the support structures in PVA which is a water soluble polymer and very often used for this purpose.

The interior trabecular structure predicted in the remodelling analysis was obtained was it is shown in Figure 8.17 for two specimens, at 50% and 33% volume fraction. Moreover, the transversal trabeculae is present for the specimen at 50% volume fraction and absent at the specimen with 33% volume fraction, just as was indicated in the simulations.



(a) Front View (b) Rear View

Figure 8.16: Example of a femur prototype based on the FEM simulation with the gyroid remodelling law 1 for an apparent density of 0.6 g/cm^3, which is equivalent to 50% volume fraction

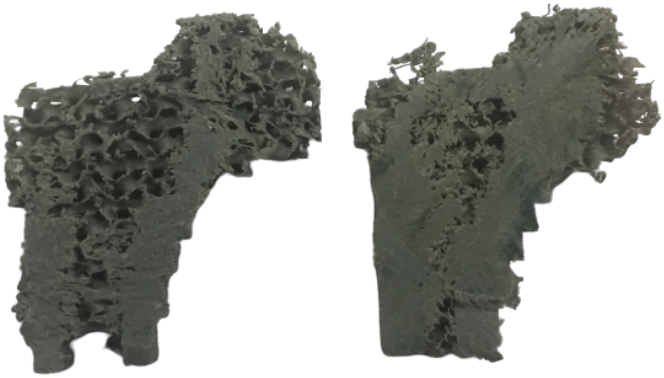


Figure 8.17: Sectional cut of two prototypes at the two tested volume fractions

8.4 Experimental testing

A load case similar to the simulated load case was recreated in order to conduct experimental testing. Only the compressive load was applied to the specimen as it is the most prominent because the tensile load is 1/3 of the compressive load. The support tool to emulate the essential boundary condition is shown in Figure 8.18 which also shows how the specimen is placed. The same machine from flexural testing was used. Lowering speed was 1mm/min.



Figure 8.18: Fixation tool and femur scaffold prototype during testing

The results from experimental testing of the femur scaffold prtotypes can be seen in Table 8.1.

Table 8.1: Experimental test results for the femur scaffold specimens

		density [g/cm^3]	m[g]	K[N/mm]
gyroid law 1	FEM	0.4	13.8	130
	NNRPIM	0.4	12.5	140
	FEM	0.6	20.3	350
	NNRPIM	0.6	18.9	330
gyroid law 2	FEM	0.4	12.3	170
	NNRPIM	0.4	12.7	130
	FEM	0.6	18.9	300
	NNRPIM	0.6	18.4	350

Theoretical results for each of these tested density levels can be seen in Table 8.2.

Table 8.2: Predicted stiffness results at the tested density levels

		density [g/cm^3]	K[N/mm]
gyroid law 1	FEM	0.4	85.23
		0.6	114.65
	NNRPIM	0.4	90.90
		0.6	115.51
gyroid law 2	FEM	0.4	90.42
		0.6	114.38
	NNRPIM	0.4	89.46
		0.6	115.28

It is therefore concluded that for a density level of 0.6, K presents a value between 300 and 350 N/mm and for a density level of 0.4, K presents a value between 130 and 170 N/mm. The supposition made earlier regarding the fact that the strength-to-weight ratio decreases with a decrease in mass is also verified here. No particular conclusion can be drawn regarding the experimental differences between specimens based on FEM and NNRPIM analyses, as testing proved complex, namely, when fixating the specimen.

Correlation between experimental testing and numerical results was poor as there was a gap between the imposed boundary conditions and tested conditions. For all specimens it was verified that measured stiffness is higher than theoretical stiffness, most likely due to a gap between imposed boundary conditions in the remodelling analysis and testing conditions, namely, over fixation during experimental testing where rotation was blocked, but allowed in numerical simulations. The impossibility to test the upwards vertical load could also have contributed to a smaller vertical displacement and, therefore, higher stiffness.

Moreover, it was not possible to bring the specimens to yield as, due to rotation (horizontal displacement) caused by the momentum of the force being applied vertically, the specimen would bounce back, thus highlighting the need for a different testing tool which would permit frictionless contact, for example, with a sphere.

To make sure that these are valid results, only small displacements were considered for stiffness calculation.

8.5 Result discussion and conclusions

Comparing the numerical simulation results with the experimental testing results, it is concluded that the numerical model of gyroid behaviour should be improved as there is still a considerable error between the stiffness predicted in the remodelling analysis and the stiffness obtained with experimental testing. Even though decent results in terms of accuracy were obtained while testing benchmark load cases, the complexity of the femur shape and boundary conditions did not allow for the same result quality. The complexity of boundary conditions applied to the numerical model

also made comparison with experimental results to be more difficult. Even though the geometry is quite complex, it was possible to fabricate a decent prototype with FFF.

The next step in prototyping is extrapolation of properties to titanium or other bio compatible metal properties. When extrapolating the results of this prototype so as to construct a metallic scaffold, density and stiffness should match those of bone for the same volume fraction in order to avoid stress shielding caused by insufficient loading to the bone (Wolff, 2012).

It should be noted that ideally, experimental testing should be done with another tool for load application which permits frictionless contact with the prototype as it deforms in the x direction.

Mass transport however was not quantified at this stage, where the focus was put mainly on mechanical behaviour and manufacturing considerations. As mentioned previously, the porous shape of TPMS promotes the correct mass transport properties vital for implantation as well as its importance on personalizing of the implant on the recipient.

Chapter 9

Conclusions

9.1 General conclusions

Overall, the methodology of this work which consists on solid creation and assembly corresponded to a simple approach with easy implementation to create functional gradients while maintaining solid geometry and reducing weight.

First of all, the Matlab script proved to be a useful and simple to use tool to create the .stl files, even though, at this stage it is limited to structured hexahedral elements. With a simple interface requiring the remodelling parameters, in a relatively short amount of time, it would provide the user with a file ready to be read by the slicer. This script could, however, be made more efficient computationally, but due to time constraints for all other tasks of this project this was not taken as a priority. Nonetheless, this script is not limited for use with an FFF slicing software. Using Boolean operations, the gyroid foam can be included in the .stl file and thus, it would be possible to employ this solid creation methodology in other additive manufacturing processes such as SLS. Moreover, even though an array of licensed and *open-source* software was used for this thesis, the developed workflow only truly requires Matlab and any slicing software, as well as having as an output a file of around 50Mb which includes all *.stl* files in a *.stl* and text format.

At a simulation stage, results were fulfilled as solutions found in the literature, especially for the three-point bending load case, including the Michell truss for the gyroid remodelling law with a lower rejection ratio, were obtained. A linear law presented better results than a parabolic law for structural optimization where convergence was difficult to achieve. In addition, the more evenly distributed the load case is, the more the simulations results will converge into the same result, which was verified for load case 3 - four point bending, where all analyses, be it structural optimization, gyroid remodelling or bone remodelling, evolved into the same trapeze-shaped truss. This stability was also shown when analysing the smoothing functions, since the structures which respected the original result presented better behaviour than specimens undergoing smoothing functions.

The similarity between the two gyroid laws at study left some questions unanswered regarding which law can more accurately represent the behaviour with some evidence to believe that gyroid

remodelling law 2 could possibly be better at describing the behaviour of the gyroid as, experimentally obtained stiffness results correlated better to theoretical results. However, the use of an adaptive law based on experimental testing of gyroid samples has proven to be far more accurate than to simply use a hard kill, linear or parabolic law from structural optimization. Moreover, the use of a gyroid law instead of structural optimization seems to be slightly more efficient at generating truss structures with higher stiffness.

It should also be noted how the gyroid remodelling simulation results would evolve into similar structures as in bone remodelling analysis, for an equivalent volume fraction. The similarity in behaviour was also verified for the femur model simulation.

Another important aspect about the simulation results is how some structures without any smoothing could only be printed if the medium density elements were included as well meaning that connectivity issues is something that should be looked into.

Regarding the gradient creation through the use of smoothing functions, due to the disparity of results between the different load cases at study, it was not possible to come to a solid conclusion on whether the smoothing process brings any benefit. There are reasons to believe that smoothing should be limited, as defining a smaller maximum distance ratio improved the ratio and also due to the fact that smoothing function 3, which accounts for every element for smoothing, overall presented the worst behaviour both in stiffness and in stiffness-to-weight ratio. On the other hand, for some load cases, the specimens without any smoothing function presented higher stiffness and smaller mass meaning that the smoothing process might bring the contrary effect of loosing the accuracy of the adapted structure.

Finally, the most important conclusion to take is the importance of building direction as the most relevant factor in performance enhancement, or, at the very least, the factor where stiffness increase is the easiest to obtain. It should be noted, however, that vertical placement of the specimens on the building surface can lead to other issues such as separation from the building surface.

9.2 Future work

The gyroid remodelling law, "as is" considers isotropy for a manufacturing process which is highly anisotropic or, at the very least, orthotropic. Inclusively, FFF is the AM process with higher anisotropy at approximately 50% anisotropy (Dizon et al., 2018; Kazmer, 2017). Further development of this law to accommodate the anisotropy of the process is likely to improve the accuracy of the model in order to show a better correlation between the numerical simulations and the tested specimens.

In order to refine the smoothing process, having concluded that the number of elements considered for the smoothing should not be too high, a stiffness study of printed specimens as a function of maximum distance ratio could achieve a more optimal solution instead of simply a "better" solution. A maximum distance ratio between 0.00 and 0.10 would be the interval where it should be tested.

Regarding the numerical simulations, having conducted a proof of concept of the methodology in order to obtain functionally graded specimens, it would be relevant to test some similar load cases using 2D elements and improving the script to handle a 2D output from the FEMAS software. The use of 2D elements allows for a finer discretization and increased accuracy. The approximation for a 3D thin plate with one element thick can be considered inefficient as it is a three-dimensional approach to an easy problem to solve with 2D-elements considering plane stress. Moreover, the use of a finer 2D mesh/node distribution could mean that the connectivity problems within the structures (for example reinforcement structures which do not connect to the main structure) could be improved or solved.

Regarding the femoral scaffold analysis, it would be interesting to refine the model to a finer mesh in order to achieve more accurate results. Replacing the structured hexahedral mesh for an hex-dominated mesh which is more faithful to femoral geometry could facilitate printing as a more organic and natural shape is obtained. This would require, however, adaptation of the matlab script to handle a mesh/nodal distribution which is not structured. Development of a more sophisticated test apparatus to test the mechanical behaviour of the printed femur would also bring important information on how to increase the accuracy of the model.

Finally, this methodology relies too heavily on the slicing software in order to create the specimens, especially, when guaranteeing bonding between solids, and this aspect should be reconsidered and improved at a scripting level.

Bibliography

Abueidda, D. W., Bakir, M., Al-Rub, R. K. A., Bergström, J. S., Sobh, N. A., and Jasiuk, I. (2017). Mechanical properties of 3D printed polymeric cellular materials with triply periodic minimal surface architectures. *Materials & Design*, 122:255–267.

Abueidda, D. W., Elhebeary, M., Shiang, C. S. A., Pang, S., Abu Al-Rub, R. K., and Jasiuk, I. M. (2019). Mechanical properties of 3D printed polymeric Gyroid cellular structures: Experimental and finite element study. *Materials and Design*, 165:107597.

Afonso, J. (2019). Influence of process parameters on the properties of 3D printed components and predictive model.

An, N. (2013). Femur 3D model.

Anderson, C. (2012). Makers: The New Industrial Revolution (p. 257).

Atluri, S. N. and Zhu, T. (1998). A new Meshless Local Petrov-Galerkin (MLPG) approach in computational mechanics. *Computational Mechanics*, 22(2):117–127.

Bathe, K. J. (1996). *Finite Element Procedures*. Number pt. 2 in Finite Element Procedures. Prentice Hall.

Beaupré, G. S., Orr, T. E., and Carter, D. R. (1990a). An approach for time-dependent bone modeling and remodeling—application: A preliminary remodeling simulation. *Journal of Orthopaedic Research*, 8(5):662–670.

Beaupré, G. S., Orr, T. E., and Carter, D. R. (1990b). An approach for time-dependent bone modeling and remodeling—theoretical development. *Journal of Orthopaedic Research*, 8(5):651–661.

Belinha, J. (2014). *Meshless Methods in Biomechanics - Bone Tissue Remodelling Analysis*. Springer, Porto, Portugal.

Belinha, J., Dinis, L., and Natal Jorge, R. M. (2013a). The natural radial element method. *International Journal for Numerical Methods in Engineering*, 93(January):1286–1313.

Belinha, J., Dinis, L. M., and Jorge, R. M. (2013b). Composite laminated plate analysis using the natural radial element method. *Composite Structures*, 103:50–67.

Belinha, J., Dinis, L. M., and Natal Jorge, R. M. (2013c). Analysis of thick plates by the natural radial element method. *International Journal of Mechanical Sciences*, 76:33–48.

Belinha, J., Jorge, R. M. N., and Dinis, L. M. J. S. (2013d). A meshless microscale bone tissue trabecular remodelling analysis considering a new anisotropic bone tissue material law. *Computer methods in biomechanics and biomedical engineering*, 16(11):1170–1184.

Belinha, J., Natal Jorge, R. M., and Dinis, L. M. (2012). Bone tissue remodelling analysis considering a radial point interpolator meshless method. *Engineering Analysis with Boundary Elements*, 36(11):1660–1670.

Belytschko, T., Krongauz, Y., Organ, D., Fleming, M., and Krysl, P. (1996). Meshless methods: An overview and recent developments. *Computer Methods in Applied Mechanics and Engineering*, 139(1-4):3–47.

Belytschko, T., Lu, Y., and Gu, L. (1994). Element-Free Galerkin Methods. *International Journal of Numerical Methods in Engineering*, 37:229–256.

Bendsoe, M. and Sigmund, O. (2004). *Topology Optimization. Theory,Methods and Applications*. Springer.

Berman, B. (2012). 3-D printing: The new industrial revolution. *Business Horizons*, 55(2):155–162.

Bogers, M., Hadar, R., and Bilberg, A. (2016). Additive manufacturing for consumer-centric business models: Implications for supply chains in consumer goods manufacturing. *Technological Forecasting and Social Change*, 102:225–239.

Brackett, D. J., Ashcroft, I. A., Wildman, R. D., and Hague, R. J. (2014). An error diffusion based method to generate functionally graded cellular structures. *Computers and Structures*, 138:102–111.

Braconnier, D. J., Jensen, R. E., and Peterson, A. M. (2020). Processing parameter correlations in material extrusion additive manufacturing. *Additive Manufacturing*, 31(October 2019):100924.

Braun, J. and Sambridge, M. (1995). A numerical method for solving partial differential equations on highly irregular evolving grids.

Carter, D. R., Fyhrie, D. P., and Whalen, R. T. (1987). Trabecular bone density and loading history: Regulation of connective tissue biology by mechanical energy. *Journal of Biomechanics*, 20(8):785–794.

Carter, D. R. and Hayes, W. C. (1977). The compressive behavior of bone as a two-phase porous structure. *The Journal of bone and joint surgery. American volume*, 59(7):954–962.

Carter, D. R., Orr, T. E., and Fyhrie, D. P. (1989). Relationships between loading history and femoral cancellous bone architecture. *Journal of Biomechanics*, 22(3):231–244.

Carter, D. R. and Spengler, D. M. (1978). Mechanical properties and composition of cortical bone. *Clinical Orthopaedics and Related Research (1976-2007)*, 135:192–217.

Cavalcanti, P. and Mello, U. (1970). Three-Dimensional Constrained Delaunay Triangulation: A Minimalist Approach.

Cheah, C. M., Chua, C. K., Leong, K. F., and Chua, S. W. (2003a). Development of a tissue engineering scaffold structure library for rapid prototyping. Part 1: investigation and classification. *The International Journal of Advanced Manufacturing Technology*, 21(4):291–301.

Cheah, C. M., Chua, C. K., Leong, K. F., and Chua, S. W. (2003b). Development of a tissue engineering scaffold structure library for rapid prototyping. Part 2: parametric library and assembly program. *The International Journal of Advanced Manufacturing Technology*, 21(4):302–312.

Chen, J. S., Yoon, S., and Wu, C. T. (2002). Non-linear version of stabilized conforming nodal integration for Galerkin mesh-free methods. *International Journal for Numerical Methods in Engineering*, 53(12):2587–2615.

Chen, Y. (2006). A mesh-based geometric modeling method for general structures. *Proceedings of the ASME Design Engineering Technical Conference*, 2006(McDowell 1998).

Chu, S., Gao, L., Xiao, M., and Zhang, Y. (2019). Multiscale topology optimization for coated structures with multifarious-microstructural infill. *Structural and Multidisciplinary Optimization*.

Cowin, S. C. (1985). The relationship between the elasticity tensor and the fabric tensor. *Mechanics of Materials*, 4(2):137–147.

Cowin, S. C. and Hegedus, D. H. (1976). Bone remodeling I: theory of adaptive elasticity. *Journal of Elasticity*, 6(3):313–326.

Cowin, S. C., Sadegh, A. M., and Luo, G. M. (1992). An Evolutionary Wolff's Law for Trabecular Architecture. *Journal of Biomechanical Engineering*, 114(1):129–136.

Creality (2018). Ender 3 3D Printer.

Crump, S. S. (1991). Fast, precise, safe prototypes with FDM. *ASME, PED*, 50:53–60.

Cueto, E., Doblaré, M., and Gracia, L. (2000). Imposing essential boundary conditions in the natural element method by means of density-scaled α-shapes. *International Journal for Numerical Methods in Engineering*, 49(4):519–546.

Currey, J. D. (1969). The mechanical consequences of variation in the mineral content of bone. *Journal of biomechanics*, 2(1):1–11.

Currey, J. D. (1988). The effect of porosity and mineral content on the Young's modulus of elasticity of compact bone. *Journal of biomechanics*, 21(2):131–139.

De, S. and Bathe, K. J. (2000). The method of finite spheres. *Computational Mechanics*, 25(4):329–345.

Delaunay, B. (1934). Sur la sphére vide. A la memoire de Georges Voronoi. *Izv. Akad. Nauk SSSR.Otdelenie Matematicheskih i Estestvennyh Nauk*, 12(7):793–800.

Di Cesare, N. and Domaszewski, M. (2019). A new hybrid topology optimization method based on I-PR-PSO and ESO. Application to continuum structural mechanics. *Computers and Structures*, 212:311–326.

Dinis, L. M., Natal Jorge, R. M., and Belinha, J. (2007). Analysis of 3D solids using the natural neighbour radial point interpolation method. *Computer Methods in Applied Mechanics and Engineering*, 196(13-16):2009–2028.

Dinis, L. M., Natal Jorge, R. M., and Belinha, J. (2008). Analysis of plates and laminates using the natural neighbour radial point interpolation method. *Engineering Analysis with Boundary Elements*, 32(3):267–279.

Dizon, J. R. C., Espera, A. H., Chen, Q., and Advincula, R. C. (2018). Mechanical characterization of 3D-printed polymers. *Additive Manufacturing*, 20:44–67.

Dong, G., Tang, Y., Li, D., and Zhao, Y. F. (2020). Design and optimization of solid lattice hybrid structures fabricated by additive manufacturing. *Additive Manufacturing*, 33(February):101116.

Du, Y., Gu, D., Xi, L., Dai, D., Gao, T., Zhu, J., and Ma, C. (2020). Laser additive manufacturing of bio-inspired lattice structure: Forming quality, microstructure and energy absorption behavior. *Materials Science and Engineering A*, 773(December 2019):138857.

du Plessis, A., Broeckhoven, C., Yadroitsava, I., Yadroitsev, I., Hands, C. H., Kunju, R., and Bhate, D. (2019). Beautiful and Functional: A Review of Biomimetic Design in Additive Manufacturing. *Additive Manufacturing*, 27(March):408–427.

Elmer, W., Chen, J. S., Puso, M., and Taciroglu, E. (2012). A stable, meshfree, nodal integration method for nearly incompressible solids. *Finite Elements in Analysis and Design*, 51:81–85.

Feng, J., Fu, J., Lin, Z., Shang, C., and Li, B. (2018a). A review of the design methods of complex topology structures for 3D printing. *Visual Computing for Industry, Biomedicine, and Art*, 1(1):1–16.

Feng, J., Fu, J., Shang, C., Lin, Z., and Li, B. (2018b). Porous scaffold design by solid T-splines and triply periodic minimal surfaces. *Computer Methods in Applied Mechanics and Engineering*, 336:333–352.

FormFutura (2020). Premium PLA Robotic Grey.

Fyhrie, D. P. and Carter, D. R. (1986). A unifying principle relating stress to trabecular bone morphology. *Journal of Orthopaedic Research*, 4(3):304–317.

Gao, W., Zhang, Y., Ramanujan, D., Ramani, K., Chen, Y., Williams, C. B., Wang, C. C., Shin, Y. C., Zhang, S., and Zavattieri, P. D. (2015). The status, challenges, and future of additive manufacturing in engineering. *CAD Computer Aided Design*, 69:65–89.

Gaynor, A. T., Guest, J. K., and Moen, C. D. (2013). Reinforced concrete force visualization and design using bilinear truss-continuum topology optimization. *Journal of Structural Engineering (United States)*, 139(4):607–618.

Giannitelli, S. M., Accoto, D., Trombetta, M., and Rainer, A. (2014). Current trends in the design of scaffolds for computer-aided tissue engineering. *Acta Biomaterialia*, 10(2):580–594.

Gibson, L. (1985). The mechanical behaviour of cancellous bone. *Journal of biomechanics*, 18(5):317–328.

Gibson, L. J. and Ashby, M. F. (1999). *Cellular solids: structure and properties*. Cambridge university press.

Gingold, R. and Monaghan, J. (1977). Smoothed particle hydrodynamics: theory and application to non-spherical stars. *Monthly Notices of the Royal Astronomical Society*, 181(3):375–389.

Goel, A. and Anand, S. (2019). Design of functionally graded lattice structures using B-splines for additive manufacturing. *Procedia Manufacturing*, 34:655–665.

Goldstein, S. A. (1987). The mechanical properties of trabecular bone: dependence on anatomic location and function.

Gomez Gonzalez, S. (2016). *Impresión 3D*. Marcombo, 1st edition.

Gorguluarslan, R. M., Gandhi, U. N., Song, Y., and Choi, S. K. (2017). An improved lattice structure design optimization framework considering additive manufacturing constraints. *Rapid Prototyping Journal*, 23(2):305–319.

Grames, E. (2019). 3D printer bed - How to choose the right bed.

Gregurić, L. (2019). MATERIAL JETTING, SIMPLY EXPLAINED.

Gu, Y. T. (2005). Meshfree Methods and Their Comparisons. *International Journal of Computational Methods*, 02(04):477–515.

Huang, X. and Xie, M. (2010). *Evolutionary topology optimization of continuum structures: methods and applications*. John Wiley & Sons.

Huang, X. and Xie, Y. M. (2007). Convergent and mesh-independent solutions for the bi-directional evolutionary structural optimization method. *Finite Elements in Analysis and Design*, 43(14):1039–1049.

Hullette, T. (2020). Direct vs Bowden Extruder: Does It Make a Difference?

Idelsohn, S. R., Onate, E., Calvo, N., and Del Pin, F. (2003). The meshless finite element method. *International Journal for Numerical Methods in Engineering*, 58(6):893–912.

Idhammad, A., Abdali, A., and Alaa, N. (2013). Computational simulation of the bone remodeling using the finite element method: An elastic-damage theory for small displacements. *Theoretical Biology and Medical Modelling*, 10(1).

Ishii, S., Cauley, J. A., Greendale, G. A., Danielson, M. E., Safaei Nili, N., and Karlamangla, A. (2012). Ethnic differences in composite indices of femoral neck strength. *Osteoporosis International*, 23(4):1381–1390.

ISO (2015). SO/ASTM 52900:2015 Additive manufacturing — General principles — Terminology. Technical report, ISO/ASTM.

Jewett, J. L. and Carstensen, J. V. (2019). Experimental investigation of strut-and-tie layouts in deep RC beams designed with hybrid bi-linear topology optimization. *Engineering Structures*, 197(December 2018):109322.

Kansa, E. J. (1990a). Multiquadrics-A scattered data approximation scheme with applications to computational fluid-dynamics-I surface approximations and partial derivative estimates. *Computers and Mathematics with Applications*, 19(8-9):127–145.

Kansa, E. J. (1990b). Multiquadrics-A scattered data approximation scheme with applications to computational fluid-dynamics-II solutions to parabolic, hyperbolic and elliptic partial differential equations. *Computers and Mathematics with Applications*, 19(8-9):147–161.

Kapfer, S. C., Hyde, S. T., Mecke, K., Arns, C. H., and Schröder-Turk, G. E. (2011). Minimal surface scaffold designs for tissue engineering. *Biomaterials*, 32(29):6875–6882.

Kazmer, D. (2017). Three-dimensional printing of plastics. In *Applied Plastics Engineering Handbook*, pages 617–634. Elsevier.

Keller, T. S. (1994). Predicting the compressive mechanical behavior of bone. *Journal of biomechanics*, 27(9):1159–1168.

Keyak, J. H., Lee, I. Y., and Skinner, H. B. (1994). Correlations between orthogonal mechanical properties and density of trabecular bone: use of different densitometric measures. *Journal of biomedical materials research*, 28(11):1329–1336.

Kumar, A., Collini, L., Daurel, A., and Jeng, J. Y. (2020). Design and additive manufacturing of closed cells from supportless lattice structure. *Additive Manufacturing*, 33(43):101168.

Kummer, B. K. E. (1972). Biomechanics of bone: mechanical properties, functional structure, functional adaptation. *Biomechanics: its foundations and objectives*, pages 237–271.

Lancaster, P. and Salkauskas, K. (1981). Surfaces generated by moving least squares methods. *Mathematics of Computation*, 37(155):141–141.

Li, D., Dai, N., Jiang, X., and Chen, X. (2016). Interior structural optimization based on the density-variable shape modeling of 3D printed objects. *International Journal of Advanced Manufacturing Technology*, 83(9-12):1627–1635.

Li, D., Dai, N., Zhou, X., Huang, R., and Liao, W. (2018a). Self-supporting interior structures modeling for buoyancy optimization of computational fabrication. *International Journal of Advanced Manufacturing Technology*, 95(1-4):825–834.

Li, D., Liao, W., Dai, N., Dong, G., Tang, Y., and Xie, Y. M. (2018b). Optimal design and modeling of gyroid-based functionally graded cellular structures for additive manufacturing. *CAD Computer Aided Design*, 104:87–99.

Li, G. and Yao, Y. (2019). Manufacturable Gradient-Variable Cellular Structures Design. *IOP Conference Series: Materials Science and Engineering*, 692(1).

Liu, G. R. (2002). A point assembly method for stress analysis for two-dimensional solids. *International Journal of Solids and Structures*, 39(1):261–276.

Liu, G. R. (2003). *Mesh Free Methods - Moving Beyond the Finite Element Method*. CRC Press, Boca Raton.

Liu, W. K., Jun, S., and Zhang, Y. F. (1995). Reproducing kernel particle methods. *International Journal for Numerical Methods in Fluids*, 20(8-9):1081–1106.

Liu, Y., Lo, S. H., Guan, Z.-Q., and Zhang, H.-W. (2014). Boundary recovery for 3D Delaunay triangulation. *Finite Elements in Analysis and Design*, 84:32–43.

Liu, G. R. Gu, Y. (2001). A point interpolation method for stress analysis for two-dimensional solids. *International Journal for Numerical Methods in Engineering*, 50:937–951.

Lotz, J. C., Gerhart, T. N., and Hayes, W. C. (1991). Mechanical properties of metaphyseal bone in the proximal femur. *Journal of biomechanics*, 24(5):317–329.

Lu, L., Sharf, A., Zhao, H., Wei, Y., Fan, Q., Chen, X., Savoye, Y., Tu, C., Cohen-Or, D., and Chen, B. (2014). Build-to-last: Strength to weight 3D printed objects. *ACM Transactions on Graphics*, 33(4):1–10.

Lu, Y., Zhao, W., Cui, Z., Zhu, H., and Wu, C. (2019). The anisotropic elastic behavior of the widely-used triply-periodic minimal surface based scaffolds. *Journal of the Mechanical Behavior of Biomedical Materials*, 99(2):56–65.

Ma, S., Tang, Q., Feng, Q., Song, J., Han, X., and Guo, F. (2019). Mechanical behaviours and mass transport properties of bone-mimicking scaffolds consisted of gyroid structures manufactured using selective laser melting. *Journal of the Mechanical Behavior of Biomedical Materials*, 93(January):158–169.

Martin, R. B. (1991). Determinants of the mechanical properties of bones. *Journal of biomechanics*, 24:79–88.

Martínez, J., Dumas, J., and Lefebvre, S. (2016). Procedural voronoi foams for additive manufacturing. *ACM Transactions on Graphics*, 35(4).

Martínez, J., Song, H., Dumas, J., and Lefebvre, S. (2017). Orthotropic k-nearest foams for additive manufacturing. *ACM Transactions on Graphics*, 36(4):1–12.

Maskery, I., Aboulkhair, N. T., Aremu, A. O., Tuck, C. J., and Ashcroft, I. A. (2017). Compressive failure modes and energy absorption in additively manufactured double gyroid lattices. *Additive Manufacturing*, 16:24–29.

Maskery, I., Sturm, L., Aremu, A. O., Panesar, A., Williams, C. B., Tuck, C. J., Wildman, R. D., Ashcroft, I. A., and Hague, R. J. M. (2018). Insights into the mechanical properties of several triply periodic minimal surface lattice structures made by polymer additive manufacturing. *Polymer*, 152:62–71.

MecMesin (2020a). MultiTest-dV.

MecMesin (2020b). VectorPro.

Medeiros e Sá, A., Mello, V. M., Rodriguez Echavarria, K., and Covill, D. (2015). Adaptive voids: Primal and dual adaptive cellular structures for additive manufacturing. *Visual Computer*, 31(6-8):799–808.

Melchels, F. P. W., Bertoldi, K., Gabbrielli, R., Velders, A. H., Feijen, J., and Grijpma, D. W. (2010). Mathematically defined tissue engineering scaffold architectures prepared by stereolithography. *Biomaterials*, 31(27):6909–6916.

Nayroles, B., Touzot, G., and Villon, P. (1992). Generalizing the finite element method: Diffuse approximation and diffuse elements. *Computational Mechanics*, 10(5):307–318.

Neovius, E. R. (1883). Bestimmung zweier speciellen periodischen Minimalflächen, auf welchen unendlich viele gerade Linien und unendlich viele ebene geodätische Linien liegen.

Nguyen, D. S. and Vignat, F. (2016). A method to generate lattice structure for Additive Manufacturing. In *2016 IEEE International Conference on Industrial Engineering and Engineering Management (IEEM)*, pages 966–970.

Nguyen, V. P., Rabczuk, T., Bordas, S., and Duflot, M. (2008). Meshless methods: A review and computer implementation aspects. *Mathematics and Computers in Simulation*, 79(3):763–813.

Onate, E. (2013). *Structural analysis with the finite element method : linear statics Volume 1*. Springer, 1 edition.

Onate, E., Idelsohn, S., Zienkiewicz, O., Taylor, R., and Sacco, C. (1996a). A stabilized finite point method for analysis of fluid mechanics problems. *Computer Methods in Applied Mechanics and Engineering*, 7825(96):315–346.

Onate, E., Idelsohn, S., Zienkiewicz, O. C., and Taylor, R. L. (1996b). A finite point method in computational mechanics. Applications to convective transport and fluid flow. *International Journal for Numerical Methods in Engineering*, 39(22):3839–3866.

Onate, E., Perazzo, F., and Miquel, J. (2001). A finite point method for elasticity problems. *Computers and Structures*, 79(22-25):2151–2163.

Pauwels, F. (2013). *Gesammelte abhandlungen zur funktionellen anatomie des bewegungsapparates*. Springer-Verlag.

Peyroteo, M., Belinha, J., Dinis, L., and Natal Jorge, R. (2018). Chapter 17 - The Mechanologic Bone Tissue Remodeling Analysis: A Comparison Between Mesh-Depending and Meshless Methods. pages 303–323. Academic Press.

Prusa, J. (2020). Prusa Slicer.

Querin, O. M., Young, V., Steven, G. P., and Xie, Y. M. (2000). Computational efficiency and validation of bi-directional evolutionary structural optimisation. *Computer methods in applied mechanics and engineering*, 189(2):559–573.

Rajagopalan, S. and Robb, R. A. (2006). Schwarz meets Schwann: design and fabrication of biomorphic and durataxic tissue engineering scaffolds. *Medical image analysis*, 10(5):693–712.

Reddy, J. (2005). An Introduction to the Finite Element Method, 3rd Edition-McGraw-Hill Education (ISE Editions).

Rice, J. C., Cowin, S. C., and Bowman, J. A. (1988). On the dependence of the elasticity and strength of cancellous bone on apparent density. *Journal of biomechanics*, 21(2):155–168.

Rodrigues, H., Jacobs, C., Guedes, J. M., and Bendsøe, M. P. (1999). Global and local material optimization models applied to anisotropic bone adaptation. In *IUTAM Symposium on Synthesis in Bio Solid Mechanics*, pages 209–220. Springer.

Schaedler, T. A. and Carter, W. B. (2016). Architected Cellular Materials. *Annual Review of Materials Research*, 46(1):187–210.

Schaffler, M. B. and Burr, D. B. (1988). Stiffness of compact bone: effects of porosity and density. *Journal of biomechanics*, 21(1):13–16.

Schoen, A. H. (1970). *Infinite periodic minimal surfaces without self-intersections*. National Aeronautics and Space Administration.

Schwarz, H. A. (1871). *Bestimmung einer speciellen Minimalfläche: eine von der Königlichen Akademie der Wissenschaften zu Berlin am 4. Juli 1867 gekrönte Preisschrift; nebst einem Nachtrage, einem Anhange und 6 Figurentafeln*. F. Dümmler's Verlags-Buchhandlung.

Shojib Hossain, M., Espalin, D., Ramos, J., Perez, M., and Wicker, R. (2014). Improved Mechanical Properties of Fused Deposition Modeling-Manufactured Parts Through Build Parameter Modifications. *Journal of Manufacturing Science and Engineering*, 136(6).

Sibson, R. (1981). A brief description of natural neighbour interpolation. *Interpreting Multivariate Data*.

Silva, C. M. M. d. (2019). 3D printing of gyroid structures for superior structural behaviour.

Simonetti, H. L., Almeida, V. S., Leitão, V. M. A., and de Assis das Neves, F. (2019). Application of evolutionary structural optimization based on the boundary element method using initial stress fields. *Structures*, 20(March):550–559.

Singh, S., Singh, G., Prakash, C., and Ramakrishna, S. (2020). Current status and future directions of fused filament fabrication. *Journal of Manufacturing Processes*, 55:288–306.

Sokół, T. (2011). A 99 line code for discretized Michell truss optimization written in Mathematica. *Structural and Multidisciplinary Optimization*, 43(2):181–190.

Sukumar, N., Moran, B., and Belytschko, T. (1998). The natural element method in solid mechanics. *International Journal for Numerical Methods in Engineering*, 43(5):839–887.

Sukumar, N., Moran, B., Semenov, A. Y., and Belikov, V. V. (2000). Natural neighbour Galerkin methods. *International Journal for Numerical Methods in Engineering*, 50(1):1–27.

Suresh, S. and Mortensen, A. (1998). *Fundamentals of functionally graded materials*. Number BOOK. The Institut of Materials.

Sze, K. Y., Chen, J. S., Sheng, N., and Liu, X. H. (2004). Stabilized conforming nodal integration: Exactness and variational justification. *Finite Elements in Analysis and Design*, 41(2):147–171.

Tang, Y., Kurtz, A., and Zhao, Y. F. (2015). Bidirectional Evolutionary Structural Optimization (BESO) based design method for lattice structure to be fabricated by additive manufacturing. *CAD Computer Aided Design*, 69:91–101.

Tanskanen, P. (2002). The evolutionary structural optimization method: Theoretical aspects. *Computer Methods in Applied Mechanics and Engineering*, 191(47-48):5485–5498.

Torres, J., Cole, M., Owji, A., DeMastry, Z., and Gordon, A. P. (2016). An approach for mechanical property optimization of fused deposition modeling with polylactic acid via design of experiments. *Rapid Prototyping Journal*, 22(2):387–404.

Traversoni, L. (1994). Natural neighbour finite elements. *International Conference on Hydraulic Engineering Software, Hydrosoft, Proceedings*, 2:291–297.

Turner, C. H., Cowin, S. C., Rho, J. Y., Ashman, R. B., and Rice, J. C. (1990). The fabric dependence of the orthotropic elastic constants of cancellous bone. *Journal of Biomechanics*, 23(6):549–561.

Ultimaker (2019). Cura.

Umetani, N. and Schmidt, R. (2013). Cross-sectional structural analysis for 3D printing optimization. *SIGGRAPH Asia 2013 Technical Briefs, SA 2013*.

Upputuri, R. (2017). INTAMSYS launches PEEK 3D Printer View Larger Image.

Varotsis, A. B. (2020). Industrial FDM vs. desktop FDM.

Vitale, M., Cotteleer, M., and Holdowsky, J. (2016). An Overview of Additive Manufacturing. *Defense AT&L, November-December*.

Voronoi, G. (1908). Nouvelles applications des paramètres continus à la théorie des formes quadratiques. *Journal für die reine und angewandte Mathematik*, 134:198–287.

Wang, J. G. and Liu, G. R. (2002a). A point interpolation meshless method based on radial basis functions. *International Journal for Numerical Methods in Engineering*, 54(11):1623–1648.

Wang, J. G. and Liu, G. R. (2002b). On the optimal shape parameters of radial basis functions used for 2-D meshless methods. *Computer Methods in Applied Mechanics and Engineering*, 191(23-24):2611–2630.

Wang, W., Liu, Y. J., Wu, J., Tian, S., Wang, C. C., Liu, L., and Liu, X. (2018). Support-Free Hollowing. *IEEE Transactions on Visualization and Computer Graphics*, 24(10):2787–2798.

Wang, W., Wang, T. Y., Yang, Z., Liu, L., Tong, X., Tong, W., Deng, J., Chen, F., and Liu, X. (2013). Cost-effective printing of 3D objects with skin-frame structures. *ACM Transactions on Graphics*, 32(6):1–10.

Whalen, R. T., Carter, D. R., and Steele, C. R. (1988). Influence of physical activity on the regulation of bone density. *Journal of Biomechanics*, 21(10):825–837.

Wohlers, T. (2019). Wohlers report 2019: Additive manufacturing and 3D printing state of the industry: Annual worldwide progress report. Technical report.

Wohlers, T., Campbell, I., Diegel, O., and Kowen, J. (2018). Wohlers Report - 3D Printing and Additive Manufacturing State of the Industry - Annual Worldwide Progress Report. Technical report, Wohlers associates.

Wolff, J. (2012). *The law of bone remodelling*. Springer Science & Business Media.

Wu, J. (2018). Continuous optimization of adaptive quadtree structures. *CAD Computer Aided Design*, 102:72–82.

Wu, J., Clausen, A., and Sigmund, O. (2017). Minimum compliance topology optimization of shell–infill composites for additive manufacturing. *Computer Methods in Applied Mechanics and Engineering*, 326:358–375.

Wu, J., Wang, C. C., Zhang, X., and Westermann, R. (2016). Self-supporting rhombic infill structures for additive manufacturing. *CAD Computer Aided Design*, 80:32–42.

Xie, Y. M. and Steven, G. P. (1993). A simple evolutionary procedure for structural optimization. *Computers & Structures*, 49(5):885–896.

Xie, Y. M. and Steven, G. P. (1997). *Evolutionary structural optimization*. Springer, London.

Yang, L., Mertens, R., Ferrucci, M., Yan, C., Shi, Y., and Yang, S. (2019). Continuous graded Gyroid cellular structures fabricated by selective laser melting: Design, manufacturing and mechanical properties. *Materials and Design*, 162:394–404.

Yang, X. Y., Xie, Y. M., Steven, G. P., and Querin, O. M. (1999). Bidirectional evolutionary method for stiffness optimization. *AIAA journal*, 37(11):1483–1488.

Yoo, D.-J. (2011a). Computer-aided porous scaffold design for tissue engineering using triply periodic minimal surfaces. *International Journal of Precision Engineering and Manufacturing*, 12(1):61–71.

Yoo, D. J. (2011b). Porous scaffold design using the distance field and triply periodic minimal surface models. *Biomaterials*, 32(31):7741–7754.

Yoo, D. J. (2014). Advanced porous scaffold design using multi-void triply periodic minimal surface models with high surface area to volume ratios. *International Journal of Precision Engineering and Manufacturing*, 15(8):1657–1666.

Yoshida, S. (1978). Michell Truss : Shape Optimization vs. Analytical Solution. (each iv):3–19.

Yu, S., Sun, J., and Bai, J. (2019). Investigation of functionally graded TPMS structures fabricated by additive manufacturing. *Materials and Design*, 182:108021.

Zhang, X. Y., Yan, X. C., Fang, G., and Liu, M. (2020). Biomechanical influence of structural variation strategies on functionally graded scaffolds constructed with triply periodic minimal surface. *Additive Manufacturing*, 32(December 2019):101015.

Zhao, B., Lin, Z., Fu, J., and Sun, Y. (2017). Generation of truss-structure objects with implicit representation for 3D-printing. *International Journal of Computer Integrated Manufacturing*, 30(8):871–879.

Zienkiewicz, O. C. and Taylor, R. L. (2005). The Finite Element Method Volume 1 : Its Basis & Fundamentals (sixth edition). page 13.

Zioupos, P., Cook, R. B., and Hutchinson, J. (2008). Some basic relationships between density values in cancellous and cortical bone. *Journal of biomechanics*, 41:1961–1968.

Appendix A

Matlab script

As it was previously mentioned, the Matlab script developed in this work has the function of generating the *.stl* files which are read by the *slicing* software to generate the *g-code* file. This section dwells further into the code itself. It should be noted that some built-in Matlab functions are used and therefore, immediate transcription into other programming languages is not possible.

A.1 Inputs

This section collects all the information necessary about the type of analysis being done.

```
clc
clear all
close all

dens_PLA = 1.25;
uibox_inputs;
uibox_smoothinginputs;
thicken = 1; %it is necessary to add thickness to the plate

N = 3; %how many density levels is the structure going to be divided into
bone = true; %means that the division is done according to density levels instead
    of stress levels

filename = strcat(date,'__','iteration_',num2str(IT_number),'_',id);

if FEM == 1
    filename = strcat(string(filename),'_FEM');
    mkdir(filename);
    FEM_STL;
else
    filename = strcat(filename,'_MESHLESS');
    mkdir(filename);
    meshless_stl;
```

```
23 end
```

The difference between FEM_STL and meshless_stl is that, since the density value of each element is calculated through the average density value of the integration points and while in the FEM files that information is explicit, using meshless methods, a fake mesh is created and the integration points need to be atributed to a pseudo-element.

A.2 FEM_STL.m

The *mesh* subfunction present in this script reads the files from the FEMAS file to atribute density values and stress values to each of the elements. In addition to this it also saves the information of the node coordinates for the element as well as its centroid coordinates.

```
1  [file,folder]=uigetfile('.zip','MultiSelect','on');
2  unzip(strcat(folder,file),filename);
3  cd(filename);
4  %getting the FEMAS file with all the information. this is chosen by the user
5  %%
6  femasfile = strcat('femas',num2str(10000+IT),'.mat');
7  load(femasfile)
8  %opens the file correspondent to the chosen iteration
9  %% read element information
10 cd ..
11 element = mesh(num_e,x_nod,e_nod,n\_nodes,gp_elem);
```

Then, after creating the element array, density and stress values are atributed to the each element. In FEM there is a possibility of creating a smaller mesh by dividing each element into 8 with a single integration point inside it. That way, the density or stress value is that of that integration point.

```
1   % associating each integration point to a node (the closest node inside
2      % its corresponding element)
3
4  %       n8 -> gp3
5  %       O--------------O n7 -> gp4
6  %       |\             |\
7  %       | \ n5 -> gp1  | \
8  %       |  O-----------+--O n6 -> gp2
9  %       |  |           |  |
10 %       |  |           |  |
11 %       O--+-----------O n3 -> gp8
12 %     n4 -> gp7          \ |
13 %         \|              \|
14 %          O--------------O
```

```
%        n1 -> gp5       n2 -> gp6
```

However, since that is not applicable in meshless methods, it will not be used.

```
%calculates the average value for each element from the integration points apparent
     density value
%gp stands for gauss point
for i =1:num_e
    element{i}.stress_eff = mean(stress_ef(1,element{i}.gp(1,1):element{i}.gp(1,
        n_nodes)));
    element{i}.dens_app = mean(app_gp(1,element{i}.gp(1,1):element{i}.gp(1,n_nodes)
        ));
end
%%
```

A.3 Meshless_stl.m

As it was mentioned previously, if the input file is from an NNRPIM analysis

```
%% create a mesh from the information of the elements
element = cell(1,num_e);
for i = 1:num_e
    element{i}.x = x_nod(1,e_nod(1:n_nodes,i))';
    element{i}.y = x_nod(2,e_nod(1:def_theory,i))';
    element{i}.z = x_nod(3,e_nod(1:def_theory,i))';
    element{i}.cent_x = mean(x_nod(1,e_nod(1:def_theory,i)));
    element{i}.cent_y = mean(x_nod(2,e_nod(1:def_theory,i)));
    element{i}.cent_z = mean(x_nod(3,e_nod(1:def_theory,i)));
    element{i}.gp = zeros(1,1);
end
%% gathers information of what integration points are in each element
for i = 1:length(gp)
    k = 1;
    enc = 0;
    while enc == 0
        x = element{k}.x;
        y = element{k}.y;
        z = element{k}.z;
        if isInside(x,y,z,gp(1,i),gp(2,i),gp(3,i)) == 1
        %isInside is a separate function
            enc = 1;
           element{k}.gp = [element{k}.gp; i];
        else
            k = k + 1;
            enc = 0;
```

```
        end
    end
end

for i = 1:num_e
    element{i}.gp(1) = [];
    nn = length(element{i}.gp);
    element{i}.dens_app = mean(app_gp(element{i}.gp(1:nn)));
end
disp('fake mesh is finished')
```

A.4 Common script

After atributing density values to each element the plate may have to be thickened, that is, the elements are repeated in the direction of the thickness of the plate. That happens beacuse in order to save computer time, the simulation is conducted in a 1mm plate which would not be printable nor testable. Briefly, what $thicken_{plate}$ does is to copy each element n times changing the z coordinate of all nodes in $z = z + thickness_{currentPlate} * k$ where k varies from 1 to the number of plates that must be added which is given by $thickness_{newPlate} - thickness_{currentPlate}$. When creating the file for the femur specimens, no thickening is done as it is not necessary.

As it was previously mentioned, some of the samples may be smoothed according to the functions presented in 5.3.2. In these functions, respectively *ratio_smooth1*, *ratio_smooth2* and *ratio_smooth3* which create a matrix with the coefficient ω_{ij} used in equation 5.1.

```
if thicken == 1
thicken_plate;
end
%% ratios
if smoothingType == 1
    ratio = ratio_smooth1(element,max_dist_ratio);
elseif smoothingType == 2
    ratio = ratio_smooth2(element,max_dist_ratio);
elseif smoothingType == 3
    ratio = ratio_smooth3(element);
elseif smoothingType == -1
    ratio = zeros(num_e);
end
```

Next, the script will create the solids to perform the triangulation. First, it performs the smoothing with the ratio matrix and equation 5.1 in the subroutine *smoothing* and then, with the *groups* subroutine it creates a matrix with the list of element numbers for each density level.

Then, it is necessary to, within the density groups constitute the solids which are made up of elements in contact with each other. That way, the density level is made up of several solids

that can be triangulated. If the elements do not have contact it is not possible to conduct the triangulation. Subroutine *groups* goes along each density level and verifies, through the nodes of each element if one element is contact with another. If an element *j* shares 4 nodes with another element *i* then element *j* is added to the same solid where element *i* belongs. If element *j* does not share any 4 nodes with any other element in the previously created solids, then, another solid is created. However if element *j* shares 4 nodes with elements in more than one solid, then those solids are merged.

```
smoothing;
groups;
%%
```

The *createSolids* subroutine creates a cell array with all elements which constitute that solid.

After having those solids, triangulation of those solids must be conducted which is done in subroutine *triangulateSolids*.

```
createSolids;
%%
triangulateSolids;
%%
```

The final step is to use the information above to write an .stl file for each solid. The solids defined in *createSolids* are concatenated into a single .stl file correspondant to that density level.

An .stl file follows the following structure:

```
    solid <nameofsolid1>
    facet normal x y z
    outer loop
    vertex x y z
    vertex x y z
    vertex x y z
    end loop
    ...
    end solid <nameofsolid1>
    ...
    solid <nameofsolidN>
    facet normal x y z
    outer loop
    vertex x y z
    vertex x y z
    vertex x y z
    end loop
    ...
    end solid <nameofsolidN>
```

This structure allows for concatenation of the solids by changing the name. The density value as well as its percentage of infill is added to the name of the document to facilitate its usage in the slicing software.

```
cd(filename)
cd .\stl_solid
mkdir stl_byDensityGroups
fileList = dir('*.csv');
file_data = cell(length(fileList),1);
for i = 1:length(fileList)
    file_data{i,1} = readtable(fileList(i).name,'ReadVariableNames',false);
    file_data{i,1}{1,1} = strcat('solid',{' '},fileList(i).name);
    file_data{i,1}{size(file_data{i},1),1} = strcat('endsolid',{' '},fileList(i).
        name);
    strfind_temp = strfind(fileList(i).name,'_');
    file_data{i,2} = fileList(i).name(strfind_temp(1)+1:strfind_temp(2)-1);
    file_data{i,1} = table2array(file_data{i,1});
end

cd .\stl_byDensityGroups
for i = 1:N
    c = 0;
    for j = 1:length(fileList)
        if str2num(file_data{j,2}) == i
            c = c+1;
            if c ==1
                temp = file_data{j,1};
            else
                temp = [temp;file_data{j,1}];
            end
        end
    end
        writecell(temp,strcat('dens_',num2str(i),'_',num2str(dens_med(i)),'_',
            num2str(dens_med(i)/dens_PLA),'.txt'));
        movefile(strcat('dens_',num2str(i),'_',num2str(dens_med(i)),'_',num2str(
            dens_med(i)/dens_PLA),'.txt'),strcat('dens_',num2str(i),'_',num2str(
            dens_med(i)),'_',num2str(dens_med(i)/dens_PLA),'.stl'));
        writecell(temp,strcat('dens_',num2str(i),'_',num2str(dens_med(i)),'_',
            num2str(dens_med(i)/dens_PLA),'.txt'));
end
cd ..
```

A.4.1 mesh.m

The variables num_e, x_nod, e_nod, n_nodes and gp_elem stand for the the total number of elements, a matrix with the coordinates of each node, a matrix with all nodes in each element, number

of nodes in each element and a matrix with the element in which an *i* gauss point is

```
function [element] = mesh_a(num_e,x_nod,e_nod,n_nodes,gp_elem)
element = cell(num_e,1);
for i =1:1:num_e
    element{i}.x = x_nod(1,e_nod(1:n_nodes,i))';
    element{i}.y = x_nod(2,e_nod(1:n_nodes,i))';
    element{i}.z = x_nod(3,e_nod(1:n_nodes,i))';
    element{i}.cent_x = mean(x_nod(1,e_nod(1:n_nodes,i)));
    element{i}.cent_y = mean(x_nod(2,e_nod(1:n_nodes,i)));
    element{i}.cent_z = mean(x_nod(3,e_nod(1:n_nodes,i)));
    element{i}.gp = zeros(1,1);
    c = 0;
    for j = 1:length(gp_elem)
        if gp_elem(j) == i
            c = c+1;
            if c ==1
                element{i}.gp = j;
            else
                element{i}.gp = [element{i}.gp j];
            end
        end
    end
end
end
```

A.4.2 smoothing.m

```
if smoothingType == 1 || smoothingType == 2 || smoothingType == 3
    for i = 1:num_e
        element{i}.dens_smooth = 0;
        for j = 1:num_e
            element{i}.dens_smooth = element{i}.dens_smooth + (ratio(i,j)*element{j
                }.dens_app);
        end
        element{i}.dens_smooth = element{i}.dens_smooth/sum(ratio(i,1:num_e));
    end
elseif smoothingType == -1
    for i = 1:num_e
        element{i}.dens_smooth = element{i}.dens_app;
    end
end
for i = 1:num_e
    maxdens(i) = max(element{i}.dens_smooth);
    mindens(i) = min(element{i}.dens_smooth);
end
```

```
min_dens = min(mindens);
max_dens = max(maxdens);
delta = (max_dens-min_dens)/N;

k = 1;
for i = 1:num_e
    while k<=N-1
        if element{i}.dens_smooth<= min_dens + k*delta
            element{i}.pos = k;
            k = N;
        else
            if k+1==N
                element{i}.pos = N;
                k = N;
            else
                k = k+1;
            end
        end
    end
    k = 1;
end
dens_med  = zeros(N,1);
for i = 1:N
    c = 1;
    for j = 1:num_e
        if element{j}.pos ==i
            dens_med(i) = ((dens_med(i)*c) + element{j}.dens_smooth)/(c+1);
            c = c+1;
        end
    end
end
```

A.4.3 groups.m

```
matrix = zeros(num_e,2);
[posmat,lengths] = sortbypos(element,N,num_e);
    for i = 1:N
        c_group = 0;
        for j = 1:lengths(i) %lengths is the an array with the number of elements
            per solid
            matrix(posmat(i,j)) = i;
            if j ==1
                c_group =c_group +1;
                element{posmat(i,j)}.group = c_group;
                matrix(posmat(i,j),1) = i;
                matrix(posmat(i,j),2) = element{posmat(i,j)}.group;
```

```
            else
                ck = 0;
                groups_to_merge = zeros(1,1);
                for k = 1:j-1
                     if length(intersect(e_nod(1:n_nodes,posmat(i,k)),e_nod(1:
                         n_nodes,posmat(i,j)))) == 4
                         ck = ck + 1;
                         groups_to_merge(ck) = matrix(posmat(i,k),2);
                     end
                end
                if ck >0
                    for k = 1:j-1
                        if ismember(matrix(posmat(i,k),2),gtm)==1
                            matrix(posmat(i,k),2) = gtm(1);
                            element{posmat(i,k)}.group = gtm(1);
                        end
                    end
                    matrix(posmat(i,j),2) = gtm(1);
                    element{posmat(i,j)}.group = gtm(1);
                elseif ck == 0
                    c_group = c_group +1;
                    element{posmat(i,j)}.group = c_group;
                    matrix(posmat(i,j),2) = c_group;
                end
            end
        end
    end
```

A.4.3.1 Function sortbypos

```
function [pos,lengths] = sortbypos(element,N,num_e)
c = 0;
pos = zeros(N,1);
lengths = zeros(N,1);
for i =1:N
    c = 0;
    for j = 1:num_e
        if element{j}.pos ==i
            c = c+1;
            pos(i,c) = j;
        end
    end
    lengths(i) = c;
end
end
```

A.4.4 createSolids

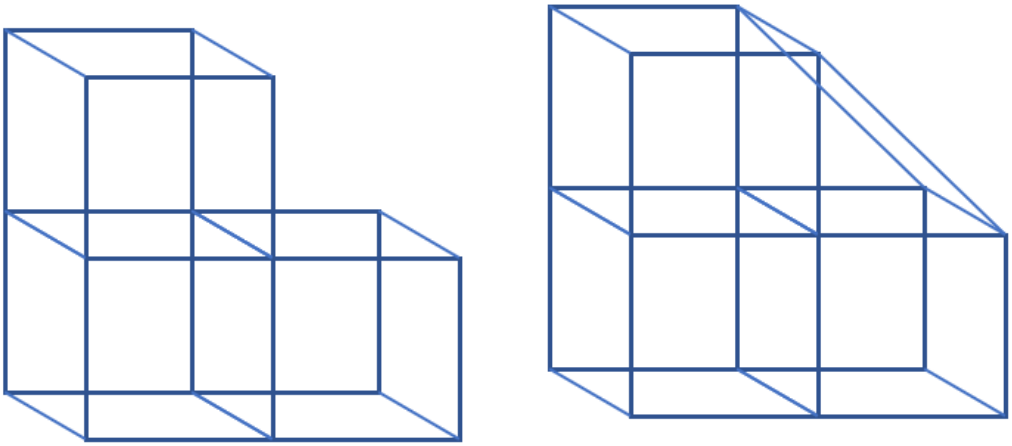
```
m = unique(matrix,'rows','stable');
for i = 1:length(m)
    c = 0;
    solid{i}.name = strcat('dens_',num2str(m(i,1)),'_group_',num2str(m(i,2)));
    for j = 1:num_e
        if element{j}.pos == m(i,1) && element{j}.group == m(i,2)
          c = c+1;
          solid{i}.element(c) = j;
        end
    end
end
```

A.4.5 triangulateSolids.m

This subroutine was constructed to overcome the difficulty in replicating the ladder effect while doing the convex hull of a three-dimensional Delaunay triangulation (Delaunay, 1934). The convex triangulation deletes the ladder effect as shown in Figure A.1. Unlike in two-dimensional triangulation, it is not possible to apply constrains as to which edges the triangulation must include in the matlab function. However some studies have been conducted in order to overcome this limitation (Cavalcanti and Mello, 1970; Liu et al., 2014).

Given that the development of a new algorithm is not the purpose of this thesis, a simpler algorithm was created. This algorithm is based on the fact that the inputs for the creation of a triangulation object in matlab are two matrices. A matrix with the coordinates of the points and a *connectivity list* which referenciates the line indexes of the points which constitute a facet. These arrays are created in the function *createList*.

```
cd(filename)
mkdir stl_solid
cd ..
ll = length(solid);
for i = 1:ll
    if length(solid{i}.element) <= 100 %adjust this tolerance as an input elsewhere
        [pointsAll,cH_All] = create_list(solid{i},element);
        cd(filename)
        cd .\stl_solid
        tri = triangulation(cH_All,pointsAll);
        stlwrite(tri,strcat(solid{i}.name,'.stl'),'text');
        movefile(strcat(solid{i}.name,'.stl'),strcat(solid{i}.name,'.csv'));
        stlwrite(tri,strcat(solid{i}.name,'.stl'),'text');
        disp(strcat('solid ',num2str(i),'/',num2str(ll),' is triangulated'))
        cd ..
        cd ..
```



(a) Correct solid

(b) Solid without the ladder effect due to the convex hull

Figure A.1: Correct solid vs inaccurate convex hull

```
17      elseif length(solid{i}.element) >100
18          disp('this solid has too many elements to handle, lets split it into
                smaller solids :))')
19          k = 1;
20          for ii = 1:100:length(solid{i}.element)
21              if ii + 99 <length(solid{i}.element)
22                  sub_solid{k}.element = solid{i}.element(ii:ii+99);
23                  sub_solid{k}.name = strcat('sub',num2str(k),solid{i}.name);
24                  k = k+1;
25              else
26                  sub_solid{k}.element = solid{i}.element(ii:length(solid{i}.element)
                        );
27                  sub_solid{k}.name = strcat('sub',num2str(k),solid{i}.name);
28              end
29          end
30          disp('the sub solids are defined :)')
31          for ii = 1:k
32              [pointsAll,cH_All] = create_list(sub_solid{ii},element);
33              cd(filename)
34              cd .\stl_solid
35              tri = triangulation(cH_All,pointsAll);
36              stlwrite(tri,strcat(sub_solid{ii}.name,'.stl'),'text');
37              movefile(strcat(sub_solid{ii}.name,'.stl'),strcat(sub_solid{ii}.name,'.
                    csv'));
38              stlwrite(tri,strcat(sub_solid{ii}.name,'.stl'),'text');
39              disp(strcat('solid ',num2str(i),' / ',num2str(ll)))
40              disp(strcat('sub_solid ',num2str(ii),' / ',num2str(k),' is triangulated
                    '))
41              cd ..
42              cd ..
43          end
```

```
44      end
45  end
```

A.4.5.1 createList

The *createList* function gradually triangulates each hexahedral element and adds it to the main connectivity list. If some triangles are repeated then those will be eliminated.

This process takes an exponentially longer time as long as the element list for a solid is. For that reason, if a list is longer than 100 elements, it is split into 100 elements sub-groups which are indivudually traingulated and concatenated. The 100 element threshold was defined in an iterative way as the amount of elements triangulated in 1 minute. Moreover, it is important to point out that *cH* is referent to the connectivity lost formed by the *convexHull* and dT is referent to the *delaunayTriangulation* which is necessary to generate the *convexHull*.

```
1  function [pointsAll,cH_All] = create_list(obj,element)
2      dT_temp = delaunayTriangulation(element{obj.element(1)}.x,element{obj.element
           (1)}.y,element{obj.element(1)}.z);
3      cH_temp = convexHull(dT_temp);
4      tri_temp = triangulation(cH_temp,dT_temp.Points);
5      normals = faceNormal(tri_temp);
6      normals = round(normals,1);
7      [normals,~,ic] = unique(normals,'rows');
8      obj.faces = zeros(1,4);
9      obj.normals = zeros(1,3);
10     for ii = 1:length(ic)-1
11         for jj = ii+1:length(ic)
12             if ic(ii) == ic(jj)
13                 a = [cH_temp(ii,:) cH_temp(jj,:)];
14                 obj.faces = [obj.faces; unique(a)];
15                 obj.normals= [obj.normals; normals(ic(ii),:)];
16             end
17         end
18     end
19     obj.faces(1,:) = [];
20     obj.normals(1,:) = [];
21     pointsAll = dT_temp.Points;
22     cH_All = cH_temp;
23     if length(obj.element)>1
24         for j = 2:length(obj.element)
25             disp(j)
26             dT_temp = delaunayTriangulation(element{obj.element(j)}.x,element{obj.
                   element(j)}.y,element{obj.element(j)}.z);
27             cH_temp = convexHull(dT_temp);
28             pointsTemp = dT_temp.Points;
29             tri_temp = triangulation(cH_temp,dT_temp.Points);
30             normals = faceNormal(tri_temp);
```

```
            normals = round(normals,1);
            [normals,~,ic] = unique(normals,'rows');
            [~,indices] = ismember(pointsTemp,pointsAll,'rows');
            ch_2 = zeros(length(cH_temp),3);
            for kk = 1:length(indices)
                if indices(kk) == 0
                    ch_2(cH_temp == kk) = length(pointsAll)+1;
                    pointsAll = [pointsAll;pointsTemp(kk,:)];
                else
                    ch_2(cH_temp == kk) = indices(kk);
                end
            end
            cH_All = [cH_All;ch_2];
            for ii = 1:length(ic)-1
                for jj = ii+1:length(ic)
                    if ic(ii) == ic(jj)
                        a = [ch_2(ii,:) ch_2(jj,:)];
                        disp(unique(a))
                        obj.faces = [obj.faces; unique(a)];
                        obj.normals= [obj.normals; normals(ic(ii),:)];
                    end
                end
            end
            c = 0;
            facetemp = zeros(1,4);
            remove_i = zeros(1,1);
            remove_j = zeros(1,1);
            for ii = 1:length(obj.faces)-1
                for jj = ii+1:length(obj.faces)
                    if length(intersect(obj.faces(ii,:),obj.faces(jj,:))) == 4
                    % if the points are the same then it is the same face
                        c = c+1;
                        facetemp(c,:) = obj.faces(ii,:);
                        remove_i(c) = ii;
                        remove_j(c) = jj;
                    end
                end
            end
            if all(facetemp) == 1
            clear remove
            remove = unique([remove_i remove_j],'rows','sorted');
            k = -1;
            if isempty(find(~remove))==1%%
                for kk= 1:length(remove)
                    k = k+1;
                    obj.faces(remove(kk)-k,:) = [];
                    obj.normals(remove(kk)-k,:) = [];
                end
            end
```

```
80            c = 0;
81            to_remove = zeros(1,1);
82            for kk = 1:size(facetemp,1)
83                for jj = 1:length(cH_All)
84                    if length(intersect(facetemp(kk,:),cH_All(jj,:))) == 3
85                        c = c+1;
86                        to_remove(c,1) = jj;
87                    end
88                end
89            end
90            k = -1;
91            to_remove = sort(to_remove);
92            for kk = 1:length(to_remove)
93                k = k+1;
94                cH_All(to_remove(kk)-k,:) = [];
95            end
96            end
97        end
98    end
99    end
```

Appendix B

Technical Drawings

B.1 Tool for 4 point flexural testing

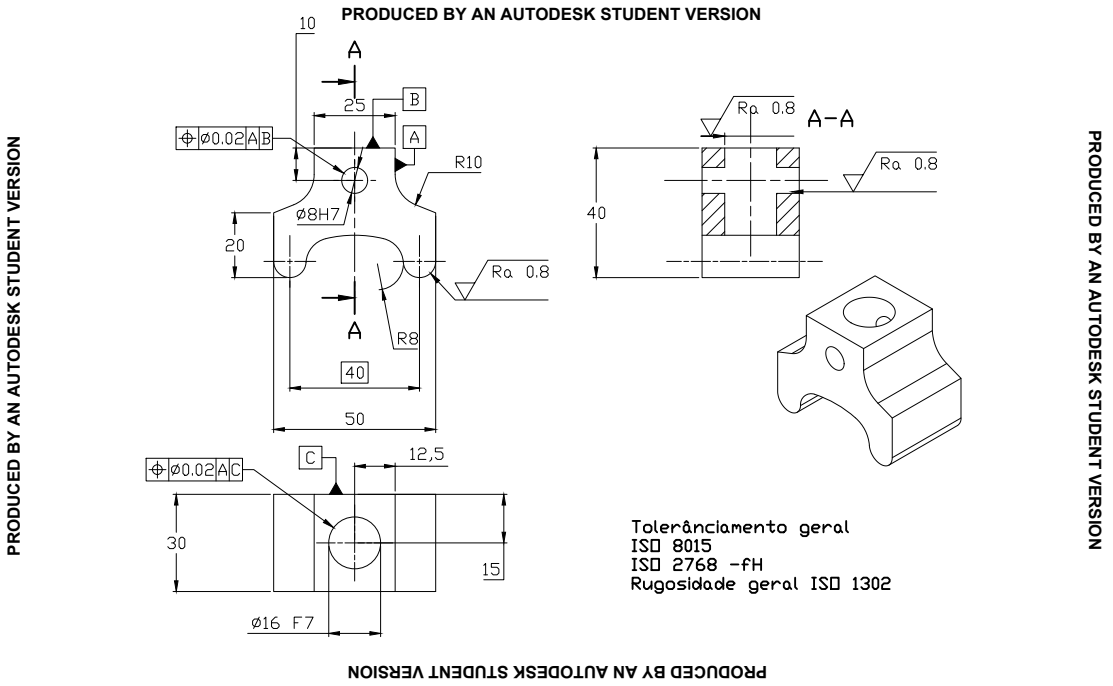


Figure B.1: Four point flexural testing tool. This part was manufactured via CNC milling in steel.

B.2 Support for the specimens while testing

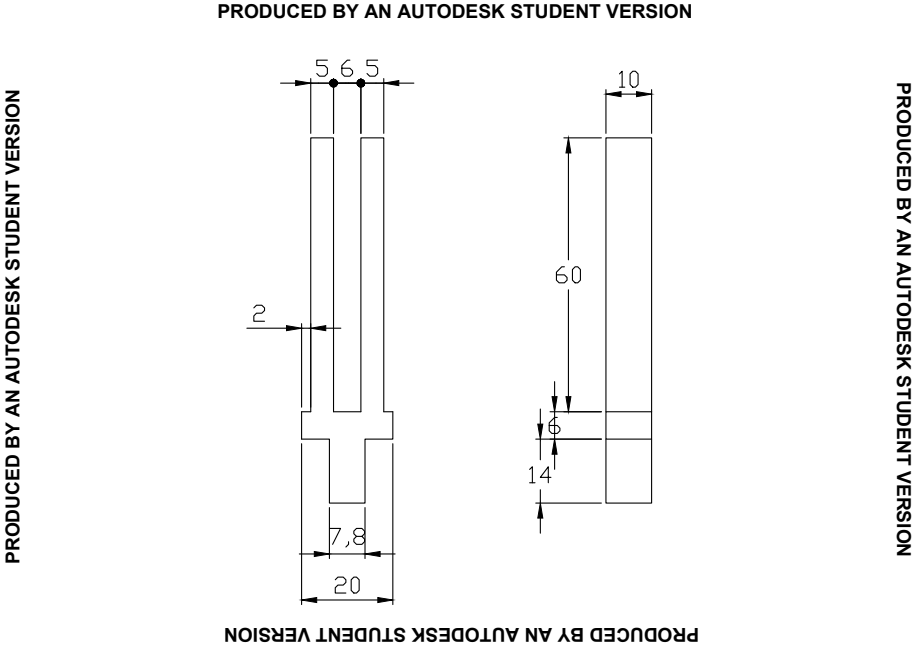


Figure B.2: Support for the specimens while testing to avoid tumbling. This part fits inside the slot on the tool already available in the testing machine and was printed via FFF in PLA.

B.3 Positioning tool

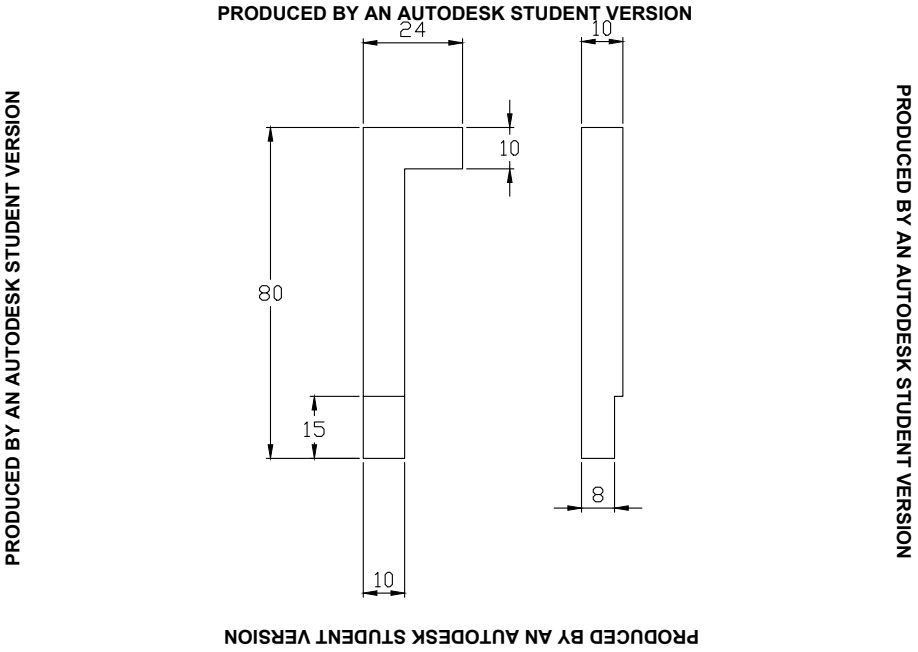


Figure B.3: Positioning tool. This part was printed via FFF in PLA.

B.4 Support tool for testing of the femur scaffold specimens

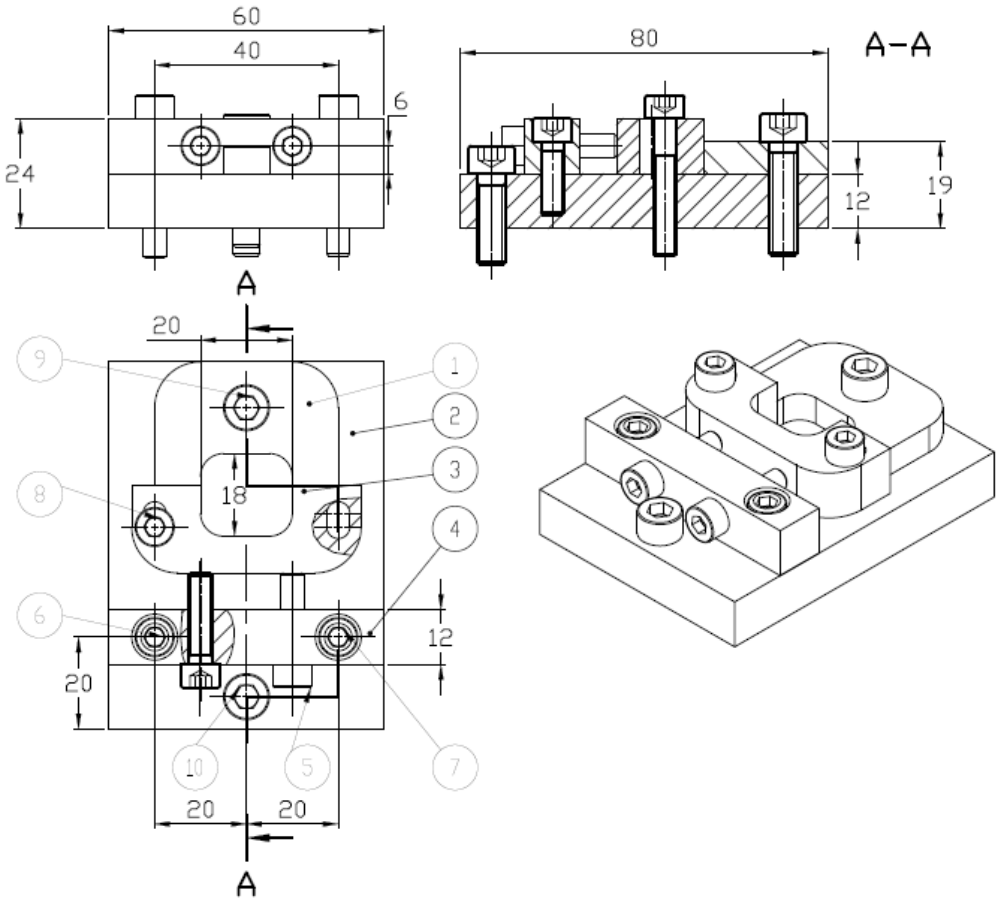


Figure B.4: Fixation tool for testing of the femur-shaped prototypes. This assembly was built in aluminium and is designed in order to fit into the already existing slot in the testing machine.

Table B.1: Part list

No.	Description	Qty.	Material
1	Fixed part	1	Aluminium
2	Moving Part	1	Aluminium
3	Base	1	Aluminium
4	Adjustment tool	1	Aluminium
5	ISO 4762 M5 x 20 - 20N	2	
6	ISO 4762 M5 x 25 - 25N	1	
7	ISO 4762 M5 x 8 - 8N	1	
8	ISO 4762 M5 x 30 - 22N	2	
9	ISO 4762 M6 x 25 - 25N	1	
10	ISO 4762 M6 x 16 - 16N	1	

Appendix C

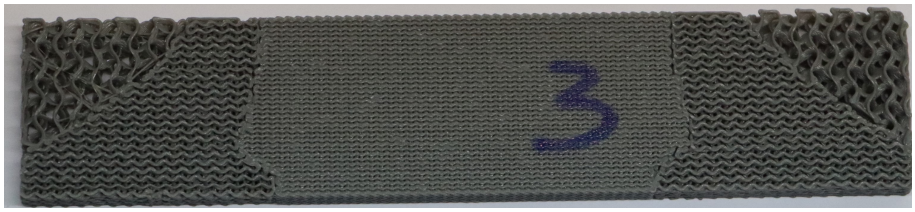
Printed and Tested Specimens

C.1 Structural optimization - Parabolic Law

It was not possible to obtain a picture regarding a sample from load case 1/FEM/smoothing type 1 MDR 0.2.



(a) No smoothing



(b) Smoothing type 1 MDR 0.1



(c) Smoothing type 1 MDR 0.1 vertical



(d) Smoothing type 3

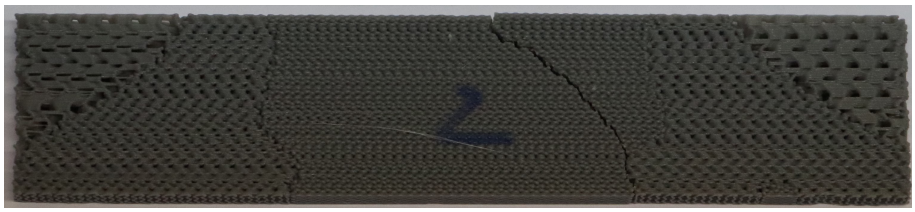
Figure C.1: Load case 1 - FEM



(a) No smoothing



(b) Smoothing type 1 MDR 0.1



(c) Smoothing type 1 MDR 0.1 vertical



(d) Smoothing type 1 MDR 0.2



(e) Smoothing type 3

Figure C.2: Load case 1 - NNRPIM



(a) Smoothing type 1 MDR 0.1



(b) Smoothing type 1 MDR 0.1 vertical



(c) Smoothing type 1 MDR 0.2



(d) Smoothing type 3

Figure C.3: Load case 2 - FEM



(a) Smoothing type 1 MDR 0.1



(b) Smoothing type 1 MDR 0.1 vertical

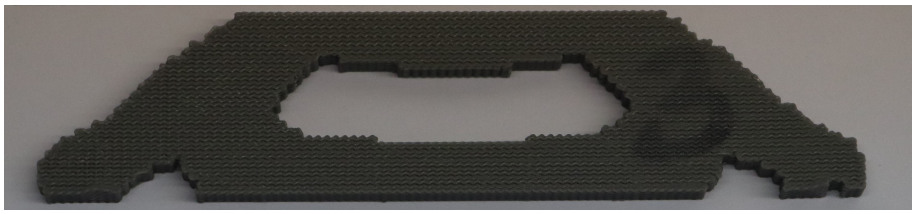


(c) Smoothing type 1 MDR 0.2



(d) Smoothing type 3

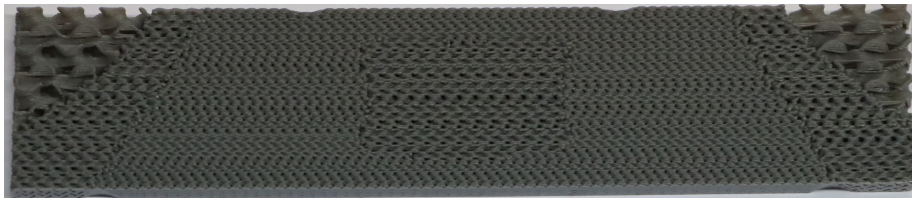
Figure C.4: Load case 2 - NNRPIM



(a) No smoothing



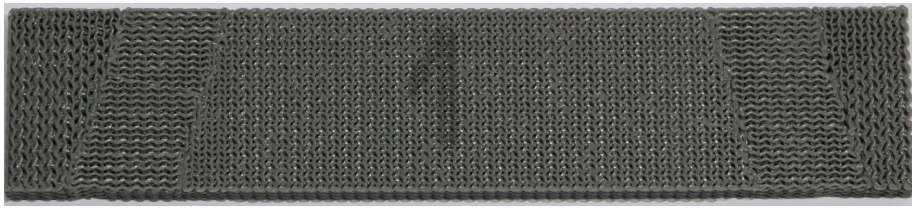
(b) Smoothing type 1 MDR 0.1



(c) Smoothing type 1 MDR 0.1 vertical



(d) Smoothing type 1 MDR 0.2



(e) Smoothing type 3

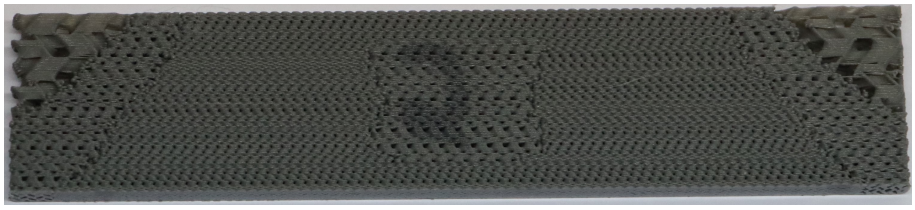
Figure C.5: Load case 3 - FEM



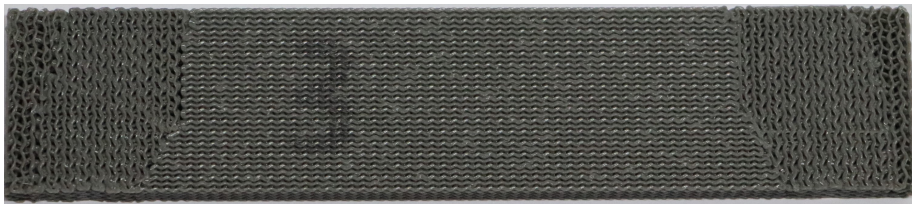
(a) No smoothing



(b) Smoothing type 1 MDR 0.1



(c) Smoothing type 1 MDR 0.1 vertical



(d) Smoothing type 1 MDR 0.2



(e) Smoothing type 3

Figure C.6: Load case 3 - NNRPIM

C.2 Structural optimization - Linear law

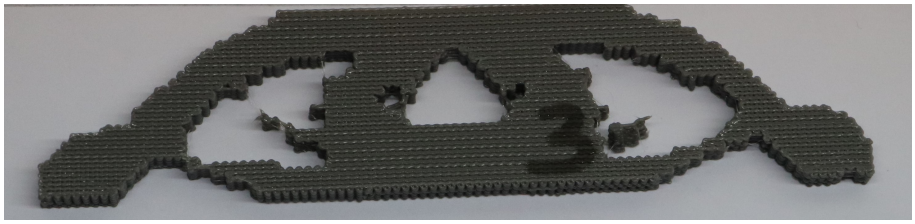


(a) No smoothing



(b) Smoothing type 1 MDR 0.1

Figure C.7: Load case 1 - FEM



(a) No smoothing



(b) No smoothing - reinforced structure

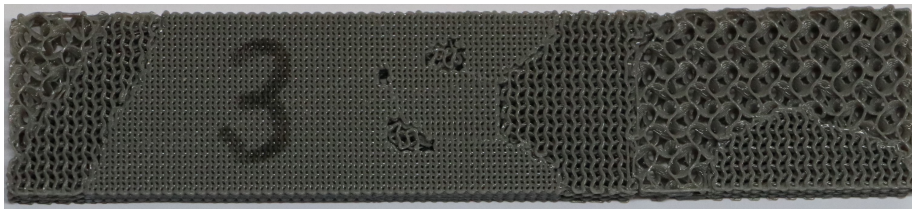


(c) Smoothing type 1 MDR 0.1

Figure C.8: Load case 1 - NNRPIM



(a) No smoothing



(b) Smoothing type 1 MDR 0.1

Figure C.9: Load case 2 - FEM

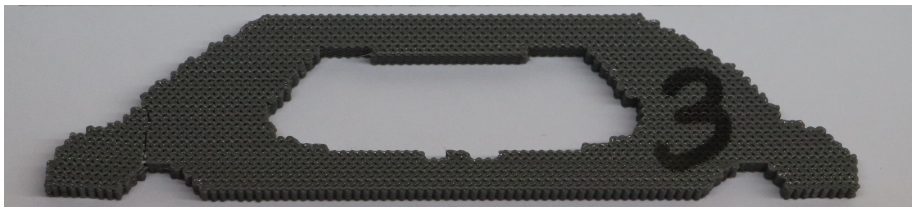


(a) No smoothing

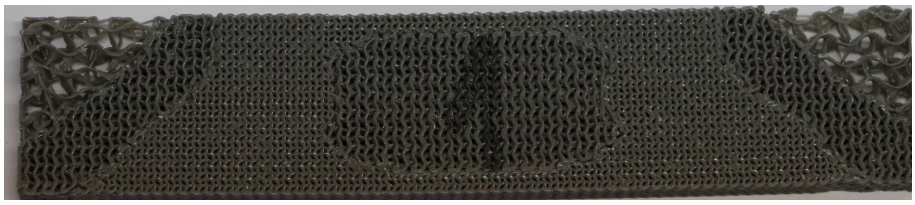


(b) Smoothing type 1 MDR 0.1

Figure C.10: Load case 2 - NNRPIM

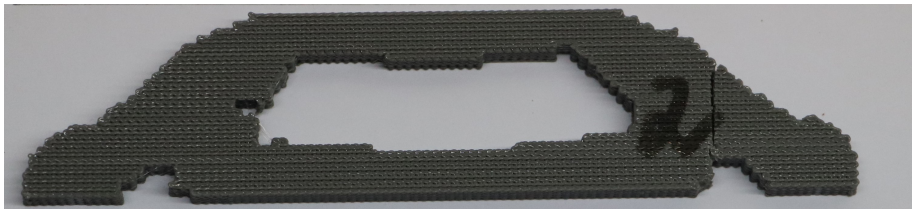


(a) No smoothing

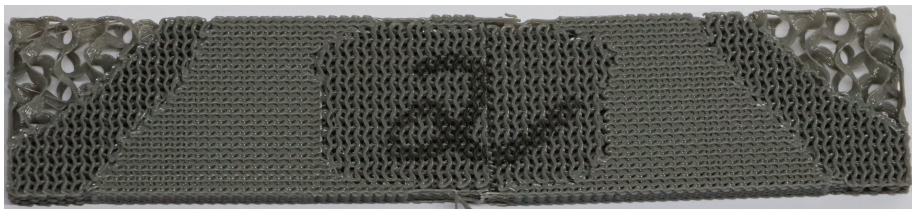


(b) Smoothing type 1 MDR 0.1

Figure C.11: Load case 3 - FEM



(a) No smoothing



(b) Smoothing type 1 MDR 0.1

Figure C.12: Load case 3 - NNRPIM

C.3 Gyroid remodelling law 1



(a) No smoothing



(b) Smoothing type 1 MDR 0.1



(c) Smoothing type 1 MDR 0.1 vertical



(d) Smoothing type 1 MDR 0.2

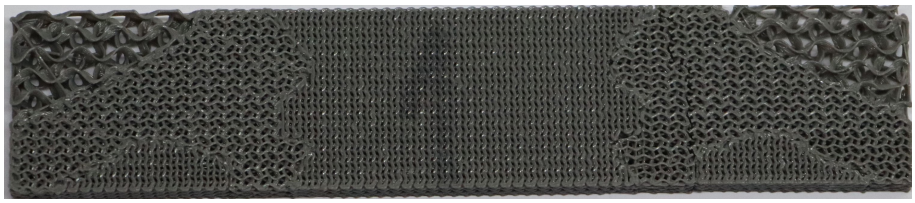


(e) Smoothing type 3

Figure C.13: Load case 1 - FEM



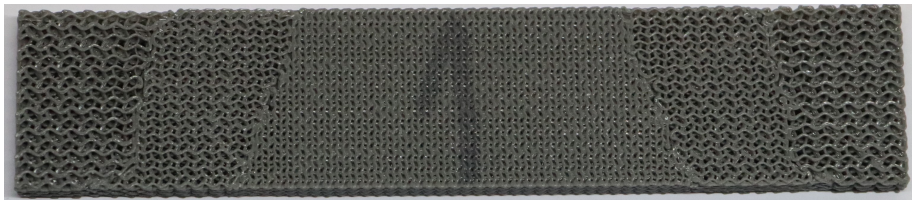
(a) No smoothing



(b) Smoothing type 1 MDR 0.1



(c) Smoothing type 1 MDR 0.1 vertical

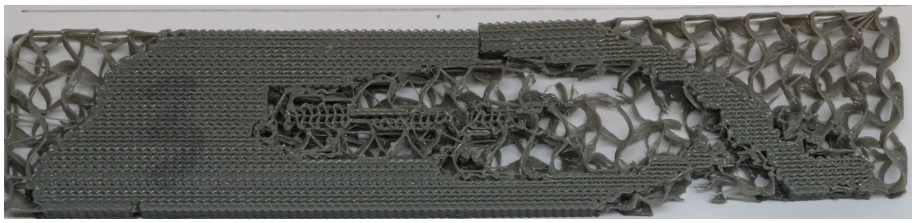


(d) Smoothing type 1 MDR 0.2



(e) Smoothing type 3

Figure C.14: Load case 1 - NNRPIM



(a) No smoothing



(b) Smoothing type 1 MDR 0.1



(c) Smoothing type 1 MDR 0.1 vertical



(d) Smoothing type 1 MDR 0.2



(e) Smoothing type 3

Figure C.15: Load case 2 - FEM



(a) No smoothing



(b) Smoothing type 1 MDR 0.1



(c) Smoothing type 1 MDR 0.1 vertical



(d) Smoothing type 1 MDR 0.2

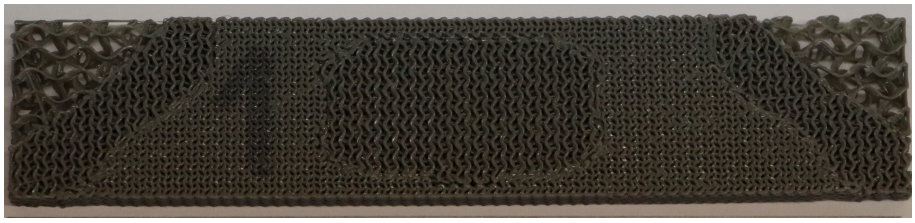


(e) Smoothing type 3

Figure C.16: Load case 2 - NNRPIM



(a) No smoothing



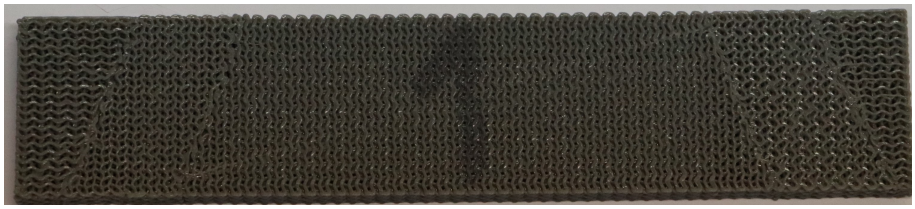
(b) Smoothing type 1 MDR 0.1



(c) Smoothing type 1 MDR 0.1 vertical



(d) Smoothing type 1 MDR 0.2

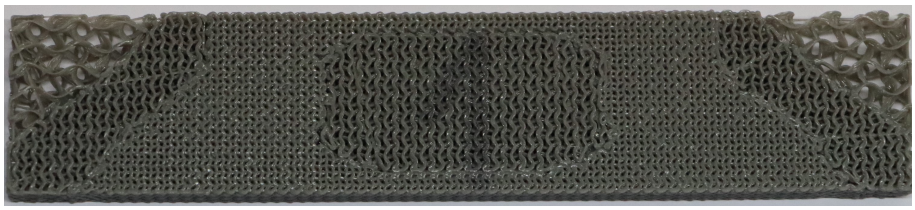


(e) Smoothing type 3

Figure C.17: Load case 3 - FEM



(a) No smoothing



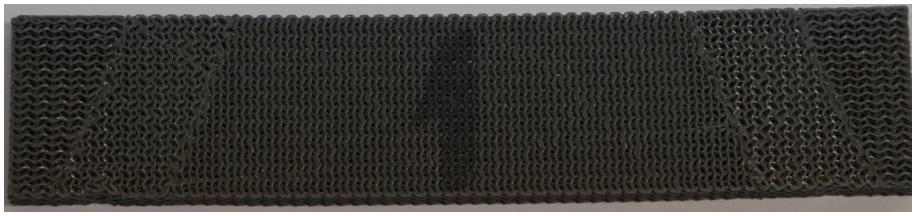
(b) Smoothing type 1 MDR 0.1



(c) Smoothing type 1 MDR 0.1 vertical



(d) Smoothing type 1 MDR 0.2



(e) Smoothing type 3

Figure C.18: Load case 3 - NNRPIM

C.4 Gyroid remodelling law 2

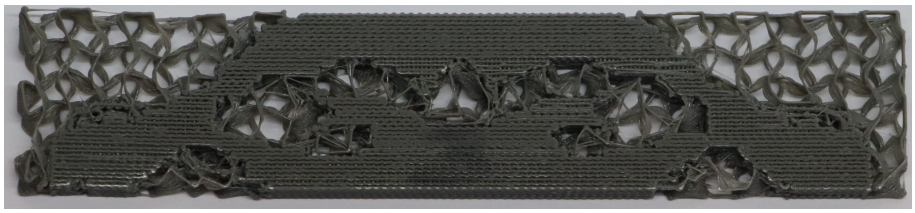


(a) No smoothing



(b) Smoothing type 1 MDR 0.1

Figure C.19: Load case 1 - FEM



(a) No smoothing



(b) Smoothing type 1 MDR 0.1

Figure C.20: Load case 1 - NNRPIM

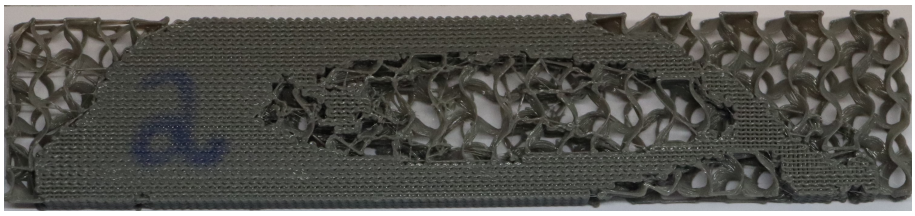


(a) No smoothing



(b) Smoothing type 1 MDR 0.1

Figure C.21: Load case 2 - FEM



(a) No smoothing

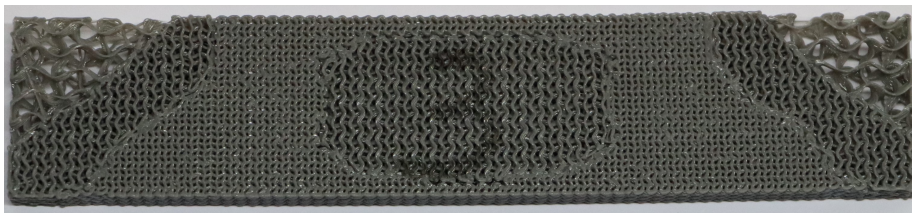


(b) Smoothing type 1 MDR 0.1

Figure C.22: Load case 2 - NNRPIM



(a) No smoothing

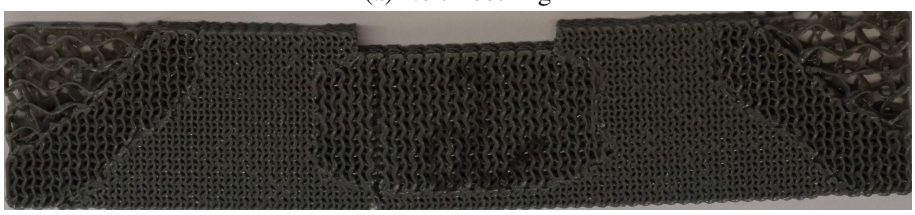


(b) Smoothing type 1 MDR 0.1

Figure C.23: Load case 3 - FEM



(a) No smoothing



(b) Smoothing type 1 MDR 0.1

Figure C.24: Load case 3 - NNRPIM

C.5 Femur scaffold prototypes

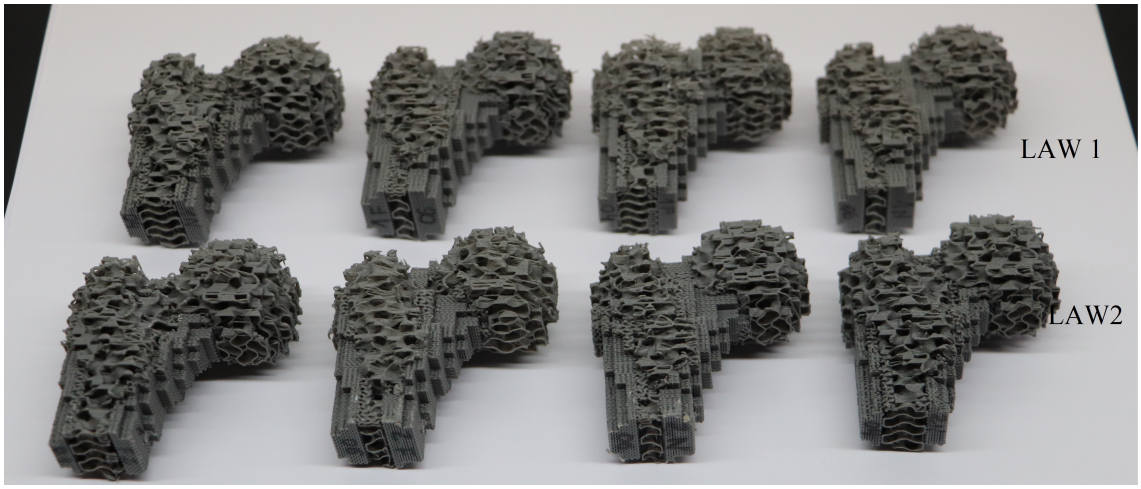


Figure C.25: Femur scaffold prototypes